Absolute densities of reactive species in a cold atmospheric pressure plasma jet:

Spatial distributions in the effluent determined by optical diagnostic methods

Inauguraldissertation

zur

Erlangung des akademischen Grades eines

Doktors der Naturwissenschaften (Dr. rer. nat.)

der

Mathematisch-Naturwissenschaftlichen Fakultät

der

Universität Greifswald

vorgelegt von

Sarah-Johanna Klose

Greifswald, den 28.02.2022

Dekan: Prof. Dr. Gerald Kerth
1. Gutachter: Prof. Dr. Jürgen Röpcke
2. Gutachter: Prof. Dr. Richard Engeln
Tag der Promotion: 15.08.2022

The three great essentials to achieve anything worth while are, first, hard work; second, sticktoitiveness; third, common sense.

Thomas A. Edison

Contents

Zusammenfassung

In dieser Arbeit wurden die räumlichen Dichteverteilungen reaktiver stabiler und transienter Spezies, die am Reaktionszyklus von H_2O_2, einer Schlüsselspezies für biomedizinische Anwendungen, beteiligt sind, direkt im Effluenten eines kINPen-sci-Plasmajets bestimmt. Der kleine Durchmesser von kalten Atmosphärendruckplasmajets und ihr Betrieb bei Atmosphärendruck, der starke Quenchingreaktionen verursacht, erschweren die Diagnostik. In dieser Arbeit wurden verschiedene Diagnostiken eingesetzt und für den Einsatz im Effluenten eines kalten Atmosphärendruckplasmajets angepasst: Atomare Laserabsorptionsspektroskopie (LAAS) bei 811,5 nm zum Nachweis von $Ar(^3P_2)$, pikosekundengepulste zweiphotonenlaserinduzierte Fluoreszenzspektroskopie (ps-TALIF) bei 225 nm und 205 nm zum Nachweis von O- und H-Atomen, und kontinuierliche Cavity-Ring-Down-Spektroskopie (cw-CRDS) bei 1,506 μm zum Nachweis von HO_2 und cw-CRDS bei 8,000 μm zum Nachweis von H_2O_2. Der Schwerpunkt dieser Arbeit lag in der Ermittlung von räumlichen absoluten Dichteverteilungen innerhalb des kleinen Durchmessers des Effluenten des kINPen-sci Plasmajets, die bisher noch nicht untersucht wurden. Auf der Grundlage der ermittelten Verteilungen für H-Atome, O-Atome, HO_2-Radikale und H_2O_2-Moleküle und des untersuchten Einflusses der Feuchtigkeit im Trägergas auf die Anregungsdynamik und die Produktion von $Ar(^3P_2)$, sowie mittels eines Vergleichs der experimentellen Ergebnisse mit einem plasmachemischen und reaktiven Strömungsmodell wurden drei verschiedene Zonen mit unterschiedlicher Reaktionskinetik identifiziert. Die Dichten in der Nähe der Düse des kINPen-sci-Plasmajets wurden von Reaktionen innerhalb der Plasmazone dominiert, einschließlich der Dissoziation von H_2O, das dem Ar-Trägergas zugesetzt wurde, und O_2, das vermutlich durch gegenläufige Ionisationswellen in die Plasmazone übertragen wurde. Bemerkenswert ist, dass auch die größeren Moleküle, wie HO_2 und H_2O_2, hauptsächlich in der Plasmazone des Plasmajets gebildet wurden. Zwischen 1,5 mm und 5 mm unterhalb der Düse wurden atomare Spezies und molekulare Radikale durch die umgebende Gaszusammensetzung verbraucht. In weiteren Entfernungen von der Düse, in der sich typischerweise biologische Proben befinden, wurden hauptsächlich H_2O_2 und HO_2 Moleküle beobachtet.

Mit dieser Arbeit wird erfolgreich demonstriert, dass selbst für die kleinen Durchmesser von kalten Atmosphärendruckplasmajets die Bestimmung von räumlichen Dichteverteilungen für reaktive transiente und stabile Spezies innerhalb des Effluenten möglich ist. Durch die Zusammenführung der experimentellen Ergebnisse konnten wichtige Erkenntnisse über die Bildung und den Verbrauch von H_2O_2 und seinen Edukten gewonnen werden, die für das Verständnis von Plasmen in biomedizinische Anwendungen wesentlich sind.

Abstract

In this work, spatial distributions for reactive stable and transient species that are involved in the reaction cycle of H_2O_2, a key species for biomedical applications, were determined directly in the effluent of a kINPen-sci plasma jet. The small diameter of cold atmospheric pressure plasma jets and their operation at atmospheric pressure that causes strong quenching reactions make diagnostics challenging. Here, various diagnostic techniques have been employed and adapted for the use in the effluent of a cold atmospheric pressure plasma jet, which were laser atomic absorption spectroscopy (LAAS) at 811.5 nm for the detection of $Ar(^3P_2)$, picosecond two-photon absorption laser-induced fluorescence spectroscopy (ps-TALIF) at 225 nm and 205 nm for the detection of O and H atoms, respectively, and continuous wave cavity ring-down spectroscopy (cw-CRDS) at 1.506 µm for the detection of HO_2, and cw-CRDS at 8000 µm for the detection of H_2O_2. All these methods provide absolute number densities. In this work, spatial distributions within the small diameter of the effluent of a CAPJ were obtained, which have not been reported so far literature. In order to overcome the line-of-sight limitations of CRDS, radial scans were performed and transformed into a spatial distribution by using Abel inversion.

Based on the determined spatial density distributions for H atoms, O atoms, HO_2 radicals, and H_2O_2 molecules, together with the investigated impact of humidity in the feed gas on the excitation dynamics and the production of $Ar(^3P_2)$, and finally on a comparison of the experimental results to a plasma chemical and reacting flow model, three different zones with varying reaction kinetics were identified. The densities close to the nozzle of the kINPen-sci plasma jet were dominated by reactions within the plasma zone including the dissociation of H_2O added to the Ar feed gas and O_2 that was presumably transferred into the plasma zone by counter-propagating ionisation waves. Notably, also the larger molecules, such as HO_2 and H_2O_2 were mainly formed within the plasma zone of the plasma jet. Between 1.5 mm and 5 mm below the nozzle, the atomic species and molecular radicals generated in the plasma zone were consumed by chemical reactions with the surrounding gas, whose composition was controlled by applying a gas curtain. At further distances from the nozzle, where typically biological samples are positioned, only H_2O_2 and HO_2 were observed.

With this work, it is successfully demonstrated that even for the small diameters of cold atmospheric pressure plasma jets the determination of spatial profiles for reactive transient and stable species is possible within the effluent. By combining the experimental results, important insights into the formation and consumption of H_2O_2 and its precursors were gained, which are essential for the understanding of use of plasmas in biomedical applications.

List of abbreviations

AOM	acousto-optic modulator
AS	absorption spectroscopy
AAS	atomic absorption spectroscopy
LAAS	laser atomic absorption spectroscopy
DLAAS	diode laser atomic absorption spectroscopy
BNC	Bayonet Neill–Concelman
CAPJ	cold atmospheric pressure plasma jet
CEAS	cavity-enhanced absorption spectroscopy
OF-CEAS	optical feedback cavity-enhanced absorption spectroscopy
CRDS	cavity ring-down spectroscopy
cw-CRDS	continuous wave cavity ring-down spectroscopy
DAQ	data acquisition unit
FC	fiber coupling
FWHM	full width at half maximum
HITRAN	high-resolution transmission molecular absorption
HWHM	half width at half maximum
iCCD	intensified charge-coupled device
LAS	laser absorption spectroscopy
TDLAS	tunable diode laser absorption spectroscopy
QCLAS	quantum cascade laser absorption spectroscopy
LIF	laser-induced fluorescence spectroscopy
MIR	mid infrared
NIR	near infrared
OAP	off-axis parabolic mirror
OES	optical emission spectroscopy
OPA	optical parametric amplifier
OPO	optical parametric oscillator
PC	personal computer
QCL	quantum cascade laser
RONS	reactive oxygen-nitrogen species
TALIF	two-photon absorption laser-induced fluorescence spectroscopy
fs-TALIF	femtosecond TALIF
ns-TALIF	nanosecond TALIF
ps-TALIF	picosecond TALIF
USB	universal serial bus
UV	ultraviolet
VUV	vacuum ultraviolet

List of chemical species

Ar	argon
Ar*	metastables of argon
Ar(^{3}P$_2$)	metastable argon atoms in the ^{3}P$_2$ state
Ar$_2^*$	excited dimers of argon, also denotes as Ar excimers
CH$_4$	methane
Cu	copper
H	atomic hydrogen
HCN	hydrogen cyanide
He	helium
He(2^3S$_1$)	metastable helium atoms in the 2^3S$_1$ state
HNO$_3$	nitric acid
HONO	nitrous acid
H$_2$O	water
HO$_2$	hydroperoxyl radical
H$_2$O$_2$	hydrogen peroxide
Kr	krypton
N	atomic nitrogen
N$_2$	molecular nitrogen
N$_2^+$	nitrogen ion
NH$_3$	ammonia
N$_2$O	nitrous oxide
N$_2$O$_5$	dinitrogen pentoxide
NO	nitric oxide
NO$_2^-$	nitrite
NO$_3^-$	nitrate
O	atomic oxygen
O$_2$	molecular oxygen
O$_2^-$	superoxide ions
O$_3$	ozone
OH	hydroxyl radical
ONOO$^-$	peroxynitrite
Xe	xenon

1 Introduction

1.1 Cold atmospheric pressure plasma jets and their applications

During the last 30 years, the development of cold atmospheric pressure plasma jets (CAPJs) has expanded the horizon for the localised treatment of heat sensitive materials. CAPJs have become an important technology for materials processing [1–3], plasma medicine [4–9] and plasma agriculture [10, 11]. In particular for the modification of polymer surfaces, such as the localised change of the adhesion for fluids [12–17], the deposition of oxide layers [18, 19], and well-controlled etching processes [20, 21], CAPJs have been proven as a powerful tool. Furthermore, CAPJ have become a valuable technology for sterilisation and decontamination in biomedical applications, as they are confirmed to inactivate (multi-resistant) bacteria on surfaces and in liquids efficiently [22–25]. Due to their potential to induce cell death while simultaneously stimulating immune reactions, CAPJs have developed to a capable device for dermatology and wound healing [25–28], and are also investigated for the employment in cancer therapy [29–31]. In particular during the last 16 years, the number of publications with the key words "cold atmospheric pressure plasma jets" documented in Web of Science [32] has increased by a factor of approximately 5.5 per year from 4 publications in 2005 to 93 publications in 2021. In figure 1.1, the number of publications documented in Web of Science [32], found by using the key words "cold atmospheric pressure plasma jet" and the sub-key words "medicine", "agriculture", and "polymers" are depicted as a function of the year of publication. Within last 6 years, more than half of the articles were connoted to the sub-key words "medicine", "agriculture", and "polymers".

A CAPJ is a device that produces a self-sustaining gas discharge at atmospheric pressure, while the electron temperature is in the order of a few electron volts (eV) and the gas temperature remains around room temperature [33]. Usually, noble gases, such as helium (He) or argon (Ar) with admixtures of a few percent of molecular oxygen (O_2), molecular nitrogen (N_2) or water (HO_2) are used as the feed gases [33–36]. Depending on the specific device, the plasma is operated between a powered and a grounded electrode with plane parallel or coaxial geometry, by applying short voltage pulses with a duration of a few nanoseconds or by applying voltages with periodic waveforms at frequencies between kHz and GHz [33–36]. An example for a plane parallel configuration is the COST-Reference plasma jet, which is operated with an excitation frequency of 13.56 MHz [37, 38]. The COST-Reference plasma jet is a derivative of the so-called µAPPJ: a plasma jet with two plane parallel electrodes with a distance of approximately
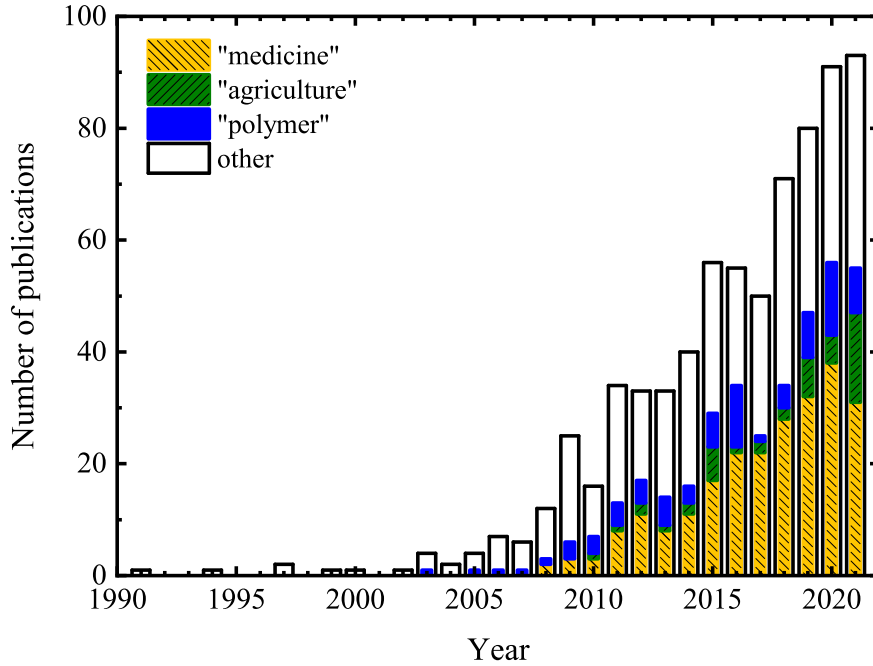
Figure 1.1: Number of publications with the key words "cold atmospheric pressure plasma jet" and the sub-key words "medicine", "agriculture", or "polymers" until 2021 as documented in Web of Science [32].

1 mm that confine, together with two plates made of fused silica, a rectangular channel for the applied gas flow [39]. For coaxial plasma jets, several configurations have been reported [34–36]. Most of the coaxial jets consist of a dielectric capillary, where at least one electrode is a surrounding ring electrode. The feed gas flow is directed through the capillary that also prevents arcing. For example, the kINPen®Med plasma jet, which has been certified for biomedical applications [40], is a coaxial plasma jet with an inner powered needle and an outer grounded ring electrode.

Due to the operation at atmospheric pressure, the dimensions of the plasma zone and of the effluent of a CAPJ is usually in the order of mm [33–36]. This enables localised treatments of substrates and biological samples with electrons, electric fields, ultraviolet/vacuum-ultraviolet photons, and a large number of reactive species including atomic and molecular radicals while having a low gas temperature. In particular, reactive species that contain oxygen, hydrogen and nitrogen, also known as reactive oxygen nitrogen species (RONS), have been found to be key species that trigger cell growth and cell death [41–43]. Among these are hydrogen atoms (H), oxygen atoms (O), nitric oxide (NO), hydroxyl radicals (OH), hydroperoxyl radicals (HO_2), superoxide ions (O_2^-), nitrite (NO_2^-), nitrate (NO_3^-), peroxynitrite ($ONOO^-$), and hydrogen peroxide (H_2O_2) [44–50].

With the increasing number of applications for CAPJs, their adaptability becomes more and more important, in particular for their utilisation for decontamination, sterilisation, wound healing and cancer therapy. One important question, on the forefront of
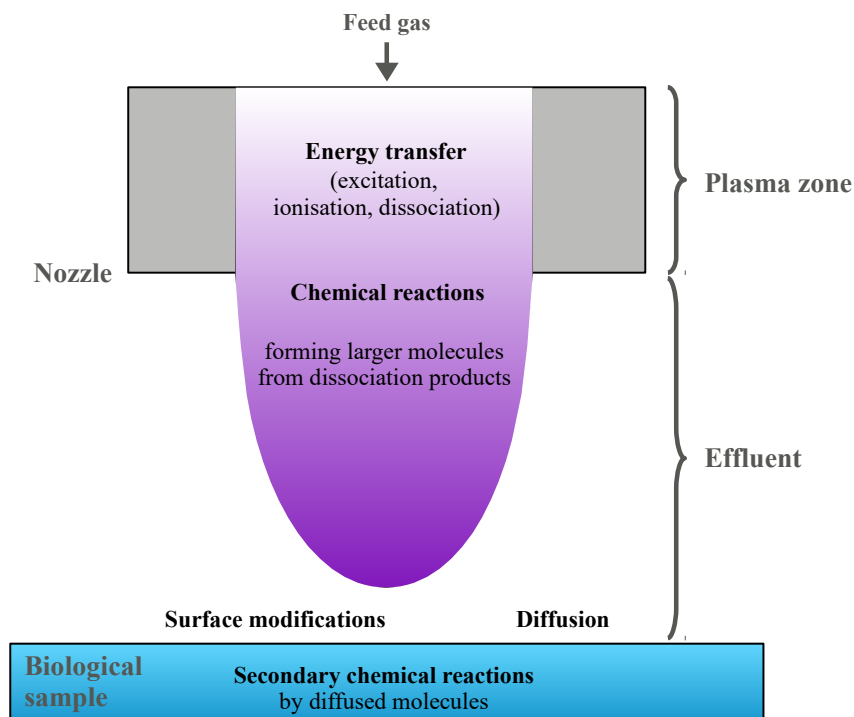
Figure 1.2: Schematic with different zones of reactions to be considered for the interaction of a cold atmospheric pressure plasma jet with a biological sample.

this research field, is how the reactive species composition can be tailored for a specific purpose. Therefore, a thorough understanding of the chemical reactions occurring in the plasma zone and the effluent is required. In figure 1.2, a schematic of the complex system of a CAPJ interacting with a biological sample is shown. In the plasma zone inside the CAPJ device, high energetic electrons and metastable atoms are produced by energy transfer reactions between species and electric fields at the electrodes. These high energetic electrons and metastable atoms initiate dissociation reactions of molecular admixtures in the feed gas. The dissociation products, often radicals, undergo chemical reactions with the feed gas admixtures to form larger molecules. In the effluent, reactions with the surrounding gas increase the number of reactive species. Those reactive species interact with the treated surface of the biological sample or diffuse into the material. Within the biological sample, further dissociation or the formation of even larger molecules can occur by secondary reactions that enable for example inter and intra cellular communication. In order to tailor the plasma reactions with the biological sample, the reactive species composition in the gas phase and the most relevant chemical reactions need to be well understood.

1.2 The kINPen-sci plasma jet

The kINPen is a cold atmospheric pressure plasma jet that was developed at the Leibniz Institute for Plasma Science and Technology in Greifswald for localised treatments of heat sensitive surfaces [51–54]. Based on the kINPen, several modified versions have emerged, including the certified model kINPen®Med that is employed for biomedical applications, and a scientific version, the kINPen-sci, that allows for more detailed adjustments of the power and the gas flow rate, for instance. The kINPen-sci plasma jet, which was investigated in this work, is composed of a dielectric capillary with an inner diameter of 1.6 mm, in which the plasma is operated between a powered needle electrode inside and a grounded ring-electrode outside. The capillary and its surrounding ring-electrode are covered by a metallic mantel piece, the head of the plasma device, which shields the environment from electric fields inside the device. A power supply is directly connected to the head, which provides an alternating voltage around 1 kV (power between 1 and 3 W) with a frequency of approximately 1 MHz at the inner needle electrode. Typically, 3 slm of Ar or He are used as a feed gas, whereby admixtures of molecular gases up to a few percent can be added. In order to control the effluents' surrounding atmosphere, a gas curtain device can be applied that provides a concentric flow of typically 5 slm. The composition of the gas curtain is typically varied from 100% O_2 to 100% N_2 by changing the mixture of O_2 and N_2. In figure 1.3, a schematic of the kINPen-sci plasma jet is illustrated. Only the effluent below the nozzle is accessible for optical diagnostic purposes.
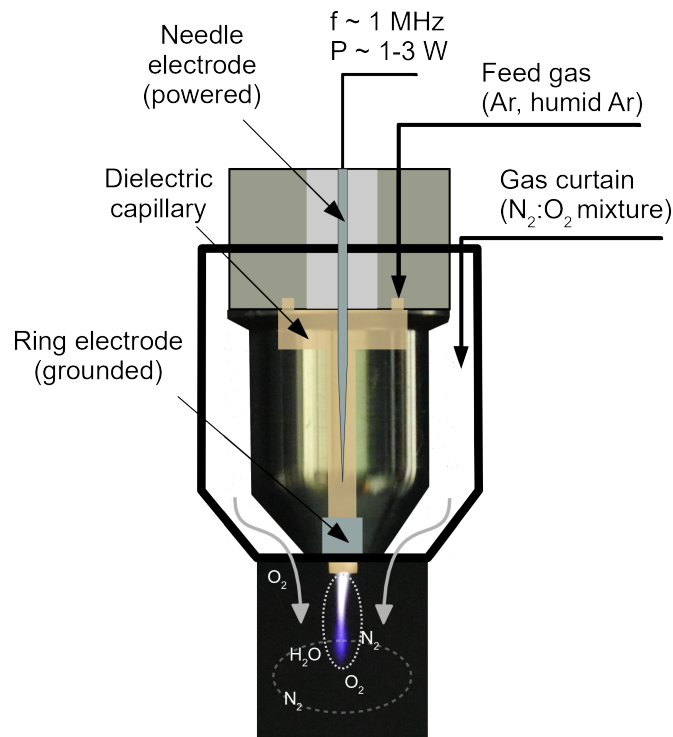
Figure 1.3: Schematic of the kINPen-sci plasma jet.

1.3 Optical diagnostic methods for reactive transient and stable species

The large number of collisions at atmospheric pressure and the interaction of the feed gas with the surrounding gas composition cause complex excitation dynamics. With the well-known optical emission spectroscopy (OES), information about excited species can be gained. In order to obtain ground state densities from OES measurements, a profound knowledge of the excitation dynamics and the electron energy distribution function is required, which is often unknown. Hence, the determination of absolute number densities of ground state species by OES becomes demanding [55]. However, spatially and temporally resolved OES is commonly used to investigate vibrational and rotational temperatures, and the propagation of excitation waves [56–61].

Besides mass spectrometry [62–67], absorption spectroscopy (AS) methods [68–74] are commonly used to determine absolute number densities of the reactive species in CAPJs [75–82]. The absorption signal depends only on the number density of the investigated species, the frequency dependent absorption cross section, and the absorption path length, and is thus calibration free. Quantities related to the absorption cross section, such as integrated absorption cross sections, line strengths, Einstein coefficients, or oscillator strengths, are often reported in literature.

The reactive species composition produced by CAPJs consists of several different types of species with varying lifetimes ranging between a few nanoseconds and several hours [53, 82]:

- Species in metastable states, e.g., $Ar(^3P_2)$ atoms or $He(2^3S_1)$ atoms, which were mainly excited due to electron impact; at atmospheric pressure, the effective lifetime for metastable species is in the order of nanoseconds because of collisional quenching reactions.

- Radicals, as a product of dissociation of molecular admixtures to the feed gas and from further reactions. In the case of water admixtures these involve H atoms, OH molecules, and HO_2 molecules, among others. The effective lifetime of those radicals is usually in the order of μs.

- Long-living molecules with an effective lifetime up to hours that were formed by reactions of fragments produced by dissociation processes with the surrounding gas composition consisting of the feed gas and the ambient gas composition.

A challenge for diagnostics of CAPJs is the small diameter over which the reactive species composition is distributed. Most of the standard diagnostic techniques are well established for low pressures in large chambers and have to be strongly modified to be used for CAPJs [83]. This is effort demanding, since it requires the entire adaptation of the measurements methodology and data analysis. Moreover, some of the species are often present only in trace amounts, although they are chemically important. Hence, a high sensitivity for the detection of species is required. As the gas temperature of CAPJs is around room temperature, most of the reactive species inhabit the ground

VUV	UV	Vis	NIR	MIR

λ [nm]   200   400   700   1000   3000   10000

electronic ground state transitions of atoms	electronic ground state transitions of molecules	metastable state transitions of atoms	vibrational combination bands of molecules	vibrational fundamental bands of molecules
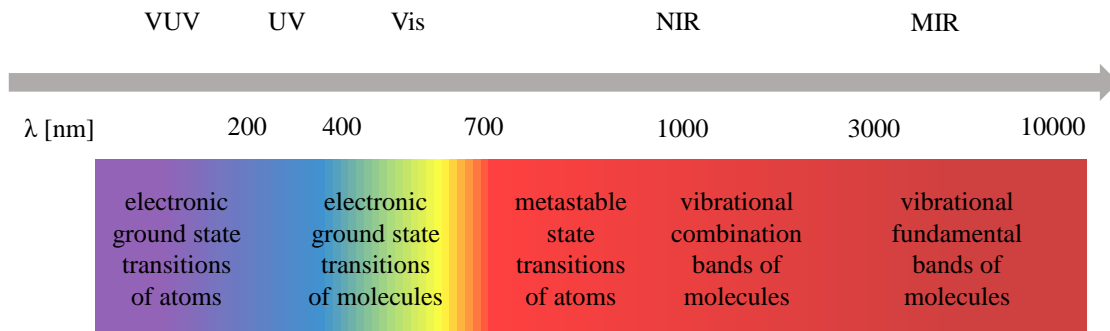
Figure 1.4: Overview of wavelength regions for the detection of metastable species, transient atomic and molecular radicals, and long-living molecules.

state. Thus, the total number densities for atoms can be obtained from the oscillator strength. The total number densities for molecules can be determined from the line strengths by assuming a Boltzmann distribution. In figure 1.4, an overview of suitable wavelength regions for the detection of various types of reactive transient and stable species is presented.

Metastable species, such as $Ar(^3P_2)$ atoms or $He(2^3S_1)$ atoms, have strong absorption bands in the near infrared (NIR) region between ($750 \text{ nm} \leq \lambda \leq 3000 \text{ nm}$). Examples for the determination of Ar and He metastables in a CAPJ can be found in references [84–86].

Due to the large energy gap between ground and electronic excited states of atomic radicals, such as H atoms or O atoms, the investigation of atomic ground state densities requires light sources in the vacuum ultra-violet (VUV) region ($\lambda < 200 \text{ nm}$), where light is strongly absorbed by air species making experiments cumbersome. Previously, O and N atoms have been quantified in a CAPJ, operating in helium, using synchrotron radiation and a spectrometer with an ultra-high spectral resolution, so-called VUV high-resolution Fourier-transform absorption spectroscopy [87, 88]. An alternative to VUV-spectroscopy for the detection of atomic species is two-photon absorption laser induced fluorescence spectroscopy (TALIF) [89–93]. Absolute number densities can be obtained by comparing the fluorescence signal of the probed reactive species composition to the fluorescence signal of a calibration gas with a known quantity. Nonetheless, a reliable result for the atomic density can only be obtained by taking into account the non-radiative losses of the excited state population by collisional quenching, as this, at atmospheric pressure, usually dominates over the spontaneous emission. To calculate the total quenching losses, a detailed knowledge of the gas composition and the specific quenching rate coefficients is essential. With pico- or femtosecond lasers, the effective lifetime of the species in the gas mixture at atmospheric pressure can be determined. Since the fluorescence is emitted by single species, high spatial resolution is possible. In table 1.1, ground state transitions for O and H atoms, and for $Ar(^3P_2)$ atoms are

Table 1.1: Oscillator strengths for electric dipole transitions between the ground state and an excited upper state for H and O atoms, and between the Ar(^{3}P$_2$) state and an excited upper state, respectively.

species	electron configuration upper state	wavelength [nm]	oscillator strength [$\cdot 10^{-2}$]	ref.
H	4	97.25	2.9	[94–96]
O	$2s^22p^3(^4S°)4d$	97.17	1.2	[94, 97, 98]
O	$2s^22p^3(^2D°)3s$	98.88	4.6	[94, 97, 98]
H	3	102.57	7.9	[94–96]
O	$2s^22p^3(^4S°)3d$	102.58	1.7	[94, 97, 98]
O	$2s^22p^3(^4S°)4s$	103.92	0.9	[94, 97, 98]
H	2	121.57	41.6	[94–96]
O	$2s^22p^3(^4S°)3s$	130.21	5.2	[94, 97, 98]
Ar(^{3}P$_2$)	$3s^23p^5(^2P°_{3/2})4p$	763.51	21.4	[94, 95, 98, 99]
Ar(^{3}P$_2$)	$3s^23p^5(^2P°_{3/2})4p$	772.38	2.9	[94, 95, 98, 99]
Ar(^{3}P$_2$)	$3s^23p^5(^2P°_{3/2})4p$	801.48	8.9	[94, 95, 98, 99]
Ar(^{3}P$_2$)	$3s^23p^5(^2P°_{3/2})4p$	811.53	46.0	[94, 95, 98, 99]
Ar(^{3}P$_2$)	$3s^23p^5(^2P°_{3/2})4p$	912.3	14.2	[94, 95, 98, 99]

summarised.

Molecular radicals can be observed in the mid-infrared region (MIR) of the electromagnetic spectrum (3000 nm $\leq \lambda \leq$ 10000 nm), where transitions of their fundamental vibrational bands occur. In this region, the absorption cross sections for electric dipole radiation reach their maximum. However, the availability of high sensitive detectors is limited in the MIR. Due to large developments in the field of telecommunications, the sensitivity of detectors in the near-infrared region (NIR) between 780 nm $\leq \lambda \leq$ 3000 nm is orders of magnitude larger than in the MIR. That is why molecules are often detected in the NIR, where combination bands of vibrational modes can be observed. Depending on the molecule of interest and its expected density, a balance between absorption cross section and detector sensitivity has to be found. Alternative to the detection of rotational-vibrational bands within the ground state, rotational-vibrational bands between the ground state and the first excited electronic states can be determined in the UV/visible region (200 nm $\leq \lambda \leq$ 750 nm), where the line strengths are orders of magnitude larger than for combination bands. For instance, the line strength of OH at 308 nm is by a factor of approximately 700 larger than for the X$^2\Pi(v'' = 1)$ ← X$^2\Pi(v' = 0)$ transition at 2.802 µm. However, in the UV/visible region, transitions from several species are overlapping. Hence, a deconvolution or simulation procedure has to be applied to interpret the signals. The determination of OH radicals in the effluent of CAPJs by broadband absorption spectroscopy has been reported previously in references [71, 89, 100]. For the determination of the broadband absorption of the investigated species, the emission of the plasma jet has to be taken into account, which requires a stable plasma source, and a collimated stable light

Table 1.2: Line strengths for electric dipole transitions between the ground state and an excited upper state for H_2O, OH, HO_2, and H_2O_2 molecules, respectively.

species	transitions	example wavelength [μm]	line strength $\cdot 10^{-20}$ [cm^2 cm^{-1}]	ref.
OH	$A^2\Sigma^+(v''=3) \leftarrow X^2\Pi(v'=0)$	0.2450	51	[101, 102]
OH	$A^2\Sigma^+(v''=2) \leftarrow X^2\Pi(v'=0)$	0.2616	315	[101, 102]
OH	$A^2\Sigma^+(v''=1) \leftarrow X^2\Pi(v'=0)$	0.2821	1800	[101, 102]
OH	$A^2\Sigma^+(v''=0) \leftarrow X^2\Pi(v'=0)$	0.3081	6500	[101, 102]
H_2O	$4\nu_1 + \nu_3$	0.5903	0.00028	[101, 103, 104]
OH	$X^2\Pi(v''=5) \leftarrow X^2\Pi(v'=0)$	0.6172	0.00053	[101, 105, 106]
H_2O	$3\nu_1 + \nu_2 + \nu_3$	0.6478	0.00030	[101, 103, 104]
H_2O	$3\nu_1 + \nu_3$	0.7193	0.0038	[101, 104, 107]
OH	$X^2\Pi(v''=4) \leftarrow X^2\Pi(v'=0)$	0.7526	0.0066	[101, 105, 106]
H_2O	$2\nu_1 + \nu_2 + \nu_3$	0.8179	0.00515	[101, 104, 107]
H_2O	$2\nu_1 + \nu_3$	0.9374	0.0621	[101, 104, 108]
OH	$X^2\Pi(v''=3) \leftarrow X^2\Pi(v'=0)$	0.9790	0.11	[101, 105, 106]
H_2O	$\nu_1 + \nu_2 + \nu_3$	1.125	0.15	[101, 104, 109]
HO_2	$2\nu_1$	1.506	0.71	[74, 110]
H_2O	$\nu_1 + \nu_3$	1.369	1.8	[101, 109]
OH	$X^2\Pi(v''=2) \leftarrow X^2\Pi(v'=0)$	1.434	2.6	[101, 105, 106]
H_2O	$\nu_2 + \nu_3$	1.914	1.6	[101, 109]
H_2O	ν_3	2.606	25	[101, 111]
OH	$X^2\Pi(v''=1) \leftarrow X^2\Pi(v'=0)$	2.802	9.0	[101, 105, 106]
HO_2	ν_1	2.893	0.21	[101, 112, 113]
H_2O_2	ν_5	2.770	≈ 1.2	[114, 115]
H_2O	ν_1	2.788	3.7	[101, 111]
H_2O	ν_2	5.935	32	[101, 109]
H_2O_2	ν_6	7.960	3.5	[101, 115]
HO_2	ν_2	7.077	0.67	[101, 112, 116]
HO_2	ν_3	8.945	0.40	[101, 112, 117]

source. Another method for the detection of molecular radicals is laser-induced fluorescence spectroscopy (LIF). A calibration for absolute densities of OH by observing the Rayleigh scattered intensities is reported, for instance, in reference [89]. However, quenching needs to be taken into account, which is strong in CAPJs. In table 1.2, ground state transitions and transitions from an electronic excited state for OH, HO_2, H_2O, and H_2O_2 are summarised.

In order to increase the sensitivity for absorption spectroscopy measurements, the absorption length can be increased by employing a multi-pass cell. Therefore, the reactive species composition is collected in a large box, which allows investigations of the far ef-

fluent region [86, 118]. Henceforth, no direct localised in-situ measurements are possible and the chemistry in the plasma jet can only be deduced indirectly by modelling.

Another approach is the utilization of high-finesse optical cavities that enhances the effective absorption path length and thus the sensitivity. Within such a cavity, which normally consists of two highly reflective mirrors, the effective absorption path length through the sample under investigation can easily be increased by a factor of thousand to ten thousand [119, 120]. With cavity-enhanced spectroscopy techniques, detection limits of parts-per-million (ppm) up to parts-per-trillion (ppt) can be achieved, as for example shown for methane in reference [121]. For the detection of species in CAPJs, cavity ring-down spectroscopy (CRDS) has been the most widely used cavity-enhanced spectroscopy technique. Applications of CRDS for the analysis of atmospheric pressure plasma jets, including the detection of positively charged nitrogen molecules (N_2^+), excited nitrogen molecules ($N_2(A)$), OH and metastables of He, are reported in references [72, 82, 122]. In order to detect HO_2 radicals in the effluent of a CAPJ, Gianella et al. have recently applied optical feedback cavity-enhanced absorption spectroscopy (OF-CEAS) [73] and continuous wave cavity ring-down spectroscopy (cw-CRDS) [74]. The latter has the advantage to cover a broader wavelength range, which is important to deconvolute absorption features of the molecules of interest from absorption features of the background, and to be less susceptible to fluctuations of the base line. Moreover, with CRDS, real in-situ measurements can be achieved. Nevertheless, up to now, no spatial resolution was obtained. Furthermore, the employment of cavities for CAPJs requires a particular care of the cavity designs due to strong changes of the refractive index, temperature gradients, or turbulent gas flows.

All in all, the determination of reactive transient and stable species in the plasma zone and the effluent of a CAPJ remains challenging, since non-intrusion and high selectivity at high sensitivity is required. Up to now, there is a lack of reported studies determining spatial distributions, which are essential to deduce chemical reactions and thus to be able to tailor the reactive species composition.

1.4 Previous studies of the kINPen-sci plasma jet

In table 1.3, previous studies on the determination of absolute number densities for reactive species in the kINPen plasma jet are summarised. It was demonstrated that the composition of reactive species in the effluent of the kINPen can be changed by adding molecular gases to the argon feed gas [73, 118, 123–127] or by changing the surrounding gas composition [74, 86, 125, 126, 128–131]. For example, it was reported that the addition of water to the feed gas of a CAPJ reduces the ozone (O_3) and NO production [132], and increases the HO_2 formation [73]. The O, O_3, NO, and NO_2 production, for instance, could be controlled by the addition of a few percent of O_2 to the feed gas [118, 123, 127, 133]. By varying the surrounding gas composition from pure nitrogen to pure oxygen, the dominant plasma chemical reaction scheme changes from an oxygen-nitrogen to a pure oxygen-based set [74, 128]. The HO_2 and the O_3

Table 1.3: Previous investigations on absolute number densities of reactive species in the effluent and far effluent of the kINPen plasma jet.

species	feed gas admixture	curtain	diagnostic	Ref.
$Ar(^3P_2)$			LAAS [a]	[86]
O	O_2		TALIF [b]	[133, 134]
NO	dry air or H_2O		TDLAS [c]+ MPC [d]	[123]
NO	dry air	dry air	LIF [e]	[135]
NO_2	dry air	dry air	QCLAS [f]+ MPC [d]	[124]
NO_2	N_2 or O_2	dry air	QCLAS [f]+ MPC [d]	[118]
NO_2		N_2/O_2	FTIR [g]+ MPC [d]	[86, 130, 131]
N_2O		N_2/O_2	FTIR [g]+ MPC [d]	[130]
N_2O_5		N_2/O_2	FTIR [g]+ MPC [d]	[130]
O_3		N_2/O_2	FTIR [g]+ MPC [d]	[131]
O_3		N_2/O_2	FTIR [g]+ MPC [d]	[86]
O_3		$N_2/O_2 + H_2O$	FTIR [g]+ MPC [d]	[130]
O_3	O_2	N_2/O_2	UV AS [h]	[127]
O_3	N_2 or O_2	dry air	QCLAS [f]+ MPC [d]	[118]
O_3	H_2O	synth. air	QCLAS [f]+ MPC [d]	[126]
HO_2	H_2O	synth. air	OF-CEAS [i]	[73]
HO_2	H_2O	N_2/O_2	cw-CRDS [j]	[74]
H_2O_2		N_2/O_2	FTIR [g]+ MPC [d]	[86]
H_2O_2	H_2O	N_2/O_2	FTIR [g]+ MPC [d]	[125]
HNO_3		N_2/O_2	FTIR [g]+ MPC [d]	[86]

[a] laser atomic absorption spectroscopy,
[b] two-photon absorption laser-induced fluorescence spectroscopy,
[c] tunable diode laser absorption spectroscopy,
[d] multi-pass cell,
[e] laser-induced fluorescence spectroscopy,
[f] quantum cascade laser absorption spectroscopy,
[g] Fourier-transform infrared absorption spectroscopy,
[h] broadband ultraviolet absorption spectroscopy,
[i] optical feedback cavity-enhanced absorption spectroscopy,
[j] continuous wave cavity ring-down spectroscopy

concentration, for example, increased with a rising amount of O_2 in the gas curtain [74, 86, 118, 126, 127, 130, 131], whereas the NO_2 density decreased for O_2 amounts larger than 20% in the surrounding atmosphere [86, 130].

Except for the determination of $Ar(^3P_2)$ atoms by laser atomic absorption spectroscopy (LAAS), NO by laser-induced fluorescence spectroscopy (LIF) and of O atoms by two-photon absorption laser-induced fluorescence (TALIF), the absolute densities for reactive species were measured either 10 mm below the nozzle, as it was done for broadband

ultraviolet absorption spectroscopy, optical feedback cavity-enhanced absorption spectroscopy (OF-CEAS), and continuous wave cavity ring-down spectroscopy (cw-CRDS), or were collected in a multi-pass-cell (MPC) for further detection by tunable diode laser absorption spectroscopy (TDLAS), quantum cascade laser absorption spectroscopy (QCLAS) or Fourier-transform infrared spectroscopy (FTIR). A spatial distribution in the effluent was only reported for $Ar(^3P_2)$ atoms [86], and for NO radicals with an admixture of 1% air to the feed gas, whereas O atom densities were given at 5 mm and 7 mm below the nozzle [133]. Based on the FTIR measurements performed in the MPC for the far effluent on the kINPen plasma jet, and on the results for the $Ar(^3P_2)$ densities in the effluent close to the nozzle, Schmidt-Bleker et al. deduced the chemical reaction set in the effluent by considering several reaction steps from the effluent into the MPC. However, direct measurements of the spatial distributions of reactive species in the effluent with feed gas humidity have not been reported, yet.

1.5 Scope of this work

The scope of this work is the determination of spatial distributions for reactive transient and stable species, which are involved in the reaction cycle of H_2O_2 in the effluent of the kINPen-sci plasma jet. In order to gain further insights into the formation and loss mechanism of H_2O_2 and its precursors, spatial information is required. However, obtaining spatial density distributions with absorption spectroscopy techniques is demanding, as commonly line-of-sight densities are determined, assuming a constant density that is homogeneously distributed over the effective absorption length. In this work, various absorption spectroscopy methods, namely laser atomic absorption spectroscopy (LAAS), picosecond two-photon absorption laser-induced fluorescence spectroscopy (ps-TALIF), and continuous wave cavity ring-down spectroscopy (cw-CRDS) are adapted for the determination of spatial distributions for absolute number densities in the effluent of a CAPJ.

H_2O_2 is a key species for biomedical applications, which is known to induce oxidative stress that reduces the cell viability and leads to cell death at high concentrations [44, 46, 48, 125]. In order to improve the understanding of the impact of the plasma on cells, a dedicated knowledge of the reactions occurring in the effluent of the plasma jet is pivotal for further, application-dependent, tailoring of the production of H_2O_2. In the reaction cycle of H_2O_2 several reactive species are involved including metastable species, such as $Ar(^3P_2)$ atoms, and atomic and molecular radicals, such as H, O, OH and HO_2, which are important agents for the interaction with cells either directly or as precursors for the formation of larger molecules or ion-clusters [45, 46, 50]. OH and the HO_2 are known precursors that drive the low temperature oxidation chemistry. The HO_2 radical, in particular, is involved in biological oxidation reactions, such as lipid peroxidation [136], as it can enter cell membranes. In a liquid, a chemical equilibrium will develop between HO_2 and the superoxide anion, O_2^-, which is responsible for a
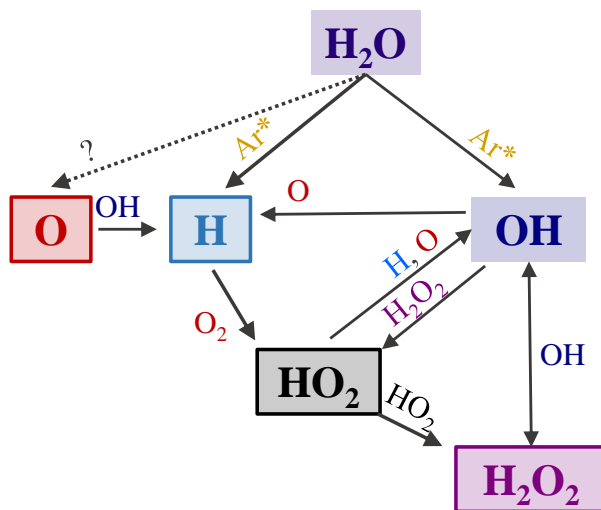
Figure 1.5: Schematic of the reaction cycle for H_2O_2 investigated in this work.

change of the pH-value in plasma-treated liquids [137]. A schematic of the reaction cycle for H_2O_2 that was investigated in this work is depicted in figure 1.5.

The production of the hydrogen containing atomic and molecular radicals is initiated by the dissociation of water by electrons and metastable species in the plasma zone of the kINPen-sci. Water is ubiquitous in air and thus a considerable impurity of the feed gas, and an important component of the laboratory and clinical air the plasma is operated in. Reuter et al. reported that the addition of water to the feed gas has a much higher impact on the reactive species composition than the water content in the surrounding gas [126], whereas Winter et al. have shown that a high feed gas humidity increases the production of H_2O_2, leading to a decreasing cell viability of human skin cell [132]. In this work, humidity is added on purpose to the feed gas to obtain a sufficient control of the water content in the feed gas. In particular the impact of feed gas humidity on the excitation dynamics and the densities of $Ar(^3P_2)$ atoms is investigated by means of LAAS. Metastable species play an important role in the formation and development of gas discharges. For example, stepwise ionization and Penning-ionization processes of metastable species influence the electron density and, thus, the breakdown dynamics, discharge regimes, and lengths [138]. In order to investigate whether the production of metastable species of Ar in the effluent plays a role in the reaction scheme for H_2O_2, the densities and the effective lifetimes for $Ar(^3P_2)$ atoms are analysed.

By using ps-TALIF, the spatial distributions of O and H atoms are determined, while a gas curtain of 5 slm O_2 is applied and 3000 ppm water is added to the Ar feed gas. Due to the employment of picosecond laser pulses, the effective lifetime for O atoms can be obtained experimentally. However, for H atoms, quenching reactions lead to an effective lifetime that is smaller than the detection limit of the experimental setup. Hence, the effective lifetimes for H atoms are calculated from quenching coefficients reported in

literature. Absolute densities for O and H atoms are obtained by calibration procedures with Xe and Kr, respectively.
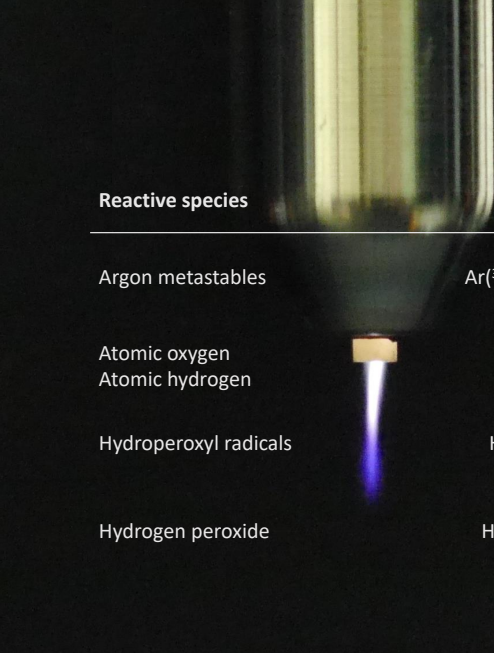
To determine the spatial distributions for the densities of HO_2 radicals in the effluent of the kINPen-sci plasma jet, while a gas curtain of 5 slm O_2 is applied and 3000 ppm water is added to the Ar feed gas, cw-CRDS in the NIR is employed. Notably, with CRDS, commonly densities averaged over the line-of-sight are obtained. In particular for CAPJs, the exact absorption length is crucial for the determination of the absolute densities. In this work, detailed investigations on the spatial distribution of the absorption coefficient for HO_2 are performed in both directions, axial and radial. Instead of taking full spectra with several spectral points, in this work, a time efficient method for cw-CRDS measurements, called on/off-resonance method, is presented, where the absorption coefficient at two different wavelengths was measured on and off the molecular resonance. The on/off-resonance method enables the determination of the absorption of HO_2 at various radial and axial positions with a moderate effort of time. Based on the radial distributions for the absorption coefficient, the effective absorption length is determined. Furthermore, by applying an Abel inversion on the radial and axial distributions, spatial distributions for the densities of HO_2 are obtained.

A similar setup as used for HO_2 is employed for the determination of the spatial distributions for the densities of H_2O_2. Commonly, H_2O_2 is determined in a liquid by colorimetric assays or by test stripes [46], whereas H_2O_2 in the gas phase in the effluent of a CAPJ has only been determined indirectly over a large volume by FTIR that was combined with a multi-pass cell [86]. In this work, cw-CRDS at 8 μm is used to determine the spatial distributions for the densities of H_2O_2 directly in the effluent of the kINPen-sci plasma jet, while a gas curtain of 5 slm O_2 is applied and 3000 ppm water is added to the Ar feed gas.

Based on the spatial distributions for H, O, HO_2, and H_2O_2, and the investigations on the impact of water on the densities of $Ar(^3P_2)$ atoms, the most important chemical reactions are deduced. The role of the plasma zone is investigated indirectly by analysing the spatial distributions in the effluent. Additionally, the experimental results are compared to the results of a plasma chemical and reacting flow model for the kINPen that includes reactions in the plasma zone and reactions in the effluent.

In figure 1.6, an overview of the employed diagnostic techniques and the corresponding reactive species measured is given. The remainder of this work is as follows: In chapter 2, the investigations on the densities and the quenching for $Ar(^3P_2)$ atoms by means of LAAS are presented, in chapter 3, the determinations of spatial distributions for H and O atoms by ps-TALIF are described, in chapter 4, the method and analysis to obtain the spatial density distribution of HO_2 radicals by means of cw-CRDS are elucidated, and in chapter 5 the determinations of the spatial density distribution of H_2O_2 molecules by cw-CRDS are discussed. In chapter 6, the experimental results are consolidated to determined the roles of the plasma zone and the plasma effluent on the formation of transient and stable reactive species. In chapter 7, a comparison of the experimental results and simulated densities obtained from a plasma chemical and

reacting flow model is presented. This work is finalised by the conclusions drawn in chapter 8.

Figure 1.6: Overview of the employed diagnostic methods to investigate the reaction cycle of H_2O_2 in the effluent of the kINPen-sci plasma jet.

1.6 Bibliography

[1] G. S. Selwyn, H. W. Herrmann, J. Park, and I. Henins. Materials processing using an atmospheric pressure, rf-generated plasma source. *Contrib. Plasma Phys.*, 6(610-619), 2001.

[2] O. V. Penkov, M. Khadem, W.-S. Lim, and D.-E. Kim. A review of recent applications of atmospheric pressure plasma jets for materials processing. *J. Coat. Technol. Res.*, 12(225-235), 2015.

[3] F. Fanelli and F. Fracassi. Atmospheric pressure non-equilibrium plasma jet technology: general features, specificities and applications in surface processing of materials. *Surf. Coat. Technol.*, 322(174-201), 2017.

[4] M. Laroussi, M. G. Kong, G. Morfill, and W. Stolz, editors. *Plasma Medicine - Applications of Low-Temperature Gas Plasmas in Medicine and Biology.* Cambridge University Press, 2012.

[5] A. Kramer, S. Bekeschus, R. Matthes, C. Bender, M. B. Stope, M. Napp, O. Lademann, J. Lademann, K.-D. Weltmann, and F. Schauer. Cold Physical Plasmas in the Field of Hygiene - Relevance, Significance, and Future Applications. *Plasma Process. Polym.*, 12(12), 2015.

[6] K.-D. Weltmann and T. von Woedtke. Plasma medicine - current state of research and medical application. *Plasma Phys. Control. Fusion*, 59(014031), 2017.

[7] H.-R. Metelmann, T. von Woedtke, and K.-D. Weltmann, editors. *Comprehensive Clinical Plasma Medicine - Cold Physical Plasma for Medical Applications.* Springer International Publishing AG, 2018.

[8] A. Privat-Maldonado, A. Schmidt, A. Lin, K.-D. Weltmann, K. Wende, A. Bogaerts, and S. Bekeschus. ROS from Physical Plasmas: Redox Chemistry for Biomedical Therapy. *Oxid. Med. Cell. Longev.*, 2019(9062098), 2019.

[9] T. Von Woedtke, S. Emmert, H.-R. Metelmann, S. Rupf, and K.-D. Weltmann. Perspectives on cold atmospheric plasma (CAP) applications in medicine. *Phys. Plasmas*, 27(070601), 2020.

[10] R. Brandenburg, A. Bogaerts, W. Bongers, A. Fridman, G. Gridman, B. R. Locke, V. Miller, S. Reuter, M. Schiorlin, T. Verreycken, and K. Ostrikov. White paper on the future of plasma science in environment, for gas conversion and agriculture. *Plasma Process Polym.*, 16(e1700238), 2019.

[11] M. Ito, J.-S. Oh, T. Ohta, M. Shiratani, and M. Hori. Current status and future prospects of agricultural applications using atmospheric-pressure plasma technologies. *Plasma Process. Polym.*, 15(20l700073), 2017.

[12] K. Gotoh, Y. Kobayashi, A. Yasukawa, and Y. Ishigami. Surface modification of PET films by atmospheric pressure plasma exposure with three reactive gas sources. *Colloid Polym. Sci.*, 290(1005-1014), 2012.

[13] H. B. Baniya1, R. P. Guragain1, B. Baniya, and D. P. Subedi. Experimental Study of Cold Atmospheric Pressure Plasma Jet and Its Application in the Surface Modification of Polypropylene. *Rev. Adhesion Adhesives*, 8(2), 2020.

[14] M. Kehrer, A. Rottensteiner, W. Hartl, J. Duchoslav, S. Thomas, and D. Stifter. Cold atmospheric pressure plasma treatment for adhesion improvement on polypropylene surfaces. *Surf. Coat. Technol.*, 403(126389), 2020.

[15] A. Y. Nikiforov, A. Sarani, and Ch. Leys. The influence of water vapor content on electrical and spectral properties of an atmospheric pressure plasma jet. *Plasma Sources Sci. Technol.*, 20(015014), 2011.

[16] R. Wang, Y. Shen, C. Zhang, P. Yan, and T. Shao. Comparison between helium and argon plasma jets on improving the hydrophilic property of PMMA surface. *App. Surf. Sci.*, 367(401-406), 2016.

[17] R. Zaplotnik and A. Vesel. Effect of VUV Radiation on Surface Modification of Polystyrene Exposed to Atmospheric Pressure Plasma Jet. *Polymers*, 12(1136), 2020.

[18] J. Benedikt, V. Raballand, A. Yanguas-Gil, K. Focke, and A. von Keudell. Thin film deposition by means of atmospheric pressure microplasma jet. *Plasma Phys. Control. Fusion*, 47(B419-B427), 2007.

[19] S. Bornholdt, M. Wolter, and H. Kersten. Characterization of an atmospheric pressure plasma jet for surface modification and thin film deposition. *Eur. Phys. J. D*, 60(653-660), 2010.

[20] K. Fricke, H. Steffen, T. von Woedtke, K. Schröder, and K.-D. Weltmann. High Rate Etching of Polymers by Means of an Atmospheric Pressure Plasma Jet. *Plasma Process. Polym.*, 8(51-58), 2011.

[21] P. Luan, V. S. S. K. Kondeti, A. J. Knoll, P. J. Bruggeman, and G. S. Oehrlein. Effect of water vapor on plasma processing at atmospheric pressure: Polymer etching and surface modification by an ar/h$_2$o plasma jet. *J. Vac. Sci. Technol. A*, 37(031305), 2019.

[22] K. Fricke, I. Koban, H. Tresp, L. Jablonowski, K. Schröder, A. Kramer, K.-D. Weltmann, T. von Woedtke, and T. Kocher. Atmospheric Pressure Plasma: A High-Performance Tool for the Efficient Removal of Biofilms. *PLoS ONE*, 7(8), 2012.

[23] J. Pawlat. Atmospheric pressure plasma jet for decontamination purposes. *Eur. Phys. J. Appl. Phys.*, 61(2), 2013.

[24] A.-A. H. Mohamed, S. M. Al Shariff, S. A. Ouf, and M. Benghanem. Atmospheric pressure plasma jet for bacterial decontamination and property improvement of fruit and vegetable processing wastewater. *J. Phys. D: Appl. Phys.*, 49(195401), 2016.

[25] Y. Morabit, M. I. Hasan, R. D. Whalley, E. Robert, M. Modic, and J. L. Walsh. A review of the gas and liquid phase interactions in low-temperature plasma jets used for biomedical applications. *Eur. Phys. J. D*, 75(32), 2021.

[26] R. Tiede, J. Hirschberg, G. Daeschlein, T. von Woedtke, W. Vioel, and S. Emmert. Plasma applications: A Dermatological View. *Contrib. Plasma Phys.*, 54(2), 2014.

[27] S. Bekeschus, A. Schmidt, K.-D. Weltmann, and T. von Woedtke. The plasma jet kINPen - A powerful tool for wound healing. *Clinical Plasma Medicine*, 4(1), 2016.

[28] L. Boeckmann, M. Schäfer, T. Bernhardt, M. L. Semmler, O. Jung, G. Ojak, T. Fischer, K. Peters, B. Nebe, B. Müller-Hilke, C. Seebauer, S. Bekeschus, and S. Emmert. Cold Atmospheric Pressure Plasma in Wound Healing and Cancer Treatment. *Appl. Sci.*, 10(6898), 2020.

[29] M. Keidar. Plasma for cancer treatment. *Plasma Sources Sci. Technol.*, 24(033001), 2015.

[30] D. Yan, J. H. Sherman, and M. Keidar. Cold atmospheric plasma, a novel promising anti-cancer treatment modality. *Oncotarget*, 8(9), 2017.

[31] Z. Xu, Y. Lan, J. Ma, J. Shen, W. Han, S. Hu, C. Ye, W. Xi, Y. Zhang, C. Yang, X. Zhai, and C. Cheng. Applications of atmospheric pressure plasma in microbial inactivation and cancer therapy: a brief review. *Plasma Sci. Technol.*, 22(103001), 2020.

[32] Clarivate. Web of Science, 2022. https://www.webofscience.com/wos/woscc/basic-search.

[33] A. Schütze, J. Y. Jeong, S. E. Babayan, J. Park, G. S. Selwyn, and R. F. Hicks. The Atmospheric-Pressure Plasma Jet: A Review and Comparison to Other Plasma Sources. *IEEE Trans. Plasma Sci.*, 26(6), 1998.

[34] M. Laroussi and T. Akan. Arc-Free Atmospheric Pressure Cold Plasma Jets: A Review. *Plasma Process. Polym.*, 4(9), 2007.

[35] X. Lu, M. Laroussi, and V. Puech. On atmospheric-pressure non-equilibrium plasma jets and plasma bullets. *Plasma Sources Sci. Technol.*, 21(034005), 2012.

[36] J. Winter, R. Brandenburg, and K.-D. Weltmann. Atmospheric pressure plasma jets: an overview of devices and new directions. *Plasma Sources Sci. Technol.*, 24(064001), 2015.

[37] J. Golda, J. Held, B. Redeker, M. Konkowski, P. Beijer, G. Sobota, A. amd Kroesen, N. S. J. Braithwaite, S. Reuter, M. M. Turner, T. Gans, D. O'Connell, and V. Schulz-von der Gathen. Concepts and characteristics of the 'COST Reference Microplasma Jet'. *J. Phys. D: Appl. Phys.*, 49(084003), 2016.

[38] F. Riedel, J. Golda, J. Held, H. L. Davies, M. W. van der Woude, J. Bredin, K. Niemi, T. Gans, V. Schulz-von der Gathen, and D. O'Connell. Reproducibility of 'COST reference microplasma jets'. *Plasma Sources Sci. Technol.*, 29(095018), 2020.

[39] V. Schulz-von der Gathen, L. Schaper, N. Knake, S. Reuter, K. Niemi, T. Gans, and J. Winter. Spatially resolved diagnostics on a microscale atmospheric pressure plasma jet. *J. Phys. D: Appl. Phys.*, 41(194004), 2008.

[40] M. S. Mann, R. Tiede, K. Gavenis, G. Daeschlein, R. Bussiahn, K.-D. Weltmann, S. Emmert, T. von Woedtke, and R. Ahmed. Introduction to DIN-specification 91315 based on the characterization of the plasma jet kINPen MED. *Clinical Plasma Medicine*, 4(2), 2016.

[41] X. Lu, G. V. Naidis, M. Laroussi, S. Reuter, D. B. Graves, and K. Ostrikov. Reactive species in non-equilibrium atmospheric-pressure plasmas: Generation, transport, and biological effects. *Phys. Rep.*, 630(1-84), 2016.

[42] S. Arndt, A. Schmidt, S. Karrer, and T. von Woedtke. Comparing two different plasma devices kINPen and Adtec SteriPlas regarding their molecular and cellular effects on wound healing. *Clinical Plasma Medicine*, 9(24-33), 2018.

[43] A. Khlyustova, C. Labay, Z. Machala, M.-P. Ginebra, and C. Canal. Important parameters in plasma jets for the production of RONS in liquids for plasma medicine: A brief review. *Front. Chem. Sci. Eng.*, 13(2), 2019.

[44] S. Bekeschus, J. Kolata, C. Winterbourn, A. Kramer, R. Turner, K. D. Weltmann, B. Bröker, and K. Masur. Hydrogen peroxide: A central player in physical plasma-induced oxidative stress in human blood cells. *Free Radic. Res.*, 48(5), 2014.

[45] H. J. Ahn, K. I. Kim, N. N. Hoan, C. H. Kim, E. Moon, K. S. Choi, S. S. Yang, and J.-S. Lee. Targeting Cancer Cells with Reactive Oxygen and Nitrogen Species Generated by Atmospheric-Pressure Air Plasma. *PLoS ONE*, 9(1), 2014.

[46] H. Jablonowski and T. von Woedtke. Research on plasma medicine-relevant plasma-liquid interaction: What happened in the past five years? *Clinical Plasma Medicine*, 3(42-52), 2015.

[47] P.-M. Girard, A. Arbabian, M. Fkeury, G. Bauville, V. Puech, M. Dutreix, and J. S. Sousa. Synergistic Effect of H_2O_2 and NO_2 in Cell Death Induced by Cold Atmospheric He Plasma. *Sci. Rep.*, 6(29098), 2016.

[48] Y. F. Yue, S. Mohades, M. Laroussi, and X. Lu. Measurements of Plasma-Generated Hydroxyl and Hydrogen Peroxide Concentrations for Plasma Medicine Applications. *IEEE Trans. Plasma Sci.*, 44(11), 2016.

[49] S. Bekeschus, A. Lin, A. Fridman, K. Wende, K.-D. Weltmann, and V. Miller. A Comparison of Floating - Electrode DBD and kINPen Jet: Plasma Parameters to Achieve Similar Growth Reduction in Colon Cancer Cells Under Standardized Conditions. *Plasma Chem. Plasma Process.*, 38(1-12), 2018.

[50] N. Gaur, H. Kurita, J.-S. Oh, S. Miyachika, M. Ito, A. Mizuno, A. J. Cowin, S. Allinson, R. D. Short, and E. J. Szili. On cold atmospheric-pressure plasma jet induced DNA damage in cells. *J. Phys. D: Appl. Phys.*, 54(035203), 2021.

[51] P. J. Cullen and A. Milosavljevic. Spectroscopic characterization of a radio-frequency argon plasma jet discharge in ambient air. *Prog. Theor. Exp. Phys.*, 6(063J01), 2015.

[52] S. Bekeschus, A. Schmidt, K.-D. Weltmann, and T. von Woedtke. The plasma jet kINPen – A powerful tool for wound healing. *Clinical Plasma Medicine*, 4(19-28), 2016.

[53] S. Reuter, T. von Woedtke, and K.-D. Weltmann. The kINPen—a review on physics and chemistry of the atmospheric pressure plasma jet and its applications. *J. Phys. D: Appl. Phys.*, 51(233001), 2018.

[54] S. Arndt, A. Schmidt, S. Karrer, and T. von Woedtke. Comparing two different plasma devices kINPen and Adtec SteriPlas regarding their molecular and cellular effects on wound healing. *Clinical Plasma Medicine*, 9(24-33), 2018.

[55] T. Belmonte, C. Noël, T. Gries, J. Martin, and G. Henrion. Optical Diagnostics of Micro Discharge Jets. *Contrib. Plasma Phys.*, 47(7), 2007.

[56] B. L. Sands, B. N. Ganguly, and K. Tachibana. Time-Resolved Imaging of "Plasma Bullets" in a Dielectric Capillary Atmospheric Pressure Discharge. *IEEE Trans. Plasma Sci.*, 36(4), 2008.

[57] Q. Xiong, X. Lu, Y. Xian, Z. Xiong, F. Zou, C. Zou, W. Gong, J. Hu, K. Chen, X. Pei, Z. Jiang, and Y. Pan. Temporal and spatial resolved optical emission behaviors of a cold atmospheric pressure plasma jet. *J. Appl. Phys.*, 106(083302), 2009.

[58] A. Sarani and C. Nikiforov, A. Y. an Leys. Atmospheric pressure plasma jet in Ar and Ar/H₂O mixtures: Optical emission spectroscopy and temperature measurements. *Physics of Plasmas*, 17(063504), 2010.

[59] S. Reuter, J. Winter, S. Iseni, S. Peters, A. Schmidt-Bleker, M. Dünnbier, J. Schäfer, R. Foest, and K.-D. Weltmann. Detection of ozone in a MHz argon plasma bullet jet. *Plasma Sources Sci. Technol.*, 21(034015), 2012.

[60] X. Lu, G. V. Naidis, M. Laroussi, and K. Ostrikov. Guided ionization waves: Theory and experiments. *Physics Reports*, 540(123-166), 2014.

[61] A. Schmidt-Bleker, S. A. Norberg, J. Winter, E. Johnsen, S. Reuter, K.-D. Weltmann, and M. J. Kushner. Propagation mechanisms of guided streamers in plasma jets: the influence of electronegativity of the surrounding gas. *Plasma Sources Sci. Technol.*, 24(035022), 2015.

[62] G. Willems, J. Golda, D. Ellerweg, J. Benedikt, A. von Keudell, N. Knake, and V. Schulz-von der Gathen. Corrigendum: Characterization of the effluent of a He/O$_2$ microscaled atmospheric pressure plasma jet by quantitative molecular beam mass spectrometry (2010 New J. Phys. 12 013021). *New J. Phys.*, 21(059501), 2019.

[63] M. Dünnbier, A. Schmidt-Bleker, J. Winter, M. Wolfram, R. Hippler, K.-D. Weltmann, and S. Reuter. Ambient air particle transport into the effluent of a cold atmospheric-pressure argon plasma jet investigated by molecular beam mass spectrometry. *J. Phys. D: Appl. Phys.*, 46(435203), 2013.

[64] B. T. J. van Ham, S. Hofmann, R. Brandenburg, and P.J. Bruggeman. In situ absolute air, O$_3$ and NO densities in the effluent of a cold RF argon atmospheric pressure plasma jet obtained by molecular beam mass spectrometry. *J. Phys. D: Appl. Phys.*, 47(224013), 2014.

[65] S. Schneider, M. Dünnbier, S. Hübner, S. Reuter, and J. Benedikt. Atomic nitrogen: a parameter study of a micro-scale atmospheric pressure plasma jet by means of molecular beam mass spectrometry. *J. Phys. D: Appl. Phys.*, 47(505203), 2014.

[66] J.-S. Oh, H. Furuta, A. Hatta, and W. Bradley. Investigating the effect of additional gases in an atmospheric-pressure helium plasma jet using ambient mass spectrometry. *Jpn. J. Appl. Phys.*, 54(01AA03), 2015.

[67] G. Willems, A. Hecimovic, K. Sgonina, E. Carbone, and J. Benedikt. Mass spectrometry of neutrals and positive ions in He/CO$_2$ non-equilibrium atmospheric plasma jet. *Plasma Phys. Control. Fusion*, 62(034005), 2020.

[68] J. Winter, M. Dünnbier, A. Schmidt-Bleker, A. Meshchanov, S. Reuter, and K.-D. Weltmann. Aspects of UV-absorption spectroscopy on ozone in effluents of plasma jets operated in air. *J. Phys. D: Appl. Phys.*, 45(385201), 2012.

[69] S. Zhang, W. van Gaens, B. van Gessel, S. Hofmann, E. van Veldhuizen, A. Bogaerts, and P. Bruggeman. Spatially resolved ozone densities and gas temperatures in a time modulated RF driven atmospheric pressure plasma jet: an analysis of the production and destruction mechanisms. *J. Phys. D: Appl. Phys.*, 46(205202), 2013.

[70] A. Wijaikhum, D. Schröder, S. Schröter, A. R. Gibson, K. Niemi, J. Friedrich, A. Greb, V. Schulz-von der Gathen, D. O'Connell, and T. Gans. Absolute ozone densities in a radio-frequency driven atmospheric pressure plasma using two-beam UV-LED absorption spectroscopy and numerical simulations. *Plasma Sources Sci. Technol.*, 26(115004), 2017.

[71] S. Schröter, A. Wijaikhum, A. R. Gibson, A. West, H. L. Davies, N. Minesi, J. Dedrick, E. Wagenaars, N. de Oliveira, L. Nahon, M. J. Kushner, J.-P. Booth, K. Niemi, T. Gans, and D. O'Connell. Chemical kinetics in an atmospheric pressure helium plasma containing humidity. *Phys. Chem. Chem. Phys.*, 20(24263), 2018.

[72] R. Zaplotnik, M. Bišćan, N. Krstulović, D. Popović, and S. Milošević. Cavity ring-down spectroscopy for atmospheric pressure plasma jet analysis. *Plasma Sources Sci. Technol.*, 24(054004), 2015.

[73] M. Gianella, S. Reuter, A. L. Aguila, G. A. D. Ritchie, and J. H. van Helden. Detection of HO$_2$ in an atmospheric pressure plasma jet using optical feedback cavity-enhanced absorption spectroscopy. *New J. Phys.*, 18(113027), 2016.

[74] M. Gianella, S. Reuter, S. A. Press, A. Schmidt-Bleker, J. H. van Helden, and G. A. D. Ritchie. HO$_2$ reaction kinetics in an atmospheric pressure plasma jet determined by cavity ring-down spectroscopy. *Plasma Sources Sci. Technol.*, 27(095013), 2018.

[75] V. Schulz-von der Gathen, V. Buck, T. Gans, N. Knake, K. Niemi, S. Reuter, L. Schaper, and J. Winter. Optical Diagnostics of Micro Discharge Jets. *Contrib. Plasma Phys.*, 47(7), 2007.

[76] V. Schulz-von der Gathen, L. Schaper, N. Knake, S. Reuter, K. Niemi, T. Gans, and J. Winter. Spatially resolved diagnostics on a microscale atmospheric pressure plasma jet. *J. Phys. D: Appl. Phys.*, 41(194004), 2008.

[77] G. D. Stancu, F. Kaddouri, D. A. Lacoste, and C. O. Laux. Atmospheric pressure plasma diagnostics by OES, CRDS and TALIF. *J. Phys. D: Appl. Phys.*, 43(124002), 2010.

[78] P. Bruggeman and R. Brandenburg. Atmospheric pressure discharge filaments and microplasmas: physics, chemistry and diagnostics. *J. Phys. D: Appl. Phys.*, 46(464001), 2013.

[79] S. Reuter, J. S. Sousa, G. D. Stancu, and J. H. van Helden. Review on VUV to MIR absorption spectroscopy of atmospheric pressure plasma jets. *Plasma Sources Sci. Technol.*, 24(054001), 2015.

[80] R. Ono. Optical diagnostics of reactive species in atmospheric-pressure nonthermal plasma. *J. Phys. D: Appl. Phys.*, 49(083001), 2016.

[81] M. Laroussi, X. Lu, and M. Keidar. Perspective: The physics, diagnostics, and applications of atmospheric pressure low temperature plasma sources used in plasma medicine. *J. Appl. Phys.*, 122(020901), 2017.

[82] R. Perverall and G. A. D. Ritchie. Spectroscopy techniques and the measurement of molecular radical densities in atmospheric pressure plasmas. *Plasma Sources Sci. Technol.*, 28(073002), 2019.

[83] I. Adamovich, S. D. Baalrud, A. Bogaerts, P. J. Bruggeman, M. Cappelli, V. Colombo, U. Czarnetzki, U. Ebert, J. G. Eden, and P. Favia. The 2017 Plasma Roadmap: Low temperature plasma science and technology. *J. Phys. D: Appl. Phys.*, 50(323001), 2017.

[84] R. Bussiahn, E. Kindel, H. Lange, and K.-D. Weltmann. Spatially and tempo-rally resolved measurements of argon metastable atoms in the effluent of a cold atmospheric pressure plasma jet. *J. Phys. D: Appl. Phys.*, 43(165201), 2010.

[85] K. Urabe, T. Morita, K. Tachibana, and B. N. Ganguly. Investigation of discharge mechanisms in helium plasma jet at atmospheric pressure by laser spectroscopic measurements. *J. Phys. D: Appl. Phys.*, 43(095201), 2010.

[86] A. Schmidt-Bleker, J. Winter, A. Bösel, S. Reuter, and K.-D. Weltmann. On the plasma chemistry of a cold atmospheric argon plasma jet with shielding gas device. *Plasma Sources Sci. Technol.*, 25(015005), 2016.

[87] K. Niemi, D. O'Connell, N. de Oliveira, D. Joyeux, L. Nahon, J.-P. Booth, and T. Gans. Absolute atomic oxygen and nitrogen densities in radio-frequency driven atmospheric pressure cold plasmas: Synchrotron vacuum ultra-violet high-resolution Fourier-transform absorption measurements. *Appl. Phys. Lett.*, 103(034102), 2013.

[88] J. Dedrick, S. Schröter, K. Niemi, A. Wijaikhum, E. Wagenaars, N. de Oliveira, L. Nahon, J.-P. Booth, D. O'Connell, and T. Gans. Controlled production of atomic oxygen and nitrogen in a pulsed radio-frequency atmospheric-pressure plasma. *J. Phys. D: Appl. Phys.*, 50(455204), 2017.

[89] T. Verreycken, R. Mensink, R. van der Horst, N. Sadeghi, and P. J. Bruggeman. Absolute OH density measurements in the effluent of a cold atmospheric-pressure Ar-H_2O RF plasma jet in air. *Plasma Sources Sci. Technol.*, 22(055014), 2013.

[90] G. Dilecce, L. M. Martini, P. Tosi, M. Scotoni, and S. De Benedictis. Laser induced fluorescence in atmospheric pressure discharges. *Plasma Sources Sci. Technol.*, 24(034007), 2015.

[91] J. B. Schmidt, B. Sands, J. Scofield, J. R. Gord, and S. Roy. Comparison of femtosecond- and nanosecond-two-photon-absorption laserinduced fluorescence (TALIF) of atomic oxygen in atmospheric-pressure plasmas. *Plasma Sources Sci. Technol.*, 26(055004), 2017.

[92] S. Schröter, J. Bredin, A. R. Gibson, A. West, J. P. Dedrick, E. Wagenaars, K. Niemi, T. Gans, and D. O'Connell. The formation of atomic oxygen and hydrogen in atmospheric pressure plasmas containing humidity: picosecond two-photon absorption laser induced fluorescence and numerical simulations. *Plasma Sources Sci. Technol.*, 29(105001), 2020.

[93] D. Steuer, I. Korolov, S. Chur, J. Schulze, V. Schulz-von der Gathen, J. Golda, and M. Böke. 2D spatially resolved O atom density profiles in an atmospheric pressure plasma jet: from the active plasma volume to the effluent. *J. Phys. D: Appl. Phys.*, 54(355204), 2021.

[94] A. Kramida, Yu. Ralchenko, J. Reader, and NIST ASD Team. NIST Atomic Spectra Database (ver. 5.9), [Online]. Available: https://physics.nist.gov/asd [2022, February 9]. National Institute of Standards and Technology, Gaithersburg, MD., 2021.

[95] W. L. Wiese and J. R. Fuhr. Accurate atomic transition probabilities for hydrogen, helium, and lithium. *J. Phys. Chem. Ref. Data*, 38(565-726), 2009.

[96] A. E. Kramida. A Critical Compilation of Experimental Data on Spectral Lines and Energy Levels of Hydrogen, Deuterium, and Tritium. *At. Data Nucl. Data Tables*, 96(586-644), 2010.

[97] W. L. Wiese, J. R. Fuhr, and T. M. Deters. *Atomic transition probabilities of carbon, nitrogen, and oxygen - A critical data compilation*, chapter J. Phys. Chem. Ref. Data, Monograph No. 7. AIP Press, Melville, NY, 1996.

[98] J. Reader, C. H. Corliss, W. L. Wiese, and G. A. Martin. *Wavelengths and Transition Probabilities for Atoms and Atomic Ions, Part. I. Wavelengths, Part II. Transition Probabilities*, chapter Nat. Stand. Ref. Data Ser., NSRDS-NBS 68. U.S. Government Printing Office, Washington, D.C., 1980.

[99] W. L. Wiese, J. W. Brault, K. Danzmann, V. Helbig, and M. Kock. Unified set of atomic transition probabilities for neutral argon. *Phys. Rev. A*, 39(2461-2471), 1989.

[100] P. Bruggeman, G. Cunge, and N. Sadeghi. Absolute OH density measurements by broadband UV absorption in diffuse atmospheric-pressure He-H_2O RF glow discharges. *Plasma Sources Sci. Technol.*, 21(035019), 2012.

[101] I.E. Gordon, L.S. Rothman, and R.J. Hargreaves. The HITRAN2020 molecular spectroscopic database. *J. Quant. Spectrosc. Radiat. Transf.*, 277(107949), 2022.

[102] M. Yousefi, P. F. Bernath, J. Hodges, and T. Masseron. A new line list for the $A^2\Sigma^+$ - $X^2\Pi$ electronic transition of OH. *J. Quant. Spectrosc. Radiat. Transf.*, 217(416-424), 2018.

[103] R. N. Tolchenov, O. Naumenko, N. F. Zobov, Shirin S. V., O . L. Polyansky, J. Tennyson, M. Carleer, P.-F. Coheur, S. Fally, A. Jenouvriere, and A. C. Vandaele. Water vapour line assignments in the 9250–26000 cm^{-1} frequency range. *J. Mol. Spectrosc.*, 233(1), 2005.

[104] T. Furtenbacher, R. Tóbiás, J. Tennyson, O. L. Polyansky, A. A. Kyuberis, R. I. Ovsyannikov, N. F. Zobov, and A. G. Császár. The W2020 Database of Validated Rovibrational Experimental Transitions and Empirical Energy Levels of Water Isotopologues. II. $H_2^{17}O$ and $H_2^{18}O$ with an Update to $H_2^{16}O$. *J. Phys. Chem. Ref. Data*, 49(043103), 2020.

[105] J. S. A. Brooke, P. F. Bernath, C. M. Western, C. Sneden, M. Afşar, G. Li, and I. E. Gordon. Line strengths of rovibrational and rotational transitions in the ground state of OH. *J. Quant. Spectrosc. Radiat. Transf.*, 168(142-157), 2016.

[106] S. Noll, H. Winkler, O. Goussev, and B. Proxauf. Oh level populations and accuracies of Einstein-A coefficients from hundreds of measured lines. *Atmos. Chem. Phys.*, 20(5269-5292), 2020.

[107] R. N. Tolchenov and J. Tennyson. Water line parameters from refitted spectra constrained by empirical upper state levels: Study of the 9500-14.500 cm^{-1} region. *J. Quant. Spectrosc. Radiat. Transf.*, 109(4), 2008.

[108] M. Birk, G. Wagner, J. Loos, L. Lodi, O. L. Polyansky, A. A. Kyuberis, N. F. Zobov, and J. Tennyson. Accurate line intensities for water transitions in the infrared: Comparison of theory and experiment. *J. Quant. Spectrosc. Radiat. Transf.*, 203(88-102), 2017.

[109] E. K. Conway, I. E. Gordon, A. A. Kyuberis, O. L. Polyansky, J. Tennyson, and N. F. Zobov. Calculated line lists for $H_2^{16}O$ and $H_2^{18}O$ with extensive comparisons to theoretical and experimental sources including the HITRAN2016 database. *J. Quant. Spectrosc. Radiat. Transf.*, 241(106711), 2020.

[110] J. Thiebaud, S. Crunaire, and C. Fittschen. Measurements of Line Strengths in the $2\nu_1$ Band of the HO_2 Radical Using Laser Photolysis/Continuous Wave Cavity Ring-Down Spectroscopy (cw-CRDS). *J. Phys. Chem. A*, 111(30):6959–6966, 2007.

[111] J. Loos, M. Birk, and G. Wagner. Measurement of positions, intensities and self-broadening line shape parameters of h_2o lines in the spectral ranges 1850–2280 cm^{-1} and 2390–4000 cm^{-1}. *J. Quant. Spectrosc. Radiat. Transf.*, 203(119-132), 2017.

[112] M. S. Zahniser, K. E. McCurdy, and A. C. Stanton. Quantitative spectroscopic studies of the hydroperoxo radical: band strength measurements for the ν_1 and ν_2 vibrational bands. *J. Phys. Chem.*, 3(1065-1070), 1989.

[113] C. Yamada, Y. Endo, and E. Hirota. Difference frequency laser spectroscopy of the ν_1 band of the HO_2 radical. *J. Chem. Phys.*, 78(4379), 1983.

[114] O. Bain and P. A. Giguère. Hydrogen Peroxide and its Analogues. *Can. J. Chem.*, 33(3), 1955.

[115] S. Klee, M. Winnewisser, A. Perrin, and J.-M. Flaud. Absolute Line Intensities for the ν_6 Band of H_2O_2. *J. Mol. Spectrosc.*, 195(1), 1999.

[116] K. Nagai, Y. Endo, and E. Hirota. Diode laser spectroscopy of the HO_2 ν_2 band. *J. Mol. Spectrosc.*, 89(2):520–527, 1981.

[117] D. D. Nelson jr. and M. S. Zahniser. Diode laser spectroscopy of the ν_3 vibration of the HO_2 radical. *J. Mol. Spectrosc.*, 150(2):527–534, 1991.

[118] W. Van Gaens, S. Iséni, A. Schmidt-Bleker, K.-D. Weltmann, S. Reuter, and A. Bogaerts. Numerical analysis of the effect of nitrogen and oxygen admixtures on the chemistry of an argon plasma jet operating at atmospheric pressure. *New J. Phys.*, 17(033003), 2015.

[119] G. Gagliardy and H.-P. Look, editors. *Cavity-Enhanced Spectroscopy and Sensing.* Springer-Verlag Berlin Heidelberg, 2014.

[120] G. Berden and R. Engeln, editors. *Cavity Ring-Down Spectroscopy: Techniques and Applications.* Blackwell Publishing Ltd., 2009.

[121] N. Lang, U. Macherius, M. Wiese, H. Zimmermann, J. Röpcke, and van Helden J. H. Sensitive CH_4 detection applying quantum cascade laser based optical feedback cavity-enhanced absorption spectroscopy. *Opt. Express*, 24(A537–43), 2016.

[122] J. Benedikt, D. Schröder, S. Schneider, G. Willems, A. Pajdarová, J. Vlček, and V. Schulz-von der Gathen. Absolute OH and O radical densities in effluent of a He/H_2O micro-scaled atmospheric pressure plasma jet. *Plasma Sources Sci. Technol.*, 25(045013), 2016.

[123] A. V. Pipa, S. Reuter, R. Foest, and K.-D. Weltmann. Controlling the NO production of an atmospheric pressure plasma jet. *J. Phys. D: Appl. Phys.*, 45(085201), 2012.

[124] S. Iséni, P. J. Bruggeman, K.-D. Weltmann, and S. Reuter. Nitrogen metastable $(N_2(A^3\Sigma_u^+))$ in a cold argon atmospheric pressure plasma jet: Shielding and gas composition. *Appl. Phys. Lett.*, 108(184101), 2016.

[125] J. Winter, H. Tresp, M. U. Hammer, S. Iséni, S. Kupsch, A. Schmidt-Bleker, K. Wende, M. Dünnbier, K. Masur, K.-D. Weltmann, and S. Reuter. Tracking plasma generated H_2O_2 from gas into liquid phase and revealing its dominant impact on human skin cells. *J. Phys. D: Appl. Phys.*, 47(285401), 2014.

[126] S. Reuter, J. Winter, S. Iséni, A. Schmidt-Bleker, M. Dünnbier, K. Masur, K. Wende, and K.-D. Weltmann. The Influence of Feed Gas Humidity Versus Ambient Humidity on Atmospheric Pressure Plasma Jet-Effluent Chemistry and Skin Cell Viability. *IEEE Trans. Plasma Sci.*, 43(9), 2015.

[127] H. Jablonowski, A. Schmidt-Bleker, K.-D. Weltmann, T. von Woedtke, and K. Wende. Non-touching plasma-liquid interaction - where is aqueous nitric oxide generated? *Phys. Chem. Chem. Phys.*, 20(25387), 2018.

[128] S. Reuter, H. Tresp, K. Wende, M. U. Hammer, J. Winter, K. Masur, A. Schmidt-Bleker, and K.-D. Weltmann. From RONS to ROS: Tailoring Plasma Jet Treatment of Skin Cells. *IEEE Trans. Plasma Sci.*, 40(11), 2012.

[129] S. Reuter, J. Winter, A. Schmidt-Bleker, H. Tresp, M. U. Hammer, and K.-D. Weltmann. Controlling the Ambient Air Affected Reactive Species Composition in the Effluent of an Argon Plasma Jet. *IEEE Trans. Plasma Sci.*, 40(11), 2012.

[130] A. Schmidt-Bleker, J. Winter, S. Iséni, M. Dünnbier, K.-D. Weltmann, and S. Reuter. Reactive species output of a plasma jet with a shielding gas device - combination of FTIR absorption spectroscopy and gas phase modelling. *J. Phys. D: Appl. Phys.*, 47(145201), 2014.

[131] L. Hansen, A. Schmidt-Bleker, R. Bansemer, H. Kersten, K.-D. Weltmann, and S. Reuter. Influence of a liquid surface on the no$_x$ production of a cold atmospheric pressure plasma jet. *J. Phys. D: Appl. Phys.*, 51(474002), 2018.

[132] J. Winter, K. Wende, K. Masur, S. Iséni, M. Dünnbier, M. U. Hammer, H. Tresp, K.-D. Weltmann, and S. Reuter. Feed gas humidity: a vital parameter affecting a cold atmospheric-pressure plasma jet and plasma-treated human skin cells. *J. Phys. D: Appl. Phys.*, 46(295401), 2013.

[133] K. Fricke, S. Reuter, D. Schröder, V. Schulz-von der Gathen, K.-D. Weltmann, and T. von Woedtke. Investigation of Surface Etching of Poly(Ether Ether Ketone) by Atmospheric-Pressure Plasmas. *IEEE Trans. Plasma Sci.*, 40(11), 2012.

[134] S. Reuter, J. Winter, A. Schmidt-Bleker, D. Schröder, H. Lange, N. Knake, V. Schulz-von der Gathen, and K.-D. Weltmann. Atomic oxygen in a cold argon plasma jet: TALIF spectroscopy in ambient air with modelling and measurements of ambient species diffusion. *Plasma Sources Sci. Technol.*, 21(024005), 2012.

[135] S. Iseni, S. Zhang, A. F. H. van Gessel, S. Hofmann, B. T. J. van Ham, S. Reuter, K.-D. Weltmann, and P. J. Bruggeman. Nitric oxide density distributions in the effluent of an RF argon APPJ: effect of gas flow rate and substrate. *New J. Phys.*, 16(12301), 2014.

[136] A. Panov. Perhydroxyl Radical (HO$_2$ •) as Inducer of the Isoprostane Lipid Peroxidation in Mitochondria. *J. Mol. Biol.*, 52(295–305), 2018.

[137] S. Ikawa, K. Kitano, and S. Hamaguchi. Effects of pH on Bacterial Inactivation in Aqueous Solutions due to Low-Temperature Atmospheric Pressure Plasma Application. *Plasma Process. Polym.*, 7(33-42), 2010.

[138] Q. Li, X.-M. Zhu, J.-T. Li, and Y.-K. Pu. Role of metastable atoms in the propagation of atmospheric pressure dielectric barrier discharge jets. *J. Appl. Phys.*, 107(043304), 2010.

2 Determination of the densities of Ar(^{3}P$_2$) atoms in the effluent of the kINPen-sci plasma jet
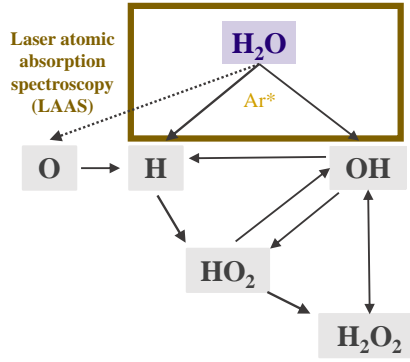
Metastable species play an important role in the formation and development of gas discharges. For instance, stepwise ionization and Penning-ionization processes of metastable species influence the electron density that determines breakdown dynamics and discharge regimes, among others [1]. Atoms in metastable states drive, besides electrons, energy transfer reactions in the plasma zone due to their high potential energy (Ar: 11.5 eV). Those energy transfer reactions include the dissociation of molecular species, by which the formation of reactive species in the plasma zone and in the plasma effluent is initiated. With the addition of humidity to the feed gas, metastable species are strongly quenched by water species, thereby producing H and OH radicals due to the dissociation of H$_2$O. By analysing the effective lifetimes of Ar(^{3}P$_2$) atoms and the axial distribution of the densities for Ar(^{3}P$_2$) atoms in the effluent of the kINPen-sci plasma jet, localised information about production mechanisms of H atoms and OH molecules can be deduced. A common technique to determine Ar(^{3}P$_2$) densities is laser atomic absorption spectroscopy (LAAS).

This chapter is adapted from reference [2]. Firstly, the principles of laser atomic absorption spectroscopy are introduced, and the experimental setup used in this work is presented. After a description of the method employed to determine absolute number densities and effective lifetimes, the determined temporal evolutions for Ar(^{3}P$_2$) atoms are discussed. Based on the obtained effective lifetimes, the quenching coefficient for Ar(^{3}P$_2$) atoms by water is determined. The axial distributions for Ar(^{3}P$_2$) atoms are presented, and the impact on the dissociation of water is examined.

2.1 Introduction to laser atomic absorption spectroscopy (LAAS)

Absorption spectroscopy is a well-known technique based on the Beer-Lambert law to determine absolute number densities of various atomic and molecular species [3–6]. The applications of absorption spectroscopy for diagnostic purposes is strongly connected to the development of lasers [6]. Before the building of the first ruby laser, atomic absorption spectroscopy (AAS) with a hollow cathode lamp as a light source has already been used to determine trace metal impurities [3, 7, 8]. With the development of semiconductor diode lasers emitting in the visible and near-infrared region, the selectivity and the tuning range could be increased [4, 9, 10]. Laser atomic absorption spectroscopy (LAAS), also known as diode laser atomic absorption spectroscopy (DLAAS), became a powerful tool for the analysis of low-pressure plasmas, since metastable states of noble gases, halogen elements, or non-metals, such as hydrogen atoms, carbon atoms, oxygen atoms, or sulfur atoms, can be probed in the near infrared region [9]. Further developments of tuneable diode lasers, in particular of lead-salt lasers emitting between 3 and 20 µm, extended the applicability of laser absorption spectroscopy (LAS) successfully to molecular species [11]. Tuneable diode laser absorption spectroscopy (TDLAS) and quantum cascade laser absorption spectroscopy (QCLAS) are nowadays valuable plasma diagnostic tools to investigate reaction kinetics in both low and high pressure plasmas [5, 12, 13].

In the following, a brief (mathematical) description of absorption spectroscopy is provided. In a medium where no power is gained (i.e. by stimulated emission), the propagation of a plane transversal-electro-magnetic wave in z-direction with the angular frequency $\omega = 2\pi\nu$ can be described by the complex wave vector $\overline{k}$ [14]:

$$\overline{k} = \frac{2\pi\nu}{c}\overline{n} = \frac{2\pi\nu}{c}n + j\kappa\frac{2\pi\nu}{c}. \tag{2.1}$$

Here, $\overline{n}$ is the complex refractive index, $n = \frac{c}{v_p}$ is the real part of the refractive index, which is defined by the phase velocity v_p, c is the speed of light in vacuum, j is the imaginary unit, and $\kappa(\nu, z)$ is the extinction coefficient that accounts for all loss terms. The intensity of the electro-magnetic wave at each position z is then given by [14]:

$$I(z,\nu) = I_0(\nu)\exp\left(-\frac{4\pi\nu}{c}\int_0^z \kappa(\nu, \tilde{z})d\tilde{z}\right) \tag{2.2}$$

Here, $I_0(\nu) = \vec{E_0}^2$ is the amplitude of the intensity for the plane wave with an electric field amplitude of $\vec{E_0}$. By neglecting losses of the intensity due to scattering, equation 2.2 is the integrated form of the Beer-Lambert law [15]:

$$I(d,\nu) = I_0(\nu)e^{(-\alpha d)}, \tag{2.3}$$

with

$$\alpha(\nu)d = \frac{4\pi\nu}{c} \int_0^d \kappa(\nu, z)dz. \tag{2.4}$$

Here, $\alpha(\nu)$ is the frequency dependent absorption coefficient of the absorbing species, and d is the diameter of the volume, in which the absorbing species are assumed to be distributed homogeneously along the line-of-sight of the incident beam.

In order to obtain the absolute number densities, light is transmitted through a volume that contains the species under investigation, and the intensities $I(\nu)$ with absorbing species and without absorbing species $I_0(\nu)$ are determined as a function of the frequency ν:

$$\mathcal{A}(\nu) = -\ln\left(\frac{I(\nu)}{I_0(\nu)}\right) = \alpha(\nu)d \tag{2.5}$$

Here, $\mathcal{A}(\nu)$ is denoted as the absorbance. Instead of dividing $I(\nu)$ by a measured reference spectrum $I_0(\nu)$ that induces additional noise, a baseline $\mathcal{I}_0(\nu)$ can be obtained from a polynomial fit of a measured spectrum, where the absorption lines are excluded.

According to the Beer-Lambert law, the densities of the absorbing species N_i in the lower state i of the probed transition are proportional to the absorption coefficient $\alpha(\nu)$. By integrating the absorbance $\mathcal{A}(\nu)$ for a single absorption line, number densities N_i can be obtained by:

$$\int \mathcal{A}(\nu)\ d\nu = \int \alpha(\nu)d\ d\nu = \int N_i\sigma_{int}f(\nu)d\ d\nu = N_id\sigma_{int}. \tag{2.6}$$

Here, σ_{int} is the integrated absorption cross section, d is the the diameter of the volume, in which the absorbing species are assumed to be distributed homogeneously, and $f(\nu)$ is the normalised line profile of the probed transition with:

$$\int f(\nu)d\nu = 1. \tag{2.7}$$

For atoms, often oscillator strengths f_{ik} are reported, which are related to the integrated absorption cross section σ_{int} by:

$$\sigma_{int} = f_{ik}\frac{e^2}{4\epsilon_0 m_e c^2}. \tag{2.8}$$

Here, e denotes the elementary charge, ϵ_0 is the dielectric permittivity, m_e is the electron mass, and c is the speed of light in vacuum. The observed line profile $f(\nu)$ of an absorption process in a gas ensemble is strongly influenced by broadening mechanisms, such as Doppler broadening, collisional broadening (Stark broadening), and saturation broadening in the case of optical pumping.

Saturation broadening can be avoided by a reduction of the energy of the incident beam. By considering spontaneous emission as the only relaxation mechanism, while light is absorbed from a lower state i to a higher state k, the saturation parameter S is defined

by [16]:

$$S = \frac{2\sigma_{ik}(\nu)\,I(\nu)}{h\nu_{ik}A_{ki}} \overset{!}{\ll} 1. \tag{2.9}$$

Here, $\sigma_{ik}(\nu)$ is the frequency dependent absorption cross section for the probed transition, $I(\nu)$ is the intensity of the incident beam, h is the Planck constant, ν_{ik} is the frequency of the probed transition, and A_{ki} is the corresponding Einstein coefficient for spontaneous emission. In order to avoid saturation broadening by optical pumping, the energy of the incident beam has to be chosen that the saturation parameter S becomes less than 1.

In an ideal gas ensemble, the species are randomly moving with a Maxwellian velocity distribution defining the gas temperature T, where the mean velocity $<v>$ is given by [16]:

$$<v> = \sqrt{\frac{8k_BT}{\pi m}}. \tag{2.10}$$

Here, k_B denotes the Boltzmann constant, and m is the species mass. The transition frequency ν_{ij} for an absorption process for a single species moving with the velocity v is shifted according to the Doppler effect. In the ensemble, this results in an inhomogeneous broadening of the measured absorption line, which has a Gaussian shape $f_G(\nu)$ [16, 17]:

$$f_G(\nu) = \sqrt{\frac{\ln(2)}{\pi}}\frac{1}{\gamma_G}\exp\left[-\ln(2)\left(\frac{\nu-\nu_{ij}}{\gamma_G}\right)^2\right]. \tag{2.11}$$

The half width at half maximum (HWHM) γ_G of this Gaussian profile is given by:

$$\gamma_G = \frac{1}{2}\nu_{ij}\sqrt{\frac{8k_B\ln(2)}{c^2}}\sqrt{\frac{T}{m}} \approx \frac{7.16\cdot10^{-7}}{2}\nu_{ij}\sqrt{\frac{T}{M}} \tag{2.12}$$

Here, c is the speed of light in vacuum, T is the gas temperature in Kelvin and M is the species mass in atomic mass units.

If a species B in an ensemble approaches another species A, the electric potential of the approaching species B influences the potential curves of species A temporally during a collision process. This results in a shift $\delta\nu_{ik}$ of the transition frequency $\nu'_{ik} = \frac{(E'_k - E'_i)}{h}$ of species A, and thus of the photon frequency that can be absorbed. Here, h denotes the Planck constant and E'_i and E'_k describe the energy of the shifted potential curves, which depends on the distance between the centres of mass of the two species involved. Since in an ensemble at a given temperature and pressure the distances between the species are statistically distributed, the absorption line is also broadened. Collision processes lead to a homogeneous broadening with a Lorentzian shape [16, 17]:

$$f_L(\nu) = \frac{1}{\pi}\frac{\gamma_L}{\gamma_L^2 + (\nu - (\nu_{ik} + \delta\nu_{ik}))^2} \tag{2.13}$$

The HWHM γ_L of this Lorentzian profile is given by:

$$\gamma_L = \gamma_{gas}(p_{gas} - p_{self}) + \gamma_{self} \cdot p_{self}. \tag{2.14}$$

Here, γ_{gas} denotes the pressure broadening coefficient of species A by species B, p_{gas} is the gas pressure in the probed volume, γ_{self} describes the self-broadening coefficient of species A, and p_{self} is the partial pressure of species A. Pressure broadening coefficients vary from absorption line to absorption line and depend on the colliding species. Hence, pressure broadening coefficients are either reported in literature or have to be investigated carefully for the gas mixture employed.

The resulting profile for an absorption line at atmospheric pressure is given by a convolution of the inhomogeneously and homogeneously broadened parts, which can be described by a Voigt profile $\mathcal{V}(\nu, \gamma_G, \gamma_L)$ [16, 18]:

$$\mathcal{V}(\nu, \gamma_G, \gamma_L) = \frac{\text{Re}\left(w\left(\frac{\nu + j\gamma_L}{\sqrt{2}\gamma_G}\right)\right)}{\sqrt{2\pi}\gamma_G}, \tag{2.15}$$

approximated by the real part of the Faddeeva function w, with the imaginary unit j, the Gaussian HWHM γ_G and the Lorentzian HWHM γ_L. The Faddeeva function is defined by [19]:

$$w(z) = e^{-z^2}\left(1 + \frac{2j}{\sqrt{\pi}}\int_0^z e^{t^2}dt\right). \tag{2.16}$$

For atmospheric pressure plasmas, most of the reactive species remain in the ground state. In particular for atoms, where the population densities of excited states are small compared to the population density of the ground state due to the large energy gap between the ground state and excited states, the ground state density can be approximated by the total density n. By assuming a Voigt-profile for the frequency dependant absorption cross section, absolute number densities can be obtained by:

$$n = \frac{\mathcal{A}(\nu)}{f_{ik}\mathcal{V}(\nu, \gamma_G, \gamma_L)d}\frac{4\epsilon_0 m_e c^2}{e^2}. \tag{2.17}$$

Here, $\mathcal{A}(\nu)$ is the absorbance at frequency ν, f_{ik} is the oscillator strength, $\mathcal{V}(\nu, \gamma_G, \gamma_L)$ is the normalized line profile, d is the diameter of the volume, in which the absorbing species are assumed to be distributed homogeneously along the line-of-sight of the incident beam, ϵ_0 is the dielectric permittivity, m_e is the electron mass, c is the speed of light in vacuum, and e is the elementary charge.

Since the determination for the density strongly depends on the measured wavelength, a precise information about the exact laser position is crucial for LAAS. In order to obtain spectral information about the tuneable laser, commonly one of the following options is employed:

    a) Frequency determination based on a reference discharge
      In the works of Niermann et al. [20, 21] and of others [22–29] a beam splitter has been used to guide a part of the laser intensity through a reference discharge with a known quantity of Ar or He at low pressure. The absorption spectra of the reference discharge have been compared to the absorption spectra of the plasma jet, providing a reference frequency at the position of the strongest low pressure absorption line. For a relative scale, another part of the incident light has been transferred to a Fabry-Perot-interferometer (etalon) by using a second beam splitter. Since the maxima in the etalon are separated by a constant frequency value that depends on the length of the etalon, a relative frequency scale can be obtained.

    b) Spectrometer-based frequency determination
      In order to allow an absolute frequency scaling, wavelength analysers based on Fourier transformation are used, since they provide a sufficient resolution in the order of hundredths of wavenumbers. However, those devices are expensive. Examples for the determination of Ar and He metastables in atmospheric pressure plasma jets, where wavelength analysers were employed, can be found in references [30, 31]. In this work, the spectrometer-based frequency determination was utilised.

Besides time-averaged densities of metastable states, their temporal density distribution is a focus of research, in particular for CAPJs that are operated with an AC voltage at frequencies in the MHz range, [21, 22, 26, 28, 30, 32]. Therefore, the laser has been tuned to the maximum of the absorption and kept constant, while the transmitted intensity was detected as a function of time.

2.2 Experimental setup for LAAS

In this work, laser atomic absorption spectroscopy (LAAS) was used to determine Ar metastable densities in the effluent of the kINPen-sci plasma jet. Therefore, the kINPen-sci was operated with 3 slm Ar, of which a part was guided through a water bubbler to humidify the feed gas up to 1370 ppm. The humidity was determined by a chilled mirror hygrometer (EdgeTech, DewMaster). The maximum humidity level was set to 1370 ppm, as for higher humidity contents no absorption peaks of Ar($^3P_2$) atoms above the detection limit could be observed in the effluent. The discharge is stable for humidity contents larger than 3000 ppm, which was used in previous investigations, for example [33]. In order to control the surrounding gas composition, a gas curtain made
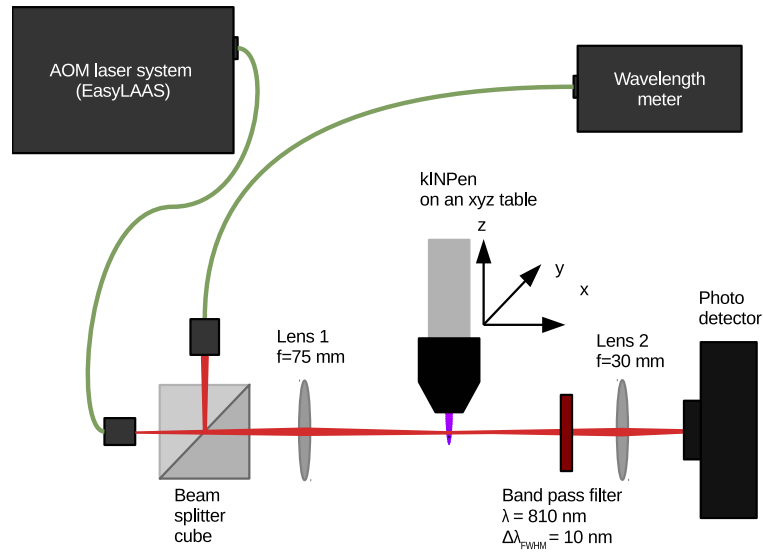
Figure 2.1: Experimental setup for the determination of $Ar(^3P_2)$ atoms in the effluent of the kINPen-sci plasma jet comprising an AOM laser system with a fibre, a beam splitter cube, a wavemeter with fibre connection, a lens, a bandpass filter, a focusing lens, a photo detector, and the kiNPen-sci plasma jet.

of a mixture of O_2 and N_2 with a total flow rate of 5 slm was applied. The gas mixture could be varied between 100% O_2 and 100% N_2.

In figure 2.1, a schematic of the experimental setup for the detection of $Ar(^3P_2)$ atoms is presented. The optical $Ar(1s_5 - 2p_9)$ transition was probed by a novel acousto-optic modulated (AOM) laser system (EasyLAAS, neoplas control GmbH, Germany) at a wavelength of 811.53 nm [34, 35]. This laser system was composed of a laser diode, an external cavity-like setup made of two acousto-optic modulators, a grating in Littrow configuration, as well as a Michelson-Morley interferometer for the coarse determination of the laser wavelength. With this setup, a tuning range of about 50 GHz at a frequency of 4.5 GHz was accessible. However, in this work, the laser was operated at a constant wavelength of 811.534 nm with a laser linewidth of approximately 15 fm (0.0002 cm^{-1}). The laser output beam was guided through an optical fibre to a beam splitter cube. 50% of the laser intensity was reflected into a second fibre, which was connected to a wavemeter (High Finesse, WSG-200) in order to determine the exact laser wavelength. The remaining 50% (approximately 50 µW) were focused by a lens (focal length 75 mm) to a spot of approximately 100 µm in the effluent of the plasma jet. By employing three step motors, the plasma jet's position in axial and radial direction was adjusted. In order to avoid the detection of plasma emission close to the transmitted laser light, the laser beam was filtered by a 10 nm band pass filter at 810 nm behind the plasma effluent. The filtered laser beam was then focused by a second lens onto a photo detector (Femto, current amplifier HCA-S, 200 MHz band width), which was connected to an oscilloscope (Tektronix, DPO 4104). In order to process the detector signal by a customised python code, the data of the oscilloscope were directly transferred to a standard computer.

2.3 Determination of absolute number densities with LAAS

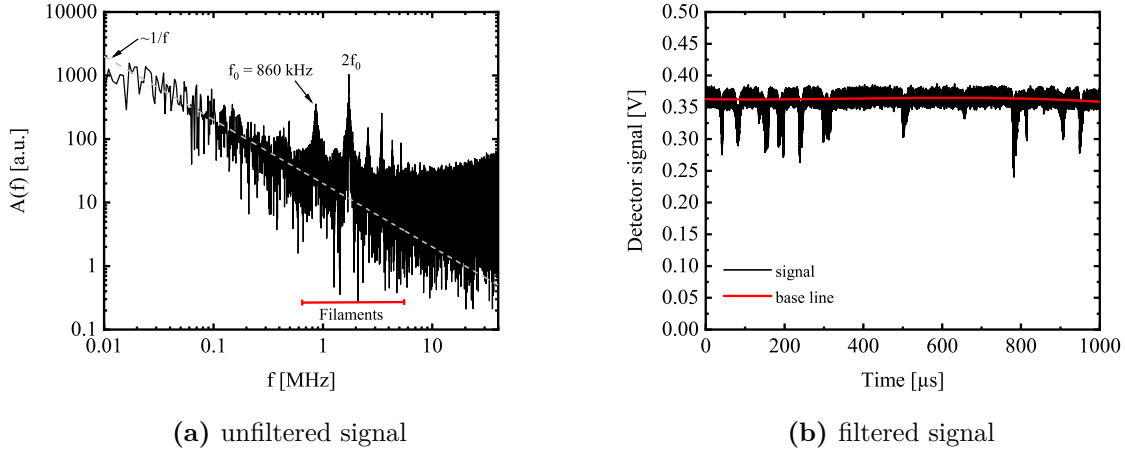**(a)** unfiltered signal　　　　　　　　　　　　　**(b)** filtered signal

Figure 2.2: (a) Fourier transform of the unfiltered detector signal and (b) filtered detector signal. The laser beam was focussed 0.1 mm below the nozzle. A feed gas of 3 slm Ar with 70 ppm humidity was used, while a gas curtain of 5 slm O_2 was applied.

In order to improve the signal to noise ratio, the detector signal was cleaned by a digital low pass filter. Therefore, the unfiltered signal was analysed by a Fourier transformation to identify a suitable cutoff frequency. In figure 2.2a, the Fourier transformed, unfiltered signal is presented together with a straight line proportional to the inverse of the frequency, which represents electrical $1/f$-noise. Discrete peaks at $f_0 = 860$ kHz and its higher harmonics up to the 6th order deviating from the $1/f$-noise were identified. Those peaks peaks correspond to the occurrence of absorption events, whereby the width was influenced by the turbulent gas flow, the gas temperature, and by quenching [21]. Similar observations have been reported previously by Niermann et al. investigating a CAPJ operating at 13.56 MHz [21]. However, in contrast to those measurements, in this work, the peaks correspond to the excitation frequency of 860 kHz for the kINPen-sci plasma jet. This discrepancy could be due to the different driving frequencies of 860 kHz in this work, and 13.56 MHz previously, which could lead to different excitation mechanisms. While the plasma jet studied by Niermann et al. is in steady state operation due to the short period of the high voltage cycle (96 ns), the high voltage period of about 1.16 μs in the current work is much longer and exceeds the lifetime of the metastable states. Therefore, in our case, in each half wave of the high voltage period, new filaments are ignited, as will be discussed in the remainder of this chapter. The width of the peaks of the Fourier transformed detector signal was influenced by the turbulent gas flow, the gas temperature, and by quenching. In order to include the absorption events while reducing the noise as much as possible, a cutoff frequency of 39 MHz for the low pass filter was chosen. In figure 2.2b, an example of the filtered detector signal as a function of time is illustrated together with a 3rd order polynomial fit of the base line, while the

laser frequency was kept constant and the plasma jet was switched on. 3 slm Ar with less than 70 ppm humidity were used as a feed gas, and a gas curtain of 5 slm O_2 was applied.

The time dependent absorption signal $\mathcal{A}(t)$ was obtained by dividing the detector signal $I(t)$ by a 3rd order polynomial fit of the base line $I_0(t)$ according to equation 2.5:

$$\mathcal{A}(t) = -\ln\left(\frac{I(t)}{I_0(t)}\right) = n(t)\sigma(\nu)d. \tag{2.18}$$

Here, $n(t)$ is the time dependent density of $\text{Ar}(^3\text{P}_2)$ atoms, $\sigma(\nu)$ is the frequency dependent absorption cross section, and d is the diameter of the volume, in which $\text{Ar}(^3\text{P}_2)$

(a) complete signal, 70 ppm humidity

(b) complete signal, 879 ppm humidity

(c) close up, 70 ppm humidity

(d) close up, 879 ppm humidity
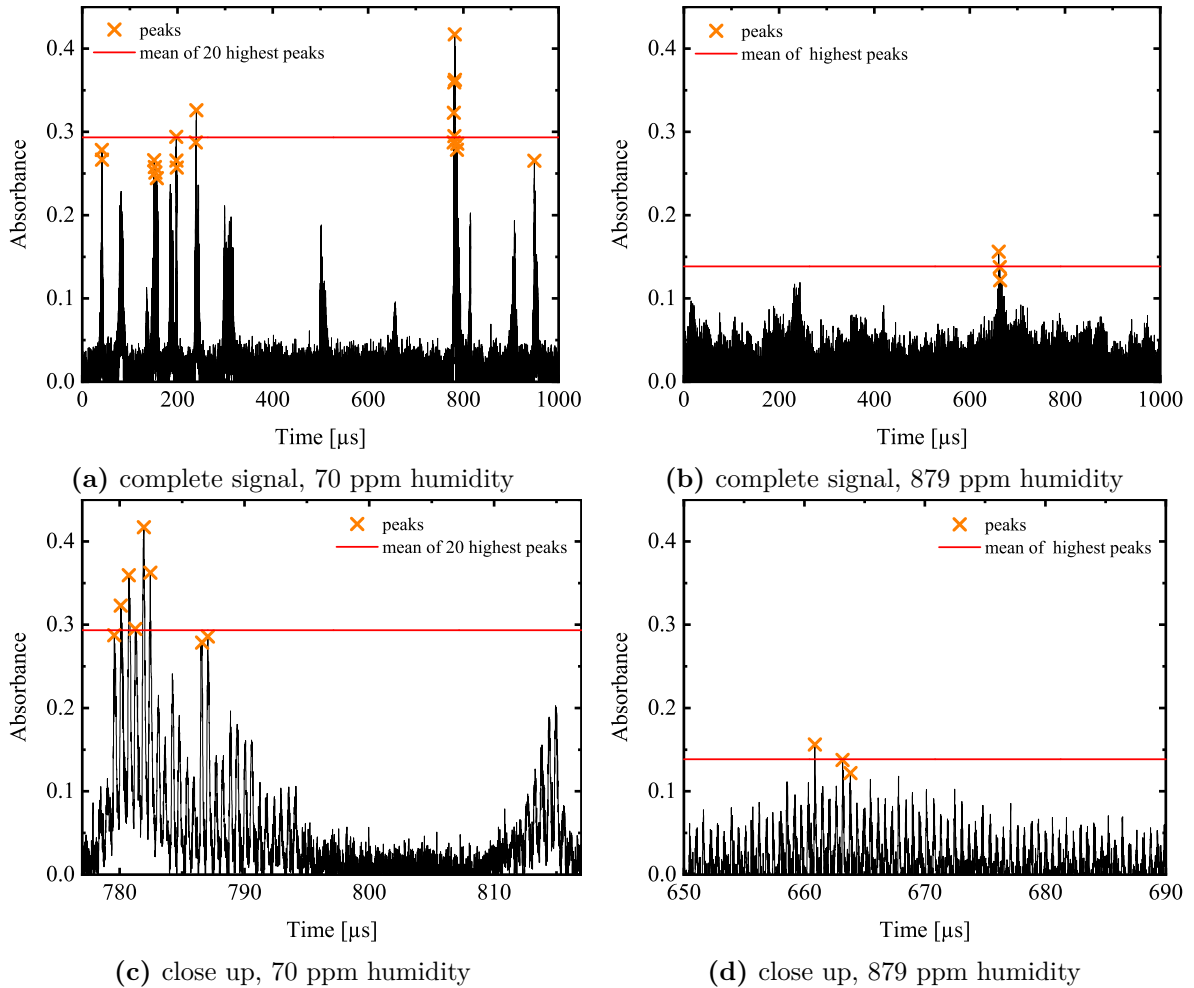
Figure 2.3: Absorbance as a function of time for (a) 70 ppm humidity in the feed gas, and (b) 879 ppm humidity in the feed gas, while a gas curtain of 5 slm O_2 was applied. The distance to the nozzle was set to $z = 0.1$ mm. The highest absorption peaks are also shown as well as the mean absorbance. Close ups of (a) and (b) illustrated between (c) 777 to 817 µs for 70 ppm humidity in the feed gas, and between (d) 650 to 690 µs for 879 ppm humidity in the feed gas.

atoms are assumed to be distributed homogeneously.

By using a customised python code, peaks were identified by their height, which was set to be larger than 0.07, and a minimum distance between subsequent peaks of 160 ns. In figures 2.3a and 2.3b, the absorption signal at $z = 0.1$ mm and a constant laser wavelength as a function of time is depicted for a water content of 70 ppm and 879 ppm, respectively, while a gas curtain of 5 slm O$_2$ was applied. The time range covers about 862 high voltage cycles with a time duration of 1.16 µs each. The highest peaks are marked by crosses and their mean value is represented by the straight line. At 70 ppm humidity, several absorption peaks with an absorbance of approximately 0.3 were detected. These peaks appear in groups with a varying number of single events. 12 groups were identified, whereas the 20 highest peaks were included in 6 of these groups. For 879 ppm humidity, the total absorption decreased by more than a factor of 2 compared to the measurement at 70 ppm humidity. In this example, only three peaks within one group were identified. In figures 2.3c and 2.3d, close ups of the examples in figures 2.3a and 2.3b are illustrated between 777 and 817 µs, and between 650 and 690 µs for respectively 70 ppm and 879 ppm humidity in the feed gas. For 70 ppm humidity, two groups are shown, whereby the first group includes 8 of the 20 highest peaks. 6 of these peaks appeared in quick succession in the first group, which lasted for approximately 15 µs. The second group had a shorter lifetime of approximately 7 µs, whereas the maximum absorbance was at 0.2. For 879 ppm in the feed gas, a single peak group between 650 and 690 µs was recorded. The maximum absorbance of 0.16 was reached after 10 µs. The appearance of groups can be explained by the filamentary character of the plasma jet. As long as a filament crosses the laser beam, an absorption signal of Ar(^{3}P$_2$) atoms excited by the filament's ionisation wave is detected. During the time without any absorption signal between the peak groups, the filament was outside the position of the laser beam and no absorption of Ar(^{3}P$_2$) atoms was measured.

In order to determine the absorption length d, over which the Ar(^{3}P$_2$) atoms were assumed to be distributed homogeneously, the diameter of the emission of a filament was measured. This is a reasonable approximation, since Ar(^{3}P$_2$) atoms are short living and produced in a filament, and the absorption length is expected to be equal to the diameter of the filaments' emission patterns. In figure 2.4, images of the plasma emission between 845 nm and 855 nm for 3 slm Ar with 20 ppm humidity (figure 2.4a and 2.4b) and 3000 ppm humidity (figure 2.4c and 2.4d) in the feed gas and 5 slm O$_2$ in the gas curtain, taken by an iCCD camera (Stanford Computer Optics, 4Picos dig) at a gate time of 120 ns, are shown together with a shadow image of the plasma jet's nozzle exit. The spectral region was chosen due to the emission lines of Ar, including transitions ending on metastable energy levels. To allow a comparison of the emission pattern to a fixed laser spot, a red ellipse is depicted. In these short exposure time images of individual discharge events, the emission signal of Ar appeared as a thin channel with a diameter of approximately $d = 120 \pm 15$ µm, which was also taken as the absorption length. The pathways for these filamentary discharge events were varying due to the influence of the surrounding gas composition within the turbulent feed gas and were sometimes crossing the laser beam. The admixture of water to the feed gas was found
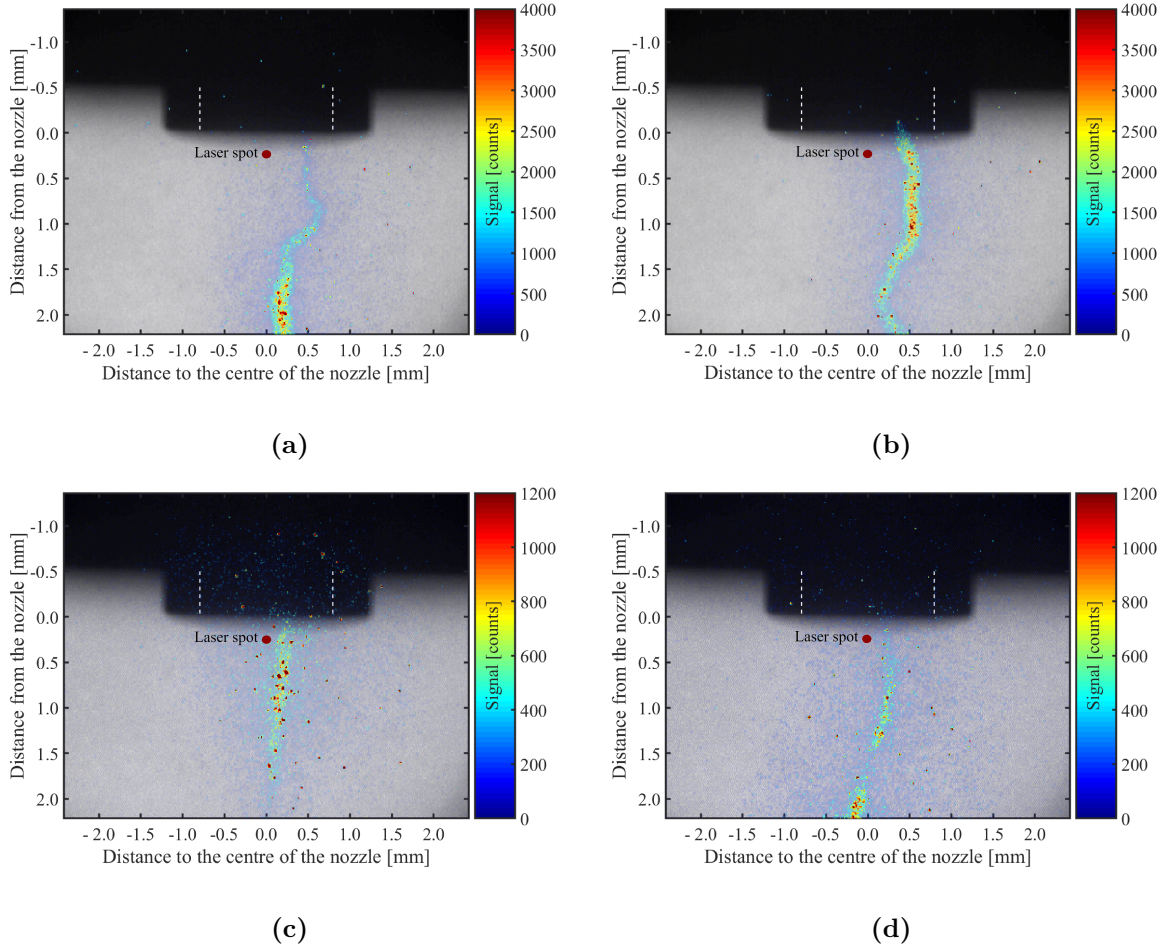
(a)

(b)

(c)

(d)

Figure 2.4: Snapshots of the plasma emission between 845 nm and 855 nm for (a) and (b) with 3 slm Ar with 20 ppm humidity, (c) and (d) with 3 slm Ar with 3000 ppm humidity, taken by an iCCD camera at a gate time of 120 ns, together with a schematic of the laser spot. A gas curtain of 5 slm O_2 was applied.

to have no influence on the diameter of the emission pattern. However, with a high water content in the feed gas, the maximum intensity decreased by a factor of 3.3. This is most likely due to the lower electron temperature and thus, a lower rate coefficient for argon excitation, as well as due to the quenching of excited species by water molecules. As the pathways of the filaments were varying stochastically due to the surrounding gas within the turbulent gas flow [36], the appearance and the shape of absorption peak groups can be explained by the overlap of the filament with the laser beam. Apparently, the position of a filament was approximately constant for a few voltage periods before changing the direction.

For the observed Ar($1s_5 - 2p_9$) transition, the integrated absorption cross section yields $\sigma_{int} = 4.07 \cdot 10^{-17}$ m^{2}cm^{-1} with an oscillator strength of $f_{ik} = 0.46$ [37]. The frequency dependent absorption cross section $\sigma(\nu)$ was calculated by assuming a Voigt profile $\mathcal{V}(\nu, \gamma_G, \gamma_L)$:

$$\sigma(\nu) = \sigma_{int}\mathcal{V}(\nu, \gamma_G, \gamma_L). \tag{2.19}$$

Therefore, the Gaussian HWHM γ_G was determined by the Doppler broadening to be:

$$\gamma_G = \frac{1}{2}\frac{1}{c\lambda}\sqrt{\frac{8k_BT\ln(2)}{m_{Ar}}} = 0.013 \text{ cm}^{-1}. \tag{2.20}$$

Here, $\lambda = 811.534$ nm is the laser wavelength, k_B is the Boltzmann constant, $T = 300\ K$ is the temperature, and $m_{Ar} = 39.948$ amu is the argon mass. For the Lorentzian HWHM γ_L, the pressure broadening coefficient HWHM/N= $7.1 \cdot 10^{-21}$ cm^{-1} cm^3 reported in reference [38], was evaluated with a density of $N = 2.45 \cdot 10^{19}$ cm^{-3} obtaining a value of $\gamma_L = 0.17$ cm^{-1} for Ar. This value is close to the experimental values of 0.21 cm^{-1}, 0.15 cm^{-1}, and 0.14 cm^{-1} reported previously [21, 22, 26], and one order of magnitude larger than the Doppler broadening. To take the stochastic pathway of the filaments into account, the average and the standard deviation of the 20 highest absorption peaks $\langle\mathcal{A}(\nu)\rangle$, and $\delta\langle\mathcal{A}(\nu)\rangle$, respectively, were determined to calculate the number densities n and the corresponding error, as previously reported [26, 39]. The number density was then obtained with $d = 120$ μm by:

$$n = \frac{\langle\mathcal{A}(\nu)\rangle}{\sigma_{int}\mathcal{V}(\nu, \gamma_G, \gamma_L)d}, \tag{2.21}$$

and the corresponding error by:

$$\Delta n = \frac{\delta\langle\mathcal{A}(\nu)\rangle}{\sigma_{int}\mathcal{V}(\nu, \gamma_G, \gamma_L)d}. \tag{2.22}$$

Next to the value for the number density of Ar(^{3}P$_2$) atoms, the decay time is important to deduce the impact of Ar(^{3}P$_2$) atoms on the reactive species composition in the effluent of the kINPen-sci plasma jet. The decay time is strongly influenced by quenching reactions of water. In order to analyse the quenching for various water contents in the feed gas, the effective lifetime for each absorption peak was determined by analysing the time evolution of absorption events. An example of such a time evolution at a constant laser frequency is presented in figure 2.5, together with an exponential fit. Within about 100 ns, the absorbance reached its maximum value, followed by a decay, which was not purely exponential in the case of water admixture as shown exemplarily in figure 2.5 for 70 ppm water in the feed gas. To obtain a robust data analysis procedure, the half time $t_{1/2}$ of each peak was determined instead of fitting each decay by an exponential function, as was done in previous investigations [26, 39]. The decay time τ_{eff}, denoted as the effective lifetime, was determined from the mean half time of the 20 highest peaks
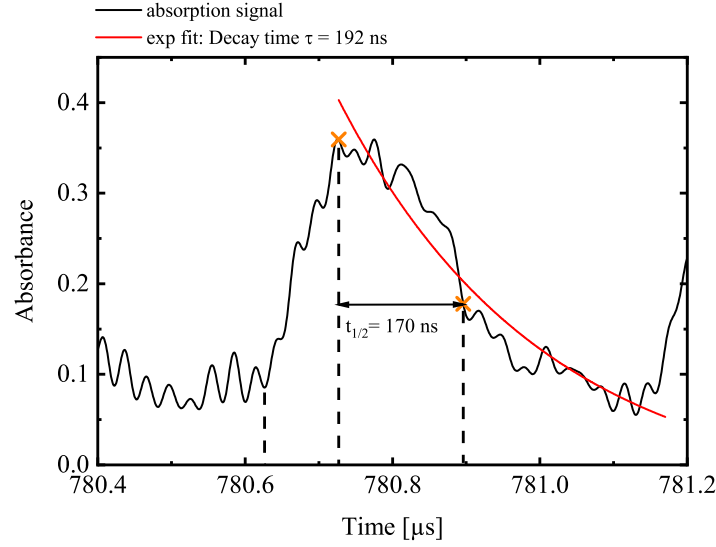
Figure 2.5: Example of the temporal evolution of the $Ar(^3P_2)$ density at $z = 0.1$ mm, 70 ppm water in 3 slm Ar feed gas, and a gas curtain of 5 slm O_2, together with a fit of the exponential decay.

$\left\langle t_{1/2} \right\rangle$ by:

$$\tau_{eff} = \frac{\left\langle t_{1/2} \right\rangle}{\ln(2)}. \tag{2.23}$$

In the case for a lower amount of detected peaks, the mean of all detected peaks were taken to calculate the effective lifetime. The error $\Delta\tau_{eff}$ for the effective lifetime was obtained from the standard deviation of $\left\langle t_{1/2} \right\rangle$. Compared to an exponential fit, this method yields an error of about 20%.

2.4 Results

2.4.1 Temporal evolution of the density for Ar(^{3}P$_2$) atoms

In figure 2.6, examples of the temporal evolution of the $Ar(^3P_2)$ densities are depicted together with a voltage signal with an arbitrary amplitude and phase. The feed gas humidity, the distance from the nozzle, and the gas curtain composition were varied: 70 ppm water in the feed gas, 5 slm O_2 for the gas curtain at $z = 0.1$ mm shown in figure 2.6a, 879 ppm water in the feed gas, 5 slm O_2 for the gas curtain at $z = 0.1$ mm illustrated in figure 2.6b, 70 ppm water in the feed gas, 5 slm O_2 for the gas curtain at $z = 4.0$ mm depicted in figure 2.6c, and 75 ppm water in the feed gas, 5 slm N_2 for the gas curtain at $z = 0.1$ mm presented in figure 2.6d. A straight line shows the mean of the 20 largest peaks, whereas crosses indicate the considered peaks.
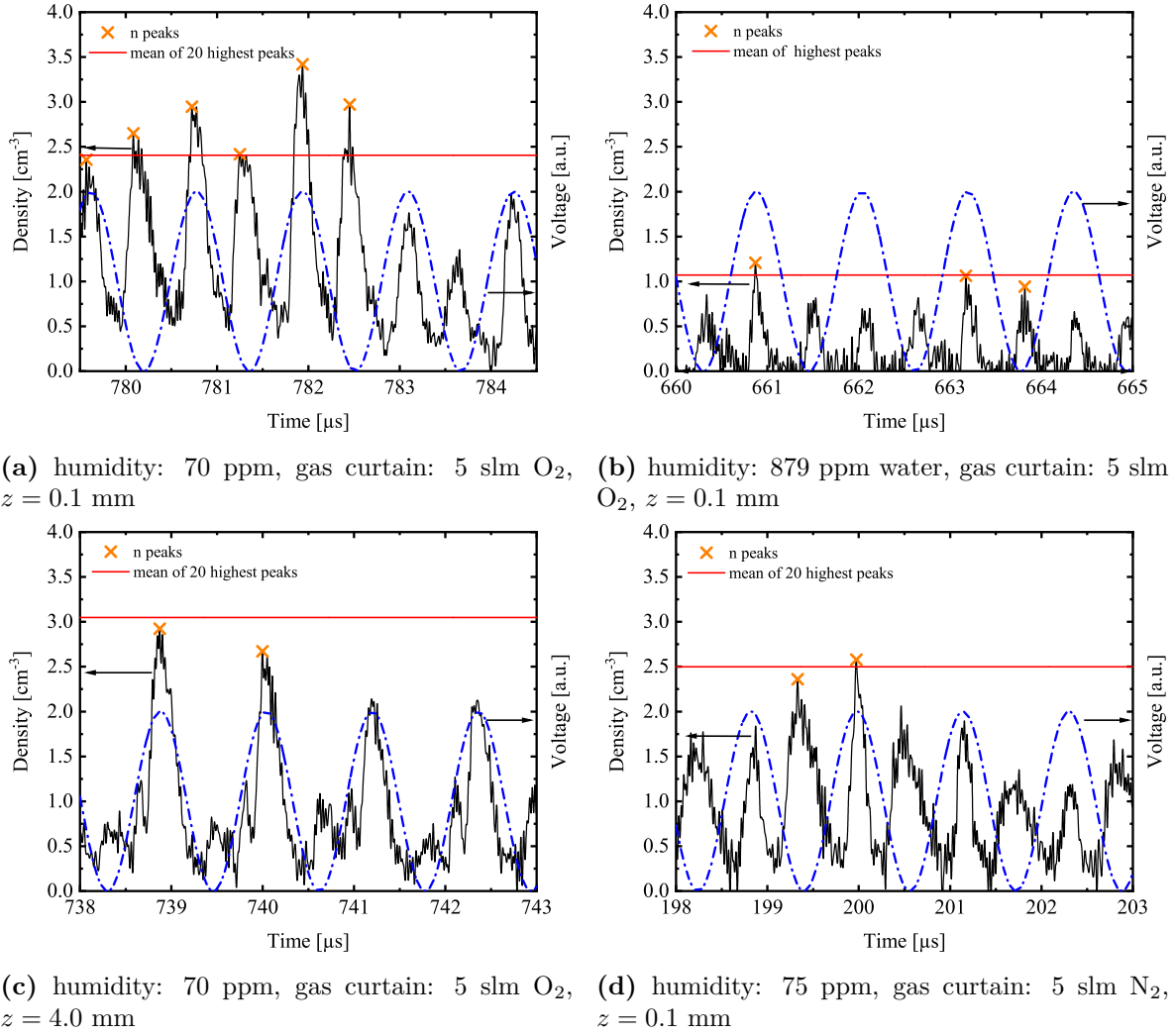
(a) humidity: 70 ppm, gas curtain: 5 slm O$_2$, $z = 0.1$ mm

(b) humidity: 879 ppm water, gas curtain: 5 slm O$_2$, $z = 0.1$ mm

(c) humidity: 70 ppm, gas curtain: 5 slm O$_2$, $z = 4.0$ mm

(d) humidity: 75 ppm, gas curtain: 5 slm N$_2$, $z = 0.1$ mm

Figure 2.6: Examples for the temporal evolution of the Ar(^{3}P$_2$) densities, the detected peaks, and the mean of the 20 highest peaks, shown together with a voltage signal with an arbitrary amplitude and phase, and a frequency equal to the operating frequency of the plasma jet. The humidity of the feed gas, the curtain gas composition, and the distance to the nozzle z were varied: (a) humidity: 70 ppm, gas curtain: 5 slm O$_2$, $z = 0.1$ mm, (b) humidity: 879 ppm water, gas curtain: 5 slm O$_2$, $z = 0.1$ mm, (c) humidity: 70 ppm, gas curtain: 5 slm O$_2$, $z = 4.0$ mm, (d) humidity: 75 ppm, gas curtain: 5 slm N$_2$, $z = 0.1$ mm.

Having a closer look on the individual density peaks, a strong increase within approximately 190 ns to its maximum value and an exponential decay with a decay time of a approximately 130 ns was observed, while a oxygen gas curtain was applied. Applying a gas curtain consisting of pure nitrogen changed the decay time of the density peaks: in the first half wave of the applied voltage they were similar to the measurements with an oxygen gas curtain, whereas in the second half wave the decay time increased by a factor of approximately 1.75. Moreover, the exponential decay in the case of an nitrogen curtain changed to a linear decay. In figure 2.7, close ups of 4 peaks are shown together
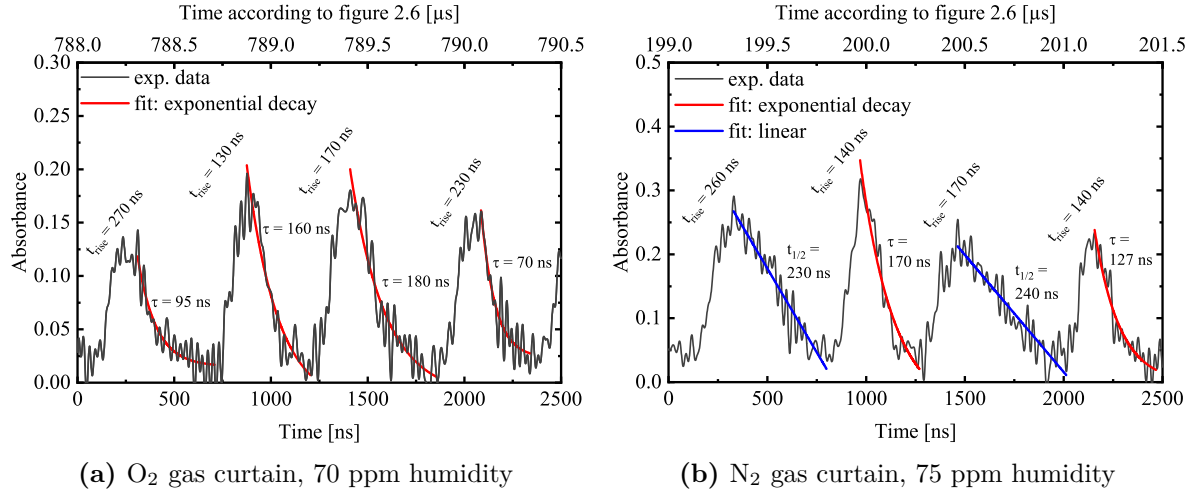
(a) O_2 gas curtain, 70 ppm humidity

(b) N_2 gas curtain, 75 ppm humidity

Figure 2.7: Close ups of figures 2.6a and 2.6d with 4 absorption events as a function of time, together with exponential and linear fits on the decay, respectively for (a) an oxygen gas curtain, and (b) a nitrogen gas curtain.

with values for the rise time, as well as exponential fits of the decay in the case of an exponentially decay. In the case of a rather linear decay, the half time is depicted.

At $z = 0.1$ mm, density peaks in both half waves of the applied voltage with similar intensity were observed. For larger distances from the nozzle, the $Ar(^3P_2)$ density in the second half wave decreased for all gas curtain compositions. In order to investigate the occurrence of two density peaks within one voltage period in more detail, the detector signal was analysed by applying a Fourier transformation. The Fourier amplitudes $A(f_0)$ and $A(2f_0)$ of the frequencies $f_0 = 860$ kHz and $2f_0 = 1720$ kHz are a value for the number of voltage periods that include one absorption peak per cycle and two absorption peaks per cycle, respectively. In figure 2.8, the ratio $\frac{A(2f_0)}{A(f_0)}$ at $z = 0.1, 1.0, 2.0, 3.0$, and 4.0 mm, is illustrated as a function of the feed gas humidity for three different gas curtain compositions, 5 slm O_2, 5 slm N_2, and 4 slm N_2 with 1 slm O_2. Close to the nozzle at $z = 0.1$ mm, the ratio $\frac{A(2f_0)}{A(f_0)}$ decreases from a value higher than 1 to less than 0.5 with increasing humidity up to 200 ppm. For larger amounts of humidity, the ratio increased again to values higher than 9 for all gas curtain compositions in the case of $z = 0.1$ mm. At larger distances from the nozzle, the ratio $\frac{A(2f_0)}{A(f_0)}$ decreased for humidities up to 200 ppm to a value below 1 with no further increase for larger amounts of humidity. The gas curtain composition had no significant impact on the occurrence of absorption peaks within the first observed 4 mm below the nozzle.

The occurrence of two absorption peaks within one voltage cycle shows that active plasma channels were formed in both half waves of the applied voltage cycle. As the polarity of the voltage changes between these subsequent half waves, a different breakdown process in such an asymmetric plasma source can be expected. Bussiahn et al. and Gerling et al. reported about cathode directed ionisation waves developing in a discharge with a needle-to-ring and needle-to-plane electrode configuration, respectively, along the direction of the gas flow in one half wave, when the needle electrode was the
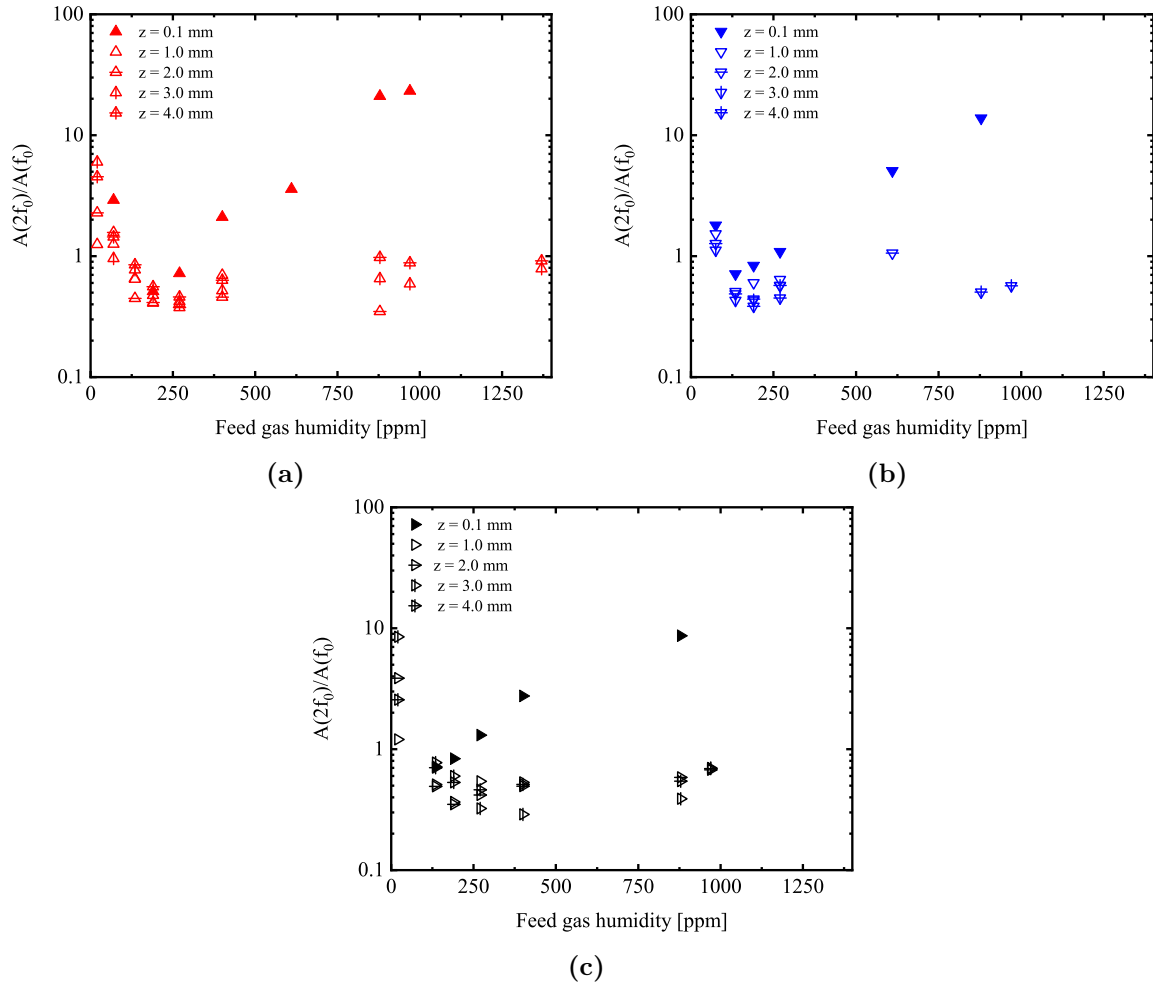
Figure 2.8: Ratio of the Fourier amplitudes of the first harmonic and the fundamental excitation frequency as a function of the feed gas humidity for three different gas curtain compositions (a) 5 slm O_2, (b) 5 slm N_2, and (c) 4 slm N_2, 1 slm O_2, and various distances from the nozzle z.

anode, and against the gas flow direction in the following half wave, when the needle electrode was the cathode [30, 40]. An ionisation wave counter-propagating to the gas flow direction was also observed in the kINPen, operating in helium with an oxygen gas shielding [41], and operating in argon without gas shielding [42]. Sands et al. reported on investigations of the spatio-temporal distribution of Ar($^3P_2$) atoms in a filamentary CAPJ [32] and distinguished between the production by the head of an ionisation wave, a production near the anode, and a production in the residual channel. An increase of Ar($^3P_2$) atoms at the head of the ionisation wave within the first 20 ns was observed, and a production near the anode over the following 250 ns. A velocity of the ionisation wave of approximately 10^4 m/s has been reported by Reuter et al., for a kINPen plasma jet operated with 5 slm Ar with small admixtures of O_2 to the feed gas [42]. Taking this velocity into account, the absorption signal of Ar($^3P_2$) atoms would rise within 10 ns while travelling a distance of 100 μm, which is the spot size of the laser in this

work. However, it can not be excluded that after the maximum of the ionisation wave, electrons still have enough energy to excite $Ar(^3P_2)$ atoms. A production after the maximum of the ionisation wave could explain the rise times of the absorption signals, which are about a factor of 19 larger than the travelling time of an ionisation wave through the laser spot. Schmidt-Bleker et al. have reported a gas velocity of 25 m/s within the plasma zone and the effluent close to the nozzle [26]. By considering this velocity, $Ar(^3P_2)$ atoms that were produced close to the needle electrode would need 104 μs to travel 2.5 mm to $z = 0.1$ mm below the nozzle exit, which is approximately a factor of 200 larger than the duration of approximately 500 ns for an absorption event. This indicates, that $Ar(^3P_2)$ atoms were mainly produced close to where they have been detected due to the impact of an ionisation wave rather than being produced close to the needle electrode. The differences in the decay times applying an O_2 or a N_2 gas curtain were most likely due to different excitation schemes and electron energy distribution functions occurring in different gas mixtures. The water content, however, had a higher impact on the excitation dynamics: For humidity contents up to 250 ppm, the probability to observe two ionisation waves within one voltage cycle decreases to a value that indicates that mostly one ionisation wave occurs. By further increasing the humidity content, the number of voltage cycles with two ionisation waves increased to a value that in 9 out of 10 cycles two ionisation waves were occuring. Observing the absorption signal as a function of time, as shown in figure 2.3d, the position of the filament seemed to be more stable for a high humidity content. This could be due to a focusing effect of electrons by negative ions, such as OH^-, O^-, O_2^-, and O_3^-, towards the inside of the ionisation channel. In the case of an oxygen gas curtain, this effect was investigated by Schmidt-Bleker et al. previously [41]. At larger distances from the nozzle and for humidities higher than 100 ppm, two ionisation waves were observed in less than 10% of all voltage cycles. This could be due to a lower electric field at larger distances from the nozzle and from the electrodes resulting in a weaker counter-propagating ionization wave.

2.4.2 Quenching of $Ar(^3P_2)$ atoms by water species

To investigate the decay of the density peaks of $Ar(^3P_2)$ atoms in more detail, the effective lifetime of the absorption peaks was analysed. Therefore, the time between the peak and its reduction to the half of its amplitude was determined and divided by $\ln(2)$, assuming an exponential decay of the peak. In figure 2.9, the mean of the effective lifetimes of the (20) highest $Ar(^3P_2)$ absorption peaks is shown at $z = 0.1$ mm, $z = 2.0$ mm, and $z = 4.0$ mm as a function of the feed gas humidity, while a gas curtain of 5 slm O_2, 5 slm N_2, or 4 slm N_2 and 1 slm O_2 was applied. For all gas curtain compositions, the highest lifetime of about 250 ± 100 ns was obtained for a humidity content of less than 100 ppm. The lifetime decreased proportional to the inverse of the water content to approximately 70 ± 30 ns at 1000 ppm water in the feed gas. Within the error, no difference for the different distances from the nozzle, as well as for the gas curtain composition, was obtained.
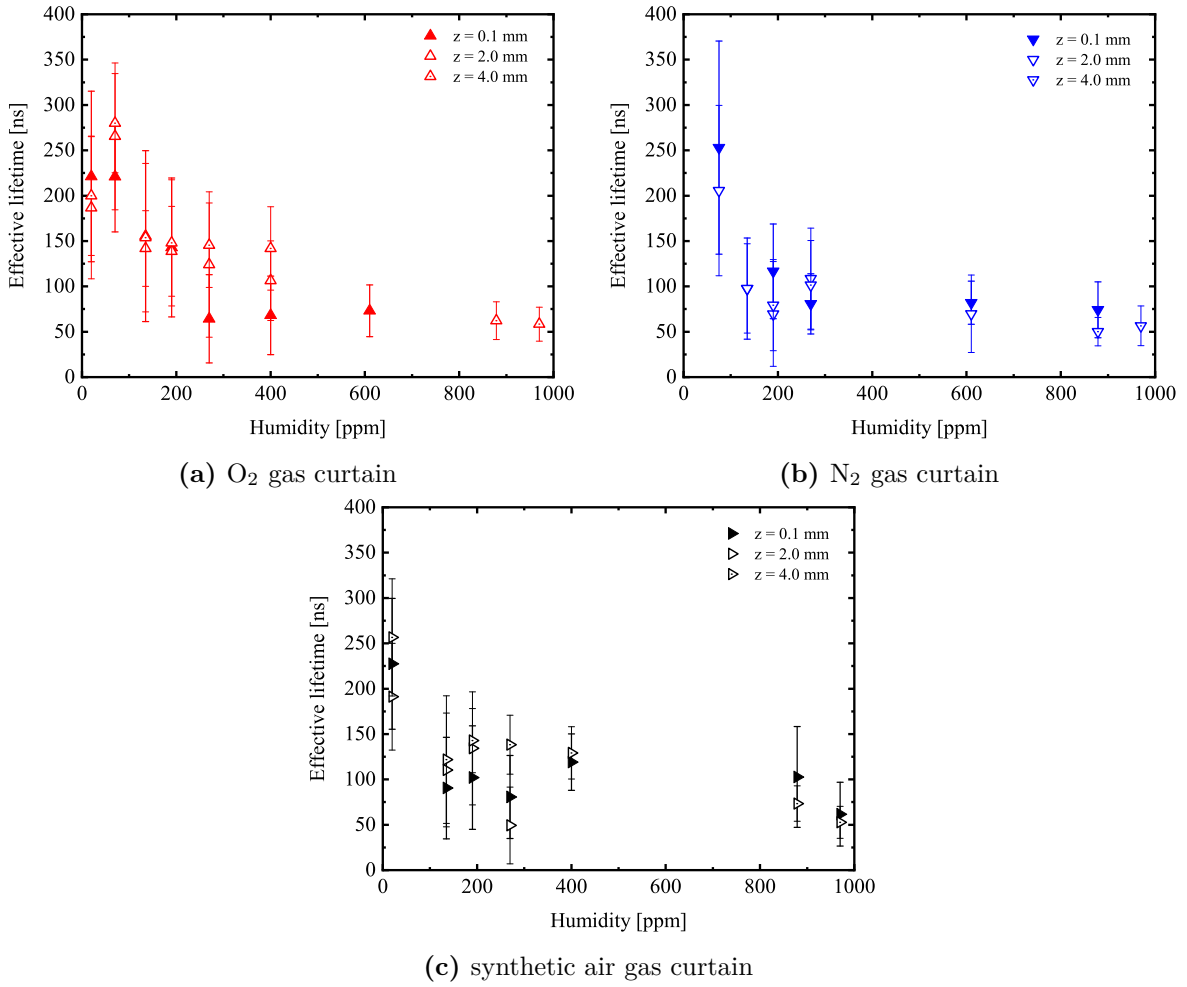
(a) O$_2$ gas curtain

(b) N$_2$ gas curtain

(c) synthetic air gas curtain

Figure 2.9: Mean of the effective lifetimes of the (20) highest Ar($^3P_2$) absorption peaks at $z = 0.1$ mm, $z = 2.0$ mm, and $z = 4.0$ mm as a function of the feed gas humidity for three different gas curtain compositions (a) 5 slm O$_2$, (b) 5 slm N$_2$, and (c) 4 slm N$_2$, 1 slm O$_2$.

In figure 2.10, the mean Ar($^3P_2$) densities out of the (20) highest peaks at $z = 0.1$ mm are depicted as a function of the humidity content in the feed gas, while the gas curtain was varied, together with a fit. At $z = 0.1$ mm, the Ar($^3P_2$) density n_{Ar^*} was independent from the gas curtain and inversely proportional to the water content n_{H_2O} as given by the fit:

$$n_{Ar^*} = (2 \pm 0.2) \cdot 10^{28} \text{ cm}^{-6} \frac{1}{n_{H_2O}} + 1 \cdot 10^{13} \text{ cm}^{-3}. \tag{2.24}$$

For water contents higher than 400 ppm in the feed gas, the Ar($^3P_2$) density seemed to level off at $1 \cdot 10^{13}$ cm^{-3}, which was close to the detection limit of the setup. This shows that even for a high water content at least close to the nozzle, Ar($^3P_2$) atoms were produced. The maximum density of $(6.0 \pm 0.7) \cdot 10^{13}$ cm^{-3} was obtained for 20 ppm water. This value is close to the densities obtained by Niermann et al. and
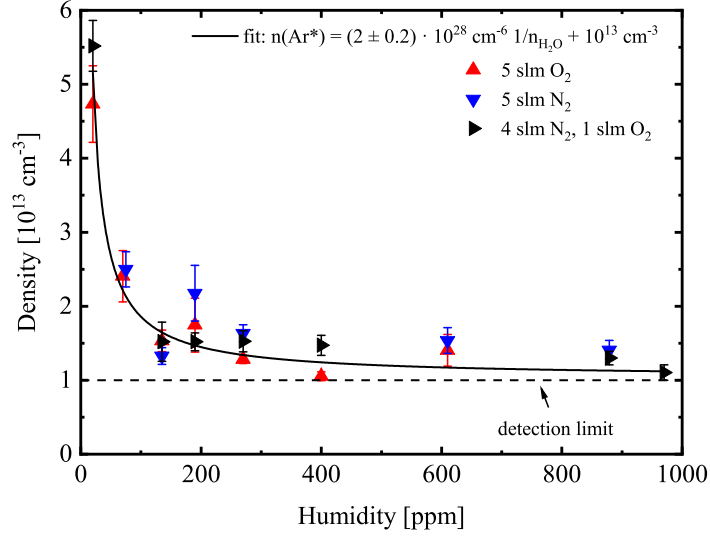
Figure 2.10: $Ar(^3P_2)$ density at $z = 0.1$ mm as a function of the humidity content in the feed gas together with a fit for three different gas curtain compositions.

Schmidt-Bleker et al. [21, 26].

The temporal evolution of $Ar(^3P_2)$ atoms can be described by the rate equation, which depends on the production and loss terms:

$$\frac{dn_{Ar^*}}{dt} = k^*\left(\frac{E}{n}\right) n_{Ar} n_e - \frac{n_{Ar^*}}{\tau_{eff}}. \tag{2.25}$$

Here, $k^*\left(\frac{E}{n}\right)$ is a coefficient for the production term for $Ar(^3P_2)$ atoms, which depends on the reduced electric field $\frac{E}{n}$, n_{Ar} is the argon density in the ground state, n_e is the electron density, and τ_{eff} is the effective lifetime of $Ar(^3P_2)$ atoms. The effective lifetime τ_{eff} is thereby given by the natural radiative life time τ_{nat} and the impact of all quenching species n_q multiplied by the corresponding quenching coefficient k_q:

$$\frac{1}{\tau_{eff}} = \sum_q n_q k_q + \frac{1}{\tau_{nat}}. \tag{2.26}$$

Due to the metastable nature of $Ar(^3P^2)$ atoms, a natural lifetime of $\tau_{nat} = 38$ s has been reported by Katori et al. [43]. Notably, since the unknown production term for $Ar(^3P_2)$ atoms is space and time dependent, only an upper limit for the effective lifetime can be determined. The effective lifetime was found to be independent from the gas curtain composition as shown in figure 2.9. As the decay rate in the inverse of the effective lifetime, the quenching coefficient of water can be obtained from the slope of a linear fit on the decay rates as a function of the amount of water in the feed gas.

In figure 2.11, the decay rates, obtained from the mean half time of the (20) highest peaks, are shown as a function of the humidity content in the feed gas at $z = 0.1$ mm, $z = 1.0$ mm, $z = 2.0$ mm, $z = 3.0$ mm, and at $z = 4.0$ mm, while the gas curtain

Figure 2.11: Decay rates of the Ar(^{3}P$_2$) densities, obtained from the mean half time of the (20) highest peaks, as a function of the humidity content in the feed gas at $z = 0.1$ mm, $z = 1.0$ mm, $z = 2.0$ mm, $z = 3.0$ 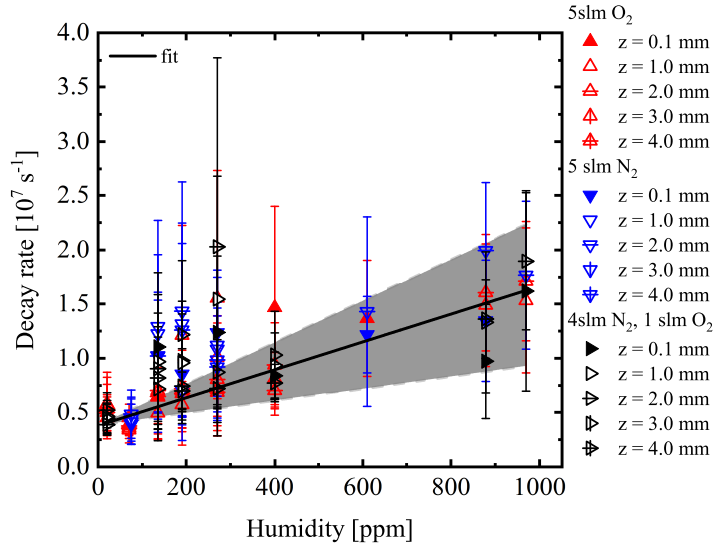mm, and at $z = 4.0$ mm, while the gas curtain was varied from 5 slm O$_2$ to 1 slm O$_2$ and 4 slm N$_2$, and to 5 slm N$_2$. Together with the decay rates, a linear fit of the data yielding a quenching coefficient of $k_{H_2O} = (5.25 \pm 0.4) \cdot 10^{-10}$ cm^3/s, and a corridor corresponding to quenching coefficients $2.3 \cdot 10^{-10}$ cm^{-3}/s and $7.8 \cdot 10^{-10}$ cm^{-3}/s, reported by [44] and [45], respectively, are shown.

was varied from 5 slm O$_2$ to 1 slm O$_2$ and 4 slm N$_2$, and to 5 slm N$_2$. Together with the decay rates, a linear fit of the data, and a corridor corresponding to quenching coefficients $2.3 \cdot 10^{-10}$ cm^{-3}/s and $7.8 \cdot 10^{-10}$ cm^{-3}/s, reported in references [44] and [45], respectively, are depicted. From the slope of the linear fit, a quenching coefficient of $k_{H_2O} = (5.25 \pm 0.4) \cdot 10^{-10}$ cm^3/s was obtained. This value is in agreement with the quenching coefficients reported in literature [44, 46, 47]. Furthermore, the determined quenching coefficient k_{H_2O} is close to the reaction rate of $7.8 \cdot 10^{-10}$ cm^3/s for the water dissociation reaction Ar(^{3}P$_2$) + H$_2$O $\rightarrow$ Ar + H + OH obtained by Novicki et al. [45]. Additional to the slope, a y-intercept of $(3.8 \pm 0.2) \cdot 10^6$ s^{-1} was obtained for the linear fit of the decay rates. This indicates that, besides water, other quenching species affected the effective lifetime. Their densities were independent from the gas curtain, as the y-intercept was the same for all gas curtain compositions.

2.4.3 Axial density distributions for Ar(^{3}P$_2$) atoms

In order to investigate the influence of the measured Ar(^{3}P$_2$) atoms on the reactive species composition in the effluent, the axial distribution of the Ar(^{3}P$_2$) density was determined. Based on the mean of the (20) highest absorption peaks, the Ar(^{3}P$_2$) peak density was obtained as a function of the distance from the nozzle. In figure 2.12, the axial density distribution is shown for different humidities in the feed gas and gas
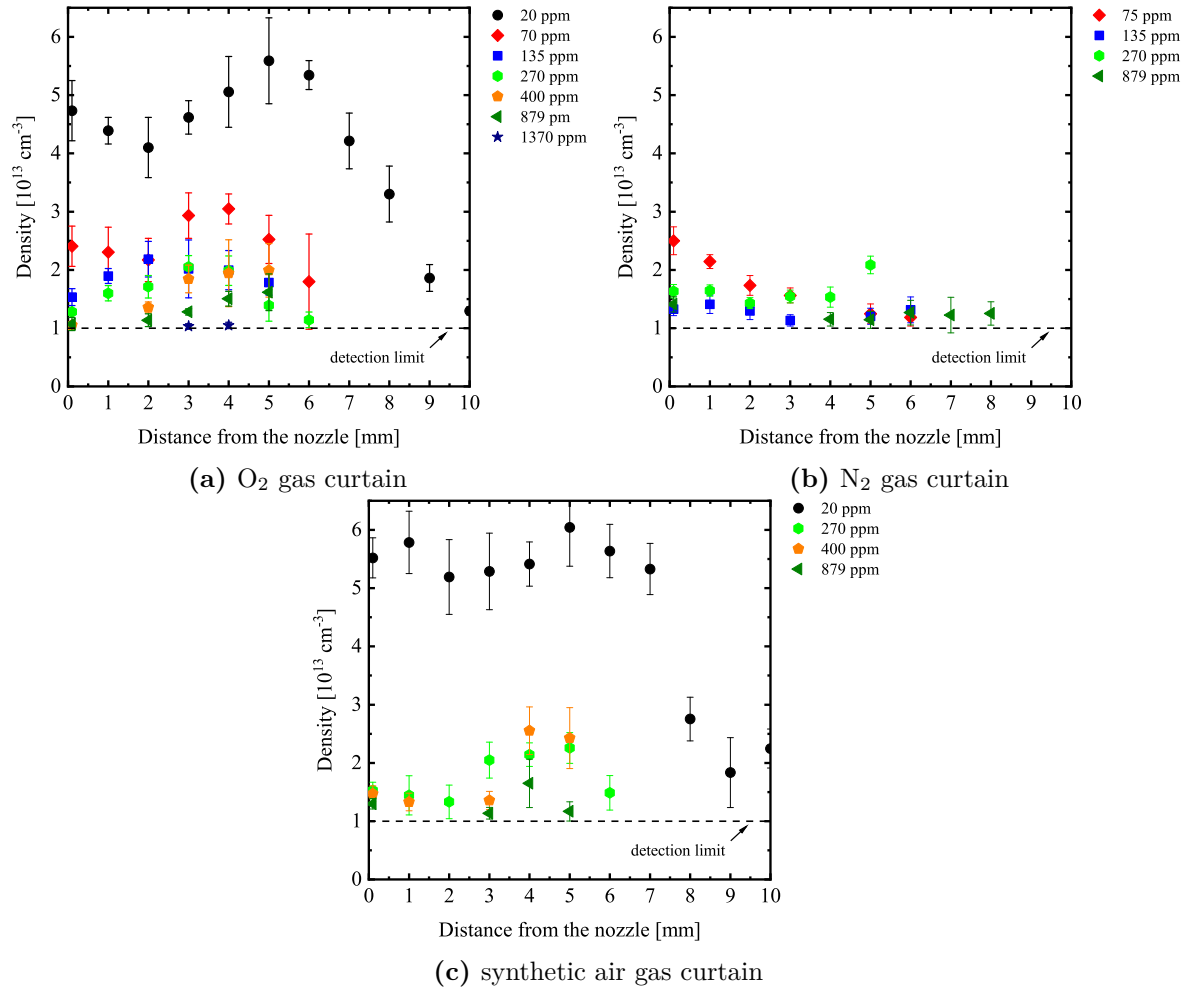
(a) O_2 gas curtain

(b) N_2 gas curtain

(c) synthetic air gas curtain

Figure 2.12: Axial $Ar(^3P_2)$ densities for various humidity contents in the feed gas and three different gas curtain compositions (a) 5 slm O_2, (b) 5 slm N_2, and (c) 4 slm N_2, 1 slm O_2.

curtain compositions. For a gas curtain of 5 slm O_2, the $Ar(^3P_2)$ density was the same within the error up to a distance of 3 mm from the nozzle, with a value of approximately $4.5 \cdot 10^{13}$ cm^{-3} for 20 ppm water in the feed gas. Between $z = 3$ mm and $z = 5$ mm, the density increased slightly to approximately $5.5 \cdot 10^{13}$ cm^{-3}, and decreased linearly for further distances reaching the detection limit at $z = 10$ mm. For higher water contents, a similar behaviour was observed: The density was approximately constant between $z = 0$ mm and $z = 2$ mm, and a maximum was reached between 3 and 5 mm. However, no $Ar(^3P_2)$ atoms were detected for higher humidities at distances further than $z = 6$ mm. The axial distributions with a gas curtain composed of 4 slm N_2 and 1 slm O_2 were analogous to the measurements for 5 slm O_2 with similar densities. With a gas curtain of 5 slm N_2, the $Ar(^3P_2)$ density was decreasing for 75 ppm water in the feed gas and approximately constant at $1.25 \cdot 10^{13}$ cm^{-3} for higher water contents. For 879 ppm water in the feed gas, even at $z = 7$ mm and $z = 8$ mm $Ar(^3P_2)$ atoms were detected.

The differences in the axial behaviour can be explained by the influx of the gas curtain. Molecular oxygen tends to attach electrons producing O^-, O_2^-, and O_3^- ions, which form an anionic volume charge around a filament [41, 48]. Because of the much lower mobility of anions compared to electrons, the conductivity in the filament channel is decreased compared to the outside. This enables a greater penetration of the electric field so that the ionisation wave propagates further with higher electric field strengths in the head, producing anions at larger distances from the nozzle. These anions provide seed electrons for ionisation waves propagating against the gas flow direction. With the influx of the oxygen gas curtain starting at approximately 3 mm below the nozzle [49], more oxygen molecules were available to form an anionic volume charge leading to a focusing of electrons in the filament, which increases the production of Ar($^3P_2$) atoms. At distances further than 6 mm, the electric field was sufficiently reduced so that the filament propagation stops. The amount of oxygen was high enough to contribute strongly to quenching reactions. This is in agreement with a reduction of the effective lifetime between 6 mm and 10 mm below the nozzle. However, even in the case of a N_2 shielding, two ionisation waves within one voltage period were observed, which occurrences increased close to the nozzle with an increasing water content in the feed gas. This is most likely due to a similar effect occurring with water forming OH^- anions, which would also explain the determined Ar($^3P_2$) density measured at $z = 7$ mm and $z = 8$ mm for a N_2 gas curtain.

2.4.4 Impact of Ar(^{3}P$_2$) atoms on the dissociation of water

In order to determine the influence of the measured Ar($^3P_2$) density on the reactive species composition in the effluent, an upper limit of the produced OH and H density
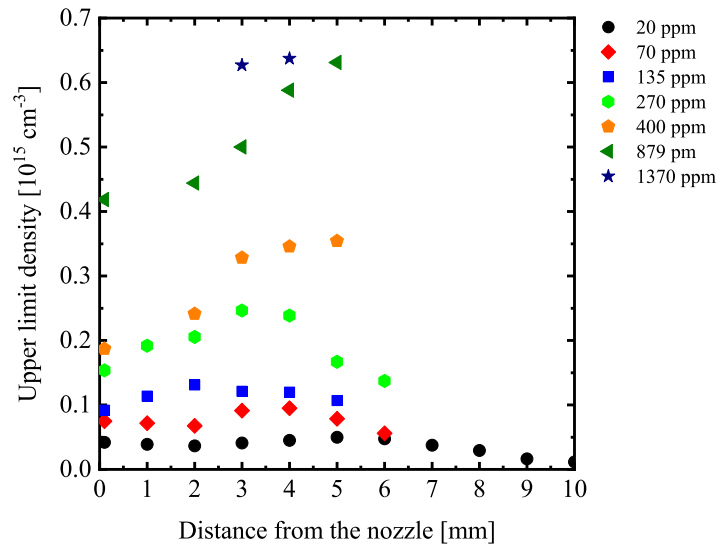

Figure 2.13: Upper limit of the OH and H density produced in the effluent by the dissociation of water by Ar($^3P_2$) atoms.

by the reaction $Ar(^3P_2)+H_2O \rightarrow Ar+H+OH$ was obtained. Therefore, it was assumed that within each voltage period, two ionisation waves were propagating, which produce the same amount of $Ar(^3P_2)$ atoms at the maximum. The upper limit density for the products of water dissociation, n_{max}, by $Ar(^3P_2)$ atoms was then calculated by:

$$n_{max} = \frac{n_{Ar^*} \cdot n_{H_2O} \cdot k_{H_2O}}{f_0/2}. \tag{2.27}$$

Here, n_{Ar^*} denotes the measured density of $Ar(^3P_2)$ atoms, n_{H_2O} is the density of water, $f_0 = 860$ kHz is the excitation frequency, and $k_{H_2O} = 7.8 \cdot 10^{-10}$ cm^3/s [45] is the reaction coefficient for water dissociation by $Ar(^3P_2)$ atoms.

In figure 2.13, the upper limit of the dissociation products of water in the effluent is shown as a function of the distance from the nozzle for different water contents, while a gas curtain of 5 slm O_2 was applied. For water contents of less than 135 ppm, less than $1.5 \cdot 10^{14}$ molecules cm^{-3} were produced in the effluent, and this value stayed approximately constant over a length of 6 mm, where the highest metastable densities have been registered. At water contents higher than 400 ppm the dissociation degree increased between 3 mm and 6 mm below the nozzle. Although the production of $Ar(^3P_2)$ atoms as well as the lifetime of $Ar(^3P_2)$ atoms decreased with increasing water content in the feed gas, the amount of dissociation products were the highest with $6.5 \cdot 10^{14}$ molecules cm^{-3} for 1370 ppm.

2.5 Summary

The temporal evolution of the density of Ar(^{3}P$_2$) atoms in the effluent of the kINPen-sci was investigated by laser atomic absorption spectroscopy. Within one voltage period, two absorption events were observed particularly close to the nozzle at a high content of humidity in the feed gas. This could be due to the formation of an anionic sheath around the filament during the first half of the voltage period. In the second half, the anions provide seed electrons for a counter-propagating ionisation wave towards the inside of the plasma jet.

Each absorption event was composed of a strong increase within 200 ns, and a subsequent exponential decay. The decay time decreased from approximately 250 ns at 70 ppm humidity in the feed gas to approximately 50 ns at 1370 ppm humidity in the feed gas. The corresponding decay rate of $(5.25 \pm 0.40) \cdot 10^{-10}$ cm^3/s was found to be independent from the composition of the gas curtain and close to the rate coefficient for the dissociation of H$_2$O molecules by Ar(^{3}P$_2$) atoms. However, the decay rate was also impacted by other species than H$_2$O molecules. By assuming O$_2$ molecules as an additional quenching species, a density of $1.8 \cdot 10^{16}$ cm^{-3} of O$_2$ would have been necessary to fully explain the observed decay rate.

The density of Ar(^{3}P$_2$) atoms decreased from approximately $5 \cdot 10^{13}$ cm^{-3} inversely proportional to the humidity in the feed gas levelling off at a value of $1 \cdot 10^{13}$ cm^{-3}, which was the detection limit. When varying the composition of the gas curtain, differences in the axial density distributions for Ar(^{3}P$_2$) atoms were observed: In the case of a gas curtain with O$_2$ content, the density was approximately constant between $z = 1$ mm and $z = 3$ mm, and increased between $z = 3$ mm and $z = 5$ mm, while the maximum for Ar(^{3}P$_2$) atoms was obtained close to the nozzle in the case of a pure N$_2$ curtain. Notably, the absolute densities close to the nozzle were unaffected by the composition of the gas curtain.

From the dissociation of H$_2$O, and from the measured density of Ar(^{3}P$_2$) atoms, the density of H atoms was estimated as a function of the feed gas humidity. Although the density of Ar(^{3}P$_2$) atoms decreased with increased humidity content in the feed gas, the dissociation of H$_2$O was determined to be more efficient for a higher water content. By extrapolation the obtained values to 3000 ppm humidity in the feed gas, an often used standard value that is also presented later in this work, a maximum H density produced in the effluent by Ar(^{3}P$_2$) atoms of $1.3 \cdot 10^{15}$ cm^{-3} was obtained.

2.6 Bibliography

[1] Q. Li, X.-M. Zhu, J.-T. Li, and Y.-K. Pu. Role of metastable atoms in the propagation of atmospheric pressure dielectric barrier discharge jets. *J. Appl. Phys.*, 107(043304), 2010.

[2] S.-J. Klose, R. Bansemer, R. Brandenburg, and J. H. van Helden. Ar metastable densities ($^3P_2$) in the effluent of a filamentary atmospheric pressure plasma jet with humidified feed gas. *J. Appl. Phys.*, 129(063304), 2021.

[3] A. Walsh. The application of atomic absorption spectra to chemical analysis. *Spectrochim. Acta*, 7(108-117), 1955.

[4] R. Hergenröder and K. Niemax. Laser atomic absorption spectroscopy applying semiconductor diode lasers. *Spectrochim. Acta B*, 43(12), 1988.

[5] J. Röpcke, S. Welzel, N. Lang, F. Hempel, L. Gatilova, O. Guaitella, A. Rousseau, and P. B. Davies. Diagnostic studies of molecular plasmas using mid-infrared semiconductor lasers. *Appl. Phys. B*, 92(335–341), 2008.

[6] H. Nasim and Y. Jamil. Recent advancements in spectroscopy using tunable diode lasers. *Laser Phys. Lett.*, 10(043001), 2013.

[7] J. W. Robinson. Atomic Absorption Spectrsocopy. *Anal. Chem.*, 32(8), 1960.

[8] A. C. Menzies. A Study of Atomic Absorption Spectroscopy. *Anal. Chem.*, 32(8), 1960.

[9] A. Zybin, J. Koch, H. D. Wizemann, J. Franzke, and K. Niemax. Diode laser atomic absorption spectrometry. *Spectrochim. Acta B*, 60(1-11), 2005.

[10] G. Galbács. A Review of Applications and Experimental Improvements Related to Diode Laser Atomic Spectroscopy. *Appl. Spectrosc. Rev.*, 41(259-303), 2006.

[11] J. Röpcke, G. Lombardi, A. Rousseau, and P. B. Davies. Application of mid-infrared tuneable diode laser absorption spectroscopy to plasma diagnostics: a review. *Plasma Sources Sci. Technol.*, 15(S148-S168), 2006.

[12] S. Welzel, F. Hempel, M. Hübner, N. Lang, P. B. Davies, and J. Röpcke. Quantum Cascade Laser Absorption Spectroscopy as a Plasma Diagnostic Tool: An Overview. *Sensors*, 10(6861-6900), 2010.

[13] S. Reuter, J. S. Sousa, G. D. Stancu, and J. H. van Helden. Review on VUV to MIR absorption spectroscopy of atmospheric pressure plasma jets. *Plasma Sources Sci. Technol.*, 24(5), 2015.

[14] W. Demtröder. *Experimentalphysik 3 - Atome, Moleküle und Festkörper*. Springer-Verlag Berlin Heidelberg, 4 edition, 2010.

[15] D. F. Swinehart. The Beer-Lambert Law. *J. Chem. Educ.*, 37(7), 1962.

[16] W. Demtröder. *Laser spectroscopy - Vol. 1: Basic Principles.* Springer-Verlag Berlin Heidelberg, 4 edition, 2011.

[17] HITRAN database. HITRAN parameters - Definitions and Units: Line-by-line Parameters. online: https://hitran.org/docs/definitions-and-units/, 2022.

[18] C. Hill. Scipython - The Voigt profile. online: https://scipython.com/book/chapter-8-scipy/examples/the-voigt-profile/, 2022.

[19] R. J. Wells. Rapid approximation to the Voigt/Faddeeva function and its derivatives. *J. Quant. Spectrosc. Rad. Transf.*, 62(29-48), 1999.

[20] B. Niermann, M. Böke, N. Sadeghi, and J. Winter. Space resolved density measurements of argon and helium metastable atoms in radio-frequency generated He-Ar micro-plasmas. *Eur. Phys. J. D*, 60(489-495), 2010.

[21] B. Niermann, R. Reuter, T. Kuschel, J. Benedikt, M. Böke, and J. Winter. Argon metastable dynamics in a filamentary jet micro-discharge at atmospheric pressure. *Plasma Sources Sci. Technol.*, 21(034002), 2012.

[22] S. Schröter, R. Pothiraja, P. Awakowicz, N. Bibinov, M. Böke, B. Niermann, and J. Winter. Time-resolved characterization of a filamentary argon discharge at atmospheric pressure in a capillary using emission and absorption spectroscopy. *J. Phys. D: Appl. Phys.*, 46(464009), 2013.

[23] C. Reininger, K. Woodfield, J. D. Keelor, A. Kaylor, F. M. Fernández, and P. B. Farnsworth. Absolute number densities of helium metastable atoms determined by atomic absorption spectroscopy in helium plasma-based discharges used as ambient desorption/ionization sources for mass spectrometry. *Spectrochim. Acta B*, 100(98-104), 2014.

[24] J. Winter, J. S. Sousa, N. Sadeghi, A. Schmidt-Bleker, S. Reuter, and V. Puech. The spatio-temporal distribution of He(2^3s_1) metastable atoms in a MHz-driven helium plasma jet is influenced by the oxygen/nitrogen ratio of the surrounding atmosphere. *Plasma Sources Sci. Technol.*, 24(025015), 2015.

[25] C. Douat, I. Kacem, N. Sadeghi, G. Bauville, M. Fleury, and V. Puech. Space-time resolved density of helium metastable atoms in a nanosecond pulsed plasma jet: influence of high voltage and pulse frequency. *J. Phys. D: Appl. Phys.*, 49(285204), 2016.

[26] A. Schmidt-Bleker, J. Winter, A. Bösel, S. Reuter, and K.-D. Weltmann. On the plasma chemistry of a cold atmospheric argon plasma jet with shielding gas device. *Plasma Sources Sci. Technol.*, 25(015005), 2016.

[27] S.-Y. Yoon, G.-H. Kim, S.-J. Kim, B. Bae, N.-K. Kim, H. Lee, N. Bae, S. Ryu, S. J. Yoo, and S. B. Kim. Bullet-to-streamer transition on the liquid surface of a plasma jet in atmospheric pressure. *Phys. Plasmas*, 24(013513), 2017.

[28] E. Es-sebbar, G. Bauville, M. Fleury, S. Pasquiers, and J. S. Sousa. Spatio-temporal distribution of absolute densities of argon metastable 1s$_5$ state in the diffuse area of an atmospheric pressure nanosecond pulsed argon microplasma jet propagating into ambient air. *J. Appl. Phys.*, 126(073302), 2019.

[29] I Korolov, M. Leimkühler, M. Böke, Z. Donkó, V. Schulz-von der Gathen, L. Bischoff, G. Hübner, P. Hartmann, T. Gans, Y. Liu, T. Mussenbrock, and J. Schulze. Helium metastable species generation in atmospheric pressure RF plasma jets driven by tailored voltage waveforms in mixtures of He and N$_2$. *J. Phys. D: Appl. Phys.*, 53(185201), 2020.

[30] R. Bussiahn, E. Kindel, H. Lange, and K.-D. Weltmann. Spatially and temporally resolved measurements of argon metastable atoms in the effluent of a cold atmospheric pressure plasma jet. *J. Phys. D: Appl. Phys.*, 43(165201), 2010.

[31] K. Urabe, T. Morita, K. Tachibana, and B. N. Ganguly. Investigation of discharge mechanisms inhelium plasma jet at atmospheric pressureby laser spectroscopic measurements. *J. Phys. D: Appl. Phys.*, 43(095201), 2010.

[32] B. L. Sands, R. J. Leiweke, and B. N. Ganguly. Spatiotemporally resolved ar(1s$_5$) metastable measurements in a streamer-like He/Ar atmospheric pressure plasma jet. *J. Phys. D: Appl. Phys.*, 43(282001), 2010.

[33] M. Gianella, S. Reuter, S. A. Press, A. Schmidt-Bleker, J. H. van Helden, and G. A. D. Ritchie. HO$_2$ reaction kinetics in an atmospheric pressure plasma jet determined by cavity ring-down spectroscopy. *Plasma Sources Sci. Technol.*, 27(095013), 2018.

[34] A. Bösel, J. Ehlbeck, N. König, K.-D. Salewski, and J. Röpcke. On Enhanced Tuning Capabilities of External Cavity Lasers Using Acousto-Optic Modulators. *Opt. Rev.*, 19(5), 2012.

[35] A. Bösel and K.-D. Salewski. Fast mode-hop-free acousto-optically tuned laser: theoretical and experimental investigations. *Appl. Opt.*, 48(5), 2009.

[36] S. Iséni, A. Schmidt-Bleker, J. Winter, K.-D. Weltmann, and S. Reuter. Atmospheric pressure streamer follows the turbulent argon air boundary in a MHz argon plasma jet investigated by OH-tracer PLIF spectroscopy. *J. Phys. D: Appl. Phys.*, 47(152001), 2014.

[37] W.L. Wiese, J.W. Brault, K. Danzmann, V. Helbig, and M. Kock. Unified set of atomic transition probabilities for neutral argon. *Phys. Rev. A*, 39(5), 1989.

[38] K. Tachibana, H. Harima, and Y. Urano. Measurements of collisional broadening and the shift of argon spectral lines using a tunable diode laser. *J. Phys. B: At. Mol. Phys.*, 15(3169-3178), 1982.

[39] R. Bansemer, J. Winter, A. Schmidt-Bleker, and K.-D. Weltmann. On the Ar(1s$_5$) density distribution in a flowdriven DBD at intermediate pressure. *Plasma Sources Sci. Technol.*, 29(035026), 2020.

[40] T. Gerling, A. V. Nastuta, R. Bussiahn, E. Kindel, and K.D. Weltmann. Back and forth directed plasma bullets in a helium atmospheric pressure needle-to-plane discharge with oxygen admixtures. *Plasma Sources Sci. Technol.*, 21(034012), 2012.

[41] A. Schmidt-Bleker, S. A. Norberg, J. Winter, E. Johnsen, S. Reuter, K.-D. Weltmann, and M. J. Kushner. Propagation mechanisms of guided streamers in plasma jets: the influence of electronegativity of the surrounding gas. *Plasma Sources Sci. Technol.*, 24(035022), 2015.

[42] S. Reuter, J. Winter, S. Iséni, S. Peters, A. Schmidt-Bleker, M. Dünnbier, J. Schäfer, R. Foest, and K.-D. Weltmann. Detection of ozone in a MHz argon plasma bullet jet. *Plasma Sources Sci. Technol.*, 21(034015), 2012.

[43] H. Katori and F. Shimizu. Lifetime Measurement of the 1s5 Metastable State of Argon and Krypton with a Magneto-Optical Trap. *Phys. Rev. Lett.*, 70(23), 1993.

[44] S. Suzuki and H. Itoh. Experimental derivation of Arrhenius equations for collisional quenching rate coefficients of Ar($^3P_2$) by Ar($^1S_0$) and H_2O. *J. Phys. D: Appl. Phys.*, 52(235203), 2019.

[45] S. Novicki and J. Krenos. Absolute quenching cross section for collisions between Ar ($^3P_{0,2}$) and H_2O. *J. Chem. Phys.*, 89(11):7031–3, 1988.

[46] H. J. D. Jong. Deactivation rate constants and cross sections for Ar $^3P_2$ metastables in collision reactions with several molecules. *Chem. Phys. Lett.*, 25(129–131), 1974.

[47] J. B. Leblond, F. Collier, F. Hoffbeck, and P. Cottin. Kinetic study of high-pressure Ar–H_2O mixtures excited by relativistic electrons. *J. Chem. Phys.*, 74(6242), 1981.

[48] R. Tschiersch, S. Nemschokmichal, and J. Meichsner. The influence of negative ions in helium-oxygen barrier discharges: I. Laser photodetachment experiment. *Plasma Sources Sci. Technol.*, 25(025004), 2016.

[49] I. L. Semenov and K.-D. Weltmann. Modelling of turbulent reacting flow for a cold atmospheric pressure argon plasma jet. *Plasma Sources Sci. Technol.*, 29(055001), 2020.

3 Spatial distributions of O and H atoms in the effluent of the kINPen-sci plasma jet
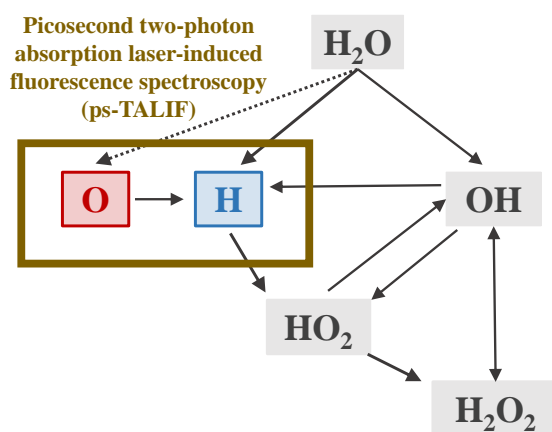
Hydrogen and oxygen atoms are among those primary reactive species that are produced directly by H_2O and O_2 dissociation in the plasma zone and in the effluent of the kINPen-sci plasma jet, respectively. They are the smallest components and the starting point for the formation of larger molecules, in particular for biologically important reactive oxygen-nitrogen species (RONS). Due to the large energy gap between the ground state of atomic species and excited states, the investigation of ground state densities for atoms requires light sources in the vacuum ultraviolet (VUV)-region, where the production of photons is complicated and light is strongly absorbed by air. An alternative to direct absorption by VUV-photons is two-photon absorption laser-induced fluorescence spectroscopy (TALIF) [1, 2]. With TALIF, two UV-photons are combined to excite the atom to a higher state, whereas the fluorescence from this higher state to an intermediate level is observed, which is commonly in the visible region of the electromagnetic spectrum. However, for CAPJs, the effective lifetime of the excited state is strongly reduced due to collisional quenching. Henceforth, laser pulses with a duration of picoseconds need to be employed to determine the effective lifetime. By a comparison of the spectrally and temporally integrated fluorescence signal of the measured species to the TALIF-signal of a calibration gas with a known quantity, absolute number densities can be obtained.

In this chapter, which is adapted from reference [3], the investigations on spatial distributions for absolute number densities of O and H atoms in the effluent of the kINPen-sci plasma jet are presented. Firstly, the principle of TALIF is introduced and the experimental setup for the determination of the spatial distributions for O and H atoms by means of picosecond TALIF (ps-TALIF) is described. The method to determine absolute number densities from the fluorescence signals of the measured atoms and of the species used for the calibration is portrayed. Based on that method, the results for the radial density distributions for O and H atoms are presented, and the impact of the gas curtain on the density distributions close to the nozzle is discussed. Finally, the spatial density distributions for O and H atoms in the effluent are illustrated.

3.1 Introduction to two-photon absorption laser-induced fluorescence spectroscopy (TALIF)

The principle of TALIF is illustrated in figure 3.1. In TALIF, a UV-photon is used to excite a low level of an atom (indicated by the index 0), usually the ground state, to a virtual state. At the same time, a second UV-photon with the same wavelength is absorbed by the virtual state to increase the energy state again by the same amount of energy to a real excited state. By this procedure, high energy gaps can be overcome with
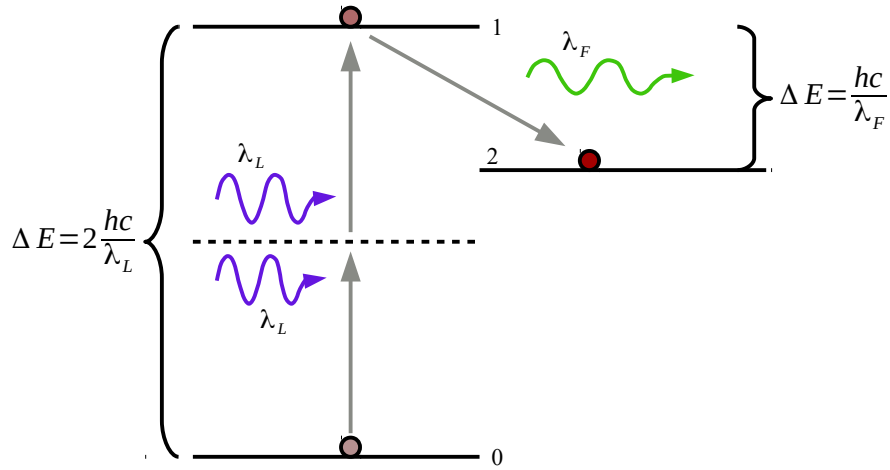

Figure 3.1: Schematic of a TALIF process, where ΔE is the energy difference between two states, h is the Planck constant, c is the speed of light in vacuum, λ_L is the the wavelength of the laser and λ_F the wavelength of the fluorescence.

photons of half of the energy needed, which are more easily produced by standard lasers. From the excited state (indicated by the index 1), spontaneous emission produced by a transition to an intermediate level (assigned by the index 2) at a much longer wavelength is observed. Due to the selection rules for two-photon absorption and electric dipole radiation, a transition from state 1 to state 0 is forbidden. More details about the selection rules can be found in [4].

A detailed physical and mathematical description of TALIF can be found in references [5–8]. The rate equation for the density in the lower state n_0 can be described by:

$$\frac{dn_0}{dt} = -B_{01} n_0 \rho(t). \tag{3.1}$$

Here, B_{01} is the wavelength dependent Einstein coefficient for absorption between states 0 and 1, and $\rho(t)$ is the spectral energy density of the incident laser beam providing the UV-photons. The solution of equation 3.1 yields the time dependent density in the lower state:

$$n_0(t) = n \; e^{-\int_0^t B_{01}\rho(t')dt'} \approx n. \tag{3.2}$$

Here, n denotes the density in the lower state before the interaction with the laser beam. The rate equation for the density in the excited level 1, n_1, can be described by:

$$\frac{dn_1}{dt} = \underbrace{B_{01} n_0 \rho(t)}_{R_{01}(t)n_0} - \left(\underbrace{\sum_k A_{1k}}_{A_1} + \underbrace{\sum_q n_q k_q^1}_{Q_1} + \Gamma_{ion}(t) \right) n_1. \tag{3.3}$$

Here, $B_{01} n_0 \rho(t)$ is the production term based on the density of species in the lower state 0, A_{1k} are the Einstein coefficients for spontaneous emission from state 1 to all possible lower levels k, n_q denotes the density of species q that is involved into quenching processes Q_1 for the excited level 1, which are described by the quenching coefficient k_q^1, and $\Gamma_{ion}(t)$ is the ionisation rate. $\Gamma_{ion}(t)$ depends on the ionisation cross section and the laser energy. For low laser energies, the lower state 0 is not depleted and ionisation can be neglected. In particular at atmospheric pressure, collisions between excited atoms and other species present lead to radiation free transitions, so called quenching processes represented by Q_1, and thus to a reduction of the effective lifetime. In the case of TALIF, the production term can be described by the rate $R_{01}(t)$:

$$R_{01}(t) = G^{(2)} \sigma^{(2)} (\lambda) \left(\frac{I(\vec{r}, t) \lambda_L}{hc} \right)^2. \tag{3.4}$$

Here, $G^{(2)}$ is the photon statistic factor, which accounts for statistical intensity fluctuations of pulsed multimode lasers used in TALIF experiments, $\sigma^{(2)}(\lambda)$ denotes the wavelength dependent two-photon absorption cross section, $I(\vec{r}, t)$ describes the spatio-temporal distribution of the laser intensity, λ_L is the laser wavelength corresponding to half on the energy for the probed transition, h is the Planck constant, and c is the speed of light in vacuum.

The density in state 1, $n_1(t)$, is given by the solution of equation 3.3, which can be expressed by:

$$n_1(t) = n \int_0^t R_{01}(t') e^{-(A_1 + Q1)(t-t')} dt',$$ (3.5)

by taking equation 3.2 into account. In TALIF, n_1, and consequently n, is determined by measuring the fluorescence signal from state 1 to state 2. In order to obtain the total number of fluorescence photons N_F that are emitted in a volume V by spontaneous emission from state 1 to state 2, $n_1(t)$ needs to be integrated in time and in space, and multiplied by the Einstein coefficient for spontaneous emission A_{12}:

$$N_F(\lambda) = A_{12} \int_V \int_0^\infty n_1(t) dt dV = n \frac{A_{12}}{A_1 + Q_1} G^{(2)} \sigma^{(2)}(\lambda) \int_V \int_0^\infty \left(\frac{I(\vec{r}, t) \lambda_L}{hc} \right)^2 dt dV.$$ (3.6)

With TALIF, these fluorescence photons are determined at the detector, that is commonly positioned at an angle of 90° to the incident laser beam. However, the number of detected fluorescence photons $s(\lambda)$ is limited by the solid angle $\Delta\Omega$, the quantum efficiency of the detector chip η, and losses by the employed optics, including focusing lenses and mirrors:

$$s(\lambda) = T(\lambda_F) \eta(\lambda_F) \frac{\Delta\Omega}{4\pi} N_F.$$ (3.7)

The total, spectrally integrated TALIF-signal, is then proportional to the density of the lower state n:

$$S_F = \int s(\lambda) d\lambda = n T(\lambda_F) \eta(\lambda_F) \frac{\Delta\Omega}{4\pi} a_{12} G^{(2)} \sigma^{(2)} \int_V \int_0^\infty \left(\frac{I(\vec{r}, t) \lambda_L}{hc} \right)^2 dt dV.$$ (3.8)

Here, a_{12} is the branching ratio for the transition of state 1 to state 2:

$$a_{12} = \frac{A_{12}}{A_1 + Q_1} = b_{12} \frac{\tau_{eff}}{\tau_{nat}}.$$ (3.9)

$b_{12} = \frac{A_{12}}{A_1}$ is the branching ratio without quenching, τ_{nat} is the natural lifetime of state 1 without considering quenching, and τ_{eff} is the effective lifetime of state 1, where quenching is included. In order to determine absolute number densities, the solid angle needs to be determined accurately, which is complex in most of the experimental setups. Henceforth, a calibration procedure is commonly employed; the fluorescence signal of the species of interest is compared to the fluorescence signal of a suitable reference gas. Relevant for this calibration is the measurement of the fluorescence signal, both spectrally and temporally integrated, as well as the effective lifetime of the upper state. As two-photon absorption cross sections are small and barely known in literature, a calibration procedure with a noble gas, such as Xe or Kr, is commonly used to obtain total number densities of O and H atoms. The noble gases are chosen due to similar excitation schemes, such that the spectrally and temporally integrated fluorescence signal differs only by the pulse energy, which is constant. Hence, the ratio of the integral for the species measurement and of the integral for the calibration measurement

becomes a constant:

$$\frac{S_F^{ref}}{S_F} = \underbrace{\frac{T^{ref}(\lambda_F)}{T(\lambda_F)}\frac{\eta^{ref}(\lambda_F)}{\eta(\lambda_F)}\frac{a_{ik}^{ref}}{a_{ik}}\frac{\sigma^{ref}}{\sigma}\left(\frac{E^{ref}}{E}\frac{\lambda_L^{ref}}{\lambda_L}\right)^2}_{\xi}\frac{n^{ref}}{n}. \tag{3.10}$$

Here, the superscript ref refers to the reference measurement with the known density n^{ref}. The density of the species to be detected is then obtained by:

$$n = \xi\frac{S_F}{S_F^{ref}}n^{ref}. \tag{3.11}$$

In 1981, Bokor et al. [9] and Bischel et al. [10] have reported on the detection of H atoms in a DC discharge, and O atoms in a flow discharge by two-photon absorption laser-induced fluorescence spectroscopy, respectively. Followed by the works of Aldén et al., who demonstrated the capability of TALIF for the detection of O atoms in a flame [11], and DiMauro et al. detecting O atoms in a plasma etching environment [12], TALIF has been developed to a valuable technique for the detection of H, O, and N atoms in non-equilibrium plasmas over the subsequent years [13–17]. For atmospheric pressure plasma jets, collisional quenching plays an important role on the effective lifetime. With the studies of Niemi et al., the calibration with Kr for H and N, and Xe for O, became the method of choice for absolute density measurements [18, 19]. Several work has been carried out with nanosecond (ns) laser pulses to detect O atoms in atmospheric pressure plasma jets [20–25], while considering quenching coefficients reported in references [18, 19, 22, 26, 27]. In order to determine the effective lifetime and therewith the quenching processes experimentally rather than calculating them by using reported quenching coefficients, Schröter et al. and Myers et al. have been using picosecond (ps) laser pulses [28, 29], whereas Schmidt et al. have been employing femtosecond (fs) laser pulses [30]. The picosecond or femtosecond time resolution allows an independent and direct measurement of the effective (reduced) lifetime of the excited state. A comparison of ns-TALIF lasers and fs-TALIF can be found in [31]. In this work, ps-TALIF was used to determine the spatial distributions of H and O atoms in the effluent of the kINPen-sci plasma jet.

3.2 Experimental setup for TALIF

The experimental setup for picosecond TALIF is schematically shown in figure 3.2 and described in detail previously [28]. The laser system (EKSPLA) is based on a Nd:YAG pump laser (1064 nm) with a mode-locked oscillator, a regenerative amplifier, and a single pulse power amplifier, producing a weak pulse train output and a strong single pulse output with a single pulse duration of 30 ps with a repetition rate of 10 Hz. In the second laser unit the weak train beam is amplified and frequency-tripled (355 nm), the strong single pulse beam is frequency-tripled only, while the left-over of the 1064 nm single pulse is the third output beam. In the third laser unit the 355 nm train enters an optical parametric oscillator (OPO) state providing tunable, but weak radiation between 420 and 710 nm, that is amplified using the strong 355 nm single pulse in a subsequent optical parametric amplifier (OPA) stage. Subsequent frequency-doubling is used to generate the UV wavelengths between 210 and 355 nm, and additional sum-frequency mixing with the left-over 1064 nm single pulse input for the deep UV wavelengths below 210 nm. In the UV range, 30 ps laser pulses were generated, with a pulse energy of a few hundred μJ at the maximum, and a spectral width of approximately 4 cm^{-1}. The applied laser pulse energy was measured behind the laser focus/plasma interaction volume with a pyroeletric detector (Gentec-EO, QE8SP-B-MT) and controlled with the help of an attenuator-compensator system, which comprises two specifically coated
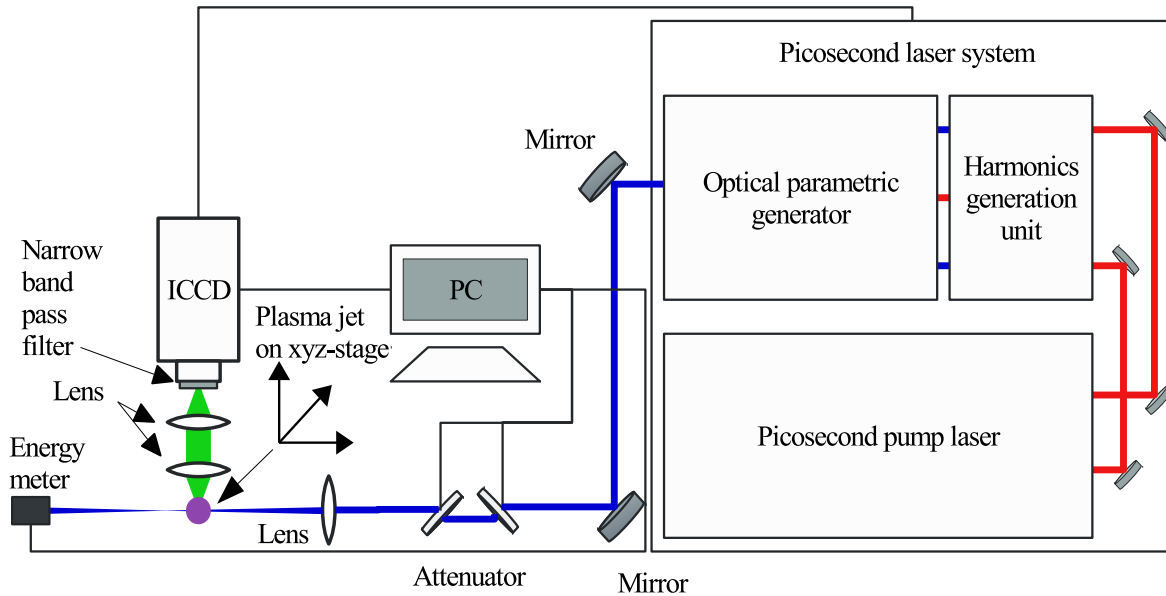

Figure 3.2: Schematic of the experimental setup illustrating the three units of the picosecond laser system, the UV output beam attenuated and focussed into the effluent of the kINPen-sci, which was mounted vertically on an xyz-translation stage, and the visible/NIR detection system (lens doublet, interference filter, and camera) perpendicular to the laser beam.

counter-rotating CaF_2 substrates that are actuated by a stepper motor. The standard deviation of the shot-to-shot fluctuations in the pulse energy is approximately 8%. The laser beam was focussed by a spherical plano-convex fused-silica lens, with a focal length of 30 cm, in a plane approximately 1 cm behind the plasma jet to avoid saturation of the two-photon transitions, and to mitigate material damage in the calibration cuvettes. The resulting interaction zone of the laser beam with the plasma effluent has a diameter of approximately 250 µm. The fluorescence signal of the excited states was detected perpendicular to the direction of the laser beam by using an intensified charge coupled device camera (iCCD: Stanford Computer Optics, 4Picos dig), after passing two achromatic lenses (Thorlabs, AC050-010-B-ML, focal length: 80 mm) and an interference filter (central wavelengths $\lambda_O = 845$ nm, $\lambda_H = 656$ nm, $\lambda_{Xe} = 835$ nm, $\lambda_{Kr} = 825$ nm, band width $\Delta\lambda = 10$ nm). This allowed the complete region of interest to be imaged and reduced the detection of broadband plasma emission. In order to synchronize the laser pulse with the acquisition by the iCCD camera, the pre-trigger output of the mode-locked pump laser was used.

The kINPen-sci plasma jet was operated with a total flow rate of 3 slm of Ar. 2.7 slm dry Ar were combined with 300 sscm Ar guided through a bubbler with distilled water at room temperature, which ensures a content of 3000 ppm humidity at full water vapour saturation. Additionally, a gas curtain with a composition that was varied from pure nitrogen to pure oxygen at a total flow rate of 5 slm was applied. The kINPen-sci was placed on a motorised xyz-translation stage (Zaber) in order to allow measurements at different radial and axial positions. A schematic for the coordinate system used in this work is presented in figure 3.3. In the following, the z-axis is defined as the axis along the symmetry axis of the effluent through the centre of the plasma jet nozzle, the x-axis is the axis parallel to the laser beam, which crosses the centre of the nozzle, and the y-axis is perpendicular to that.
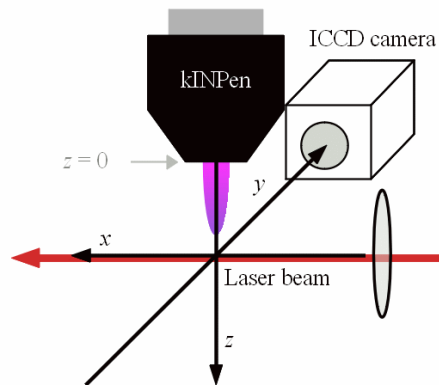

Figure 3.3: Schematic of the coordinate system used for the determination of the spatial density distributions for O ans H atoms in the effluent of the kINPen-sci plasma jet with the definitions of x, y, z.
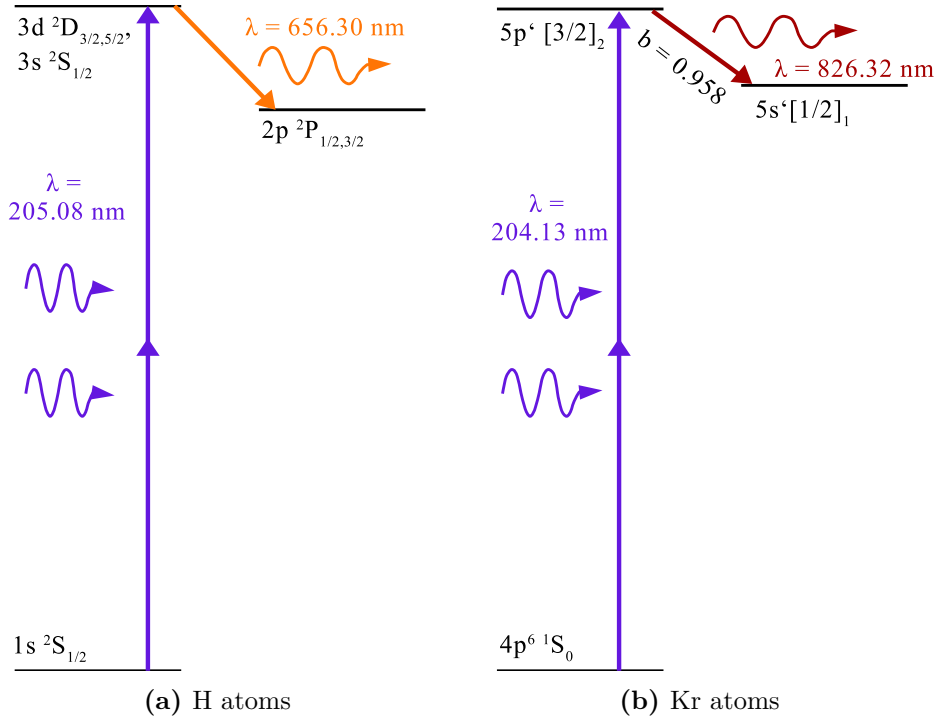
Figure 3.4: Excitation schemes of TALIF for H atoms and for Kr atoms.

For the calibration, a quartz glass cuvette was filled with either 1 Torr of Kr for the calibration of H atoms, or 10 Torr of Xe for the calibration of O atoms. This cuvette was then positioned at the same location as the plasma has been before. In the following, the excitation schemes for H atoms, O atoms, and for the calibration gases Kr and Xe are briefly discussed. A detailed description of the excitation schemes can be found in [18, 32].

The excitation schemes for H atoms and Kr atoms, respectively, are illustrated in figure 3.4. Due to the band width of the laser, which was approximately 4 cm^{-1}, the three states of the H atom, 3s ^{2}S$_{1/2}$ at 97492.22 cm^{-1} [33], 3d ^{2}D$_{5/2}$ at 97492.31 cm^{-1} [33], and 3d ^{2}D$_{3/2}$ at 97492.36 cm^{-1} [33], are excited simultaneously by two photons with a wavelength of 205.08 nm with an excitation cross section ratio $\frac{\sigma_d^{(2)}}{\sigma_s^{(2)}} = 7.56$ [34]. Niemi et al. have measured a combined natural lifetime of 17.6 ns for all states [18]. Taking the reported natural lifetimes of $\tau_{nat}^s = 159$ ns for the 3s ^{2}S$_{1/2}$ state and of $\tau_{nat}^d = 15.6$ ns of the 3d ^{2}D$_{5/2,3/2}$ states into account [35], the combined natural lifetime can be calculated by:

$$\left(\frac{1}{\tau_{nat}}\right)^{-1} = \left(1 + \frac{\sigma_d^{(2)}}{\sigma_s^{(2)}}\right)\left(\frac{1}{\tau_{nat}^s} + \frac{\frac{\sigma_d^{(2)}}{\sigma_s^{(2)}}}{\tau_{nat}^d}\right)^{-1} \approx 17.4 \text{ ns.} \tag{3.12}$$

This value is consistent to the natural lifetime measured by Niemi et al. [18]. The fluorescence at 656.3 nm is due to transitions from the 3s ^{2}S$_{1/2}$ and 3d ^{2}D$_{5/2,3/2}$ states to the 2p ^{2}P$_{1/2,3/2}$ states at 82258.92 cm^{-1} [33] and 82259.29 cm^{-1} [33], respectively.
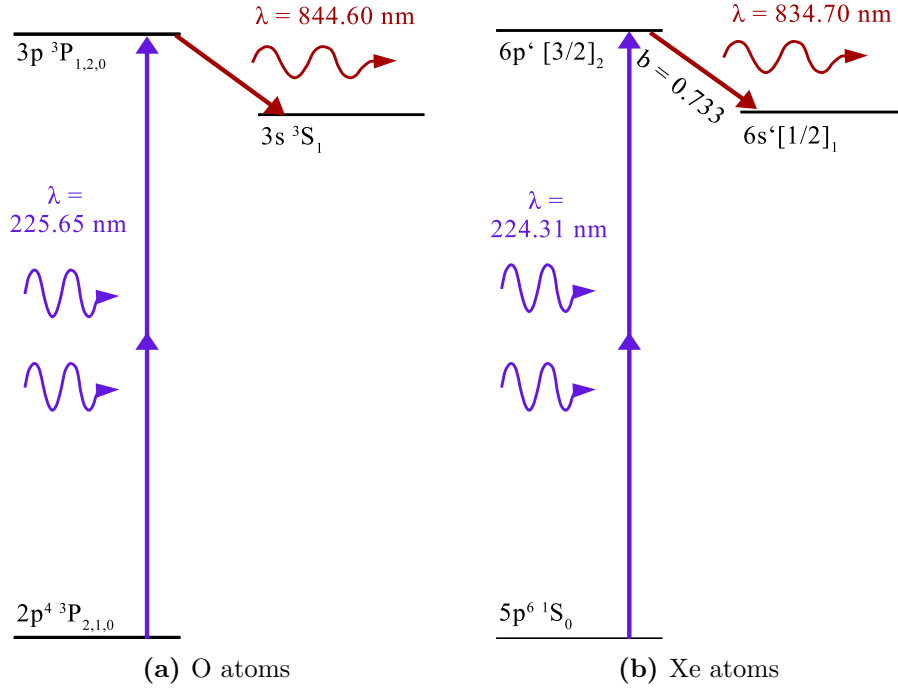
Figure 3.5: Excitation schemes of TALIF for O atoms and for Xe atoms.

The calibration gas for H atoms, Kr, is excited by two-photons with a wavelength of 204.13 nm each to the $5p'[3/2]_2$ state at 97945.17 cm^{-1} [36]. A natural lifetime of 34.1 ns for this state has been reported in [18]. The fluorescence with a branching ratio of $b_{ik,nat} = 0.958$ [18, 37] was observed at 826.3 nm, emitted by the transition from the $5p'[3/2]_2$ to the $5s'[1/2]_1$ at 85846.70 cm^{-1} [36].

In figure 3.5, the excitation schemes for O and Xe atoms are depicted. Atomic O was probed by two photons with a wavelength of 225.65 nm each, exciting the three $3p\ ^3P_{1,2,0}$ states at 88630.59 cm^{-1}, 88631.15 cm^{-1}, and 88631.3 cm^{-1} [38], respectively, with a natural lifetime of 34.7 ns [19]. The fluorescence to the $3s\ ^3S_1$ state at 76794.90 cm^{-1} [38] was observed at 844.6 nm. As a calibration gas for O atoms, Xe was excited to the $6p'[3/2]_2$ state at 89162.37 cm^{-1} [39] with two photons at 224.31 nm each. A natural lifetime of 40.8 ns has been reported in [19]. The fluorescence at 834.7 nm was due to a transition to the $5s'[1/2]_1$ state at 77185.04 cm^{-1} [39]. For the branching ratio for this transition, a value of $b_{ik,nat} = 0.733$ [40] was used.

In table 3.1, the species' excited states, their natural lifetimes, optical branching ratios, excitation wavelengths, and the corresponding two-photon absorption cross section ratios for H/Kr and O/Xe are summarised.

Table 3.1: Analysed species with natural lifetime τ_{nat}, taking fine structure splitting into account, optical branching ratio $b_{ik,nat}$, two-photon excitation wavelength λ_l, and the corresponding two-photon absorption cross section ratios $\sigma_H^{(2)}/\sigma_{Kr}^{(2)}$ and $\sigma_O^{(2)}/\sigma_{Xe}^{(2)}$.

Species (excited state)	τ_{nat} [ns]	$b_{ik,nat}$	λ_l [nm]	$\sigma^{(2)}/\sigma_{cal}^{(2)}$
H(3d ^{2}D$_J$)	17.6	1	205.11	0.62 ± 0.31 [18]
Kr(5p$'[3/2]_2$)	34.1	0.958	204.13	
O(3p ^{3}P$_J$)	34.7	1	225.64	1.90 ± 0.38 [19]
Xe(6p$'[3/2]_2$)	40.8	0.733	224.31	

In order to avoid saturation effects, such as stimulated emission, the laser energy was reduced sufficiently to ensure the unsaturated quadratic signal dependency for the TALIF signal. In figure 3.6, the saturation curves for the H and O measurements are shown. For the H atom and O atom measurements, a laser energy of 35 μJ and 40 μJ have been chosen. The laser energy for Kr and Xe was taken from [28].

(a) H atoms

(b) O atoms

Figure 3.6: Saturation curves for H and O.
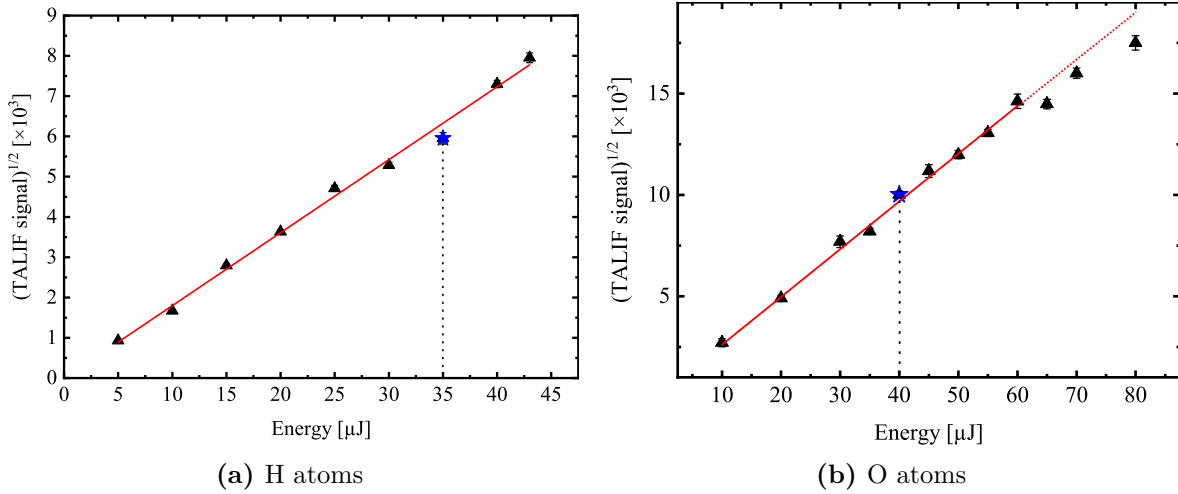
The experimental parameter for all TALIF measurements, such as the laser energy, the wavelength range of the used band pass filters to collect the fluorescence, the filter transmissions, the transmissions of the calibration cuvette in the direction of the laser and the direction of the fluorescence, the quantum efficiency of the detector, and the working pressures are given in table 3.2.

Table 3.2: Experimental parameters for all TALIF measurements, including the laser energy E_L, the wavelength range of the used band pass filters, the filter transmissions T_{filter}, the transmissions of the calibration cuvette in the direction of the laser $T_{\mathrm{optics,L}}$, the transmissions of the calibration cuvette in the direction of the fluorescence $T_{\mathrm{optics,F}}$, the quantum efficiencies of the detector η, and the working pressures [28].

Species	E_L [µJ]	Filter [nm]	T_{filter} [%]	$T_{\mathrm{optics,L}}$ [%]	$T_{\mathrm{optics,F}}$ [%]	η [%]	pressure [torr]
H	35	656±5	88.9	100	100	13	760
Kr	0.28	825±5	73.7	90	94	10	1
O	40	845±5	83.74	100	100	9.10	760
Xe	0.45	835±5	62.92	92	94	9.65	10

3.3 Determination of absolute number densities with picosecond TALIF

In figure 3.7a, an overlay of several camera images are shown: A shadow image of the plasma jet nozzle, and the on-resonance TALIF signal for H atoms at $\lambda_l(H) = 205.11$ nm as measured at various distances z from the plasma jet's nozzle. In figure 3.7b, the equivalent for the TALIF signal for O atoms at $\lambda_l(H) = 225.64$ nm is presented. Each TALIF signal measurement results from 64 or 256 accumulations (number of laser shots) with a camera gate width of 120 ns, which is sufficiently large to capture the entirety of the fluorescence decay. With a laser repetition rate of 10 Hz this corresponds to 6.4 s respectively 25.6 s measurement time. The frequency of the plasma jet was 1 MHz yielding a time interval of 1 µs between two subsequent plasma pulses. Overall, this means that 6.4 or 25.6 million plasma pulses occurred during the measurement of the H and O atoms, respectively. The accumulated background signal from the camera and the optical plasma emission as measured off-resonance was subtracted accordingly. It was observed that more accumulations were necessary in the instance of the O atom measurements (256) compared to the H atom measurements (64). This was required in order to obtain a comparable signal-to-noise ratio, most likely as a result of the delicate nature of the laser's wavelength dependency. The shadow image of the plasma jet was taken by using an LED for back illumination. By using the nozzle diameter of 2.4 mm as a reference, the scaling of the image in terms of mm length per pixel was determined.
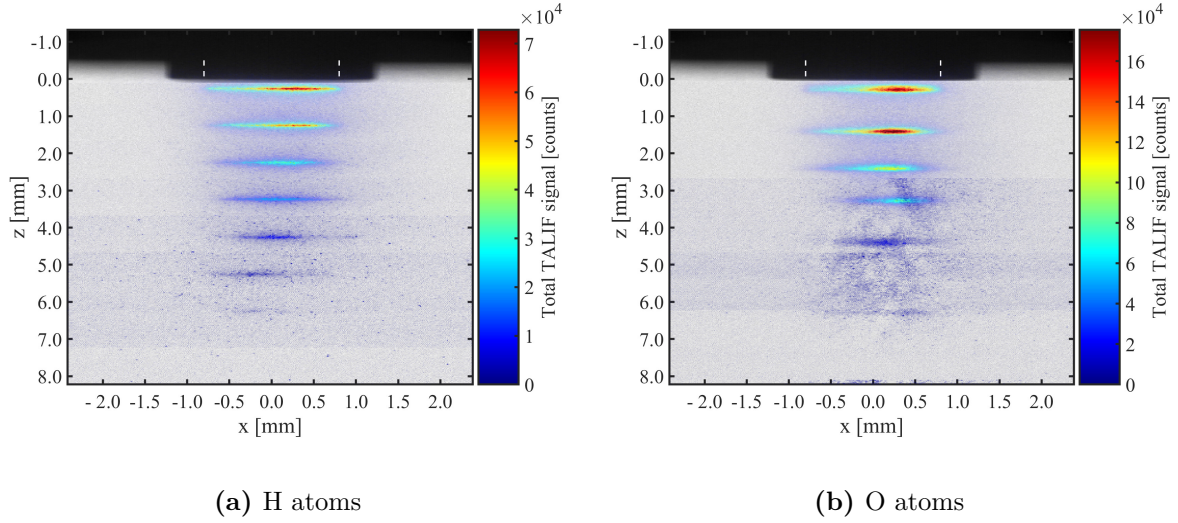
(a) H atoms   **(b)** O atoms

Figure 3.7: Overlaid images of the on-resonance fluorescence signal as measured at various distances z to the nozzle together with a shadow image of the nozzle: a) H atoms, $\lambda_l(H) = 205.11$ nm, 64 accumulations; b) O atoms, $\lambda_l(O) = 225.64$ nm, 256 accumulations.

TALIF spectra of the two-photon resonances were obtained by measuring the fluorescence signals within a region of interest on the camera chip as a function of the laser wavelength. By subdividing the interaction zone of the laser beam with the plasma effluent into frames of 4×8 pixels (50×100 μm) in x and z direction, over which the signal was accumulated, spatial resolution was achieved. In figure 3.8, a measured ex-

Figure 3.8: TALIF spectrum for the O $2p_4^3P_{J=2} \rightarrow 3p^3P_{J=1,2,0}$ transition determined at $z = 0.25$ mm, together with a Gaussian fit. Each data point was obtained by accumulating the entirety of the fluorescence signals of 256 laser shots with a camera gate width of 120 ns.

ample spectrum of the two photon excitation from the lowest component of the ground state of O $(2p_4^3P_{J=2})$ to the three close-by components of the upper state $(3p^3P_{J=1,2,0})$, accumulated over the entire region of the fl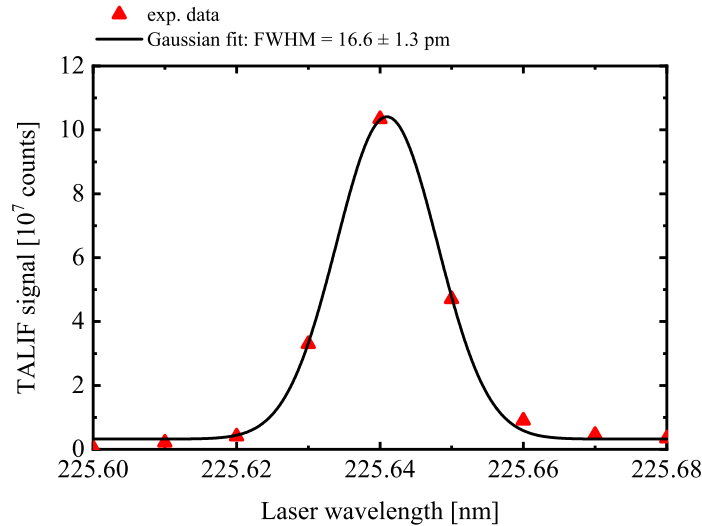uorescence signal, is shown at $z = 0.25$ mm together with a best fit of a Gaussian function (FWHM= 16.6 ± 1.3 pm). Unfortunately, the spectral resolution of the picosecond laser system of approximately 4 cm^{-1} is insufficient to resolve the O$(3p^3P_{J=1,2,0})$ fine structure of the upper level (≈ 0.7 cm^{-1}), nor to determine reliable values for the Doppler width and pressure broadening under the investigated conditions, which in contrast is possible with a conventional nanosecond TALIF laser system, e.g. see ref. [19]. In this work, the spectral profile of the TALIF measurements comprises of 6 data points, with a wavelength interval of 0.01 nm, that enables a Gaussian profile to be fitted. The area of this Gaussian profile is the total TALIF signal S_F (see equation 3.11) that is used for the calculation of ground state densities.

The effective lifetimes of the excited states were determined from the measured temporal decay of the fluorescence signal. At on-resonance laser wavelength, the delay between laser pulse and camera trigger was varied in equidistant steps, while keeping the camera gate width constant. For the slower TALIF decay of O atoms a time increment of 0.5 ns and a camera gate of 5 ns was chosen, while for the faster TALIF decay of H atoms a time increment of 50 ps, and a gate width of 800 ps was used. The oversampling is necessary to obtain a signal-to-noise ratio above the detection limit. In figure 3.9, an example of the measured TALIF signal for O atoms at $z = 0.25$ mm is shown as a function of time, where the black solid curve represent the best fit by a purely exponential decay after the laser excitation. The effective lifetime was determined for each measurement from the decay time of the exponential fit.

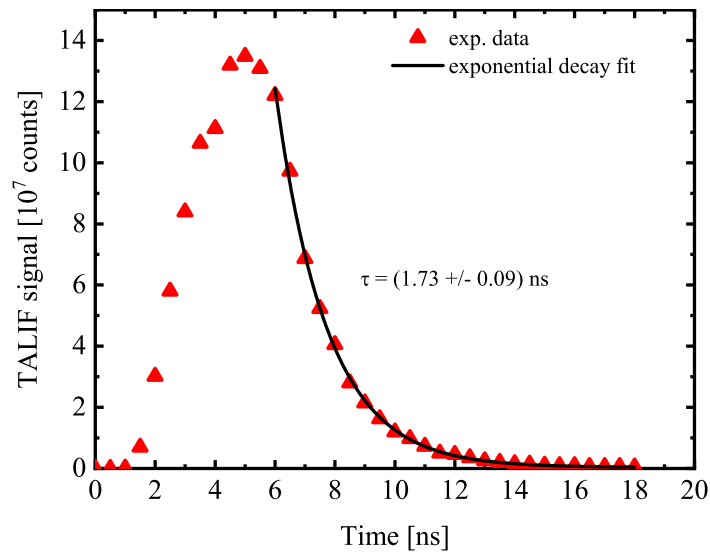At $z = 0.25$ mm, for instance, an effective lifetime of $\tau_{eff} = (1.7 \pm 0.1)$ ns was ob-

Figure 3.9: Time resolved O$(3p^3P_J)$ TALIF signal at $z = 0.25$ mm obtained with 0.5 ns time steps and 5 ns camera gate width.

served for O atoms. The measured effective lifetime is slightly lower than the calculated effective lifetime $\tau_{eff}^{theo} = 2.21 \pm 0.10$ ns (see equation 3.9) for a gas mixture of 3 slm Ar, at 300 K, mixed with 3000 ppm water, and quenching coefficients $k_{Ar}^{O} = (0.140 \pm 0.007) \cdot 10^{-10}$ cm^3/s [19] for excited O atoms quenched by Ar and $k_{H_2O}^{O} = (11.0 \pm 1.1) \cdot 10^{-10}$ cm^3/s [28] for excited O atoms quenched by water. This shows that additional quenching species need to be considered to match the theoretical value to the experimental one, which will be discussed in section 3.4 in more detail. However, for the excited atomic hydrogen state the situation is different. Schmidt and Bittner reported quenching coefficients $k_{Ar}^{H} = (4.15 \pm 0.03) \cdot 10^{-10}$ cm^3/s in the presence of Ar [41] and $k_{H_2O}^{H} = (110 \pm 10) \cdot 10^{-10}$ cm^3/s in the presence of water [27]. The corresponding quenching rate turns out to be a factor of about 20 higher than for the atomic oxygen state: $\tau_{eff} = 90 \pm 14$ ps, using the aforementioned quenching coefficients. This value is close to the detection limit of the system of about 100 ps. Hence, the effective lifetime for excited H atoms could not be determined experimentally and the calculated value was used instead in order to give an estimation for the H atom density.

A detailed description of the uncertainty analysis for the density measurements can be found in [28]. According to equation 3.11, the relative uncertainty $\frac{\Delta n}{n}$ for the density n can be calculated from the relative uncertainties for the individual experimental parameters:

$$\left(\frac{\Delta n}{n}\right)^2 = \left(\frac{\Delta T^{ref}}{T^{ref}}\right)^2 + \left(\frac{\Delta \tau_{eff}^{ref}}{\tau_{eff}^{ref}}\right)^2 + \left(\frac{\Delta \tau_{nat}^{ref}}{\tau_{nat}^{ref}}\right)^2 + \left(\frac{\Delta \tau_{eff}}{\tau_{eff}}\right)^2 + \left(\frac{\Delta \tau_{nat}}{\tau_{nat}}\right)^2$$
$$+ \left(\frac{\Delta \sigma^{ref}/\sigma}{\sigma^{ref}/\sigma}\right)^2 + \left(\frac{\Delta E^{ref}}{E^{ref}}\right)^2 + \left(\frac{\Delta E}{E}\right)^2 + \left(\frac{\Delta S_F^{ref}}{S_F^{ref}}\right)^2 + \left(\frac{\Delta S_F}{S_F}\right)^2 . \quad (3.13)$$

The error bars shown in the following comprise the total stochastic uncertainty of about

(a) H atoms: stochastic uncertainty: 31%, systematic error: 52%

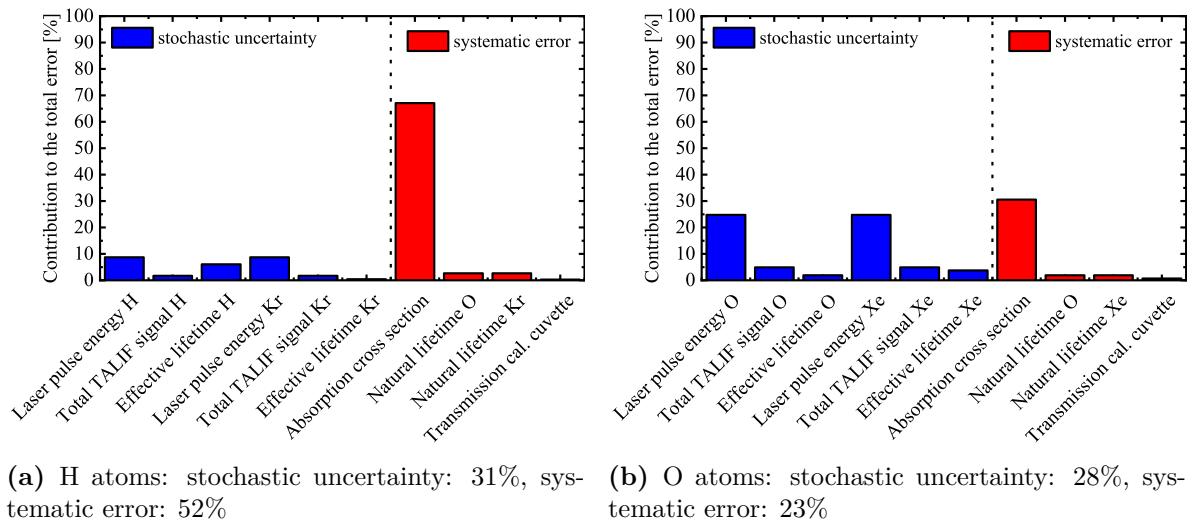**(b)** O atoms: stochastic uncertainty: 28%, systematic error: 23%

Figure 3.10: Contributions of the individual experimental parameters to the total error of the density measurements for H and O.

28% for the O atom density and approximately 31% for the H atom density. They include 9% uncertainty for the laser pulse energy, 8% for the Gaussian fit, and the error of the effective lifetimes (5% for O, 7% for Xe, 4% for Kr and 15% for H). However, for the total error of the absolute number density, the uncertainty of the two-photon absorption cross section plays an important role. Therefore, systematic errors given in [28] are used for the transmission of the calibration cuvette (3%), the natural lifetimes (5% for O and Xe and 10% for H and Kr), and the two-photon absorption cross section ratios (20% for Xe-O [19] and 50% for Kr-H [18]) to determine the absolute error of the number densities, which amounts to 36% for O atoms and 61% for H atoms. In figure 3.10, the relative contributions of the single experimental parameters, such as the laser energy, the natural and effective lifetimes, the total TALIF signals, the two-photon absorption cross sections, and the transmission of the calibration cuvette, on the total error are summarised. For both, H and O atom measurements, the systematic error of the absorption cross section, and the stochastic uncertainty of the laser energy have the largest influence on the total error.

3.4 Results

3.4.1 Radial density distributions for O and H atoms

In figure 3.11, radial density profiles (lateral direction x) for O and H atoms are depicted as measured at different distances z from the jet's nozzle, while a gas curtain of oxygen-only was applied. The shown error bars comprise the stochastic uncertainties only, excluding the systematic ones (see section 3.3). The atomic O and H densities were found to be distributed within the 2 mm diameter of the nozzle opening. They have similar distributions and decrease with increasing distance to the nozzle. The maximum is shifted to the right (between $x = 0.0$ mm and $x = 0.5$ mm) for the O atom density and moving from the right to the centre for the H atom density further away from the nozzle, which is also shown in figures 3.7a and 3.7b. The lateral O atom density distributions exhibit an asymmetry, particularly at short distances from the nozzle. For example, at $z = 0.25$ mm, the O atom density is approximately $3.8 \cdot 10^{15}$ cm^{-3} for positive x values up to $+0.5$ mm, while much lower for the corresponding negative x-values. Due to the lower number of accumulations of the H measurements, the H atom densities exhibit more scattering than the O density; nonetheless, an asymmetric distribution was observed, in particular, at $z = 0.25$ mm. These distributions can be explained by the filamentary character of the plasma jet: Guided streamers are propagating into the effluent, whose directions are determined by the turbulent nature of the plasma jet resulting in an erratic path way. Close to the nozzle, the atomic densities are produced by reactions in the plasma zone of the jet, which are determined by filaments from the tip of the inner needle electrode to the outer ring-electrode. Within the plasma zone, one direction for the filament could be preferred due to inhomogeneities at the electrodes, which would result in an asymmetric production of H and O atoms. The averaged density values between $x = 0.0$ mm and $x = 0.5$ mm, at $z = 0.25$ mm, were
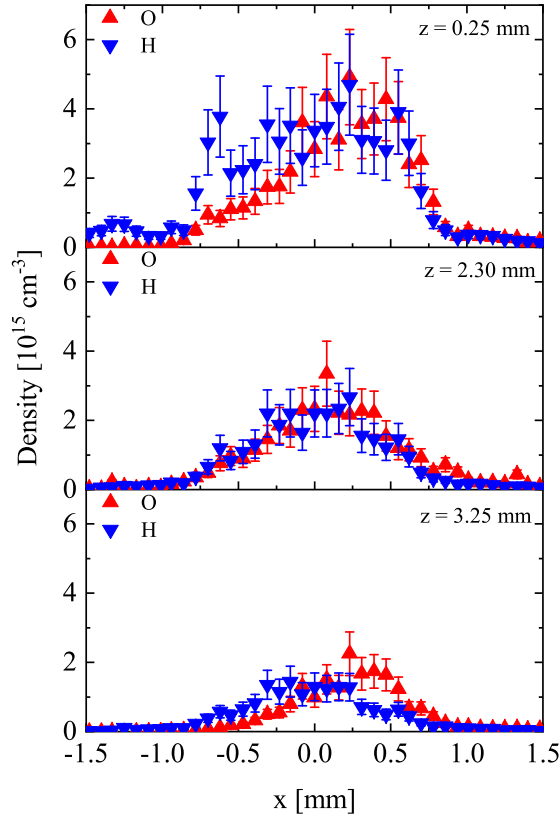
Figure 3.11: Density of O and H as a function of x at various z-positions with a gas curtain of 100% oxygen.

similar with $3.8 \cdot 10^{15}$ cm^{-3} and $3.5 \cdot 10^{15}$ cm^{-3} for O and H respectively. Considering water as the only source for atomic oxygen and atomic hydrogen, one would expect a much lower O atom density. Whereas atomic H is a direct dissociation product of water, secondary reactions, such as the recombination of two OH radicals, are necessary to form atomic O. However, since the plasma jet is turbulent and was operated with molecular oxygen as a curtain gas, there could have been diffusion of molecular oxygen into the effluent leading to the formation of O due to dissociation of O$_2$.

3.4.2 Impact of the gas curtain close to the nozzle

In order to confirm that the dissociation of H$_2$O in the feed gas and the dissociation of diffused gas from the gas curtain into the effluent cannot explain the O atom densities at short distances to the nozzle, the O atom density was determined by using 3 slm dry Ar as a feed gas, while varying the gas curtain composition. In figure 3.12, the obtained O atom densities at $z = 1$ mm, are depicted as a function of the oxygen fraction in the gas curtain. The densities resulted from averaging between $x = 0.0$ mm and $x = 0.5$ mm, and are shown together with the corresponding standard deviation.

The O atom density results exhibit a larger error bar compared to the measurements
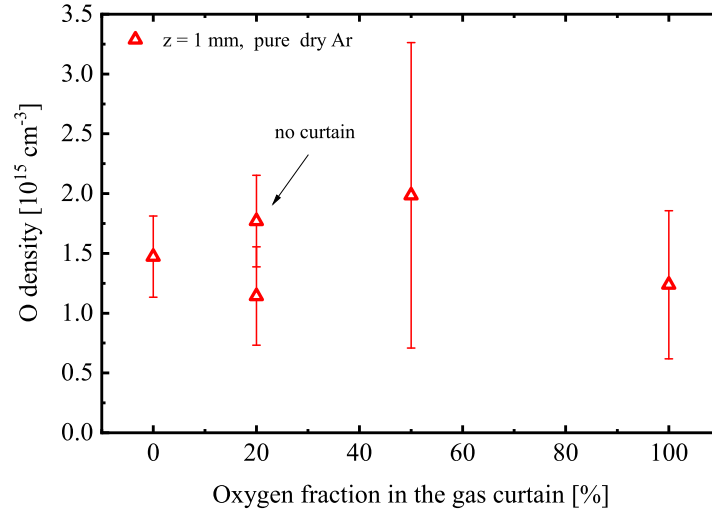
Figure 3.12: Measured O atom density at $z = 1$ mm with dry argon feed gas as a function of the oxygen content in the O_2/N_2 gas curtain.

with humidity. This is likely due to several optical emission lines of argon within the spectral bandpass of the used interference filter (840 to 850 nm). Since these excited argon levels are quenched less in the absence of water, a decrease in the overall signal to noise ratio is expected. Taking the error into account, the O atom density is constant at about $1.5 \cdot 10^{15}$ cm^{-3} for all gas curtain compositions. Even without a gas curtain, the atomic O density has the same value within the error. These findings are in accordance with gas flow simulations [42], mass spectrometry investigations [43], and measurements by Reuter et al. [20], who reported that the influx from the gas curtain starts to be efficient at distances beyond 4 mm from the nozzle. Moreover, the atomic H and O densities closer to the nozzle at $z = 0.25$ mm, obtained with 3000 ppm feed gas humidity, were independent from the gas curtain compositions. This demonstrates, that water present in the feed gas and species present in the gas curtain are not the origin of the measured O atoms, and that another source for oxygen needs to be present already in the plasma zone.

3.4.3 Spatial density distributions for O and H atoms

In figure 3.13, contour plots for the spatial distributions of O and H atoms are illustrated as a function of the radial distance from the centre of the nozzle x and the axial distance from the nozzle z for 3000 ppm water in the Ar feed gas and a gas curtain of 100% oxygen, obtained from an interpolation between the experimental data points (figure 3.13b and 3.13a). In order to fill the regular grid of the contour plot, the densities measured at $z = 0.25$ mm were interpolated to $z = 0$ mm, while averaging and interpolation was performed for z-distances further from the nozzle. Up to a distance of approximately $z = 4$ mm, H and O atoms were found to be distributed over the

(a) H atoms   **(b)** O atoms
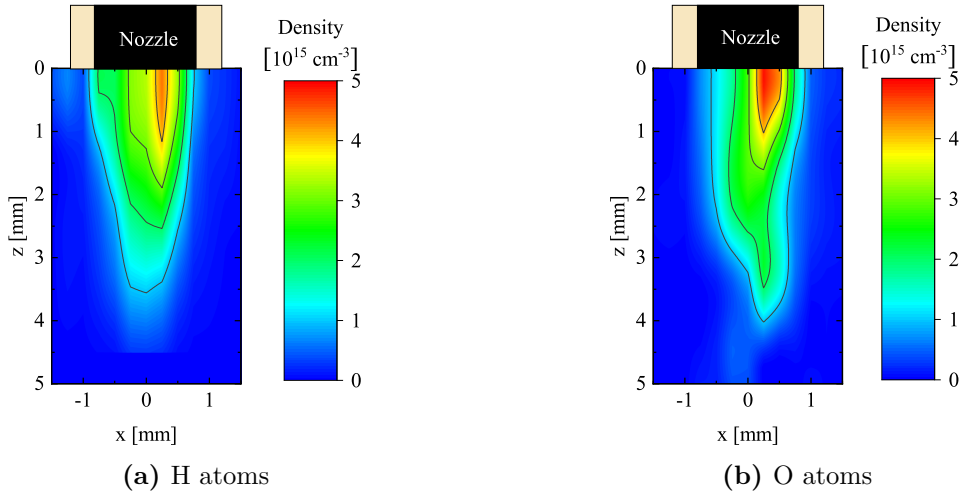
Figure 3.13: Spatial density distributions of O and H atoms as a function of the radial distance from the centre of the nozzle x and the axial distance from the nozzle z for 3000 ppm water in the Ar feed gas and a gas curtain of 100% oxygen, obtained from an interpolation between the experimental data points.

complete diameter of the nozzle. For further z-distances, the density was below the detection limit.

In figure 3.14, the resulting axial density profiles are shown. A maximum H atom density of $(3.5 \pm 0.7) \cdot 10^{15}$ cm^{-3}, and a maximum O atom density of $(3.8 \pm 0.7) \cdot 10^{15}$ cm^{-3} was obtained at $z = 0.25$ mm, where the error is the standard deviation within the averaged region. Interestingly, the density values of O atoms are in remarkably good agreement with the values obtained from TALIF measurements reported by Reuter et
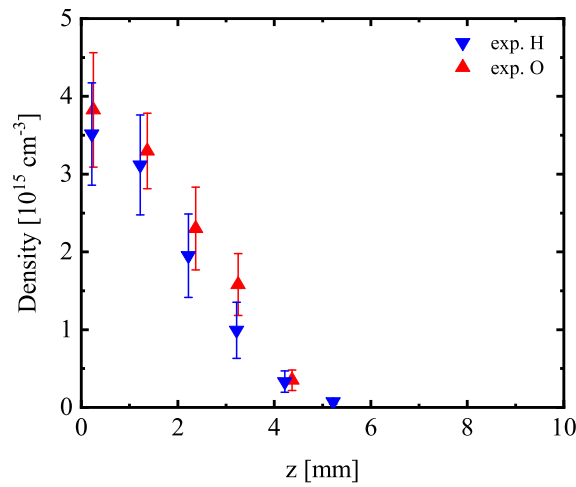
Figure 3.14: Axial density of O and H atoms as a function of the axial distance z to the nozzle.

al. [20], where the O atom density in 5 slm dry Ar with 1% feed gas admixture of molecular oxygen was determined. The strong decrease at $z = 4$ mm can be explained by the influx of the gas curtain into the plasma effluent: With a higher concentration of molecular oxygen, both, H and O radicals are consumed to form larger molecules, such as HO_2 or O_3.

The additional O_2 content in the plasma zone, resulting from other effects than an inwards diffusion of the gas curtain, can also explain the reduced effective lifetime of the measurements compared to the calculated lifetimes for the O atom measurements. Considering an additional content of 1% O_2, the calculated effective lifetime is reduced to (1.5 ± 0.1) ns, which is within the error in agreement with the measured values. Since the effective lifetime of excited O atoms was measured for each data point, additional quenching has already been considered. The effective lifetime for excited H atoms will be reduced by O_2 quenching from 90 ps to 85 ps, which is covered by the errorbars of 14 ps.

3.5 Summary

The O atom and H atom densities were investigated by picosecond two-photon absorption laser-induced fluorescence spectroscopy. In order to obtain absolute values for the densities, calibration procedures with Xe gas for O atoms and Kr gas for H atoms, respectively, were performed. The effective lifetimes for O atoms in the excited state were measured for the various gas mixtures used to account for all quenching mechanisms occurring. However, the effective lifetimes for H atoms in the excited state were close to the detection limit of the system and were hence estimated by calculations to be 90 ± 14 ps for all experimental conditions.

From the spatially and temporally integrated fluorescence signals, radial distributions for the densities for O and H atoms were determined. In particular for O atoms, an asymmetry in the radial distribution concentrated at a distance of 0.25 mm to the symmetry axis of the plasma jet was found. The absolute values for densities of O and H atoms were obtained close to the nozzle with $(3.8 \pm 0.7) \cdot 10^{15}$ cm^{-3}, and $(3.5 \pm 0.7) \cdot 10^{15}$ cm^{-3}, respectively. On balance, the values for the density distributions for O and H atoms agree within the error, which indicates that both, H and O atoms were produced by similar mechanisms. Notably, to obtain a similar value for O and H atoms, an additional source of O besides H_2O is needed within the feed gas. For further distances from the nozzle z up to approximately $z = 5$ mm, both densities decreased linearly to less than $1 \cdot 10^{14}$ cm^{-3}, which was the detection limit of the experimental setup. The decrease of the densities is most likely due to the reaction of O and H atoms with the gas curtain that diffuses into the effluent very efficiently at $z = 4$ mm.

In order to confirm that the dissociation of H_2O in the feed gas and the dissociation of diffused gas from the gas curtain into the effluent can not explain the observed O atom densities close to the nozzle, the densities for O atoms were measured without humidity in the feed gas, while varying the composition of the gas curtain. Within the error, all measured densities were in agreement. Hence, it can be concluded that the gas curtain has no impact on the densities close to the nozzle at $z \leq 1.5$ mm. In order to explain the measured densities of approximately $1.5 \cdot 10^{15}$ cm^{-3} , an amount of more than $7.5 \cdot 10^{14}$ cm^{-3} of O_2 has to be present within the plasma zone in the case of dry feed gas.

This work demonstrates that the densities of the atomic radicals, O and H, strongly depend on the molecular oxygen content in the plasma zone and in the effluent. It has been shown that even small amounts of O_2 in the plasma zone, have a drastic impact on the reactive species composition in the effluent.

3.6 Bibliography

[1] S. Reuter, J. S. Sousa, G. D. Stancu, and J. H. van Helden. Review on VUV to MIR absorption spectroscopy of atmospheric pressure plasma jets. *Plasma Sources Sci. Technol.*, 24(054001), 2015.

[2] R. Perverall and G. A. D. Ritchie. Spectroscopy techniques and the measurement of molecular radical densities in atmospheric pressure plasmas. *Plasma Sources Sci. Technol.*, 28(073002), 2019.

[3] S.-J. Klose, J. Ellis, F. Riedel, S. Schröter, K. Niemi, I. L. Semenov, K.-D. Weltmann, T. Gans, D. O'Connell, and J. H. van Helden. The spatial distribution of hydrogen and oxygen atoms in a cold atmospheric pressure plasma jet. *Plasma Sources Sci. Technol.*, 29(125018), 2020.

[4] K. D. Bonin and T. J. McIlrath. Two-photon electric-dipole selection rules. *J. Opt. Soc. Am. B*, 1(52-55), 1984.

[5] A. Goehlich, T. Kawetzki, and H. F. Döbele. On absolute calibration with xenon of laser diagnostic methods based on two-photon absorption. *J. Chem. Phys.*, 108(22):9362, 1998.

[6] H. F. Döbele, T. Mosbach, K. Niemi, and V. Schulz-von der Gathen. Laser-induced fluorescence measurements of absolute atomic densities: concepts and limitations. *Plasma Sources Sci. Technol.*, 14(S31-S41), 2005.

[7] G. D. Stancu. Two-photon absorption laser induced fluorescence: rate and density-matrix regimes for plasma diagnostics. *Plasma Sources Sci. Technol.*, 29(054001), 2020.

[8] K. Gazeli, G. Lombardi, X. Aubert, C. Y. Duluard, S. Prasanna, and K. Hassouni. Progress on the Use of Two-Photon Absorption Laser Induced Fluorescence (TALIF) Diagnostics for Measuring Absolute Atomic Densities in Plasmas and Flames. *Plasma*, 4(145-171), 2021.

[9] J. Bokor, R. R. Freeman, J. C. White, and R. H. Storz. Two-photon excitation of the n = 3 level in H and D atoms. *Phys. Rev. A*, 24(612(R)), 1981.

[10] W. K. Bischel, B. E. Perry, and D. R. Crosley. Two-photon laser-induced fluorescence inoxygen and nitrogen atoms. *Chem. Phys. Lett.*, 82(1), 1981.

[11] M. Aldén, H. Edner, P. Grafström, and S. Svanberg. Two-photon excitation of atomic oxygen in a flame. *Opt. Commun.*, 42(4), 1982.

[12] L. F. DiMauro, R. A. Gottscho, and T. A. Miller. Two-photon laser-induced fluorescence monitoring of O atoms in a plasma etching environment. *J. Appl. Phys.*, 56(7), 1984.

[13] B. L. Preppernau, D. A. Dolson, R. A. Gottscho, and T. A. Miller. Temporally Resolved Laser Diagnostic Measurements of Atomic Hydrogen Concentrations in RF Plasma Discharges. *Plasma Chem. Plasma Process.*, 9(2), 1989.

[14] J. R. Dunlop, A. D. Tserepi, B. L. Preppernau, T. M. Cerny, and T. A. Miller. H Atom Plasma Diagnostics: A Sensitive Probe of Temperature and Purity. *Plasma Chem. Plasma Process.*, 12(89-101), 1992.

[15] A. D. Tserepi and T. A. Miller. Two-photon absorption laser-induced fluorescence of H atoms: A probe for heterogeneous processes in hydrogen plasmas. *J. Appl. Phys.*, 75(7231), 1994.

[16] L. Chérigier, U. Czarnetzki, D. Luggenhölscher, V. Schulz-von der Gathen, and H. F. Döbele. Absolute atomic hydrogen densities in a radio frequency discharge measured by two-photon laser induced fluorescence imaging. *J. Appl. Phys.*, 85(696), 1999.

[17] J. Amorim, G. Baravian, and J. Jolly. Laser-induced resonance fluorescence as a diagnostic technique in non-thermal equilibrium plasmas. *J. Phys. D: Appl. Phys.*, 33(R51-R65), 2000.

[18] K. Niemi, V. Schulz-von der Gathen, and H. F. Döbele. Absolute calibration of atomic density measurements by laser-induced fluorescence spectroscopy with two-photon excitation. *J. Phys. D: Appl. Phys.*, 34:2330, 2001.

[19] K. Niemi, V. Schulz-von der Gathen, and H. F. Döbele. Absolute atomic oxygen density measurements by two-photon absorption laser-induced fluorescence spectroscopy in an rf-excited atmospheric pressure plasma jet. *Plasma Sources Sci. Technol.*, 14:375, 2005.

[20] S. Reuter, J. Winter, A. Schmidt-Bleker, D. Schröder, H. Lange, N. Knake, V. Schulz-von der Gathen, and K.-D. Weltmann. Atomic oxygen in a cold argon plasma jet: TALIF spectroscopy in ambient air with modelling and measurements of ambient species diffusion. *Plasma Sources Sci. Technol.*, 21:024005, 2012.

[21] C. Jiang and C. Carter. Absolute atomic oxygen density measurements for nanosecond-pulsed atmospheric-pressure plasma jets using two-photon absorption laser-induced fluorescence spectroscopy. *Plasma Sources Sci. Technol.*, 23(065006), 2014.

[22] S. Zhang, A. F. H. van Gessel, S. C. van Grootel, and P. J. Bruggeman. The effect of collisional quenching of the O 3p ^{3}P$_j$ state on the determination of the spatial distribution of the atomic oxygen density in an APPJ operating in ambient air by TALIF. *Plasma Sources Sci. Technol.*, 23(025012), 2014.

[23] J. Benedikt, D. Schröder, S. Schneider, G. Willems, A. Pajdarová, J. Vlček, and V. Schulz-von der Gathen. Absolute OH and O radical densities in effluent of a He/H_2O micro-scaled atmospheric pressure plasma jet. *Plasma Sources Sci. Technol.*, 25(045013), 2016.

[24] J. Conway, G. S. Gogna, C. Gaman, M. M. Turner, and S. Daniels. Two-photon absorption laser induced fluorescence measurement of atomic oxygen density in an atmospheric pressure air plasma jet. *Plasma Sources Sci. Technol.*, 25(045023), 2016.

[25] Q. Xiong, H. Liu, N. Britun, A. Y. Nikiforov, L. Li, Q. Chen, and C. Leys. Time-Selective TALIF Spectroscopy of Atomic Oxygen Applied to an Atmospheric Pressure Argon Plasma Jet. *IEEE Trans. Plasma Sci.*, 44(11), 2016.

[26] A. F. H. van Gessel, S. C. van Grootel, and P. J. Bruggeman. Atomic oxygen TALIF measurements in an atmospheric-pressure microwave plasma jet with in situ xenon calibration. *Plasma Sources Sci. Technol.*, 22(055010), 2013.

[27] J. Bittner, K. Kohse-Höinghaus, U. Meier, and T. Just. Quenching of two-photon-excited H(3s,3d) and O($3p^3P_{2,1,0}$) atoms by rare gases and small molecules. *Chem. Phys. Lett.*, 143:571–576, 1988.

[28] S. Schröter, J. Bredin, A. R. Gibson, A. West, J. P. Dedrick, E. Wagenaars, K. Niemi, T. Gans, and D. O'Connell. The formation of atomic oxygen and hydrogen inatmospheric pressure plasmas containinghumidity: picosecond two-photon absorption laserinduced fluorescence and numerical simulations. *Plasma Sources Sci. Technol.*, 29(105001), 2020.

[29] B. Myers, E. Barnat, and K. Stapelmann. Atomic oxygen density determination in the effluent of the COST reference source using in situ effective lifetime measurements in the presence of a liquid interface. *J. Phys. D: Appl. Phys.*, 54(455202), 2021.

[30] J. B. Schmidt, B. L. Sands, W. D. Kulatilaka, S. Roy, J. Scofield, and J. R. Gord. Femtosecond, two-photon laser-induced-fluorescence imaging of atomic oxygen in an atmospheric-pressure plasma jet. *Plasma Sources Sci. Technol.*, 24:032004, 2015.

[31] J. B. Schmidt, B. Sands, J. Scofield, J. R. Gord, and S. Roy. Comparison of femtosecond- and nanosecond-two-photon-absorption laserinduced fluorescence (TALIF) of atomic oxygen in atmospheric-pressure plasmas. *Plasma Sources Sci. Technol.*, 26(055004), 2017.

[32] S. Schröter. *Reactive oxygen and hydrogen species generation in radio-frequency atmospheric pressure plasmas - Experimental and Numerical Investigations.* PhD thesis, University of York, May 2017.

[33] A. Kramida. A critical compilation of experimental data on spectral lines and energy levels of hydrogen, deuterium, and tritium. *At. Data and Nucl. Data Tables*, 96(6), 2010.

[34] J. H. Tung, A. Z. Tang, G. J. Salamo, and F.T. Chan. Two-photon absorption of atomic hydrogen from two light beams. *J. Opt. Soc. Am. B*, 3(6), 1986.

[35] E. U. Condon and G. H. Shortely. *Theory of atomic spectra.* Cambridge University Press, 1951.

[36] E. B. Saloman. Energy Levels and Observed Spectral Lines of Krypton, Kr i through kr XXXVI. *J. Phys. Chem. Ref. Data*, 36(215), 2007.

[37] R. S. F. Chang, H. Horiguchi, and D. W. Setser. Radiative lifetimes and two-body collisional deactivation rate constants in argon for Kr($4p^5 5p$) and Kr($4p^5 5p$') states. *J. Chem. Phys.*, 73(778), 1980.

[38] C. E. Moore. *Tables of Spectra of Hydrogen, Carbon, Nitrogen, and Oxygen Atoms and Ions.* CRC Press, 1993.

[39] C. J. Humphreay and E. Paul. Interferometric Wavelength Determinations in the First Spectrum of ^{136}Xe. *J. Opt. Soc. Am.*, 60(10), 1970.

[40] H. Horiguchi, R. S. F. Chang, and D. W. Setser. Radiative lifetimes and two-body collisional deactivation rate constants in Ar for Xe($5p^5 6p$),Xe($5p^5 6p$), and Xe($5p^5 7p$) states. *J. Chem. Phys.*, 75(1207), 1981.

[41] J. B. Schmidt, S. Roy, W. D. Kulatilaka, I. Shkurenkov, Adamovich I. V., W. R. Lempert, and J. R. Gord. Femtosecond, two-photon-absoprtion, laser-induced-fluorescence (fs-TALIF) imaging of atomic hydrogen and oxygen in non-equilibrium plasmas. *J. Phys. D: Appl. Phys.*, 50:015204, 2016.

[42] S. Iséni, A. Schmidt-Bleker, J. Winter, K.-D. Weltmann, and S. Reuter. Atmospheric pressure streamer follows the turbulent argon air boundary in a Mhz argon plasma jet investigated by Oh-tracer PLIF spectroscopy. *J. Phys. D: Appl. Phys.*, 47(152001), 2014.

[43] M. Dünnbier, A. Schmidt-Bleker, J. Winter, M. Wolfram, R. Hippler, K.-D. Weltmann, and S. Reuter. Ambient air particle transport into the effluent of a cold atmospheric-pressure argon plasma jet investigated by molecular beam mass spectrometry. *J. Phys. D: Appl. Phys.*, 46(435203), 2013.

4 The spatial distribution of HO$_2$ in the effluent of the kINPen-sci plasma jet
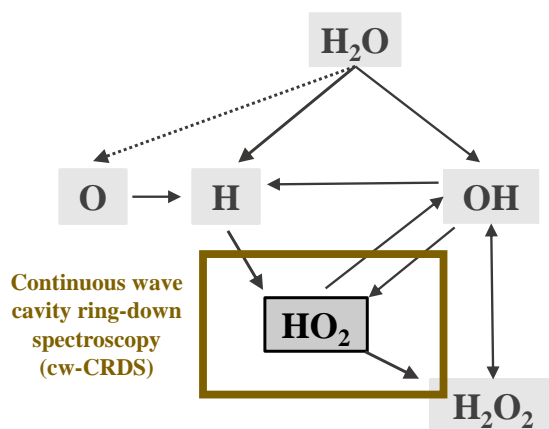
Within the formation cycle of H$_2$O$_2$, the HO$_2$ radical is an important precursor as well as a relevant consumer. Moreover, HO$_2$ is involved in biological oxidation reactions, such as lipid peroxidation, as it can enter cell membranes [1]. In a liquid, a chemical equilibrium will develop between HO$_2$ and the superoxide anion, O$_2^-$, which is responsible for a change of the pH-value in plasma-treated liquids [2]. In order to detect HO$_2$ radicals in the effluent of a CAPJ, Gianella et al. have recently applied optical feedback cavity-enhanced absorption spectroscopy (OF-CEAS) [3] and continuous wave cavity ring-down spectroscopy (cw-CRDS) [4]. The latter has the advantage to cover a broader wavelength range enabling the absorption features for HO$_2$ to be fully resolved, and to be less susceptible to fluctuations of the baseline. Moreover, with CRDS, a higher sensitivity and shorter acquisition time could be achieved.

For the determination of the density from absorption spectra, Gianella et al. have developed a fitting routine that includes 23 transitions of the second vibrational overtone of the OH stretch ($2\nu_1$) in the HO$_2$ radical around 6638.2 cm^{-1} (1506 nm), as well as overlapping transitions from water that was present in the ambient atmosphere and in the feed gas [4]. For further insights into the formation and loss mechanism of HO$_2$, spatial information is required. However, obtaining spatial density distributions with absorption spectroscopy techniques is demanding, as commonly line-of-sight densities

are determined, assuming a constant density that is homogeneously distributed over the effective absorption length.

To obtain a first indication of the radial profile of the HO$_2$ density, Gianella et al. sampled the effluent of a CAPJ through a pinhole expanding it to 5.33 kPa, while stepping the centre of the effluent relative to the centre of the pinhole. They reported on a doughnut-like shape with the highest densities at the sides and a dip in the centre of the effluent representing a formation of HO$_2$ by the reaction of H atoms produced by water dissociation in the feed gas with O$_2$ molecules diffused into the effluent from the surrounding atmosphere. The influence of the pinhole on the discharge was not investigated, but it was pointed out that it can not be excluded that the way, in which the low pressure experiment has been performed, is responsible for the observed profile.

In this chapter, which is adapted from reference [5], it is demonstrated, how spatially resolved density distributions in a CAPJ can be obtained by cw-CRDS in a time efficient way, called on/off-resonance method. At first, characteristics of optical cavities are introduced. These include descriptions of the mode structure in the frequency domain, of mode matching to improve the incoupling of a continuous wave laser into a cavity, and of the mode structure in the time domain. Based on the latter, the principle of cavity ring-down spectroscopy is explained. The experimental setup for the determination of spatial distributions for HO$_2$ in the effluent of the kINPen-sci plasma jet is presented, and the procedure to determine absolute densities from cavity ring-down spectra is elucidated. After a description of the spectroscopic parameters for HO$_2$, the on/off-resonance method is illustrated: Instead of taking full spectra for the determination of the densities for HO$_2$, it was sufficient to measure at two wavelengths; on the peak of the absorption feature at 6638.2 cm^{-1} and at a the side at 6637.6 cm^{-1}. The absorption coefficient obtained from full spectra was compared to the absorption coefficient determined by the on/off-resonance method. By performing radial scans at various distances from the nozzle, the effective absorption lengths were determined. An Abel inversion was applied to axial and radial scans in order to determine a spatial map of the density of HO$_2$ in the effluent of the kINPen-sci, which is also presented.

4.1 Introduction to optical cavities

By using optical cavities, which in the simplest configuration consist of two highly reflective mirrors positioned at a fixed distance L towards each other, the effective absorption length through a sample placed inside the cavity can be increased by orders of magnitude. In figure 4.1, a schematic of such an optical cavity with a sample placed inside is depicted. With mirrors with a reflectivity of $R = 99.98\%$, for instance, the optical path length through the sample $d = 4$ mm can be increased by a factor of $\frac{1}{1-R} = 5000$ to 200 m. In the following, the coupling of light to an optical cavity and the resulting mode structure inside the cavity is described, which can be found in detail in references [6, 7].
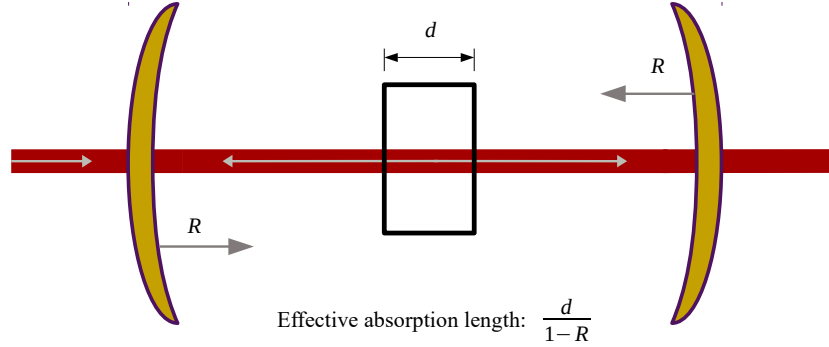
Effective absorption length: $\dfrac{d}{1-R}$

Figure 4.1: Schematic of an optical cavity with a sample placed inside. Here, R is the mirror reflectivity.

4.1.1 Mode structure of an optical cavity in the frequency domain

If an electro-magnetic wave with intensity I_0, an electric field strength $\vec{E_0}$, and wavelength λ is guided along the optical axis to the cavity, a portion of the incident wave transmits through the first cavity mirror and is reflected at the highly reflective side of the second cavity mirror. Most of the reflected wave is then again reflected at the highly reflective side of the first cavity mirror. With each round trip between the mirrors, a small portion of light transmits through the mirrors, whereas the main part is reflected, and the electric field and the magnetic field change their phase by the phase factor $e^{j2\phi}$ with every 2 reflections. The total electric field $\vec{E}$ of the electro-magnetic wave transmitting the second cavity mirror after an infinite number of round trips yields:

$$\vec{E} = t^2 \left(1 + \sum_{m=1}^{\infty} r^{2m} e^{j2m\phi} \right) \vec{E_0} = t^2 \frac{1}{1 - r^2 e^{i2\phi}} \vec{E_0}. \tag{4.1}$$

Here, j is the imaginary unit, and t is the amplitude coefficient that describes the value of the electric field amplitude after transmission through the mirror surface. Analogously, r is defined as the amplitude coefficient for reflection. The sum of the square of the amplitude coefficients equal 1, if no light is absorbed at the mirror surfaces:

$$r^2 + t^2 = R + T = 1. \tag{4.2}$$

Here, R is the mirror reflectivity and T is the mirror transmittivity. This is true for ideal mirrors with completely homogeneous coatings. In reality, the mirror reflectance is frequency dependent, as also the substrate material can lead to a small absorption within the mirrors. The transmitted intensity through the complete cavity depends on the the overlap of the cavity modes with the incident wavelength λ, and has the form
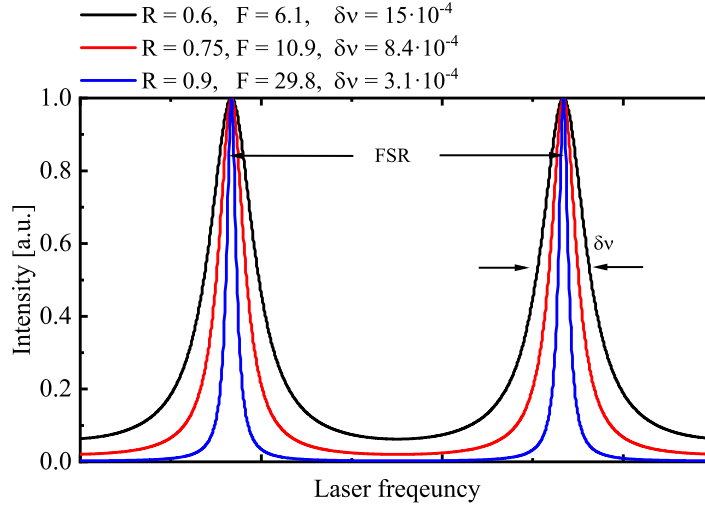
Figure 4.2: Example for the transmitted intensity through an optical cavity for three different mirror reflectivities $R = 0.6$, $R = 0.75$, and $R = 0.9$ as a function of the laser frequency. Here, F and $\delta\nu$ are the finesse and the width of the cavity modes, respectively. The distance between two longitudinal modes, the free spectra range, is denoted as FSR.

of an Airy profile:

$$I(\lambda) = \vec{E}\vec{E}^{\star} = \frac{I_0}{1 + \left(\frac{2\sqrt{R}}{1-R}\right)^2 \sin^2(\phi)} = \frac{I_0}{1 + \left(\frac{2F}{\pi}\right)^2 \sin^2\left(k\pi\frac{L}{\lambda/2}\right)}. \tag{4.3}$$

Here, k is an integer, L is the distance between the cavity mirrors, and F is a quantity called finesse, which depends on the reflectivity of the mirrors. In figure 4.2, an example for a transmitted intensity distribution is presented for three different mirror reflectivities, $R = 0.6$, $R = 0.75$, and $R = 0.9$.

With the relations $\sin(x) \sim x$ and $\lambda = \frac{c}{\nu}$, the peaks of this intensity distribution $I_{peak}(\nu)$ can be approximated by:

$$I_{peak}(\nu) = I_0 \frac{\left(\frac{\pi}{2F}\right)^2}{\left(\frac{\pi}{2F}\right)^2 + \pi^2 \left(\frac{c}{2L}\right)^{-2} \nu^2} = I_0 \frac{\left(\frac{FSR}{2F}\right)^2}{\left(\frac{FSR}{2F}\right)^2 + \nu^2}. \tag{4.4}$$

Each intensity peak can thus be approximated by a Lorentzian function with a full width at half maximum $\delta\nu$ of:

$$\delta\nu = \frac{FSR}{F}. \tag{4.5}$$

Here, FSR is the free spectra range, which describes the constant frequency spacing of longitudinal modes in the cavity:

$$FSR = \frac{c}{2L}. \tag{4.6}$$

The FSR is equivalent to the condition that the cavity length L needs to be a multiple of half of the laser wavelength λ. The variable F denotes the finesse; a quantity to account for the ratio between the width of the cavity modes $\delta\nu$ and the mode spacing that is determined by the mirror reflectivity R:

$$F = \frac{\text{FSR}}{\delta\nu} = \frac{\pi\sqrt{R}}{1-R}. \tag{4.7}$$

In order to improve the stability of an optical cavity, often curved mirrors are used. A cavity build by mirrors that fulfil the stability criterion

$$0 \leq g_1 g_2 \leq 1, \tag{4.8}$$

where $g_1 = 1 - \frac{L}{R_1}$ and $g_2 = 1 - \frac{L}{R_2}$ are the g-factor for the mirrors with a radius of curvature R_1 and R_2, respectively, allows reflections to the same focal point without leaving the cavity after a certain number of reflections. For spherical mirrors, the transmitted intensity distribution equals:

$$I_{m,n}(r, \varphi, z) = I_0 \left(\frac{2r^2}{w(z)^2} \right)^n \left[L_m^n \left(\frac{2r^2}{w(z)^2} \right) \right]^2 \cos^2(n\varphi) \, e^{-\left(\frac{2r^2}{w(z)^2} \right)}. \tag{4.9}$$

Here, m and n are integers, r is the distance to the optical axis, φ is the polar angle, L_m^n denotes the corresponding Laguerre polynomials, and w describes the beam waist of the mode:

$$w(z) = w_0 \sqrt{1 + \left(\frac{z}{z_R} \right)^2}. \tag{4.10}$$

Here, z corresponds to the propagation along the optical axis, and z_R is the Rayleigh length, which is defined by:

$$z_R = \frac{\pi w_0^2 \nu}{c}. \tag{4.11}$$

The minimum beam waist w_0 in the cavity is given by:

$$w_0 = \sqrt{\frac{Lc}{\pi\nu}} \left(\frac{g_1 g_2 (1 - g_1 g_2)}{(g_1 + g_2 - 2g_1 g_2)^2} \right)^{0.25}. \tag{4.12}$$

In figure 4.3, cross sections through the cavity modes perpendicular to the optical axis are depicted for different transversal modes, where $m = 0, 1, 2$ and $n = 0, 1, 2$. The frequency of resonant modes is determined by a combination of longitudinal modes with integer k and transversal modes with the integers m and n:

$$\nu_{kmn} = \frac{\text{FSR}}{2\pi} \left[2\pi k + 4(m + n + 1) \arctan \left(\sqrt{\frac{L}{2R_i - L}} \right) \right] \tag{4.13}$$

Here, $R_i = R_1 = R_2$ is the radius of curvature of the cavity mirrors. Higher order transversal modes have a larger spatial distribution than lower order transversal modes
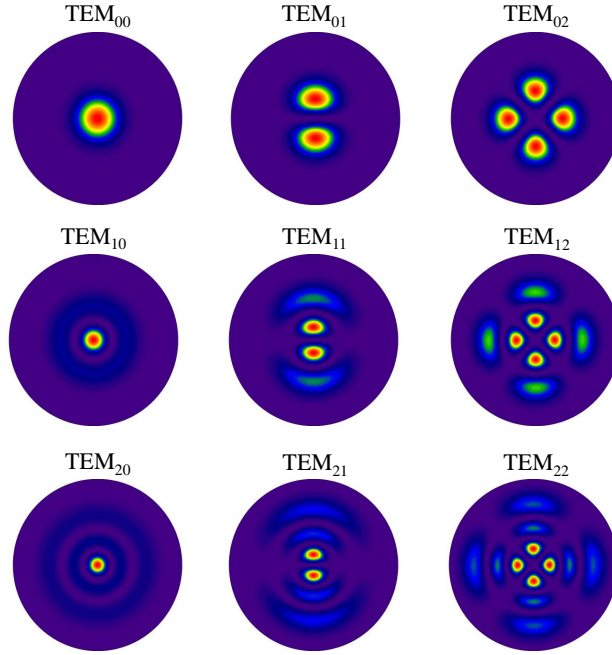
Figure 4.3: Cross sections perpendicular to the optical axis for various transversal modes inside the cavity, $m = 0, 1, 2$ and $n = 0, 1, 2$.

and are slightly shifted in frequency compared to the corresponding longitudinal modes.

4.1.2 Mode matching between cavity and laser

In order to optimise the overlap of the incident laser beam with the fundamental, so-called TEM_{00}, mode of the cavity, which is important for continuous wave cavity ring-down spectroscopy used in this work, often mode matching lenses are employed. Therefore, two lenses with a focal length f are positioned between the laser and the cavity such that the curvature of the wavefront of the laser at the first cavity mirror is in accordance with the curvature of the wavefront of the TEM_{00} mode of the cavity. A schematic of a typical beam shaping setup is depicted in figure 4.4, whereas a detailed description for beam shaping can be found in reference [7].

The radius of curvature for a Gaussian beam $r(z)$ propagating along the z-axis can be expressed by the complex beam parameter $q(z)$:

$$\frac{1}{q(z)} = \frac{1}{r(z)} + j\frac{\lambda}{\pi w^2(z)} = \frac{1}{r(z)} + j\frac{1}{z_R}. \tag{4.14}$$

Here, λ is the wavelength of the beam, $w(z)$ is the beam waist, j is the imaginary unit, and z_R is the Rayleigh length (see also equation 4.11). By ray transfer matrices, the
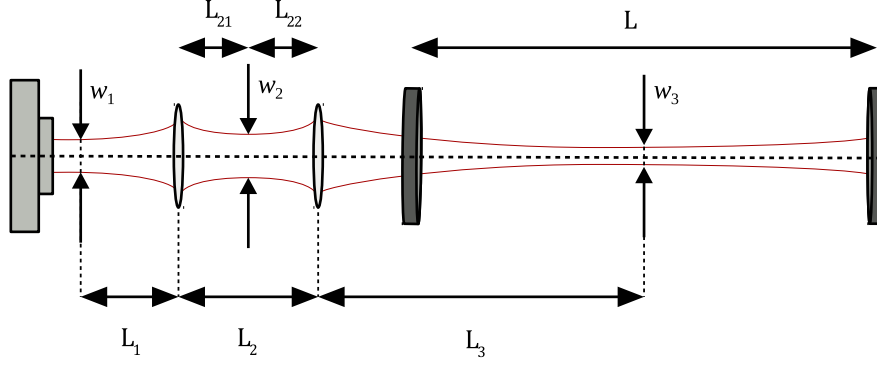
Figure 4.4: Schematic for a typical beam shaping setup with two lenses in order to match a laser beam spatially to the cavity TEM_{00} mode. L_i are the distances between the minimum beam waists w_i and the optical elements.

propagation of a Gaussian beam within an optical setup with several elements including lenses with various focal lengths can be described by:

$$\begin{bmatrix} q'(z) \\ 1 \end{bmatrix} = k\mathbf{M} \begin{bmatrix} q(z) \\ 1 \end{bmatrix}, \tag{4.15}$$

which yields

$$q'(z) = \frac{Aq(z) + B}{Cq(z) + D}, \tag{4.16}$$

by eliminating the normalisation factor k. Here, $q'(z)$ is the beam parameter behind the optical setup, $\mathbf{M} = \begin{pmatrix} A & B \\ C & D \end{pmatrix}$ is the ray transfer matrix with the generalised elements A, B, C, and D, and $q(z)$ is the beam parameter in front of the optical setup. For the mode matching setup as depicted in figure 4.4, the ray transfer matrix equals:

$$\mathbf{M} = \begin{pmatrix} 1 - \frac{L_3}{f} & L_3 + L_{22} - \frac{L_3 L_{22}}{f} \\ -\frac{1}{f} & 1 - \frac{L_{22}}{f} \end{pmatrix} \begin{pmatrix} 1 - \frac{L_{21}}{f} & L_1 + L_{21} - \frac{L_1 L_{21}}{f} \\ -\frac{1}{f} & 1 - \frac{L_1}{f} \end{pmatrix}. \tag{4.17}$$

Here, L_1 is the distance from the minimum beam waist of the laser to the first mode matching lens with focal length f, L_2 is the distance between the two lenses, L_{21} is the distance from the first lens to the minimum beam waist between the lenses, L_{22} is the distance from the minimum beam waist between the two lenses to the second lens, and L_3 is the distance from the second lens to the centre of the cavity with length L, which is at a distance $L/2$ from the first cavity mirror. The radius of curvature is infinite at the minimum beam waist. Hence, the complex beam parameter q at L_1 in front of the first lens becomes:

$$q(z_0) = jz_L. \tag{4.18}$$

Here, z_L is the Rayleigh length of the laser. This is also valid for the radius of curvature in the centre of the cavity at z_c:

$$q(z_c) = jz_C. \tag{4.19}$$

Here, z_C is the Rayleigh length of the cavity. In order to match the wavefront of the laser to the wavefront of the TEM$_{00}$ mode of the cavity, the distances L_1, L_2, and L_3 need to be chosen that the following equation is fulfilled:

$$\begin{bmatrix} jz_L \\ 1 \end{bmatrix} = jz_L = k\mathbf{M} \begin{bmatrix} jz_C \\ 1 \end{bmatrix}. \tag{4.20}$$

By eliminating the normalisation factor k, the two following equations remain:

$$f^2 = \frac{z_L}{z_C} \frac{(f - L_3)^2 + z_C^2}{(f - L_1)^2 + z_L^2} \tag{4.21}$$

and

$$L_2 = 2f + f^2 \left(\frac{f - L_3}{(f - L_3)^2 + z_C^2} - \frac{f - L_1}{(f - L_1)^2 + z_L^2} \right). \tag{4.22}$$

4.1.3 Mode structure of an optical cavity in the time domain

Since the transmitted cavity signal is often observed in the time domain rather than in the frequency domain, a Fourier transform needs to be applied, which yields [6, 7]:

$$I(t) = \mathcal{F} \left(I_0 \frac{\left(\frac{2\pi\delta\nu}{2} \right)^2}{\left(\frac{2\pi\delta\nu}{2} \right)^2 + (2\pi\nu)^2} \right) = I_0 \sqrt{\frac{\pi^3}{2}} \delta\nu e^{-2\pi\delta\nu t}. \tag{4.23}$$

Notably, only the real part for the intensity distribution is considered for frequency limits from 0 to ∞. As the mirror reflectivity is close to 1, the characteristic decay time of the exponential intensity degradation τ_0 can be expressed by:

$$\tau_0 = \frac{1}{2\pi\delta\nu} = \sqrt{R} \frac{L}{c(1-R)} \approx \frac{L}{c(1-R)}. \tag{4.24}$$

This characteristic time depends on the cavity parameters, such as the total length L and the mirror reflectivity R, and the speed of light c in the cavity. Notably, the speed of light in the cavity depends on the dispersion inside the cavity. For an evacuated cavity c is the speed of light in vacuum. However, a change of the refractive index of the medium inside a non-evacuated cavity, i.e. due to changes of the temperature, influences the decay time τ_0.

A more simplified approach to describe the transmitted intensity as a function of time is to consider the time t a light pulse needs for m round trips:

$$t = m\frac{2L}{c} \tag{4.25}$$

The transmitted intensity $I(t)$ after m round trips yields, while using the approximation

$\ln(R) \sim R - 1$:

$$I(t) = T^2 R^{2m} I_0 = T^2 \exp\left(\ln(R)\frac{c}{L}t\right) I_0 = T^2 I_0 \exp\left(-\frac{t}{\tau_0}\right). \tag{4.26}$$

4.1.4 Cavity ring-down spectroscopy (CRDS)

The use of optical cavities for absorption spectroscopy was firstly introduced by O'Keefe et al. in 1988, using a pulsed laser system to detect weak transitions of molecular oxygen [8]. In short, the decay time, also called ring-down time of the transmitted intensity through an optical cavity with absorbing media has been compared to the ring-down time without any absorbing medium. The absorption-related decay of the intensity of an electro-magnetic wave that transmits through a medium with a volume diameter d is given by the Beer-Lambert law:

$$I(d,\nu) = I_0(\nu)e^{(-\alpha(\nu)d)}. \tag{4.27}$$

Here, $\alpha(\nu)$ is the frequency dependent absorption coefficient. According to the Beer-Lambert law and equation 4.26, the transmitted intensity decay with each round trip through a cavity with absorbing species inside can be described by:

$$I(\nu,t) = T^2 I_0(\nu)\exp\left(-t\frac{c}{L}\left[\alpha(\nu)d - \ln(R(\nu))\right]\right) = T^2 I_0(\nu)\exp\left(-\frac{t}{\tau}\right), \tag{4.28}$$

when losses due to absorption are the only loss terms considered. As the mirror reflectivity is close to 1, the ring-down time τ is well approximated by:

$$\tau(\nu) = \frac{L}{c(\alpha(\nu)d + 1 - R(\nu))}. \tag{4.29}$$

By a comparison of the ring-down times for the empty cavity τ_0 and the cavity with absorbing species τ, the absorption coefficient can be evaluated by:

$$\alpha(\nu)\frac{d}{L} = \frac{1}{c\tau(\nu)} - \frac{1}{c\tau_0}. \tag{4.30}$$

An absorption spectrum from which absolute number densities can be determined, is obtained by tuning the laser. To determine absolute number densities, the integrated absorption cross section σ_{int} or the frequency dependent absorption cross section $\sigma(\nu)$ has to be known:

$$\int \alpha(\nu)d \ d\nu = \int N_i\sigma(\nu)dd\nu = N_i\sigma_{int}d. \tag{4.31}$$

Here, N_i is the number density of the lower state of the probed transition. However, for molecules σ_{int} and $\sigma(\nu)$ are barely reported, and only the number density in the lower state N_i can be obtained. Alternatively, the absorption coefficient can be also

expressed by the Einstein coefficient for absorption B_{ik}:

$$\alpha(\nu) = \frac{h\nu_{ik}}{c^2}\left(N_i - \frac{g_i}{g_k}N_k\right)B_{ik}f(\nu). \tag{4.32}$$

Here, ν_{ik} is the frequency of the probed transition, c is the speed of light in vacuum, N_k is the population density in the excited state k, g_i and g_k are the statistical weights for the states i and k, and $f(\nu)$ is the normalised line profile. By assuming a Boltzmann distribution for N_i and N_k, the integrated absorption coefficient can be described by:

$$\int \alpha(\nu)d\,d\nu = N\underbrace{\frac{h\nu_{ik}}{c^2}g_i e^{-\frac{E_i}{k_B T}}\frac{1-e^{-\frac{E_k-E_i}{k_B T}}}{Z(T)}B_{ik}}_{S_{ik}}d = NS_{ik}d. \tag{4.33}$$

Here, N is the total number density of the absorbing species, k_B is the Boltzmann constant, E_i and E_k are the energies of the states i and k, respectively, and $Z(T)$ is the partition function at the gas temperature T. S_{ik} is the line strength, which is a more often reported quantity for molecules and which can be found for example in the HITRAN-database [9]. Notably, from the integrated absorption coefficient σ_{int} in general only densities in the lower state of the probed transition N_i can be obtained, whereas the line strength S_{ik} is correlated to the total number density N. However, for atoms, where the energy gap between ground states and excited states is large, the total number density N can often be approximated by N_i. In contrast to S_{ik}, which depends on the gas temperature due to the Boltzmann distribution assumed, σ_{int} is independent from the gas temperature.

In the 1990's, several weak absorption lines of various molecules including overtone bands of HCN, and unknown Cu_2 and Cu_3 clusters could be determined by cavity ring-down spectroscopy (CRDS) due to its high sensitivity [10, 11]. Moreover, CRDS has successfully been demonstrated for trace gas detection of OH and NH_3, for instance[12]. In order to increase the frequency resolution among other advantages, continuous wave lasers have been employed [13–16]. Therefore, the light coupled to the cavity is extinguished by a fast optical switch, when the laser is in resonance with the fundamental mode of the cavity. Based on CRDS, several modified techniques have been developed, including phase shift CRDS, polarization Fourier transformed CRDS, noise-immune cavity-enhanced optical heterodyne molecular spectroscopy, cavity enhanced absorption spectroscopy (CEAS) and evanescent wave CRDS [17–22]. An overview of CRDS and its applications can be found for instance in references [6, 7, 23]. Cold atmospheric pressure plasmas have been investigated with CRDS by Yalin et al., measuring the N_2^+-ion density in pulsed N_2 plasmas [24], Liu et al. [25], and Benedikt et al. [26], while measuring the OH density in a dielectric barrier discharge, and in a micro-scaled CAPJ, respectively. Zaplotnik et al. reported on the potential of CRDS in particular for the analysis of CAPJs [27]. However, the use of CRDS for CAPJs is not well-established, in particular the small diameter of those plasma jets makes diagnostics challenging.

4.2 Experimental setup for continuous wave cavity ring-down spectroscopy (cw-CRDS) of HO$_2$

The experimental setup for a cavity ring-down spectrometer is presented schematically in figure 4.5. This setup has been adapted from the one, which has been reported previously by Gianella et al. [4]. In order to determine HO$_2$ densities, the first vibrational overtone of the OH-stretch ($2\nu_1$), which is centred at 6649 cm^{-1}, was probed by a beam of a distributed feedback diode laser emitting at 1506.4 nm (6638.2 cm^{-1}). The laser was packed in a fibre-pigtailed butterfly package (NLK1S5GAAA, NTT Electronics), and the current and temperature of the laser were controlled by a Thorlabs LDC200 current driver and a Thorlabs TED200 temperature controller, respectively. The laser beam was directed via an adjustable fibre collimation package (CFC-8X-C, Thorlabs) and two protected silver coated mirrors into the optical cavity. The cavity consisted of two high reflectivity mirrors (Layertec, reflectivity $R = 99.998\%$, radius of curvature $r = 1$ m), which were separated by a distance of $L = 80$ cm yielding a minimum beam diameter of 1 mm in the centre of the cavity. The output mirror was mounted on a hollow cylindrical piezoelectric transducer that enabled a modulation of the cavity length by a few laser wavelengths. The exiting light was then focused with an off-axis parabolic mirror onto an InGaAs photodiode (DET10C, Thorlabs), whose photocurrent was amplified by a transimpedance amplifier (DLPCA-200, FEMTO) and sent to a home-built trigger circuit. A ring-down event was initiated, when the detector signal
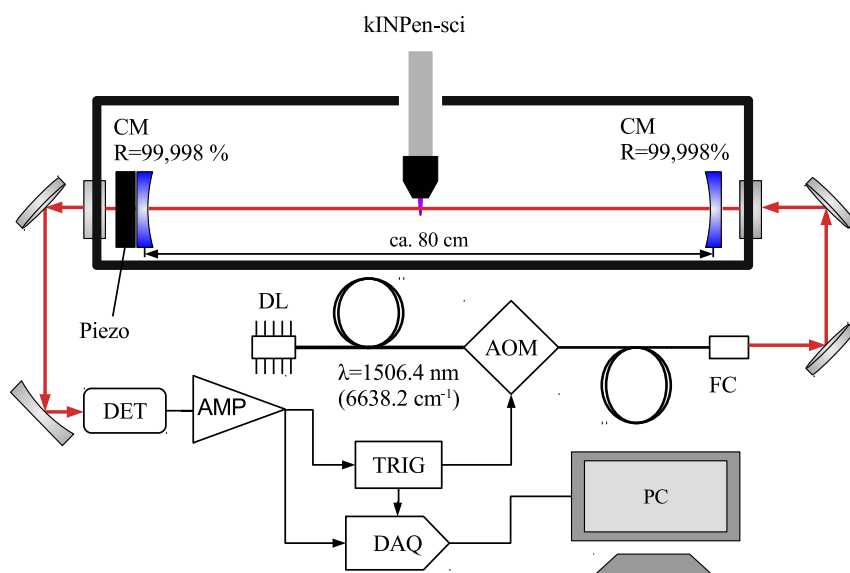

Figure 4.5: Schematic of the cw-CRDS setup for the HO$_2$ detection in the effluent of the CAPJ kINPen-sci. DL: diode laser, AOM: acousto-optic modulator, FC: fibre collimation package, CM: cavity mirror, Piezo: piezo-electric transducer, DET: detector, AMP: amplifier, TRIG: trigger circuit, DAQ: data acquisition module, PC: personal computer.
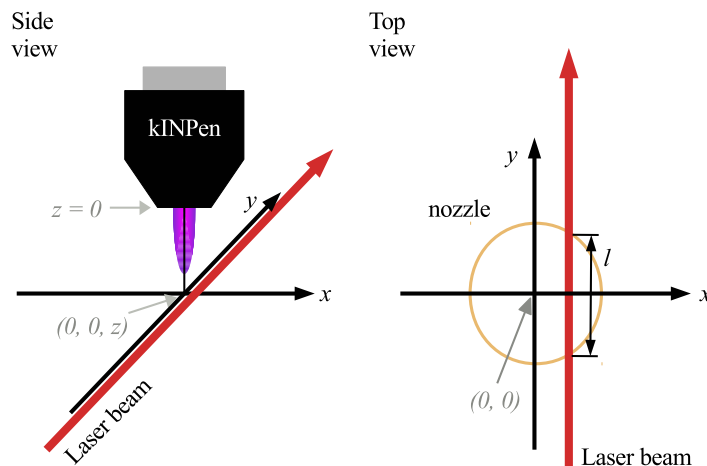
Figure 4.6: Schematic of the coordinate system with the definitions of x, y, z and the effective absorption length l.

reached a preset threshold value that triggered the switch-off of an inline acousto optic modulator (Housego Fibre-Q, Gooch), which was located between the laser and the fiber collimation package. The detector signal was simultaneously fed to a USB data acquisition unit (NIUSB6356, National Instruments), which was controlled by a custom LabVIEW (National Instruments) program running on a standard PC used for further averaging and processing of the data. The laser was tuned by changing the temperature while keeping the current constant, whereby the wavelength was calibrated with a wavemeter.

In order to avoid dust particles crossing the laser beam, the cavity was enclosed by an aluminium box with an acrylic glass lid and quartz windows (volume: 36.8 l), which had openings on the sides to enable gas exchange with the laboratory air. On top of the lid, the kINPen-sci plasma jet was fixed on a micrometer stage to allow movements in all directions relative to the intracavity laser beam. In figure 4.6, a schematic for the coordinate system used is depicted. From previous investigations it is known, that the effluent has a cylindrical shape [28]. In the following, z is defined as the distance from the nozzle outlet to the laser beam along the symmetry axis of the effluent of the plasma jet, while the y-axis is the axis parallel to the propagation direction of the intracavity laser beam, which crosses the effluent of the plasma jet in its centre, and the x-axis is perpendicular to that. The effective absorption length l is given by the intersection at given positions x and z of the absorption cylinder.

The kINPen-sci plasma jet was operated with 3 slm humidified Ar as the feed gas (humidity: 3000 ppm). Therefore, 10% of the Ar flow was guided through a water bubbler held at room temperature. In order to control the effluent's surrounding gas environment, the kINPen-sci was equipped with a gas curtain device maintaining a total oxygen flow rate of 5 slm.

4.3 Determination of spatial density distributions with cw-CRDS

With CRDS, the total cavity loss rate as a function of frequency ν is measured, which is inversely proportional to the ring-down time $\tau(\nu)$. The ring-down time includes all possible loss mechanisms in the cavity, such as light transmission through the cavity mirrors, absorption within the substrate and the dielectric coating of the mirrors, diffraction losses, scattering by the sample (e.g., due to changes in the refractive index and gas turbulences), and optical absorption, in particular, of the molecules to be detected. Over the typical range of a measured spectrum, only the optical absorption is strongly frequency dependent, so the other loss mechanisms can be described by a straight line defined by the constant b_0 and a non-zero gradient $b_1\nu$. The latter accounts for slow changes of the mirror reflectivity due for example to material deposition on the high reflective mirror coatings. The frequency-dependent absorption coefficient $\alpha(\nu)$ is then given by:

$$\alpha(\nu)\frac{d}{L} = \frac{1}{c}\left[\frac{1}{\tau(\nu)} - \frac{1}{\tau_0(\nu)}\right] \tag{4.34}$$

$$= \frac{1}{c}\frac{1}{\tau(\nu)} - [b_0 + b_1\nu]. \tag{4.35}$$

Here, d is the diameter of the volume along the line-of-sight of the laser beam, in which the absorbing species are assumed to be distributed homogeneously , c is the speed of light in vacuum, $\tau(\nu)$ is the measured ring-down time, and $\tau_0(\nu)$ is the ring-down time of a cavity without absorbing species. In addition to the density of HO_2 located in the effluent of the kINPen-sci plasma jet with an absorption length of d_{HO2}, the contribution of water that is assumed to be homogeneously distributed over the complete cavity length L resulting in an absorption length $d_{H_2O} = L$ needs to be considered:

$$\alpha(\nu)\frac{d}{L} = \frac{L}{L}[H_2O]\sigma_{H_2O}(\nu) + \frac{d_{HO2}}{L}[HO_2]\sigma_{HO_2}(\nu) + \epsilon(\nu), \tag{4.36}$$

Here, $[H_2O]$ and $[HO_2]$ denote the molecular densities of H_2O and HO_2, $\sigma_{H_2O}(\nu)$ and $\sigma_{HO_2}(\nu)$ are the corresponding frequency dependent absorption cross sections for H_2O and HO_2, respectively, and $\epsilon(\nu)$ is the residual.

One difficulty when determining the absolute species density is the necessity to use (often unknown) absorption cross sections. Furthermore, the absorption lines are significantly broadened by pressure broadening at atmospheric pressure and have to be described by an area normalized Voigt profile $\mathscr{V}\left(\nu - \nu_0^{(t)}; \gamma_L\right)$. However, the pressure broadening coefficient γ_L for the transition t with the frequency ν_0 is also often unknown. For overlapping transitions, the total absorption cross section $\sigma(\nu; \gamma_L)$ is composed of the superposition of the contributions for all transitions t at frequency ν

$$\sigma(\nu; \gamma_L) = \sum_t S_{ik}^{(t)}\mathscr{V}\left(\nu - \nu_0^{(t)}; \gamma_L\right), \tag{4.37}$$

where $S_{ik}^{(t)}$ is the line strength of transition t.

4.3.1 Spectroscopic parameters for HO$_2$

For HO$_2$, spectroscopic data are relatively rare, as these radicals are difficult to produce with a known quantity. Thiebaud et al. reported transitions of HO$_2$ between 6638.7 cm^{-1} and 6637.6 cm^{-1} measured in 50 torr of helium [29], whereas Gianella et al. have visually determined all the significant transitions in that range [4]. In table 4.1, the considered line positions with the corresponding line strengths and assignments as they have been reported by DeSain et al. in reference [30] are summarised.

Only Ibrahim et al. have reported air-broadening coefficients for 34 HO$_2$ transitions between 6631 cm^{-1} and 6671 cm^{-1} with values ranging from 0.078 to 0.154 cm^{-1}atm^{-1} (half width at half maximum) [31]. For the argon-water-oxygen mixture used in this

Table 4.1: Line positions, line strengths and assignment (as known so far [30]) for the considered HO$_2$ transitions, measured by Thiebaud et al. [29] and determined by Gianella et al. [4].

Transition frequency cm^{-1}	Line strength $\cdot 10^{-21}$cm^{2}cm^{-1}	assignment [30]
6637.47	1.00	$^qP_0(13)$
6637.60	0.99	$^qP_0(13)$
6637.64	1.11	
6637.74	1.67	
6637.78	1.28	$^qQ_3(4)$
6637.83	1.16	$^qQ_3(5)$
6637.85	1.66	
6637.87	1.12	$^qQ_3(6)$
6637.89	0.89	$^qQ_3(7)$
6637.95	0.79	
6637.97	0.87	$^qQ_3(8)$
6638.00	1.04	$^qQ_3(9)$
6638.04	1.04	
6638.12	3.86	$^qP_0(6)$
6638.16	0.67	
6638.21	7.09	$^qQ_3(4-9)$
6638.40	0.65	
6638.44	0.49	
6638.52	0.32	
6638.59	0.92	
6638.70	0.46	
6638.74	3.06	$^qP_1(5)$
6638.76	1.37	$^qP_1(5)$

work, significantly different values should be expected. Gianella et al. have determined the pressure broadening of HO_2 in argon-water-oxygen-nitrogen mixtures to be between 0.040 and 0.072 cm^{-1}atm^{-1} depending on the composition of the curtain gas, using a fitting routine of full spectra, where γ_{HO_2} was assumed to be constant for all considered transitions [3, 4]. In order to determine the absorption cross section of H_2O, Gianella et al. have computed σ_{H_2O} for the combination bands $2\nu_2 + \nu_3$ and $3\nu_2 + \nu_3$ of water for different mixtures of Ar:O_2:N_2 using the tabulated line strengths in the HITRAN database [9] and experimentally determined pressure broadening coefficients [4]. These absorption cross sections were also taken in this work.

4.3.2 Fitting procedure of full spectra

For the determination of the HO_2 density, the absorption coefficient of HO_2 is required. This was achieved by acquiring ring-down data at discrete wavelengths as the laser was tuned from 6637.6 to 6638.7 cm^{-1}. A correct evaluation of the baseline, which corresponds to the cavity losses without absorption features, is crucial for a correct determination of the HO_2 density. Therefore, a fitting procedure of a full spectrum that simulates the absorption features in order to separate absorption and non-absorption losses was applied. A detailed description of this procedure can be found in reference [4].

According to equation 4.35 and equation 4.36, the residuals for the measured absorption coefficient are given by:

$$\epsilon(\nu) = \frac{1}{c}\frac{1}{\tau(\nu)} - [H_2O]\sigma_{H_2O}(\nu) - [HO_2]'\sigma_{HO_2}(\nu) - [b_0 + b_1\nu]. \tag{4.38}$$

Here, $[HO_2]'$ denotes the density for HO_2, which is scaled by:

$$[HO_2]' = \frac{d_{HO_2}}{L}[HO_2]. \tag{4.39}$$

The best fit for the parameters $\beta = (b_0\ b_1\ [H_2O]\ [HO_2]')$ on the experimental data were obtained by minimising the sum of the squared residuals

$$\chi^2 = \sum_0^{N_\nu} \epsilon^2(\nu), \tag{4.40}$$

by fulfilling the conditions

$$\frac{\partial \chi^2}{\partial \beta} = 0. \tag{4.41}$$

Here, N_ν is the number of all spectral points. These conditions can be expressed by a 4×4 system of linear equations of the form

$$\mathbf{M}\beta = \omega, \tag{4.42}$$

where $\mathbf{M}$ is a symmetric 4×4 matrix

$$
\mathbf{M} = \begin{pmatrix}
N_\nu & \sum \nu & \sum \sigma_{H_2O} & \sum \sigma_{HO_2} \\
\sum \nu & \sum \nu^2 & \sum \sigma_{H_2O} \nu & \sum \sigma_{HO_2} \nu \\
\sum \sigma_{H_2O} & \sum \sigma_{H_2O} \nu & \sum \sigma_{H_2O}^2 & \sum \sigma_{H_2O} \sigma_{HO_2} \\
\sum \sigma_{HO_2} & \sum \sigma_{HO_2} \nu & \sum \sigma_{H_2O} \sigma_{HO_2} & \sum \sigma_{HO_2}^2
\end{pmatrix}, \tag{4.43}
$$

and ω is a vector including the measured ring-down times:

$$
\omega = \frac{1}{c} \begin{pmatrix}
\sum \tau^{-1} \\
\sum \tau^{-1} \nu \\
\sum \tau^{-1} \sigma_{H_2O} \\
\sum \tau^{-1} \sigma_{HO_2}
\end{pmatrix}. \tag{4.44}
$$

For each spectrum, the fit vector β was evaluated by using a Matlab script. Therefore, the absorption cross section $\sigma_{H_2O}(\nu)$ for H_2O was taken as reported by [4]. The absorption cross section $\sigma_{HO_2}(\nu)$ for HO_2 was computed for various values for the pressure broadening coefficient γ_{HO_2} for HO_2 by using equation 4.37 and the transitions and line strength summarised in table 4.1 . The values for β and γ_{HO_2} that yielded the lowest χ^2, and $\chi_0^2(\gamma_{HO_2})$, where

$$
\chi_0^2(\gamma_{HO_2}) = \min_{\gamma_{HO_2}} \chi^2, \tag{4.45}
$$

were retained as the best fit values.

For the 95% confidence interval for $[HO_2]'$, several values for χ^2 were determined from a fitting procedure of a constrained fit, where the value for $[HO_2]'$ was varied and γ_{HO_2} was kept constant. The ratio Q of the sum of the squares of the residuals for both, the not constrained fit (χ_0^2) and the constrained fit $(\chi_c^2([HO_2]'))$ was calculated for each chosen value for $[HO_2]'$ by:

$$
Q([HO_2]') = \frac{\chi_c^2([HO_2]') - \chi_0^2}{\chi_0^2}. \tag{4.46}
$$

For values chosen for $[HO_2]'$ within the 95% confidence interval, the likelihood of Q is within the significance interval. As Q is the ratio of variables with a χ^2-distribution with maximum $N_\nu - 4$ degrees of freedom, the cumulative probability function of Q is an F-distribution with 1 and $N_\nu - 4$ degrees of freedom:

$$
F = (N_\nu - 4) \frac{\chi_c^2 - \chi_0^2}{\chi_0^2} \sim F_{1,N_\nu-4} \tag{4.47}
$$

In order to obtain the boundaries for the 95% confidence interval, $[HO_2]'$ was varied until $(N_\nu - 4) Q([HO_2]')$ was larger than the value for an F-distribution with 1 and $N_\nu - 4$ degrees of freedom at 0.95:

$$
(N_\nu - 4) Q([HO_2]') > F_{1,N_\nu-4}(0.95). \tag{4.48}
$$

The 95% confidence interval for γ_{HO_2} was determined by an analogous F-ratio method,
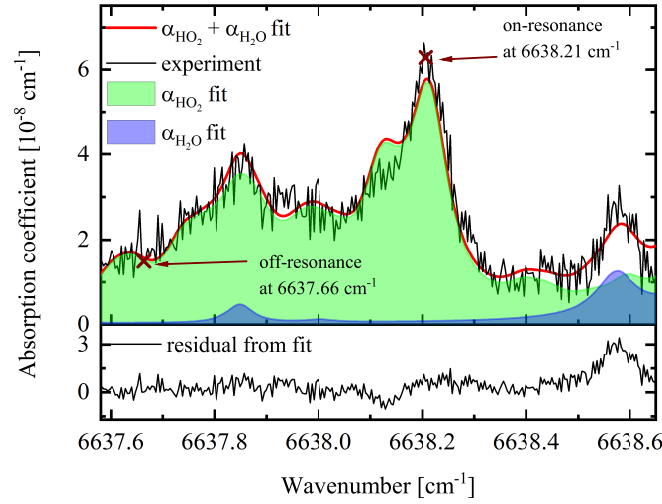
Figure 4.7: Baseline corrected absorption coefficient spectrum for 3 slm Ar with 3000 ppm water in the feed gas and a 5 slm oxygen gas curtain, taken at $x = 0$ mm and $z = 6$ mm (black line) together with the corresponding fit (red line) with the individual contributions of water (blue surface) and HO_2 (green surface). Also given is the residual of the fit.

while the values for γ_{HO_2} were varied and the value for $[HO_2]'$ was kept constant.

An example for the fitting procedure of an absorption spectrum, taken at $x = 0$ mm and $z = 6$ mm, is shown in figure 4.7, together with the fit for the contributions of water and HO_2 and the corresponding residual from the fit. In this case, γ_{HO_2} was determined to be 0.043 ± 0.004 cm^{-1}atm^{-1}.

Figure 4.8: Pressure broadening coefficients γ_{HO_2} for HO_2 obtained from a fitting procedure of absorption spectra in the effluent of the kINPen-sci plasma jet at various distances from the nozzle.
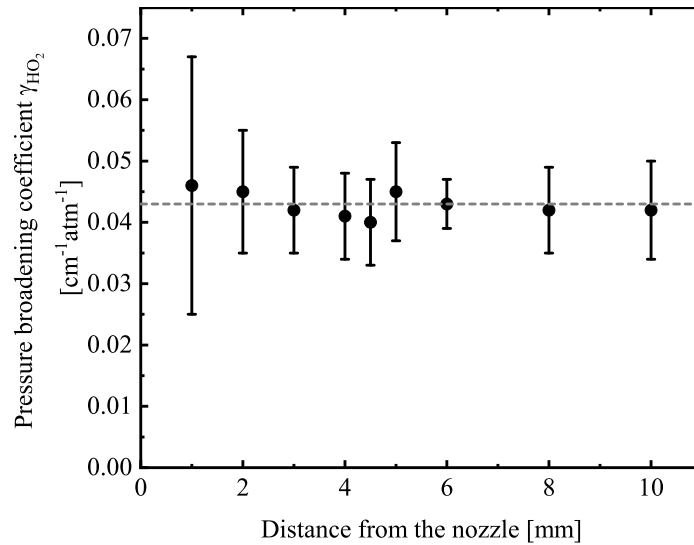
In figure 4.8, pressure broadening coefficients γ_{HO_2} for HO$_2$ obtained from a fitting procedure of absorption spectra in the effluent of the kINPen-sci plasma jet at various distances from the nozzle z are presented. For all measured z-positions, the determined values for γ_{HO_2} agree within the error with 0.043 ± 0.004 cm^{-1}atm^{-1}, which is close to the value Gianella et. al have reported [3, 4]. From gas flow experiments and simulations it is known that the gas flow through the plasma jet is turbulent [32, 33], resulting in an effective mixing of feed and curtain gases. Under these conditions, the assumption to use the same pressure broadening coefficient for all axial and radial positions seems to be valid.

4.3.3 Obtaining radial density distributions

The main drawback of absorption spectroscopy techniques, such as CRDS, is the line-of-sight limitation. In figure 4.9, a schematic for a laser beam transmitting through a cylindrical volume along the line-of-sight is depicted. Since the absorbance $\alpha(\nu)d$ is defined as the absorption losses over the line-of-sight, no spatial information of the density distributions of the absorbing species can be deduced. A common technique to correct for these limitation in the case of axial symmetries is Abel inversion [34], which has also been used for CAPJs as reported for instance in references [28, 35, 36]. Therefore, the absorbance $\alpha(x)d(x)$ is determined at various distances to the symmetry axis x, while scanning through the volume in which the absorbing species
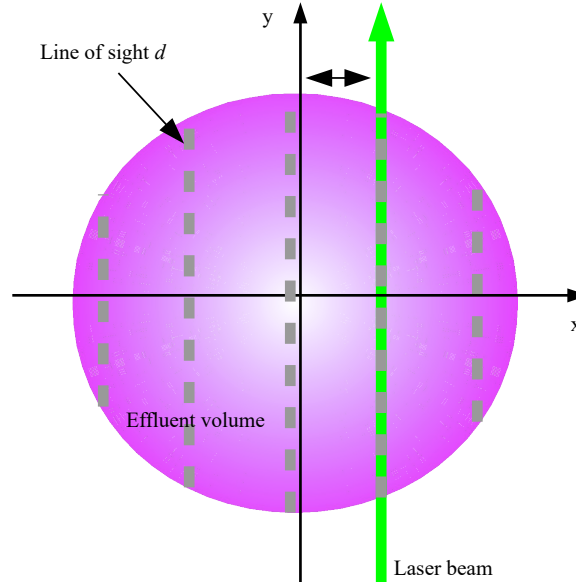

Figure 4.9: Schematic for a laser beam transmitting through a cylindrical volume along the line-of-sight.

are located. By Abel inversion, the measured absorbance $\alpha(x)d(x)$ is converted into cylinder coordinates for the sample under investigation, which yields the absorption coefficient $\alpha(\rho)$ as a function of the radial position ρ:

$$\alpha(\rho) = -\frac{1}{\pi} \int_r^R \frac{d\left(\alpha(x)d(x)\right)}{dx} \frac{dx}{\sqrt{x^2 - r^2}} \qquad (4.49)$$

Here, R is the radius of the cylinder, in which the absorbing species are located. However, as Abel inversion is highly sensitive to noise of the data, the measured data are often fitted by e.g. a Gaussian function, which is then used for computing the integral [34]. Based on $\alpha(\rho)$, the radial density distribution can be then obtained by:

$$n(\rho) = \alpha(\rho)\sigma(\nu). \qquad (4.50)$$

Here, $\sigma(\nu)$ is the frequency dependant absorption cross section.

4.3.4 The on/off-resonance method

To obtain the spatial distribution for HO_2, absorption spectra at various radial and axial positions are required. However, for a full spectrum at a specific radial and axial position, a few hundred data points need to be recorded, whereby each data point was determined by averaging 200 single ring-down events. This procedure takes about one hour per spectrum, and achieving a map of the spatial density distribution of HO_2 becomes time consuming. In this work it is demonstrated that the number of spectral points needed, and thus the acquisition time, can be reduced significantly by employing the on/off-resonance method, that is described in this section.

Instead of taking full spectra at each spatial position of interest, in this work, the ring-down times at only two spectral positions were obtained. For the first spectral position, the on-resonance position, $\nu_{on} = 6638.21$ cm^{-1}, was chosen. At this position, the absorption of HO_2 had the highest absorption cross-section within the tuning range of the laser, while the absorption cross-section of water was several orders of magnitude lower than the cross-section of HO_2. Hence, even at densities of water in the range of 10^{17} cm^{-3} expected for ambient conditions, the contribution of water to the absorption spectrum could be neglected. Unfortunately, there was no spectral position without a contribution of HO_2 within the tuning range of the laser. Therefore, for the off-resonance position, $\nu_{off} = 6637.66$ cm^{-1} was chosen because of the negligible contribution of water and the lower density of HO_2. Since the gradient of the baseline was assumed to be small, the residual for both spectral positions $\epsilon(\nu_{on})$ and $\epsilon(\nu_{off})$ was similar. By computing the difference of the cavity losses at the two chosen spectral positions according to equation 4.36, the difference of the absorption coefficient $\Delta\alpha$ was

determined by:

$$\Delta\alpha := (\alpha(\nu_{on}) - \alpha(\nu_{off})) \frac{d}{L} \tag{4.51}$$

$$= \frac{1}{c\tau(\nu_{on})} - \frac{1}{c\tau(\nu_{off})} \tag{4.52}$$

$$= [HO_2] \frac{d_{HO_2}}{L} (\sigma_{HO_2}(\nu_{on}) - \sigma_{HO_2}(\nu_{off})) \tag{4.53}$$

$$= [HO_2] \frac{d_{HO_2}}{L} \Delta\sigma_{HO_2}. \tag{4.54}$$

Here, $\alpha(\nu_{on})$ and $\alpha(\nu_{off})$ are the absorption coefficients at the spectral positions ν_{on} and ν_{off}, respectively, d is the diameter of the volume in which the absorbing species are located, L is the cavity length, c is the speed of light in vacuum, $\tau(\nu_{on})$ and $\tau(\nu_{off})$ are the measured ring-down times at the two spectral positions ν_{on} and ν_{off}, respectively, $[HO_2]$ is the density of HO$_2$ located in a volume with a diameter of d_{HO_2} along the line-of-sight for the laser beam, and $\sigma_{HO_2}(\nu_{on})$ and $\sigma_{HO_2}(\nu_{off})$ are the frequency dependent absorption cross sections for HO$_2$ at the spectral positions ν_{on} and ν_{off}, respectively. According to equation 4.37, $\Delta\sigma_{HO_2}$ can be obtained from the contributing line strengths and pressure broadening coefficients. With the assumption that the pressure broadening coefficient is the same for all contributing transitions, which was also used in reference [4], and for all axial and radial positions as depicted in figure 4.8, a value of $\Delta\sigma_{\mathrm{H}} = (4.5 \pm 0.4) \cdot 10^{-20}$ cm^2 was obtained for a pressure broadening coefficient of 0.043 ± 0.004 cm^{-1}atm^{-1}.

For each on- and off-resonance wavelength position, 2800 ring-down events were recorded and the mean value and the standard deviation were calculated to determine $\Delta\alpha$, where the uncertainty $\delta\alpha$ of $\Delta\alpha$ corresponds to:

$$\delta\alpha = \sqrt{\delta_{on}^2 + \delta_{off}^2}. \tag{4.55}$$

Here, δ_{on} and δ_{off} denote the standard deviations of $\Delta\alpha$ at the on- and off-resonance position, respectively.

4.3.5 Determination of spatial distributions by the on/off-resonance method

In order to determine the spatial distribution of HO$_2$ in the effluent of the kINPen-sci plasma jet, $\Delta\alpha(x, z)$ was determined for various distances x and z from the optical axis. Therefore, the kINPen-sci was moved along the x-axis (radial scans) and along the z-axis (axial scan), while the ring-down times at the on-resonance and off-resonance were measured. $\Delta\alpha(x, z)$ was computed subsequently by using equation 4.51. By performing an Abel inversion $\mathscr{A}$ on $\Delta\alpha(x, z)$, and applying a coordinate transformation $x \to \tilde{x} = x - x_c$, with $\rho = \sqrt{(x - x_c)^2 + y^2}$ where $(x_c, 0)$ is the centre position, the

absorption coefficient $\Delta\alpha(\rho, z)$ was obtained:

$$\Delta\alpha(\rho, z) = \mathscr{A}\left[\Delta\alpha(x, z)\right] \tag{4.56}$$

$$= -\frac{1}{\pi}\int_\rho^\infty \frac{d\Delta\alpha(\tilde{x}, z)}{d\tilde{x}} \frac{d\tilde{x}}{\sqrt{(x - x_c)^2 - \rho^2}}. \tag{4.57}$$

By assuming a Gaussian distribution for $\Delta\alpha(x, z)$, which can be expressed by:

$$\Delta\alpha(x, z) = \frac{A(z)}{w(z)\sqrt{\frac{\pi}{2}}}\exp\left\{-2\left(\frac{x - x_c}{w(z)}\right)^2\right\} + \Delta\alpha_{off}, \tag{4.58}$$

the Abel inversion can be performed analytically. Here, $A(z)$ is the area of the Gaussian function at position z, $w(z)$ is the width of the Gaussian function at position z, and $\Delta\alpha_{off}$ is an offset-value. The Abel inversion of $\Delta\alpha(x, z)$ yields:

$$\Delta\alpha(\rho, z) = \mathscr{A}\left[\Delta\alpha(x, z)\right] = \frac{2}{\pi}\frac{A(z)}{w^2(z)}\exp\left\{-2\frac{\rho^2}{w^2(z)}\right\} \tag{4.59}$$

By using the on/off-resonance method, the amplitude $A(z)$ is obtained by measuring the axial distribution of $\Delta\alpha(x = 0, z)$ through the centre of the kINPen-sci plasma jet. According to equation 4.58, $\Delta\alpha(x = 0, z)$ can be approximated by:

$$\Delta\alpha(x = 0, z) = \frac{A(z)}{w(z)\sqrt{\frac{\pi}{2}}}\exp\left\{-2\left(\frac{-x_c}{w(z)}\right)^2\right\}, \tag{4.60}$$

if the offset-value $\Delta\alpha_{off}$ is small compared to the measured absorption. The widths $w(z)$ at various z-positions are determined from fits of several radial scans by a Gaussian function as expressed by equation 4.58.

According to equation 4.50 and equation 4.51, the spatial distribution $[HO_2](x, y, z)$ of HO_2 is equal to:

$$[HO_2](x, y, z) = \frac{\Delta\alpha(\rho, z)}{\Delta\sigma_{HO_2}}L. \tag{4.61}$$

Here, $\Delta\sigma_{HO_2}$ is the difference of the frequency dependent absorption cross sections at the on-resonance and the off-resonance position, and L is the cavity length. The spatial density distribution $[HO_2](x, y, z)$ of HO_2 can then be determined by combining equations 4.59, 4.60, and 4.61 to:

$$[HO_2](x, y, z) = \frac{L}{w(z)\sqrt{\frac{\pi}{2}}}\frac{\Delta\alpha(x = 0, z)\exp\left\{-2\frac{\rho^2 - x_c^2}{w^2(z)}\right\}}{\Delta\sigma_\mathrm{H}}. \tag{4.62}$$

By considering the uncertainties $\delta A(z)$ and $\delta w(z)$ of the area and the width, respectively, obtained from the fitting procedure of the experimental radial scans by a Gaus-

sian function, the uncertainty of $\Delta\alpha(\rho, z)$ can be expressed by:

$$\delta\Delta\alpha(\rho, z) = \sqrt{\left(\frac{\Delta\alpha(\rho, z)\delta A(z)}{A(z)}\right)^2 + \left(\frac{4A(z)\exp\left\{-2\rho^2/w^2(z)\right\}\delta w(z)}{\pi w^5(z)}\right)^2}. \qquad (4.63)$$

The corresponding error for $[HO_2](x, y, z)$ was evaluated from the uncertainties of $\Delta\alpha(\rho, z)$, $\delta\Delta\alpha(\rho, z)$, and $\Delta\sigma_{HO_2}$, $\delta\Delta\sigma_{HO_2}$, respectively:

$$\delta[HO_2](x, y, z) = \sqrt{\left(\frac{\delta\Delta\alpha(\rho, z)}{\Delta\sigma_{HO_2}}L\right)^2 + \left(\frac{\Delta\alpha(\rho, z)\delta\Delta\sigma_{HO_2}}{\left(\Delta\sigma_{HO_2}\right)^2}L\right)^2}, \qquad (4.64)$$

with $\delta\Delta\sigma_{HO_2} = 0.4 \cdot 10^{-20}$ cm^2.

4.4 Results

4.4.1 Full spectra vs. on/off-resonance method

In figure 4.10, the cavity loss spectra $\frac{1}{c\tau(\nu)}$ through the centre of the effluent at $x = 0$ mm, and at various axial positions between $z = 1$ mm and $z = 10$ mm are depicted together with a spectrum taken at $z = 8$ mm and $x = 13$ mm. Here, $\tau(\nu)$ is the measured ring-down time at frequency ν and c is the speed of light in vacuum. Each spectral point shows the average loss rate calculated from 200 ring-down events. The strongest HO$_2$ absorption feature was identified at 6638.21 cm^{-1}, whereas contributions of water
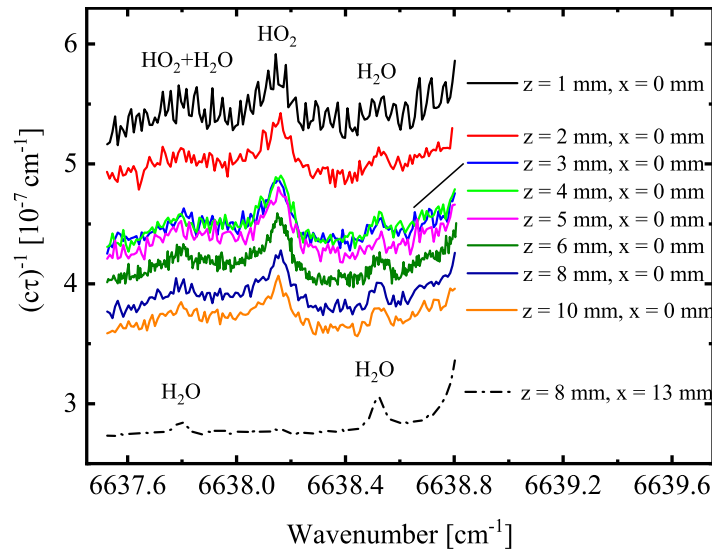

Figure 4.10: The cavity losses $\frac{1}{c\tau}$ as a function of wavenumber for different z-distances (1 to 10 mm at $x = 0$ mm and $z = 8$ mm at $x = 13$ mm).

absorption were found at 6638.57 cm^{-1} and 6637.85 cm^{-1}. Beyond the effluent at $x = 13$ mm, absorption from water transitions was dominant and the absorption by HO$_2$ barely detectable, which indicates a localised distribution of HO$_2$ in the region of the effluent.

In order to identify the cavity losses induced by the turbulent gas flow and the impact of the plasma in general, the region between 6638.33 cm^{-1} and 6638.49 cm^{-1} was investigated, as the absorption of HO$_2$ and of water are low in that region. The mean and the standard deviation of the cavity losses within this region were determined for the different axial positions to compare the non-absorption induced cavity losses and the noise of the signal for various z-positions. At $x = 13$ mm and $z = 8$ mm, the cavity losses without absorption were lower by a factor of 1.4 compared to the spectrum through the centre of the effluent at the same axial position. Additionally, the noise on the spectra decreased by a factor of 2.2 for $x = 13$ mm and $z = 8$ mm compared to $x = 0$ mm and $z = 8$ mm. While measuring through the centre of the effluent, the cavity losses without absorption increased from $3.6 \cdot 10^{-7}$ cm^{-1}, when the jet was located at $z = 10$ mm, to $5.4 \cdot 10^{-7}$ cm^{-1} for $z = 1$ mm. The noise on each spectrum increased proportional to $z^{-0.5}$. This demonstrates, that the plasma interferes with the cavity modes introducing additional fluctuations on the cavity losses due to fast changes in the refractive index and gas turbulences.

In order to consider these gas flow and plasma induced cavity losses, at least two wavelengths need to be observed. With the assumption, that the gas flow and plasma induced cavity losses are independent within the observed spectral region, the absorption induced cavity losses can be separated from the gas flow and plasma induced cavity losses by differentiating the two values. Hence, the contribution of the baseline cancels out, and the absorption induced cavity losses remain. This method is described as the
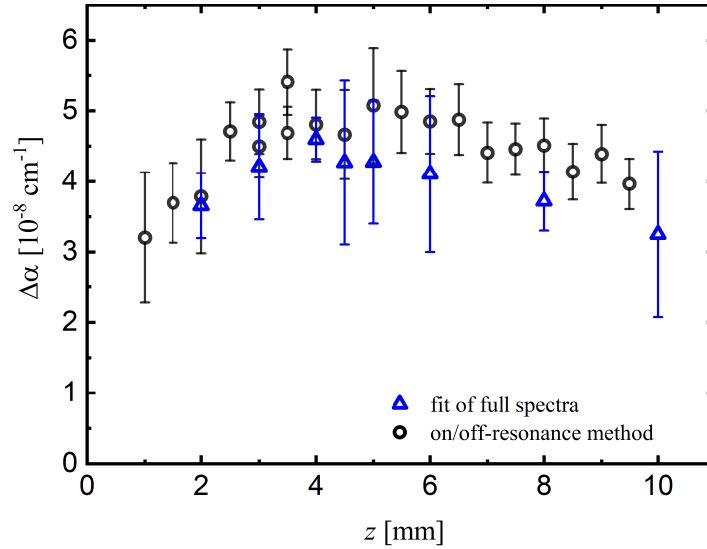

Figure 4.11: $\Delta\alpha$ as a function of z at $x = 0$ mm, obtained from on/off-resonance measurements and from a fit of full spectra.

on/off-resonance method in more detail in section 4.3.4. In figure 4.11, values for $\Delta\alpha$ at $x = 0$ mm derived from the on/off-resonance measurements as a function of z are shown together with values of $\Delta\alpha$ obtained from a fit of full spectra for various z-positions. Within the error, both data sets agree with each other. As the on/off-resonance method gives similar results to the recording of full spectra, it was concluded, that it is sufficient to measure at two wavelength positions, on- and off-resonance, in order to obtain the densities of HO_2. Therefore, the effective absorption length is crucial.

4.4.2 Determination of the effective absorption length for HO₂

In order to determine the effective absorption length as a function of z, the difference in the absorption coefficient $\Delta\alpha$ at various x-positions in steps of $\Delta x = 0.25$ mm was measured over the complete diameter of the effluent. In figures 4.12a to 4.12e the measured values for $\Delta\alpha$ as a function of the distance to the symmetry axis through the effluent centre x at $z = 2, 4, 6, 8$, and 10 mm, respectively, are presented.

All radial scans could be described by a Gaussian function (see equation 4.58), whose width increased with increasing z-distance. At $z = 2$ mm, a width w of 1.73 ± 0.20 mm was obtained, and at $z = 4$ mm, a width of 1.51 ± 0.08 mm was determined. These values are consistent with the diameter of the plasma jet nozzle, which is 1.6 mm. Between $z = 4$ mm and $z = 10$ mm, w increased linearly with

$$w(z \geq 4\text{mm}) = (0.17 \pm 0.02) \cdot (z - 4) + (1.52 \pm 0.16) \text{ mm.} \tag{4.65}$$

In order to determine the HO_2 density in the effluent, the effective absorption length l was defined by

$$l(z) = 2.576 \cdot w(z), \tag{4.66}$$

the distance between the base points of the Gaussian distributions, which represent the limits containing 99% of the area of the Gaussian functions. An effective absorption length l, which was constant at $l = (3.9 \pm 0.5)$ mm between $z = 2$ mm to $z = 4$ mm and which increased linearly to $l = (6.7 \pm 0.1)$ mm from $z = 4$ mm to $z = 10$ mm, was obtained from the measured radial scans. From Schlieren diagnostics, gas flow observations and simulations it is known that within the first 4 mm below the nozzle, the effluent diameter remains constant, which is in agreement with the observations in this work, taking the error into account. Furthermore, the values for l as a function of z are in agreement (within 10%) with those investigations [28, 32]. For all Gaussian fits, a small offset value $\Delta\alpha_{off}$ was determined, indicating an absorption of HO_2 which is distributed beyond the effluent diameter. Using this offset value for equation 4.51 and assuming an absorption length $d_{HO_2} = L = 80$ cm, a mean background density of $n_b = (6.5 \pm 1.5) \cdot 10^{10}$ cm^{-3} was obtained for all radial scans. This background density is about a factor of 2 higher than that obtained previously by Gianella et al. [4].
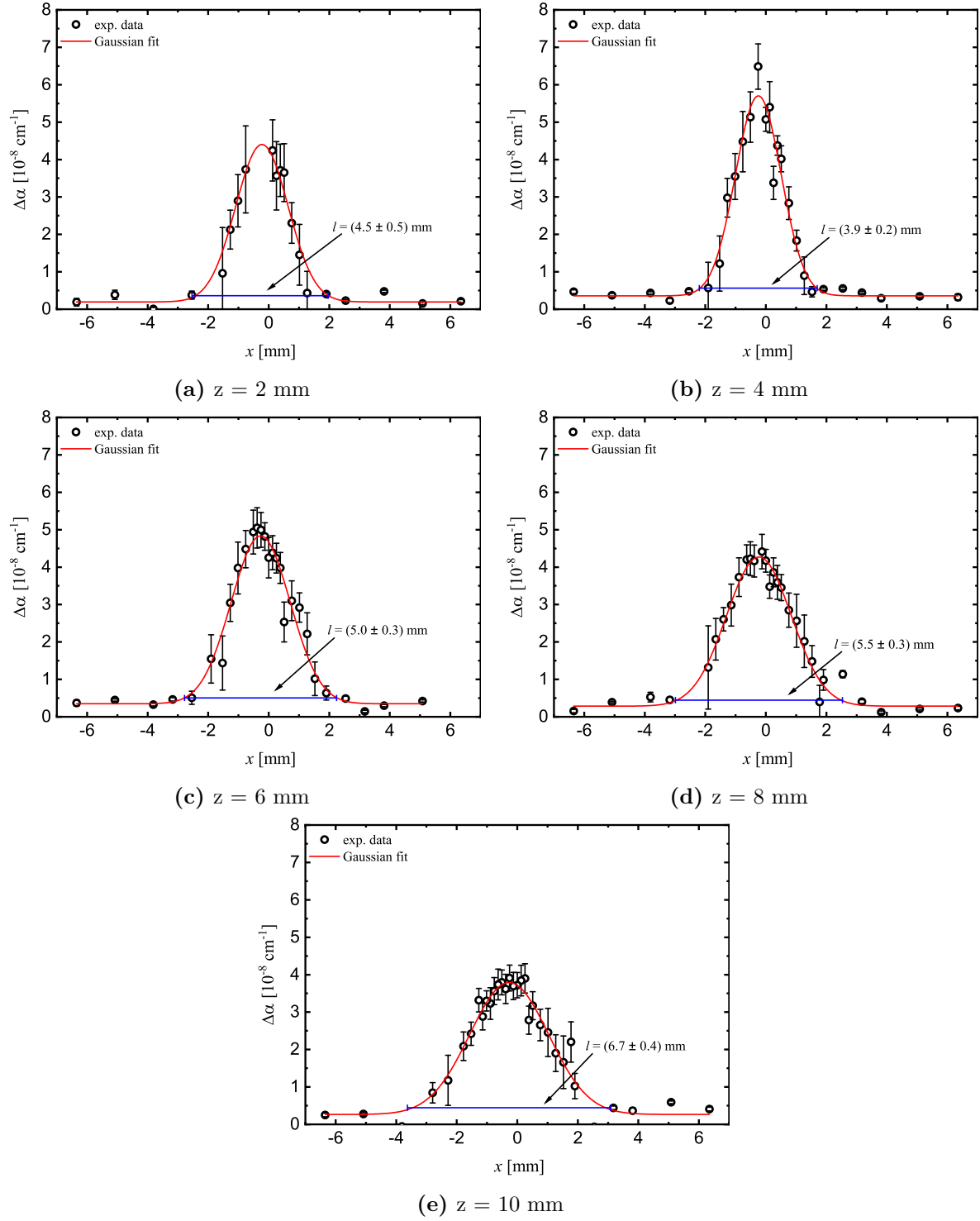
(a) z = 2 mm

(b) z = 4 mm

(c) z = 6 mm

(d) z = 8 mm

(e) z = 10 mm

Figure 4.12: $\Delta\alpha$ as a function x at various z-positions together with Gaussian fits.

4.4.3 Axial distribution of HO$_2$ (line-of-sight average)

In figure 4.13, the densities of HO$_2$ are displayed as a function of z, obtained from the on/off-resonance measurement at $x = 0$ mm and from fits of full spectra at $x = 0$ mm. The absolute number densities were determined by using an effective absorption length $d_{HO_2} = l$ as given in equation 4.66. Notably, with this approach, a line-of-sight averaged density of HO$_2$ over the length l was determined. Within the error, the densities obtained from both methods are in agreement with each other. Between $z = 1$ mm and $z = 4$ mm the density of HO$_2$ increased from $(1.4 \pm 0.4) \cdot 10^{14}$ cm^{-3} to a maximum of about $(2.3 \pm 0.3) \cdot 10^{14}$ cm^{-3}. After this, the density of HO$_2$ decreased linearly with increasing z to $(0.85 \pm 0.12) \cdot 10^{14}$ cm^{-3} at $z = 10$ mm. The density at $z = 10$ mm is about 2 times higher than the density obtained by Gianella et al. corrected for the difference in the enhanced absorption length [4]. This could be due to a higher resolution positioning system used in the current work, and the fact that the current kINPen device is of a different age than that used previously [3, 4].
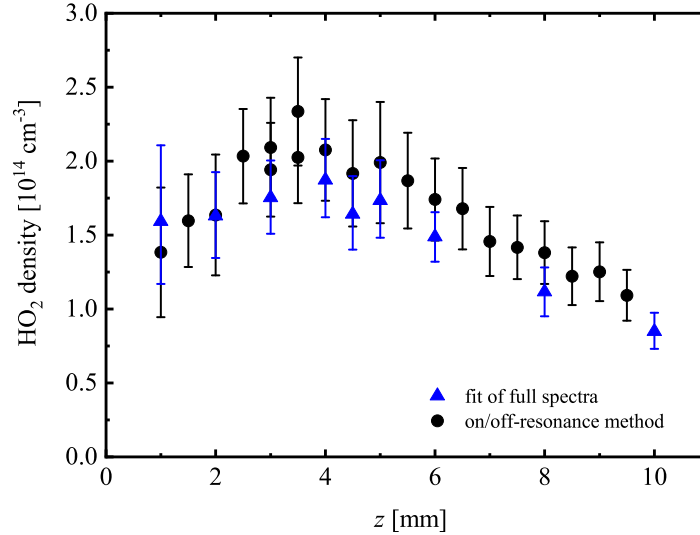

Figure 4.13: Line-of-sight averaged density of HO$_2$ as a function of z at $x = 0$ mm obtained by on/off-resonance measurements and by a fit of full spectra. The number densities were evaluated for $l(z) = 2.576 \cdot w(z)$, where $w(z)$ is the width of the radial distributions at each z-position.

4.4.4 Radial distributions of HO$_2$

To determine a radial density distribution for an axially symmetric sample from a line-of-sight measurement as given by cw-CRDS, the line-of-sight absorption $\alpha(x)d(x)$ is measured at different radial positions x maintaining the z-position and scanning at least half of the sample's diameter. By applying an Abel inversion on the radial scans as depicted in figure 4.12 to correct for the effective absorption length, multiplying the results with the cavity length, and dividing by the absorption cross section, the spatial distribution is obtained (see equation 4.50). In figure 4.14, the density distributions of HO$_2$ as a function of x for $y = 0$ mm and for various z-positions are depicted.

Previously, Gianella et al. investigated the radial distribution of HO$_2$ produced in a CAPJ by sampling the effluent over a pinhole and expanding it to 5.33 kPa. At low pressure, they obtained a doughnut-like shape with the maximum HO$_2$ density at $\rho = 1$ mm and a dip in the centre. According to their findings, they proposed a production of HO$_2$ by the reaction of H atoms, formed by the dissociation of water in the plasma zone and the effluent, and oxygen, which diffused from the surrounding atmosphere into the effluent. They also mentioned that the experimental procedure could be the reason for the observed profile and that further investigations were necessary [4]. In this work, a Gaussian distribution in radial direction was observed that has its maximum at the centre of the effluent. An inter-sectional area of the distribution of HO$_2$ as a function of x and y at $z = 6$ mm is illustrated in figure 4.15 together with a shape of the nozzle outlet, which was shifted by $x_c = 0.23$ mm compared to the maximum of the HO$_2$ density. The shift could be explained by an asymmetry in the filamentary discharge in the plasma zone of the plasma jet, where one direction for the filament is preferred. In this direction, the production of H atoms is larger than in the overall plasma zone leading to a formation of HO$_2$, which has its maximum off the centre.
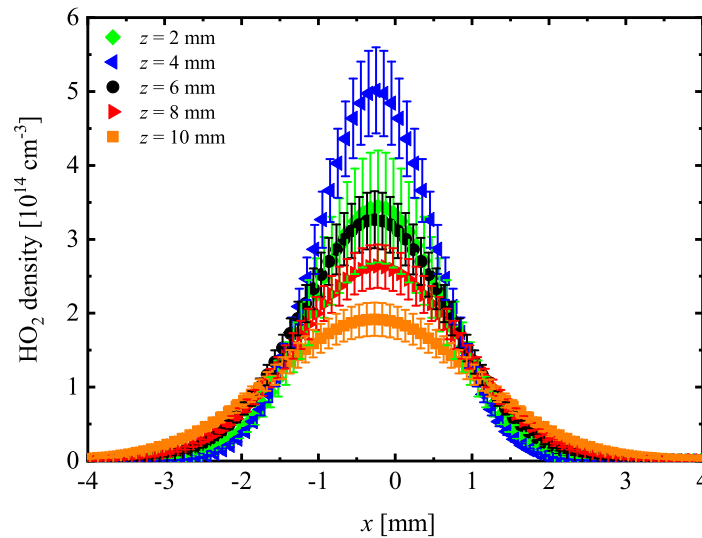

Figure 4.14: Density of HO$_2$ as a function of x for $y = 0$ and $z = 2, 4, 6, 8$, and 10 mm.
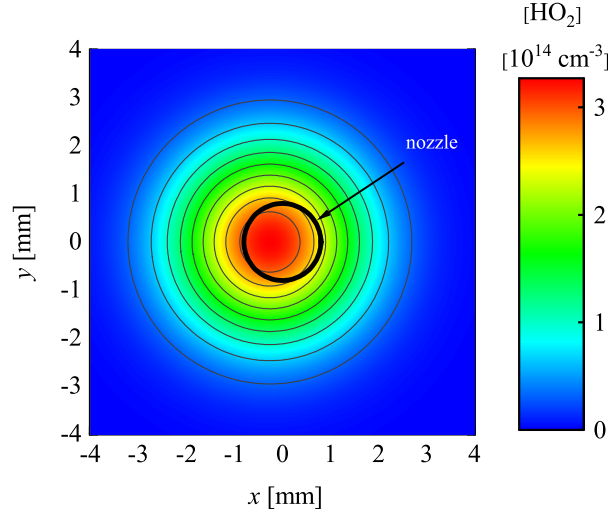
Figure 4.15: Density distribution of HO$_2$ as a function of x and y at $z = 6$ mm together with a shape of the nozzle outlet. The maximum of the distribution is slightly shifted with respect to the centre of the effluent.

4.4.5 Spatial distribution of HO$_2$

Since all radial profiles have a Gaussian shape with increasing width for an increasing z-distance, the spatial distribution of HO$_2$ along the symmetry axis of the effluent can be determined according to equation 4.62 by a combination of an axial scan of the absorption coefficient $\Delta\alpha(x = 0, z)$, which is given in figure 4.11 and by equation 4.58, and by the width $w(z)$ as a function of z as obtained from the radial scans depicted in figure 4.12. An interpolation between the measured values for the effective absorption length was performed to achieve a function for $w(z)$. Furthermore, a third order polynomial fit was used to describe the absorption coefficient $\Delta\alpha(x = 0, z)$ as a function of z.

In figure 4.16, a contourplot of the localised densities for HO$_2$ along the symmetry axis of the kINPen-sci plasma jet is presented. The spatial distribution of HO$_2$ in the effluent at $y = 0$ mm increased starting from $(1.8 \pm 0.6) \cdot 10^{14}$ cm^{-3} at the nozzle outlet to its maximum concentration of $(4.8 \pm 0.6) \cdot 10^{14}$ cm^{-3} at about 4 mm below the nozzle. After that, the density gradually decreases to $(2.0 \pm 0.6) \cdot 10^{14}$ cm^{-3}. Notably, the density of HO$_2$ at $z = 0$ mm would imply an effective diffusion of the gas curtain into the effluent beginning at the nozzle outlet, which is in contrast to the investigations by Dünnbier et al. [37] and by Schmidt-Bleker et al. [38]. Both determined that the effective diffusion of oxygen from the gas curtain starts at about 4 mm below the nozzle. Hence, we concluded that part of the HO$_2$ was already produced in the plasma zone inside the kINPen plasma jet. Therefore, a certain amount of oxygen has to be present within the feed gas. Winter et al. investigated the feed gas humidity in the plasma jet for different kinds of gas tubing, metal and polymeric tubing [39]. The initial water concentration in polymeric tubing was about 1000 ppm, which could be reduced to less than 70 ppm
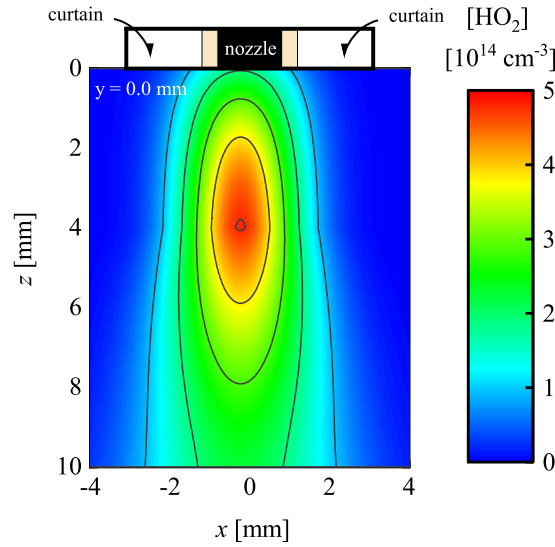
Figure 4.16: Localised density of HO_2 illustrated in a plane cut along the symmetry axis of the plasma jet at $y = 0$ mm.

after 3 h purging. This initial water concentration can be explained by diffusion of water vapour from ambient air into the tubing. As the kINPen-sci, investigated in this work, was built with the same polymeric tubing a feed gas humidity of about 100 ppm after 15 min Ar flow can be expected. If water from the surrounding atmosphere can diffuse into the tubing, it is not unreasonable to assume that O_2 and N_2 can diffuse into the gas tubing and thus into the feed gas as well. Based on the permeability of the tubing for oxygen and nitrogen, we conclude that the amount of diffused oxygen through the gas tubing is insufficient on its own to explain the HO_2 densities measured close to the nozzle.

An additional source of oxygen in the plasma zone can be found by considering the discharge dynamics of the kINPen. From previous investigations of the kINPen it is known that the discharge behaviour is similar to the guided streamer formation that occurs in kHz plasma jets [34, 40]. Schmidt-Bleker et al. observed a backwards directed excitation wave (opposite to the gas flow) in a kINPen operated in helium, which required the presence of oxygen in the curtain gas. The speed of this counter-propagating ionisation wave was 4200 m/s for a pure O_2 curtain [38], which is much higher than the gas flow of about 25 m/s. Reuter et al. also observed a similar feature when operating the kINPen in argon [35]. With this counter-propagating ionisation wave, air can diffuse into the plasma zone resulting in a source of oxygen [41], which would lead to a significant formation of HO_2 at the nozzle outlet. This aspect of the discharge dynamics and its influence on the reaction kinetics deserves further attention in future investigations.

In figure 4.17, a contourplot of the spatial distribution for HO_2 cut along the symmetry axis in a plane at $y = 1.5$ mm is shown. A significant HO_2 density could only be determined starting from $z = 4$ mm. This could either be due to the size of the
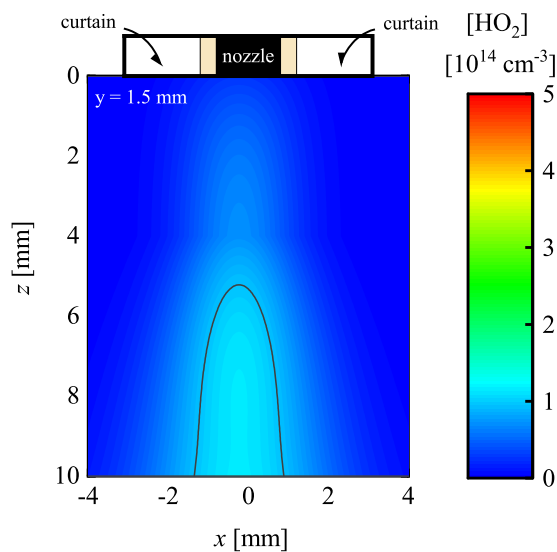
Figure 4.17: Localised density of HO₂ illustrated in a plane cut along the symmetry axis of the plasma jet at $y = 1.5$ mm.

effluent that starts widening at $z = 4$ mm or can be caused by a production of HO₂ by oxygen from the surrounding atmosphere. In the latter case, a significant density of H atoms needs to be present 4 mm below the nozzle at $y = 1.5$ mm. Therefore, further investigations are required. It is clear that a simple plug flow model cannot fully explain the spatial distribution of HO₂. Furthermore, the determined spatial distribution of HO₂ clearly demonstrates that for a reaction kinetics model, the plasma zone needs to be considered as well as the outward diffusion of the effluent gas and the inward diffusion of the surrounding atmosphere.

4.5 Summary

This work has successfully demonstrated that cw-CRDS can deliver spatial information about the density distribution of transient species. Furthermore, it is shown that instead of taking full spectra the on/off-resonance method is a viable technique to determine absolute number densities by measuring the absorption at two spectral positions, which reduces the acquisition time significantly.

A cavity ring-down spectrometer with a continuous wave laser source emitting at 1506.4 nm (6638.2 cm^{-1}) was employed in order to investigate the spatial distribution of HO_2 in the effluent of kINPen-sci plasma jet. By sampling the effluent perpendicular to the laser beam along the x-axis (radial scans), the distance d_{HO_2}, over which HO_2 was distributed, was determined. All measured distributions have a Gaussian shape. An effective absorption length l, which was constant at $l = (3.9 \pm 0.5)$ mm between $z = 2$ mm to $z = 4$ mm and increased linearly to $l = (6.7 \pm 0.1)$ mm from $z = 4$ mm to $z = 10$ mm was obtained. Accordingly, the line-of-sight averaged density distribution of HO_2 was calculated along the symmetry axis.

In order to determine the spatial distribution of HO_2, an Abel inversion was performed on the Gaussian distributions of the radial scans. By a combination of the radial distributions and an axial scan of the absorption coefficient along the z-axis, the localised density of HO_2 along the symmetry axis of the effluent in x and z direction was obtained. The maximum HO_2 concentration of $(4.8 \pm 0.6) \cdot 10^{14}$ cm^{-3} was measured on the symmetry axis through the centre of the nozzle at $z = 4$ mm, which corresponds to a line-of-sight averaged density of $(2.3 \pm 0.3) \cdot 10^{14}$ cm^{-3}.

From the local HO_2 density of $(1.8 \pm 0.6) \cdot 10^{14}$ cm^{-3} at the outlet of the nozzle, it was concluded that a significant density of HO_2 was produced within the plasma zone of the plasma jet. This requires a source of oxygen in the plasma zone, which is most likely due to diffusion of ambient air into the plasma zone caused by counter-propagating ionisation waves and by diffusion into the gas tubings.

For a more detailed analysis of the reaction cycle of HO_2, the spatial distribution of H atoms in the effluent and a 2-dimensional reaction kinetics model that includes reactions in the plasma zone and the effluent, considering also the radial diffusion of the surrounding atmosphere, are required.

4.6 Bibliography

[1] A. Panov. Perhydroxyl Radical (HO$_2$ •) as Inducer of the Isoprostane Lipid Per-oxidation in Mitochondria. *J. Mol. Biol.*, 52(295–305), 2018.

[2] S. Ikawa, K. Kitano, and S. Hamaguchi. Effects of pH on Bacterial Inactivation in Aqueous Solutions due to Low-Temperature Atmospheric Pressure Plasma Application. *Plasma Process. Polym.*, 7(33-42), 2010.

[3] M. Gianella, S. Reuter, A. L. Aguila, G. A. D. Ritchie, and J. H. van Helden. Detection of HO$_2$ in an atmospheric pressure plasma jet using optical feedback cavity-enhanced absorption spectroscopy. *New J. Phys.*, 18(113027), 2016.

[4] M. Gianella, S. Reuter, S. A. Press, A. Schmidt-Bleker, J. H. van Helden, and G. A. D. Ritchie. HO$_2$ reaction kinetics in an atmospheric pressure plasma jet determined by cavity ring-down spectroscopy. *Plasma Sources Sci. Technol.*, 27(095013), 2018.

[5] S.-J. Klose, K. M. Manfred, H. C. Norman, G. A. D. Ritchie, and J. H. van Helden. The spatial distribution of ho$_2$ in an atmospheric pressure plasma jet investigated by cavity ring-down spectroscopy. *Plasma Sources Sci. Technol.*, 29(085011), 2020.

[6] G. Gagliardi and H.-P. Loock, editors. *Cavity-enhanced spectroscopy and sensing.* Springer Series in Optical Science. Berlin: Springer, 2014.

[7] G. Berden and R. Engeln, editors. *Cavity ring-down spectroscopy: Techniques and Applications.* Oxford: Wiley-Blackwell, 2009.

[8] A. O'Keefe and D. A.G. Deacon. Cavity ring-down optical spectrometer for absorption measurements using pulsed laser sources. *Rev. Sci. Instrum.*, 59(12), 1988.

[9] I. E. Gordon, L. S. Rothman, and R. J. Hargreaves. The HITRAN2020 molecular spectroscopic database. *J. Quant. Spectrosc. Radiat. Transf.*, 277(107949), 2022.

[10] A. O'Keefe. Cavity ring down dye laser spectroscopy of jet-cooled metal clusters: Cu$_2$ and Cu$_3$. *Chem. Phys. Letters*, 172(3,4), 1990.

[11] D. Romanini and K. K. Lehmann. Ring-down cavity absorption spectroscopy of the very weak HCN overtone bands with six, seven, and eight stretching quanta. *J. Chem. Phys.*, 99(9), 1993.

[12] R. T. Jongma, M. G. H. Boogaarts, I. Holleman, and G. Meijer. Trace gas detection with cavity ring down spectroscopy. *Rev. Sci. Instrum.*, 66(4), 1995.

[13] P. Zalicki and R. N. Zare. Cavity ring-down spectroscopy for quantitative absorption measurements. *J. Chem. Phys.*, 102(2708), 1995.

[14] D. Romanini, A. A. Kachanov, N. Sadeghi, and F. Stoeckel. CW cavity ring down spectroscopy. *Chem. Phys. Letters*, 264(316-322), 1997.

[15] D. Romanini, A. A. Kachanov, and F. Stoeckel. Diode laser cavity ring down spectroscopy. *Chem. Phys. Letters*, 270(538-545), 1997.

[16] B. A. Paldus and J. S. Jr. Harris. Laser diode cavity ring-down spectroscopy using acousto-optic modulator stabilization. *J. Appl. Phys.*, 7(1), 1997.

[17] R. Engeln, G. van Helden, G. Berden, and G. Meijer. Phase shift cavity ring down absorption spectroscopy. *Chem. Phys. Lett.*, 262(105-109), 1996.

[18] R. Engeln and G. Meijer. A fourier transform cavity ring down spectrometer. *Rev. Sci. Instrum.*, 67(8), 1996.

[19] R. Engeln, G. Berden, E. van den Berg, and G. Meijer. Polarization dependent cavity ring down spectroscopy. *J. Chem. Phys.*, 107(12), 1997.

[20] O. Axner, P. Ehlers, A. Foltynowicz, I. Silander, and J. Wang. *Cavity-Enhanced Spectroscopy and Sensing*, volume 179, chapter NICE-OHMS-Frequency Modulation Cavity-Enhanced Spectroscopy-Principles and Performance. Springer Nature Switzerland AG, 2014.

[21] J. H. van Helden, N. Lang, U. Macherius, H. Zimmermann, and J. Röpcke. Sensitive trace gas detection with cavity enhanced absorption spectroscopy using a continuous wave external-cavity quantum cascade laser. *Appl. Phys. Lett.*, 103(131114), 2013.

[22] A. C. R. Pipino, J. W. Hudgens, and R. E. Huie. Evanescent wave cavity ring-down spectroscopy for probing surface processes. *Chem. Phys. Lett.*, 280(104-112), 1997.

[23] G. Berden, R. Peeters, and G. Meijer. Cavity ring-down spectroscopy: Experimental schemes and applications. *Int. Rev. Phys. Chem.*, 19(4), 2000.

[24] A. P. Yalin, R. N. Zare, C. O. Laux, and C. H. Kruger. Temporally resolved cavity ring-down spectroscopy in a pulsed nitrogen plasma. *Appl. Phys. Lett.*, 81(8), 2002.

[25] Z. W. Liu, X. F. Yang, A. M. Zhu, G. L. Zhao, and Y. Xu. Determination of the oh radical in atmospheric pressure dielectric barrier discharge plasmas using near infrared cavity ring-down spectroscopy. *Eur. Phys. J. D*, 48(365–373), 2008.

[26] J. Benedikt, D. Schröder, S. Schneider, G. Willems, A. Pajdarová, J. Vlček, and V. Schulz-von der Gathen. Absolute OH and O radical densities in effluent of a He/H_2O micro-scaled atmospheric pressure plasma jet. *Plasma Sources Sci. Technol.*, 25(045013), 2016.

[27] R. Zaplotnik, M. Bišćan, N. Krstulović, D. Popović, and S. Milošević. Cavity ring-down spectroscopy for atmospheric pressure plasma jet analysis. *Plasma Sources Sci. Technol.*, 24(054004), 2015.

[28] A. Schmidt-Bleker, S. Reuter, and K.-D. Weltmann. Quantitative schlieren diagnostics for the determination of ambient species density, gas temperature and calorimetric power of cold atmospheric plasma jets. *J. Phys. D: Appl. Phys.*, 48(175202), 2015.

[29] J. Thiebaud, S. Crunaire, and C. Fittschen. Measurements of Line Strengths in the 2ν_1 Band of the HO$_2$ Radical Using Laser Photolysis/Continuous Wave Cavity Ring-Down Spectroscopy (cw-CRDS). *J. Phys. Chem. A*, 111(30), 2007.

[30] J. D. DeSain, A. D. Ho, and C. A. Taatjes. High-resolution diode laser absorption spectroscopy of the O–H stretch overtone band (2,0,0) $\leftarrow$ (0,0,0) of the HO$_2$ radical. *J. Mol. Spectrosc.*, 219(163-169), 2003.

[31] N. Ibrahim, J. Thiebaud, J. Orphala, and C. Fittschen. Air-broadening coefficients of the HO$_2$ radical in the 2ν_1 band measured using cw-CRDS. *J. Mol. Spectrosc.*, 242(64-69), 2007.

[32] S. Iséni, A. Schmidt-Bleker, J. Winter, K.-D. Weltmann, and S. Reuter. Atmospheric pressure streamer follows the turbulent argon air boundary in a MHz argon plasma jet investigated by OH-tracer PLIF spectroscopy. *J. Phys. D: Appl. Phys.*, 47(152001), 2014.

[33] I. L. Semenov and K.-D. Weltmann. Modelling of turbulent reacting flow for a cold atmospheric pressure argon plasma jet. *Plasma Sources Sci. Technol.*, 29(5):055001, 2020.

[34] S. Reuter, J. S. Sousa, G. D. Stancu, and J. H. van Helden. Review on VUV to MIR absorption spectroscopy of atmospheric pressure plasma jets. *Plasma Sources Sci. Technol.*, 24(054001), 2015.

[35] S. Reuter, J. Winter, S. Iseni, S. Peters, A. Schmidt-Bleker, M. Dünnbier, J. Schäfer, R. Foest, and K.-D. Weltmann. Detection of ozone in a MHz argon plasma bullet jet. *Plasma Sources Sci. Technol.*, 21(034015), 2012.

[36] J. Winter, M. Dünnbier, A. Schmidt-Bleker, A. Meshchanov, S. Reuter, and K.-D. Weltmann. Aspects of UV-absorption spectroscopy on ozone in effluents of plasma jets operated in air. *J. Phys. D: Appl. Phys.*, 45(385201), 2012.

[37] M. Dünnbier, A. Schmidt-Bleker, J. Winter, M. Wolfram, R. Hippler, K.-D. Weltmann, and S. Reuter. Ambient air particle transport into the effluent of a cold atmospheric-pressure argon plasma jet investigated by molecular beam mass spectrometry. *J. Phys. D: Appl. Phys.*, 46(435203), 2013.

[38] A. Schmidt-Bleker, S. A. Norberg, J. Winter, E. Johnsen, S. Reuter, K.-D. Weltmann, and M. J. Kushner. Propagation mechanisms of guided streamers in plasma jets: the influence of electronegativity of the surrounding gas. *Plasma Sources Sci. Technol.*, 24(035022), 2015.

[39] J. Winter, K. Wende, K. Masur, S. Iséni, M. Dünnbier, M. U. Hammer, H. Tresp, K.-D. Weltmann, and S. Reuter. Feed gas humidity: a vital parameter affecting a cold atmospheric-pressure plasma jet and plasma-treated human skin cells. *J. Phys. D: Appl. Phys.*, 46(295401), 2013.

[40] R. Bussiahn, E. Kindel, H. Lange, and K.-D. Weltmann. Spatially and temporally resolved measurements of argon metastable atoms in the effluent of a cold atmospheric pressure plasma jet. *J. Phys. D: Appl. Phys.*, 43(165201), 2010.

[41] T. Gerling, R. Brandenburg, C. Wilke, and K.-D. Weltmann. Power measurement for an atmospheric pressure plasma jet at different frequencies: distribution in the core plasma and the effluent. *Eur. Phys. J. Appl. Phys.*, 78(10801), 2017.

5 The spatial distribution of H_2O_2 in the effluent of the kINPen-sci plasma jet
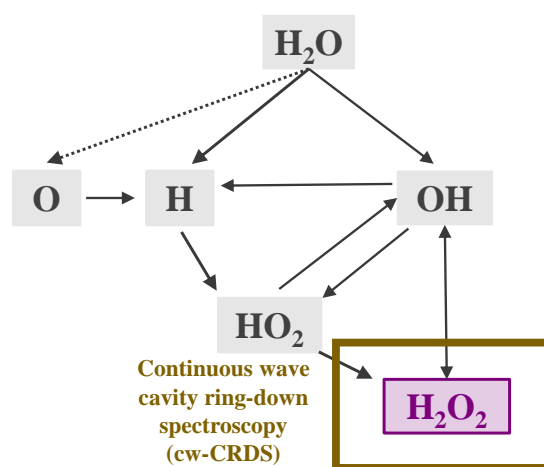
Among the reactive oxygen species that play an important role for biomedical applications is hydrogen peroxide (H_2O_2). H_2O_2 is a signalling agent which is involved in several reactions occurring in cells and leads at high concentration also to cell inhibition [1–4]. H_2O_2 is mainly produced by the reaction of two OH radicals; either in the gas phase or in a liquid. Concerning CAPJs, H_2O_2 was mainly investigated within a liquid [4–9]. Therefore, often test stripes or colorimetric assays have been employed [4, 9]. Only a few investigations of detecting H_2O_2 in the gas phase with absorption spectroscopy methods have been reported [1]. Basically, there are two absorption features for H_2O_2 that have a sufficiently high absorption cross section suitable for absorption spectroscopy: The ν_6-band of the asymmetric OH-bending between 1175 and 1340 cm^{-1} (8.510 - 7.460 µm) with a maximum line strength of approximately $3.9 \cdot 10^{-20}$ cm^{2}cm^{-1} [10–12], and the ν_5-band of the asymmetric OH-stretching at approximately 3600 cm^{-1} (2.778 µm) with a line strength of approximately $1.2 \cdot 10^{-20}$ cm^{2}cm^{-1} [10, 13]. However, in particular with the operation of CAPJs in the open air, the measured absorption is a superposition of absorption features of H_2O_2 that overlap with absorptions of H_2O significantly. Hence, the spectral region to detect H_2O_2 has to be chosen carefully. Winter et al. and Schmidt-Bleker et al. have reported previously the determination of H_2O_2 in the kINPen plasma jet by means of Fourier transform absorption spectroscopy [1, 14]. In these experiments, the effluent was collected into a large box including a

multi pass cell thereby increasing the absorption length to approximately 2 m [1]. Up to now, there is no work published, where H_2O_2 is detected in the effluent of a CAPJ directly.

In this chapter, it is demonstrated that the density of gas phase H_2O_2 can be determined by continuous wave cavity ring-down spectroscopy (cw-CRDS) at a wavelength of approximately 8 μm. Moreover, spatial resolution was obtained by determining the radial distribution for H_2O_2 and applying an Abel inversion subsequently as was discussed for the detection of HO_2 in chapter 4. Firstly, the experimental setup for the determination of H_2O_2 in the effluent of the kINPen-sci plasma jet by means of cw-CRDS is presented. The procedure to calibrate the employed quantum cascade laser spectrally, which provides the option to chose specific spectral positions for the laser, and spatially, which enables a coupling of the laser to the cavity, is described. Furthermore, the data analysis procedure is explained, and the investigations on the sensitivity of the cavity ring-down spectrometer are discussed. After an illustration of the relevant spectroscopic parameters for H_2O_2, the fitting procedure for full spectra and the on/off-resonance method used for the determination of the spatial distribution for H_2O_2 are elucidated. The determined densities for H_2O_2, which were obtained from full spectra, are provided. By performing radial scans, the effective absorption lengths were determined, which are presented together with the axial and radial density distributions. Therefore, an Abel inversion was applied on the radial scans. Based on the radial and axial distributions, the spatial distribution for H_2O_2 in the effluent of the kINPen-sci is presented.

5.1 Experimental setup for continuous wave cavity ring-down spectroscopy (cw-CRDS) of H₂O₂

In figure 5.1, a schematic of the experimental setup for the determination of H_2O_2 is depicted. As a laser source, a quantum cascade laser (QCL) in an HHL-package with horizontal polarisation with respect to the base plate (HHL-223, Alpes Lasers, tuning range: 1224 - 1234 cm^{-1} (8.170 - 8.106 μm)) was employed, which was operated with a low-noise QCL current driver (QCL1000, Wavelength Electronics) and chassis mount temperature controller (PTC5K-CH, Wavelength Electronics). The beam of the QCL was directed through an acousto-optic modulator (AOM)(1208-G80-4, Isomet, frequency: 80 MHz), while the 0th diffraction order was guided by 4 gold coated mirrors and two apertures to a wavelength analyser (Laser Spectrum Analyzer 771 B, Bristol Instruments, 1-12 μm). By applying a voltage to the AOM, the power of the 1st diffraction order increased producing a beam that was guided by two gold coated coupling mirrors to the optical cavity. In order to match the beam shape of the laser to the cavity modes, two mode matching lenses (plano-convex lens with ZnSe substrate, Thorlabs, focal length: 75 mm) were positioned between the first and the second coupling mirror as described in section 5.1.1.1, according to the criteria given in section 4.1.2 . The cavity was composed of two high reflective mirrors (Lohnstar Optics, reflectivity: 99.98%)
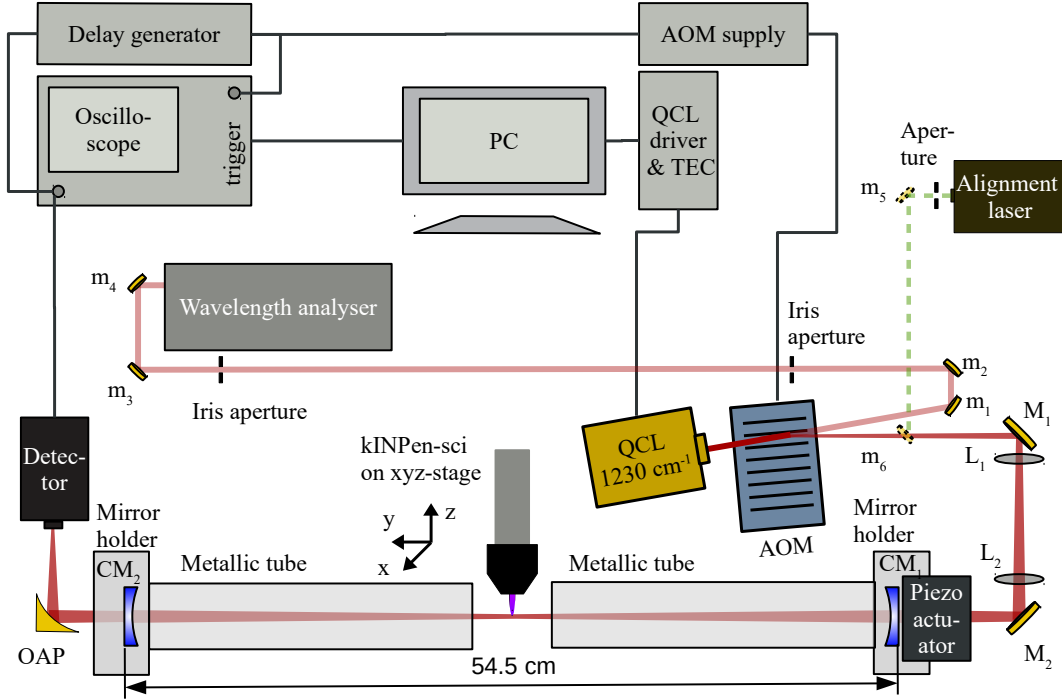
Figure 5.1: Schematic of the experimental setup to determine H_2O_2 densities in the effluent of the kINPen-sci plasma jet. QCL: quantum cascade laser, TEC: temperature control unit, AOM: acousto-optic modulator, OAP: off-axis parabolic mirror, m_i: gold coated mirrors, M_i: gold coated coupling mirrors to the cavity, L_i: beam-shaping lens with focal length of 75 mm, CM_i: cavity mirrors with 99.98% reflectivity.

at a distance of 54.5 cm, while the first cavity mirror was positioned on a piezo-electric ring actuator (RA12-24, Piezosystem Jena, total stroke: 14.8 µm). With a triangular function produced by a frequency generator (AFG 3000 C, Tektronix, frequency: 100 Hz) applied to the piezo-driver, the cavity length was constantly varied by 4 µm in order to increase the coupling efficiency of the laser to the cavity. To protect the cavity from durst particles, two metallic tubes with a diameter of 5 cm and a length of approximately 20 cm each were mounted on the holders of the cavity mirrors. They were purged by 5 slm of N_2 with a gas inlet close to the mirrors to reduce the amount of dust and of water in the beam path. The transmitted laser beam after the cavity was focused by an off-axis parabolic mirror onto a fast detector (PVI-4TE-8-1x1, Vigo systems, 790 MHz high cut-off frequency). With an oscilloscope (Waverunner Xi-A, Teledyne LeCroy, band width: 400 MHz, sample rate: 5 GS/s) the detector signal was recorded. The oscilloscope was triggered, when the detector signal reached a threshold value preset at a delay generator (DG535, Stanford Research Systems) that was also connected to the detector output. After the preset threshold value at the delay gen-

erator was reached, the AOM was switched off in order to initiate the observation of a pure ring-down event. The data from the oscilloscope were transfered to a personal computer (PC) and analysed by a custom LabView program. With the same LabView program, the laser current and temperature were set and measured at the same time by using a Bayonet Neill–Concelman connector board (BNC-board, National instruments) connected to the same PC.

The kINPen-sci plasma jet was operated with 3 slm Ar and a humidity of 3000 ppm in the feed gas. Therefore, 10% of the Ar flow were guided through a bubbler with destilled water at room temperature. A gas curtain composed of 5 slm O$_2$ was applied in order to control the effluent's surrounding atmosphere. The kINPen-sci was mounted on an xyz-stage in the gap between the metallic tubes in the centre of the cavity. For the following, z is defined as the symmetry axis through the centre of the plasma jet, y is denoted as the optical axis through the cavity, and x is the direction perpendicular to y and z while moving the plasma jet through the gap.

5.1.1 Calibration of the quantum cascade laser

In order to optimise the coupling efficiency of the laser to the cavity, and to allow a specific choice of wavelengths emitted by the QCL while maintaining a high laser output, the beam divergence and the tuning characteristics of the QCL were determined.

5.1.1.1 Beam divergence of the QCL

To determine the beam divergence, profiles of the laser beam at various distances to the laser output window were determined by measuring the power of the laser beam with the knife-edge method, which is reported for instance in reference [15]. The knife edge was moved through the beam parallel to the direction of polarisation, in the following denoted as "parallel", and perpendicular to that, in the following denoted as "perpendicular". In figure 5.2, the measured power as a function of the position for the knife edge is depicted at various distances from the laser output for both directions, parallel as a function of z and perpendicular as a function of x.

By calculating the first derivative of the measured power-profiles shown in figure 5.2, the power density at various distances from the laser output window was determined. The beam profiles in parallel and perpendicular direction to the polarisation of the QCL are illustrated in figure 5.3 for various distances from the laser output window. With increasing distance from the laser output window, the centre of the beam profile was shifted by approximately 3 mm at 335 mm compared to the centre of the laser output window. This could be due to a small angle of the lens inside the HHL-package of the QCL that collimates the beam. It was also found that the beam profile, in particular in parallel direction, was not completely Gaussian. Despite this observation, a Gaussian distribution for the power density was assumed for the following analysis.
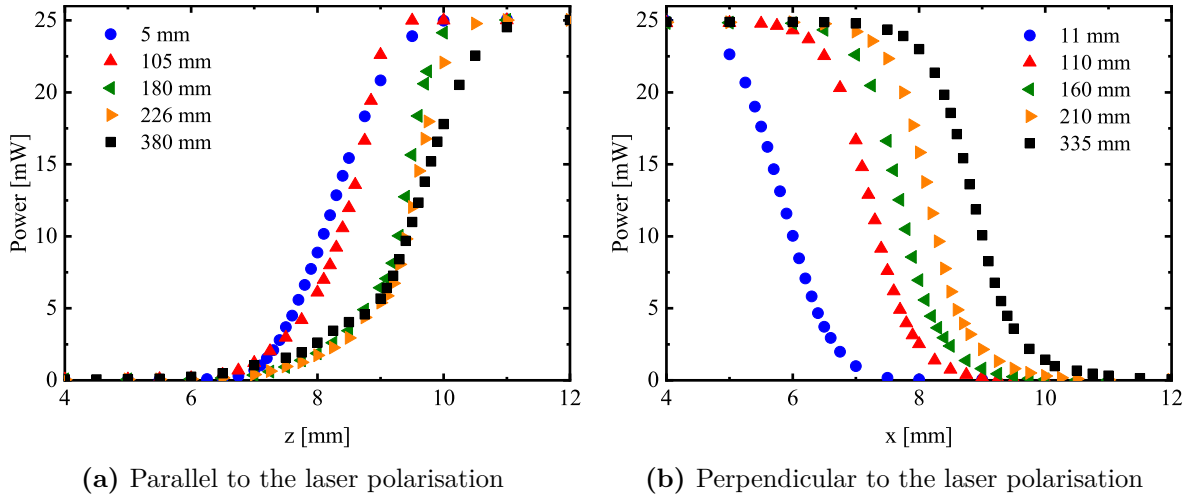
(a) Parallel to the laser polarisation

(b) Perpendicular to the laser polarisation

Figure 5.2: Power of the laser beam determined by the knife-edge method at various distances from the laser output as a function of the position for the knife edge for both directions, (a) parallel to the direction of the polarisation of the QCL as a function of z and(b) perpendicular to the direction of the polarisation of the QCL as a function of x.

In figure 5.4, the full width at half maxima (FWHM) of the Gaussian distributions for the power density as depicted in figure 5.3 in the directions parallel and perpendicular to the polarisation of the QCL are illustrated as a function of the distance from the laser output window. Together with the values for the FWHM, a polynomial fit is shown used to determine the minimum value which is a measure for the minimum beam waist w_0. The minima of 1.1 mm and 0.85 mm were found to be at 227 mm for the direction

(a) Parallel to the laser polarisation

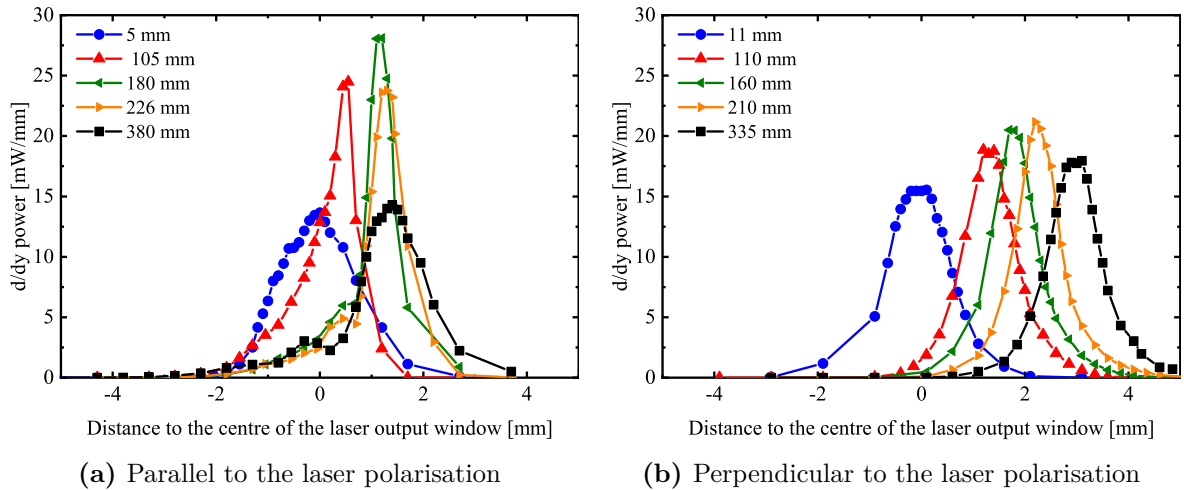**(b)** Perpendicular to the laser polarisation

Figure 5.3: Profiles of the laser beam as a function of the distance to the centre of the laser output window obtained from a derivative of the power determined by the knife-edge method as depicted in figure 5.2 at various distances from the laser output window for both directions, (a) parallel and (b) perpendicular to the polarisation of the QCL.
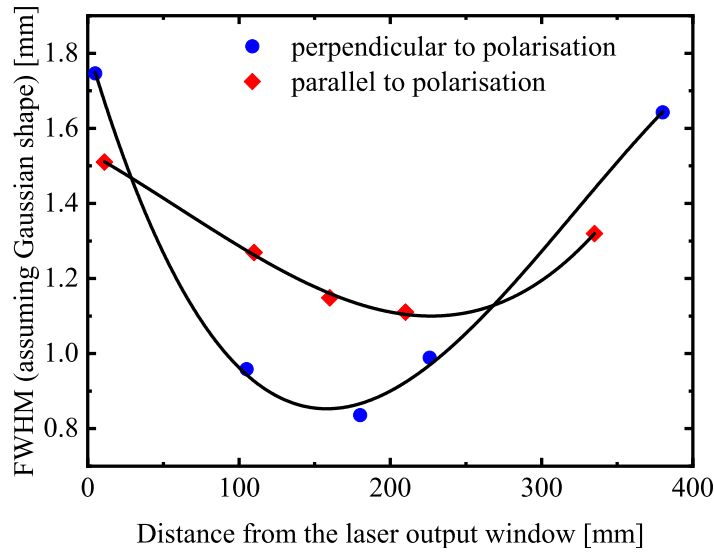
Figure 5.4: Full width at half maxima of the Gaussian distributions for the power density as depicted in figure 5.3 in the directions parallel and perpendicular to the polarisation of the QCL as a function of the distance from the laser output window.

parallel to the laser polarisation, and 154 mm for the direction perpendicular to laser polarisation, respectively. In the end, a mean value of $w_0 = 0.98$ mm at a distance of 190 mm was chosen from these minima to determine the distances for the mode matching lenses L_1 and L_2, which were positioned according to equations 4.21 and 4.22, at 4 cm behind the first coupling mirror M_1 in the case of L_1, and at 5 cm in front of the second coupling mirror M_2 in the case of L_2 as illustrated in figure 5.1.

5.1.1.2 Tuning characteristic of the QCL

The wavelength of the QCL could be varied by tuning both current and temperature. However, the values for current and temperature also determine the laser output power. In order to allow a specific choice of wavelengths emitted by the QCL at an equivalent laser output power, the tuning characteristics of the QCL for current and temperature, both as a function of the laser wavelength and the laser output power were investigated.

Commonly, only the current for the QCL is varied, while keeping the temperature constant. However, in this work, also the temperature had to be varied in order to obtain a constant laser output power. In figure 5.5, the laser output power is depicted as a function of the laser wavelength obtained by the wavelength analyser, while in figure 5.5a the current was varied at a constant temperature of $T = 5°$C, and in figure 5.5b the temperature was varied at a fixed current of $I = 397$ mA. With an increase of the current from 325 mA to 450 mA, the laser wavelength decreased by 1 cm^{-1} from approximately 1231.6 cm^{-1} to approximately 1230.6 cm^{-1} during an increase of the

(a) Current tuning
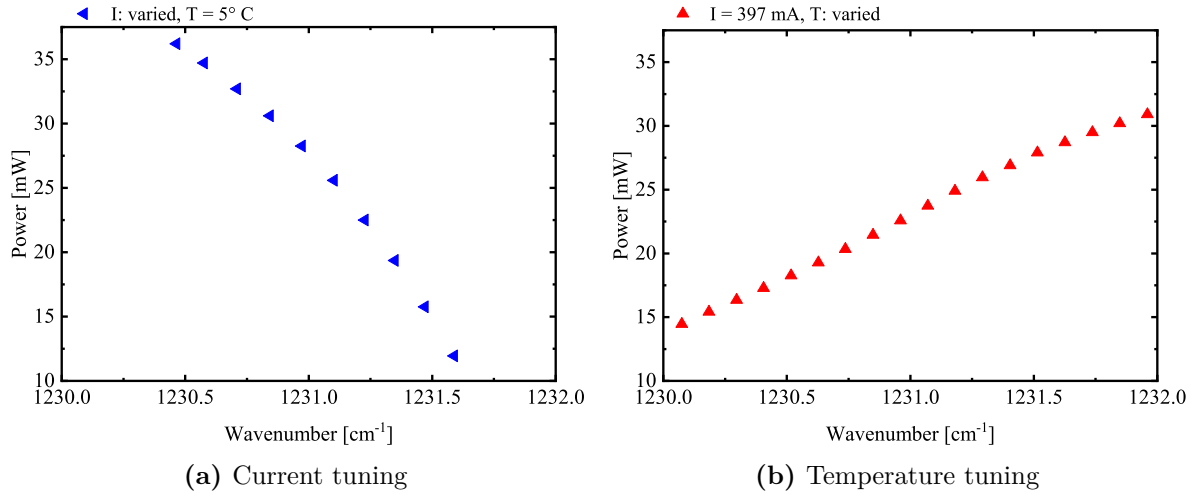

(b) Temperature tuning

Figure 5.5: Laser output power as a function of the laser wavelength obtained by the wavelength analyser, while (a) varying the current at a constant temperature of $T = 5°$C, and (b) varying the temperature at a fixed current of $I = 397$ mA.

power from approximately 11 mW to approximately 36 mW. By keeping the current constant and varying the temperature from 15° C to -10° C, the laser wavelength increased from approximately 1230.1 cm^{-1} to approximately 1231.9 cm^{-1}, while the laser output power increased from approximately 15 mW to approximately 31 mW.

In order to determine a pair of values for the current I and the temperature T that allow a specific choice for the laser wavelength λ and the laser output power P, the laser wavelength and the power were measured both as a function of the current and the temperature, while keeping the other parameter, temperature or current, constant. In figure 5.6a, the laser wavelength is depicted as a function of the temperature, while the current was set to 397 mA. A linear correlation between temperature and laser wavelength was determined to be:

$$\nu(T, I) = -0.111 \cdot T + f(I) \tag{5.1}$$

Here, $f(I)$ denotes a y-intercept related to the current. In figure 5.6b, the laser wavelength obtained at different temperatures is illustrated as a function of the laser current, which was approximated by a linear function as well. Combined with the correlation of laser wavelength and laser current, the laser wavelength was determined to be:

$$\nu(I, T) \approx -0.013 \cdot I - 0.111 \cdot T + 1236.68 \text{cm}^{-1}. \tag{5.2}$$

A linear correlation was also determined for the power and the temperature, while keeping the current constant, which is shown in figure 5.6c together with the experimental data:

$$P(T, I) = -0.94 \cdot T + f(I). \tag{5.3}$$

Here, $f(I)$ denotes a y-intercept related to the current. The laser output power at various temperatures as a function of the laser current is presented in figure 5.6d.
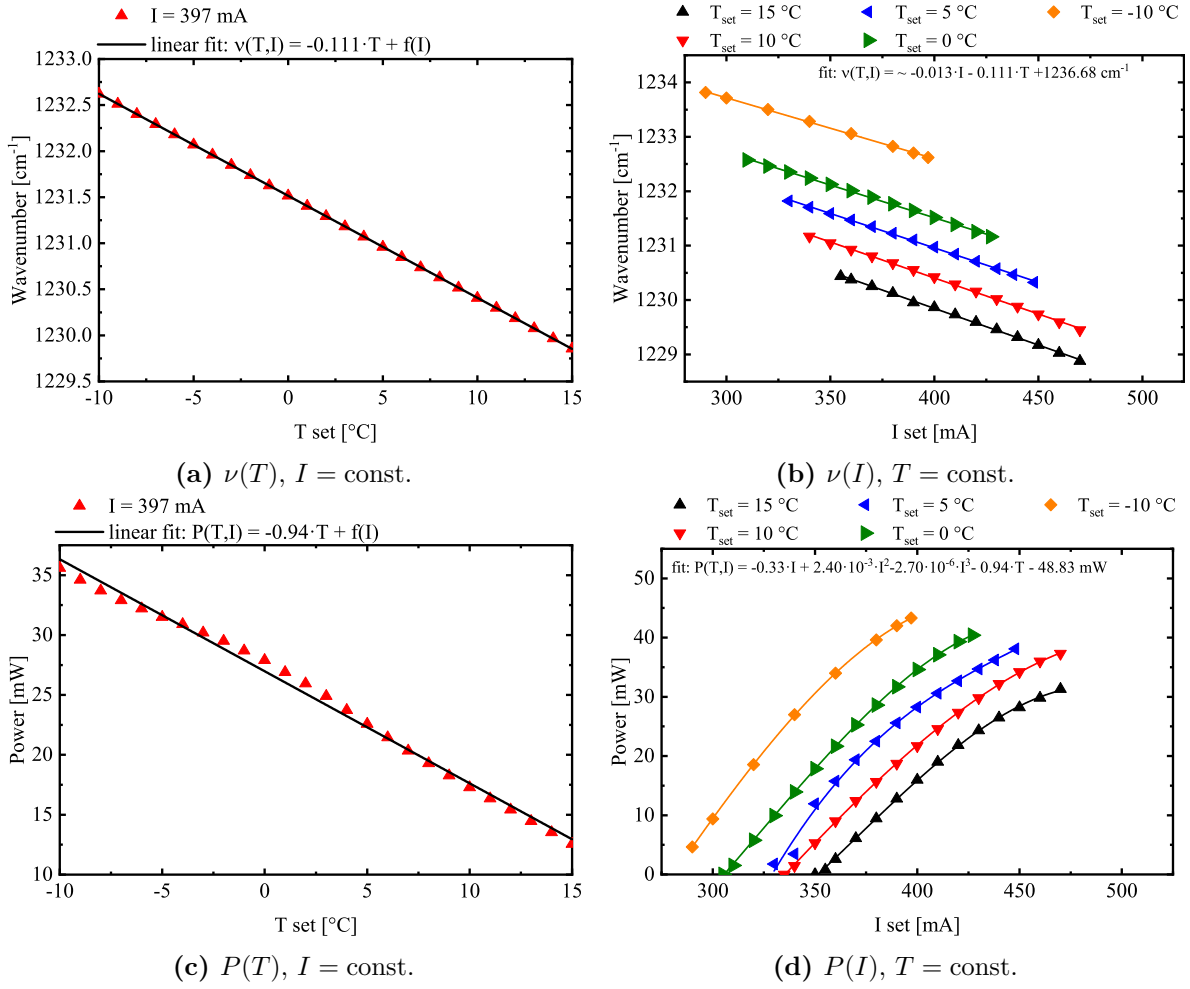
(a) $\nu(T)$, $I = \mathrm{const.}$

(b) $\nu(I)$, $T = \mathrm{const.}$

(c) $P(T)$, $I = \mathrm{const.}$

(d) $P(I)$, $T = \mathrm{const.}$

Figure 5.6: Laser wavelength as a function of (a) the temperature, while the current was set to 397 mA, and (b) the current, while the temperature was set to various values, together with the laser output power as a function of (c) the temperature, while the current was set to 397 mA, and (d) the current, while the temperature was set to various values.

For the current, an increase of the laser output power was determined, which could be approximated by a third order polynomial. Combined with the linear correlation between laser output power and temperature, the power as a function of current and temperature yields:

$$P(I,T) \approx -0.33 \cdot I + 2.4 \cdot 10^{-3} \cdot I^2 - 2.70 \cdot 10^{-6} \cdot I^3 - 0.94 \cdot T + 48.83\mathrm{mW}. \quad (5.4)$$

In order to obtain values for I and T, the equation system consisting of equation 5.2 and equation 5.4 was solved for given values for ν and P by using a LabView program. The determined values for T and I were taken as the input parameters for the QCL. However, the determined values for T and I had to be slightly adjusted, such that the measured wavelength emitted by the QCL was in accordance with the chosen preset value.

5.1.2 Data analysis procedure

The data analysis was performed with a customised LabView program, which was composed of several steps. A schematic of the LabView program is shown in figure 5.7. After starting the QCL-driver control and setting the current and temperature, the oscilloscope parameters including the trigger delay, the sample rate, and the sample length, have been set. In order to determine the ring-down time, the natural logarithm of the detector signal was plotted as a function of time. In figures 5.8a and 5.8b, examples of the transmitted intensity through the cavity, also denoted as transients, are depicted as a function of time, for when the kINPen-sci plasma jet was switched off and for the case the kINPen-sci plasma jet was switched on, respectively. A stronger decay was observed, when the kINPen-sci plasma jet was switched on due to the presence of absorbing species. Logarithmic plots of these transients are illustrated in figure 5.8c and in figure 5.8d, respectively, together with a linear fit from which the ring-down times have been determined. In order to assure a correct evaluation of the ring-down time, limits were chosen for the region, in which the ring-down time was calculated from the slope of the logarithmic plot: The left limit close to the beginning of the exponential decay, and the right limit at a distance of approximately 2τ after the starting point.
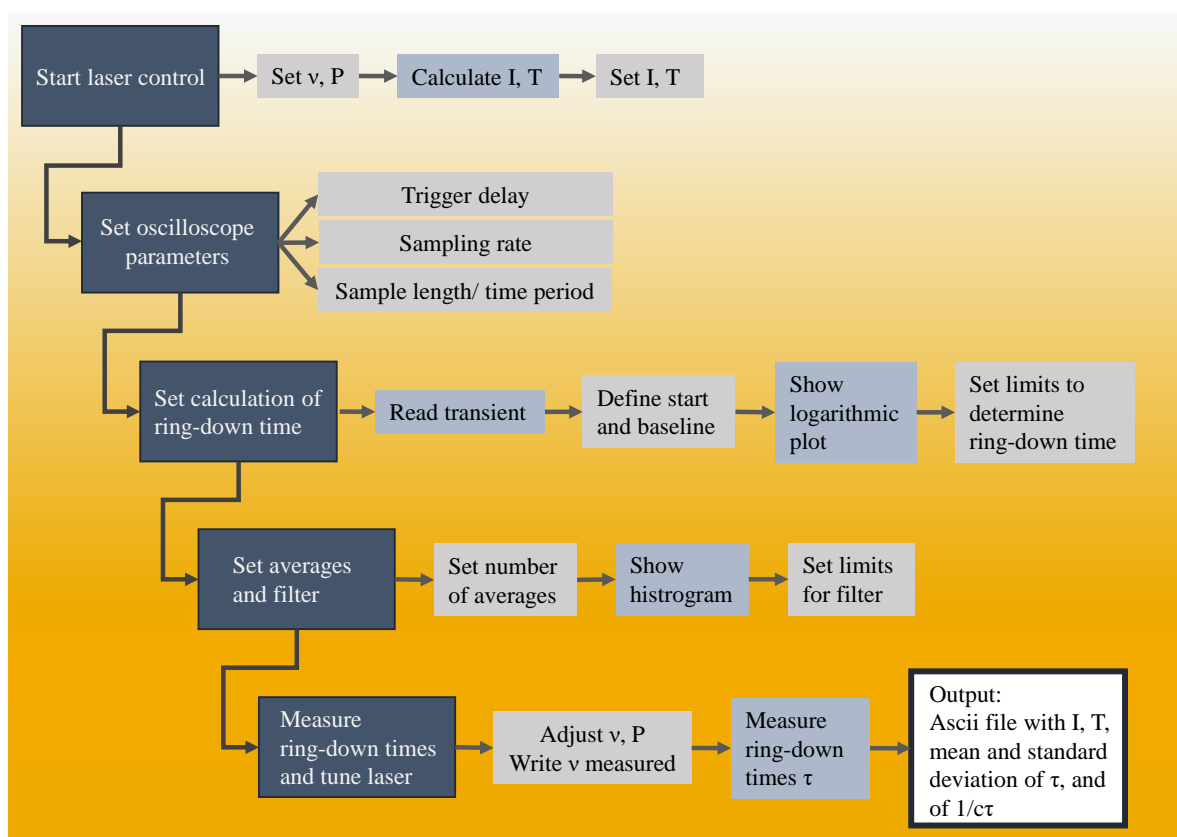

Figure 5.7: Schematic of the customised LabView program to obtain absorption coefficients.

(a) Plasma off

(b) Plasma on

(c) Plasma off
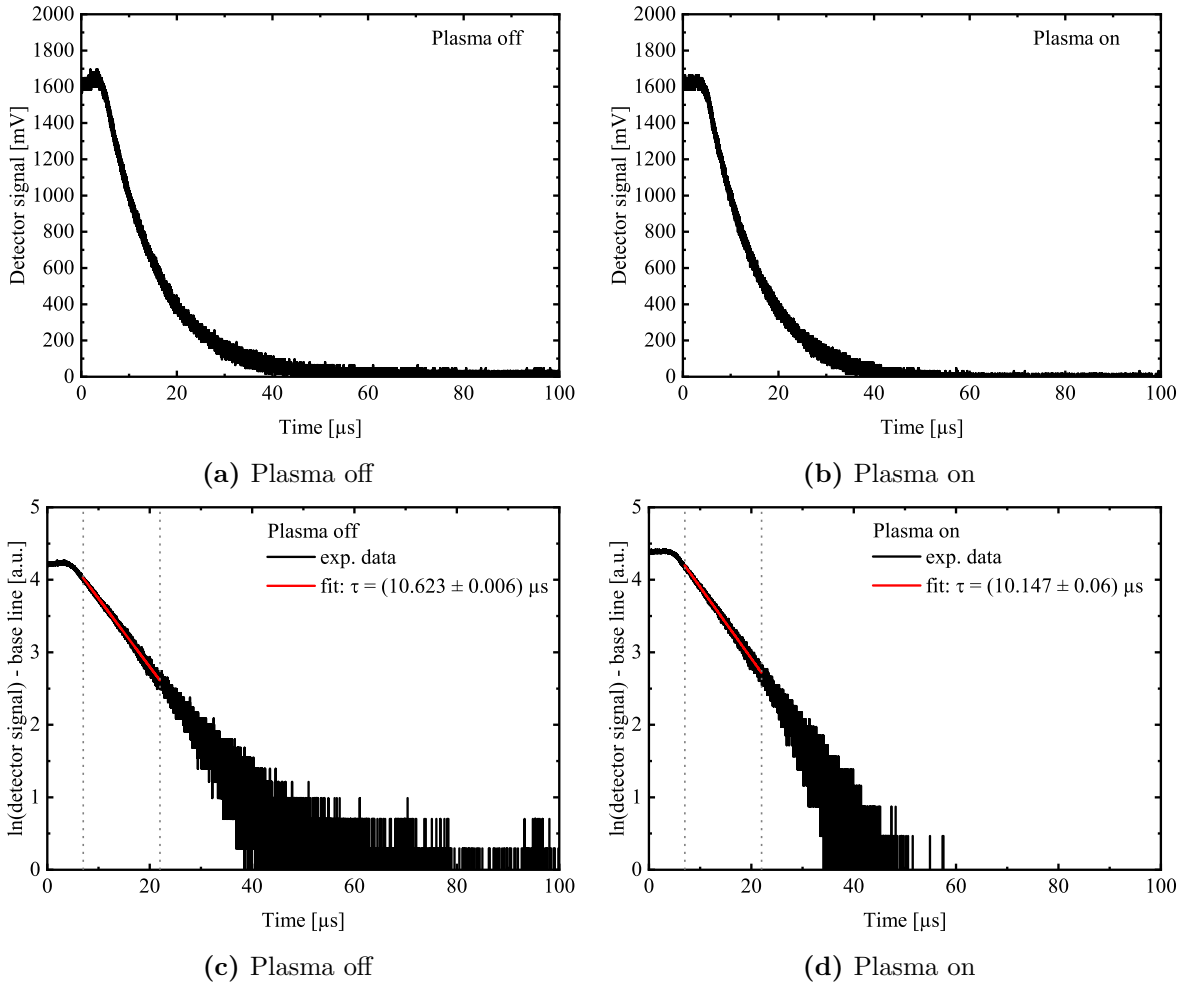
(d) Plasma on

Figure 5.8: Examples of the transmitted intensity through the cavity as a function of time with a linear scale, while (a) the kINPen-sci plasma jet was switched off, (b) the kINPen-sci plasma jet was switched on, and with a logarithmic scale, while (c) the kINPen-sci plasma jet was switched off, and the kINPen-sci plasma jet was switched on.

In order to exclude transients with a much lower ring-down time, resulting for instance from dust particles in the laser beam, or with a much higher ring-down time due to errors in the fit of the decay, an additional filter has been applied. At least 100 transients were recorded and displayed in a histogram. For a robust coupling of the laser to the cavity, the distribution of the ring-down times is Gaussian. In figure 5.9a and in figure 5.9b, two examples of histograms for the distribution of 300 ring-down times are depicted together with a Gaussian function for the two cases, plasma off and plasma on, respectively. With the plasma jet switched on, the mean value of the recorded ring-down times decreased by approximately 500 ns compared to the case, when the plasma jet was switched off; the standard deviation σ of the Gaussian distributions increased by a factor of 1.5 from 260 ns in the case of plasma off to 400 ns in the case of plasma on. The applied filter was set to $1.96 \cdot \sigma$. With these limits, which correspond to 95%
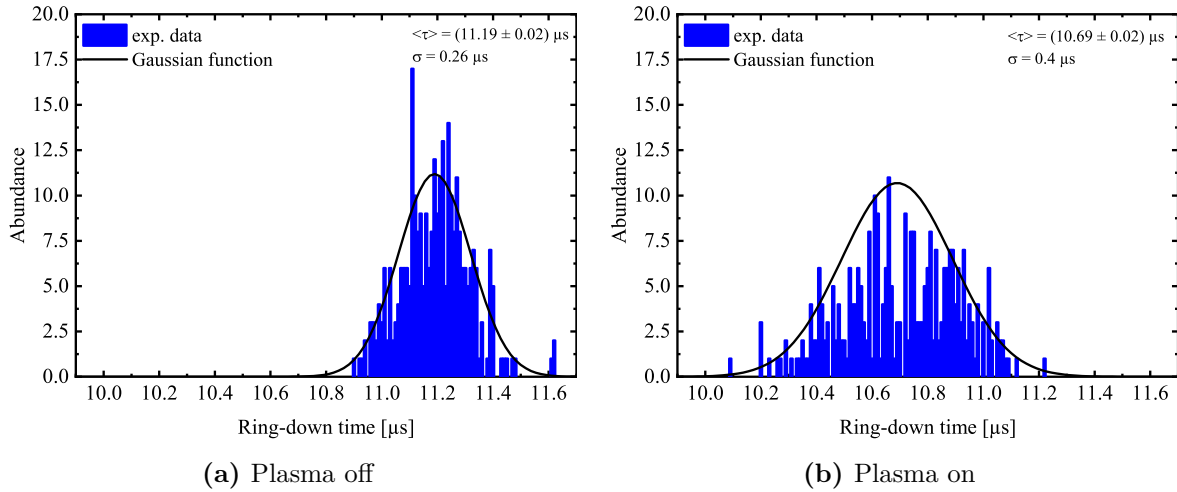
(a) Plasma off   **(b)** Plasma on

Figure 5.9: Histograms showing the distribution of the ring-down times for 300 transients in the case of (a) the kINPen-sci plasma jet was switched off and b) the kINPen-sci plasma jet was switched on, together with a Gaussian function.

of the Gaussian distribution, outliers far from the mean value could be excluded. For the subsequent analysis, the mean value of the ring-down times within the 95%-limit, and the corresponding deviation of the mean have been determined.

5.1.3 Sensitivity of the cavity ring-down spectrometer

In order to determine the stability of the cavity ring-down spectrometer, which defines an appropriate number of averages to be taken for the analysis of the ring-down times, a series of 3600 ring-down times was recorded. Based on these data, an Allan deviation analysis was performed. The Allan deviation is a measure for the number of averages that improve the signal to noise ratio. Firstly introduced in 1966 by Allan to determine the stability of atomic clocks [16], the Allan deviation became a valid method to determine the type of noise [17] and to determine the theoretical detection limit for absorption coefficients obtained by optical cavities [18–21]. In the case of an Allan deviation, firstly, the mean $\overline{y}_i$ of subsequent measurements y_k with increasing number of samples i is calculated:

$$\overline{y}_i = \frac{1}{i} \sum_{k=1}^{i} y_k.$$ (5.5)

The Allan deviation $ADEV$ is then defined as:

$$ADEV = \sqrt{\frac{1}{2} \left(\overline{y}_{i+1} - \overline{y}_i \right)^2}.$$ (5.6)

In figure 5.10a and in figure 5.10b, two example plots for the Allan deviation of the cavity losses $\frac{1}{c\tau}$ are depicted as a function of the time that was needed to measure the included number of samples, for the cases where the kINPen-sci plasma jet was
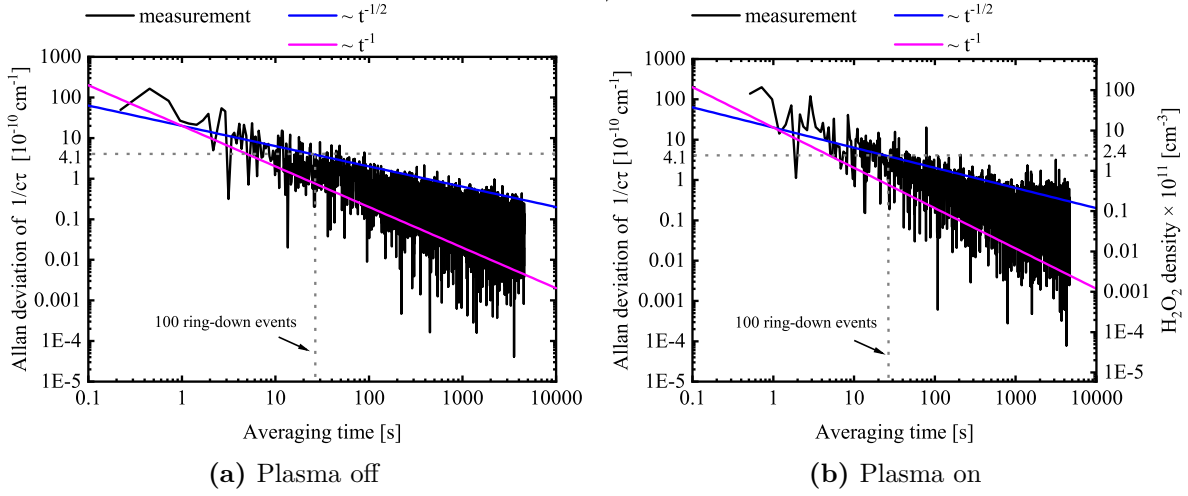
Figure 5.10: Allan deviation of a series of recorded ring-down events together with two fits, which are proportional to $\frac{1}{\sqrt{t}}$ and $\frac{1}{t}$, respectively, in the case of a) plasma off and b) plasma on.

switched off and on, respectively. The time also includes the computation time for the data transfer and analysis to determine the ring-down times. In contrast to common Allan deviation plots as reported for example in reference [20], the Allan deviation was varying by orders of magnitudes from data point to data point resulting in a broad band with an upper and a lower limit. In both cases, plasma off and plasma on, the upper limit for the Allan deviation decreased inversely proportional to the square root of the averaging time. According to Barnes et al., this corresponds to uncorrelated "white" frequency noise [22]. The lower limit decreased inversely proportional to the averaging time, which corresponds, according to Barnes et al., to uncorrelated "white" phase modulations [22].

Based on 100 ring-down events, an Allan deviation of $4.1 \cdot 10^{-10}$ cm^{-1} was determined for an averaging time of 27 s in both cases, plasma off and plasma on. Compared to the Allan deviation of the cavity used for the HO_2 measurements [20], the cavity used in this work for the determination of H_2O_2 is more noisy by approximately a factor of 10. This could be due to the fact, that the cavity used for the determination of the H_2O_2 density was operated in open air and purged with N_2. The gas flow of the purge gas was along the direction of the laser beam, and perpendicular to the gas flow through the kINPen-sci plasma jet, which could induce additional turbulences to the turbulent gas flow through the kINPen-sci plasma jet and thus lead to fluctuations of the refractive index in the cavity. Notably, in the case of plasma on, the broad band of the Allan deviation as depicted in figure 5.10b started to bend resulting in a distribution parallel to the time axis. This indicates that the cavity became unstable for averaging times larger than 1000 s, which is equivalent of averaging more than 1500 samples. However, the values for the Allan deviation of 100 ring-down events were the same for both cases, plasma off and plasma on. This indicates that the influence of the plasma on the cavity stability is smaller than the fluctuations induced by the gas flow. A more

detailed analysis of the influence of the plasma on the stability of the cavity remains for future investigations. By taking an absorption coefficient of $2.3 \cdot 10^{-19}$ cm^2 for H_2O_2 into account, the detection limit due to the cavity stability is $2.4 \cdot 10^{11}$ cm^{-3}, when 100 ring-down events are averaged, which were used for the following analysis.

5.2 Determination of absolute number densities for H_2O_2

Line positions and line strength for transitions belonging to H_2O_2 together with calculated pressure broadening coefficients in air can be found for example in the HITRAN database [23]. The most prominent absorption features around a wavelength of 8 µm result from transitions in the ν_6 band centred at around 1270 cm^{-1}, the asymmetric bending of the OH groups in H_2O_2 [10–12, 23]. An overview of the transitions from the ν_6 band with their absorption cross section $\sigma(\nu)$, which was calculated according to equation 4.37, is shown in figure 5.11 together with the absorption cross sections calculated for H_2O, CH_4, N_2O, HNO_3, with line positions, line strengths and pressure broadening coefficients taken from the HITRAN database [23] and with the absorption cross sections for HONO and N_2O_5 taken from references [24, 25], and [26], respectively. The strongest absorption features for H_2O_2 can be measured at approximately 1250 cm^{-1}. However, also broadband absorptions of HONO and of N_2O_5 molecules, and absorptions lines from H_2O, CH_4, and N_2O overlap with the H_2O_2 lines in this
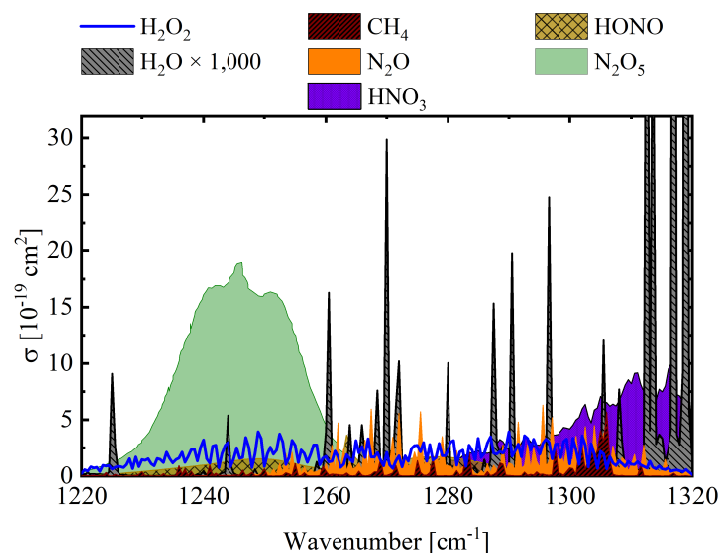

Figure 5.11: Absorption cross sections for H_2O_2, H_2O, CH_4, N_2O, and HNO_3 at 1013 hPa, calculated according to equation 4.37 from line positions, line strengths and pressure broadening coefficients taken from the HITRAN database [23], and absorption cross sections for HONO, and N_2O_5 as reported in references [24, 25], and [26], respectively.
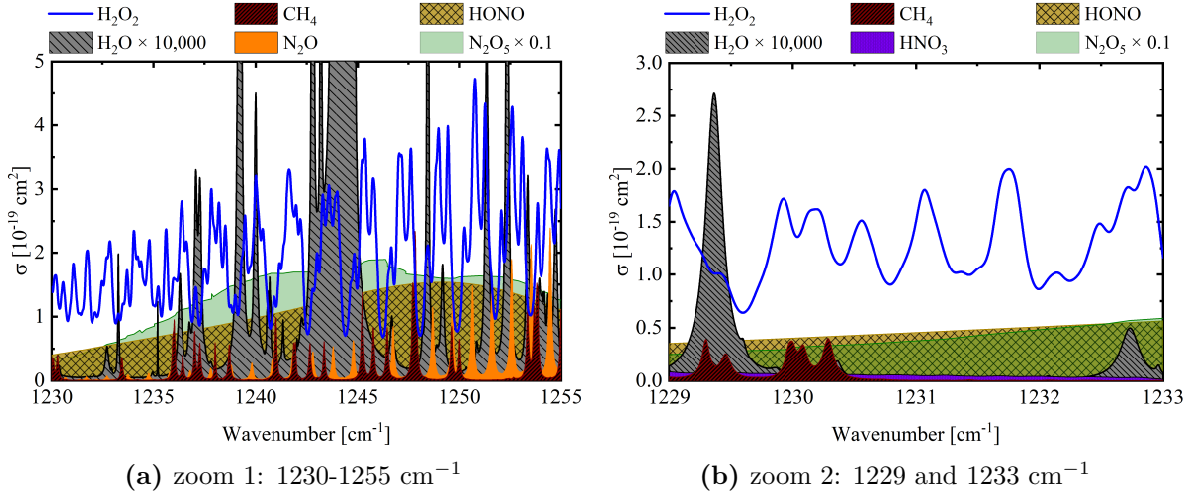
(a) zoom 1: 1230-1255 cm^{-1} **(b)** zoom 2: 1229 and 1233 cm^{-1}

Figure 5.12: Zoom-in into the absorption cross section as depicted in figure 5.11 around (a) 1245 cm^{-1} and (b) 1231 cm^{-1}.

region. As all of these species tend to either be produced by the kINPen-sci plasma jet or to be present in the laboratory air, it is difficult to distinguish between those contributions. In figure 5.12a and in figure 5.12b, a zoom-in of figure 5.11 is shown around 1245 cm^{-1}, and around 1231 cm^{-1}, respectively. Within the range between 1230.5 cm^{-1} and 1232 cm^{-1}, two prominent absorption features for H_2O_2 can be found, while contributions of other species, namely HNO_3, HONO, and N_2O_2, result in a straight line of broadband absorption. In this work, the region between 1230.8 cm^{-1} and 1231.3 cm^{-1} was chosen to determine the densities of H_2O_2.

5.2.1 Fitting procedure of full spectra for H_2O_2

To determine the density of H_2O_2 from a measured spectrum, which was obtained by measuring the ring-down times $\tau(\nu)$ at different spectral positions while the kINPen-sci plasma jet was switched on, the fitting procedure described in section 4.3.2 has been modified. In equation 5.7, the contribution of water to the absorption spectrum in has been replaced by a straight line with the coefficients b_0 and b_1, respectively, to account for the y-intercept and the slope due to the broadband absorbers:

$$\alpha(\nu)\frac{d}{L} = b_0 + b_1\nu + \frac{d_{H_2O_2}}{L}[H_2O_2]\sigma_{H_2O_2}(\nu) + \epsilon(\nu) = \frac{1}{c\tau(\nu)} - \frac{1}{c\tau_0}. \qquad (5.7)$$

Here, $\alpha(\nu)$ is the absorption coefficient, L is the cavity length, d is the diameter of the volume, in which the absorbing species are located, $d_{H_2O_2}$ is the absorption length, $[H_2O_2]$ is the density, and $\sigma_{H_2O_2}(\nu)$ is the frequency dependent absorption cross section of H_2O_2, $\epsilon(\nu)$ is the residual, c is the speed of light in vacuum, and τ_0 is the ring-down time determined while the kINPen-sci plasma jet was switched off. The frequency dependence of τ_0 within the applied tuning range of the QCL is small. Hence, τ_0 was

considered to be constant over the recorded spectral range of a spectrum.

For the determination of H_2O_2, the vector with the fitting parameters β introduced in section 4.3.2 was reduced to $\beta = (b_0, b_1, [H_2O_2])$, while the matrix describing the system of linear equations to minimise the sum of squares of the residuals was reduced to a 3×3-matrix:

$$\mathbf{M} = \begin{pmatrix} N_\nu & \sum \nu & \sum \sigma_{H_2O_2} \\ \sum \nu & \sum \nu^2 & \sum \sigma_{H_2O_2} \nu \\ \sum \sigma_{H_2O_2} & \sum \sigma_{H_2O_2} \nu & \sum \sigma_{H_2O_2}^2 \end{pmatrix}. \tag{5.8}$$

The vector ω that includes the measured ring-down times was given by:

$$\omega = \frac{1}{c} \begin{pmatrix} \sum \tau(\nu)^{-1} - \tau_0^{-1} \\ \sum \left(\tau^{-1} - \tau_0^{-1} \right) \nu \\ \sum \left(\tau^{-1} - \tau_0^{-1} \right) \sigma_{H_2O_2} \end{pmatrix}. \tag{5.9}$$

For each measured spectrum, β was computed by using a Matlab script, while the value for the pressure broadening coefficient $\gamma_{H_2O_2}$ was varied as described in section 4.3.2 for the pressure broadening coefficient for HO_2. The values for β that yielded the lowest of squares of the residuals have been retained as the best fit parameters. The error was evaluated by using the same F-ratio method described section 4.3.2.

5.2.2 On/off-resonance method for H_2O_2

Based on the on/off-resonance method described in sections 4.3.4 and 4.3.5, the absorption length for H_2O_2 has been determined from radial scans by recording 100 ring-down events at $\nu_{on} = 1231.07$ cm^{-1} for the on-resonance position, and at $\nu_{off} = 1230.82$ cm^{-1} for the off-resonance position. The broadband absorption of HNO_3, $HONO$, and N_2O_5 was assumed to be the same at the positions for the on- and the off-resonance so that $\Delta\alpha$ yields:

$$\Delta\alpha := \frac{1}{c\tau(\nu_{on})} - \frac{1}{c\tau(\nu_{off})} = \frac{d_{H_2O_2}}{L} [H_2O_2] \Delta\sigma_{H_2O_2}. \tag{5.10}$$

Here, c is the speed of light in vacuum, $\tau(\nu_{on})$ and $\tau(\nu_{off})$ are the measured ring-down times at the on-resonance and off-resonance position, respectively, while the plasma jet was switched on, $d_{H_2O_2}$ is the absorption length for H_2O_2, $[H_2O_2]$ is the density of H_2O_2 located in a volume with a diameter of $d_{H_2O_2}$ along the line-of-sight of the laser beam, and $\Delta\sigma_{H_2O_2} := \sigma_{H_2O_2}(\nu_{on}) - \sigma_{H_2O_2}(\nu_{off})$ is the difference of the frequency dependent absorption cross sections at the on-resonance and the off-resonance position.

In figure 5.13, the frequency dependent absorption cross section for H_2O_2 at 300 K with a pressure broadening coefficient of $\gamma_{H_2O_2} = 0.06$ cm^{-1}atm^{-1} is depicted as calculated according to equation 4.37, together with the corresponding line strengths of the considered H_2O_2 transitions taken from the HITRAN database [10–12, 23]. The chosen value for the pressure broadening coefficient $\gamma_{H_2O_2}$ is by a factor of 0.6 smaller than the pressure broadening coefficients reported in HITRAN for air [10–12, 23]. However, in
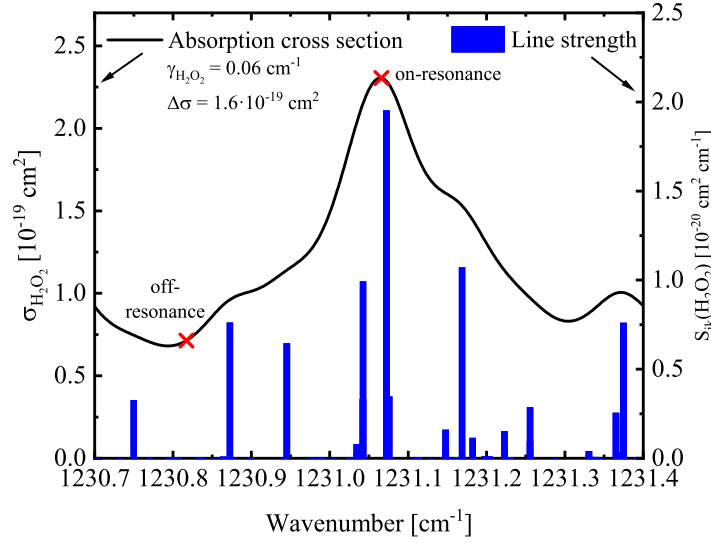
Figure 5.13: Frequency dependent absorption cross section for H_2O_2 at 300 K and 1013 hPa with a pressure broadening coefficient of $\gamma_{H_2O_2} = 0.06$ cm^{-1}atm^{-1} as calculated according to equation 4.37, together with the corresponding line strengths of the considered H_2O_2 transitions taken from the HITRAN database [10–12, 23].

the effluent of the kINPen-sci plasma jet, a mixture of O_2 and Ar is expected, which results in a significantly different pressure broadening coefficient. The pressure broadening coefficient was assumed to be the same for all transitions, as it was reported in the HITRAN database for the pressure broadening coefficients in air[10–12, 23], and previously done for the pressure broadening coefficients for HO_2 [20]. For the following analysis, $\Delta\sigma$ was determined to be:

$$\Delta\sigma(H_2O_2) = 1.6 \cdot 10^{-19} \text{ cm}^2. \tag{5.11}$$

5.3 Results

As the analysis of the spectra and the procedure to determine the spatial distribution is described in detail in section 4.3, here only the main results will be presented.

5.3.1 Full spectra for H_2O_2

In figure 5.14, absorption spectra are depicted for various z-distances between 3 mm and 10 mm below the nozzle of the kINPen-sci plasma jet, together with a fit of the baseline and the contribution of the absorption of H_2O_2. An absorption feature with the shape of the H_2O_2 absorption cross section as illustrated in figure 5.13 and a prominence of approximately $10 \cdot 10^{-8}$ cm^{-1} was observed at each z-position. The peak height

(a) $z = 3$ mm

(b) $z = 4$ mm

(c) $z = 5$ mm

(d) $z = 6$ mm

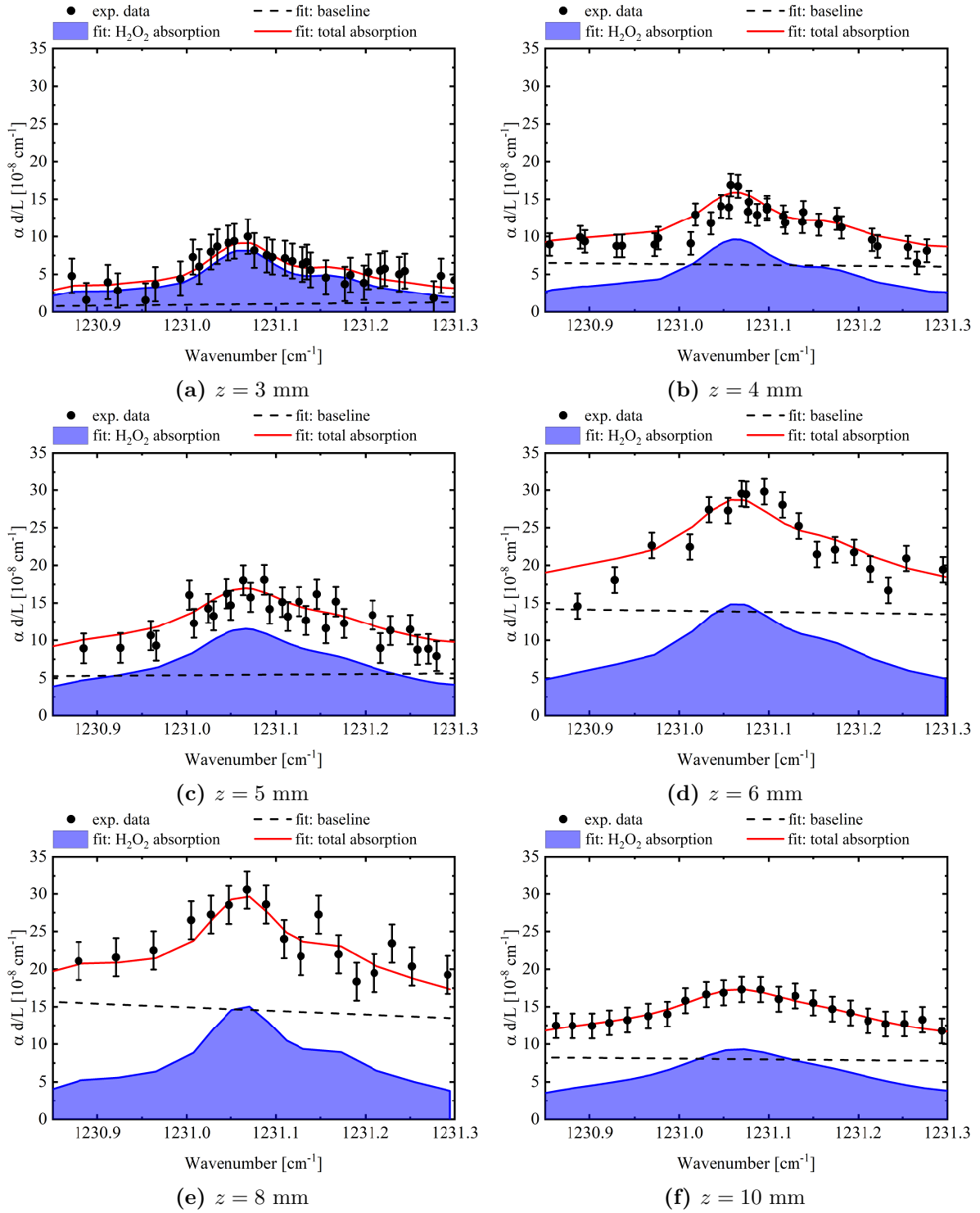**(e)** $z = 8$ mm

(f) $z = 10$ mm

Figure 5.14: Absorption spectra at various z-positions together with a fit of the baseline and the contribution of the absorption of H_2O_2.

was varying due to a subjacent baseline, whose mean value increased with increasing z-position. This baseline accounts for broadband absorptions resulting from transitions of

HNO_3, HONO, and N_2O_5, which could not be further specified due to their broadband character.

In figure 5.15, the pressure broadening coefficients $\gamma_{H_2O_2}$ for the observed H_2O_2 transitions determined from the spectra shown in figure 5.14 are depicted as a function of the distance from the nozzle z. Within the error, no significant relation between the z-position of the kINPen-sci plasma jet, and the pressure broadening coefficient for H_2O_2 could be observed. This indicates that a change of the gas mixture at various z-positions due to diffusion of the gas curtain into the effluent was not influencing the pressure broadening coefficient of the investigated transitions of H_2O_2. Hence, a mean value of $\gamma_{H_2O_2} = 0.06$ cm^{-1}atm^{-1} was chosen for all transitions, and for all radial and axial positions. Notably, this value is by a factor of 0.6 smaller than the value for the pressure broadening coefficient in air reported in the HITRAN database [10–12, 23]. A similar relation between the pressure broadening coefficients in air and the one determined for the gas mixture in the kINPen-sci plasma jet has been found previously for HO_2 summarised in sections 4.3.1 and 4.3.2 of this work, and reported in reference [20].

In order to compare the evolution of the baseline with the evolution of the absorption of H_2O_2, both as a function of z, the density for H_2O_2 was evaluated by assuming an absorption length of $d = 4$ mm. In figure 5.16, the density of H_2O_2 is depicted as a function of the distance from the nozzle z, together with the value of the baseline at 1230.066 cm^{-1}. The density of H_2O_2 increased between $z = 3$ mm and $z = 8$ mm linearly by approximately a factor of 2.3 to its maximum $9.7 \cdot 10^{13}$ cm^{-3}, and decreased to $7.1 \cdot 10^{13}$ cm^{-3} between $z = 6$ mm and $z = 10$ mm. If the error of the density is considered, the baseline had a similar trend; the baseline increased up to $z = 8$ mm,
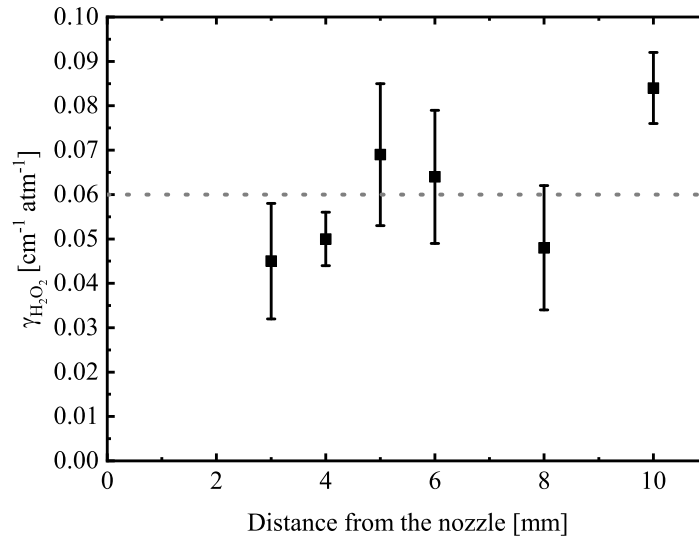

Figure 5.15: Pressure broadening coefficients for the observed H_2O_2 transition obtained from a fit of absorption spectra as a function of the distance from the nozzle z.
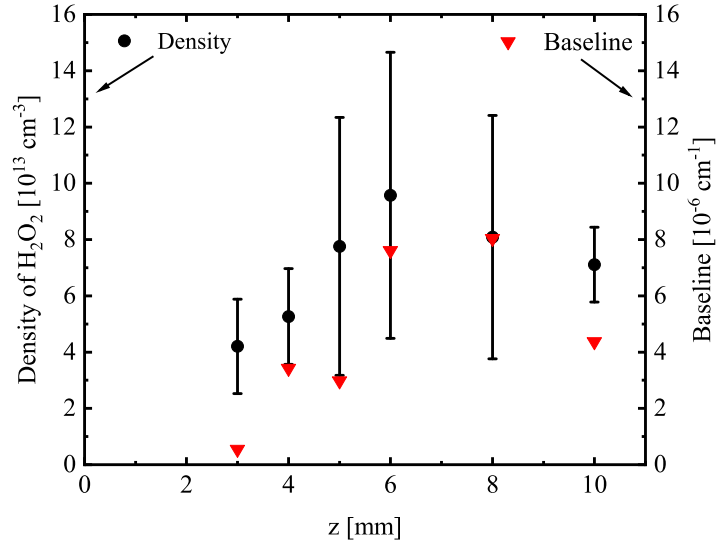
Figure 5.16: Density of H_2O_2 as a function of the distance to the nozzle z obtained from the fit of a full spectrum by assuming an absorption length of 4 mm, together with the value of the baseline at 1230.066 cm^{-1}.

and decreased between $z = 8$ mm and $z = 10$ mm. This indicates that besides H_2O_2, also the mean densities of HNO_3, HONO, and N_2O_5 increased. However, the effective absorption length needs to be considered to compare the densities at various z-positions. Due to the on/off-resonance method employed in this work, this can only be performed for the density of H_2O_2.

5.3.2 Determination of the effective absorption length for H_2O_2

In order to determine the effective absorption length, the on/off-resonance method was used to determine radial scans for $\Delta\alpha$ at z-positions between $z = 3$ mm and $z = 10$ mm. In figure 5.17, radial scans for $\Delta\alpha$ as a function of the distance to the symmetry axis through the kINPen-sci plasma jet, x, are depicted for $z = 3, 4, 6, 8$, and 10 mm together with a Gaussian fit, and a line representing the effective absorption length. Due to the diameter of the observed cavity mode, which was 5.5 mm in the focal point the cavity, no ring-down measurement closer than 3 mm below the nozzle could be performed. The effective absorption length l was determined by the limits that contain 99% of the area $A(z)$ of the Gaussian fit:

$$l(z) = 2.576 \cdot w(z). \tag{5.12}$$

Here, $w(z)$ is the width of the Gaussian function, which is determined by:

$$\Delta\alpha(x, z) = \frac{A(z)}{w(z)\sqrt{\frac{\pi}{2}}} \exp\left\{-2\left(\frac{x - x_c}{w(z)}\right)^2\right\} + \Delta\alpha_{off}. \tag{5.13}$$

(a) $z = 3$ mm

(b) $z = 4$ mm

(c) $z = 6$ mm

(d) $z = 8$ mm

(e) $z = 10$ mm
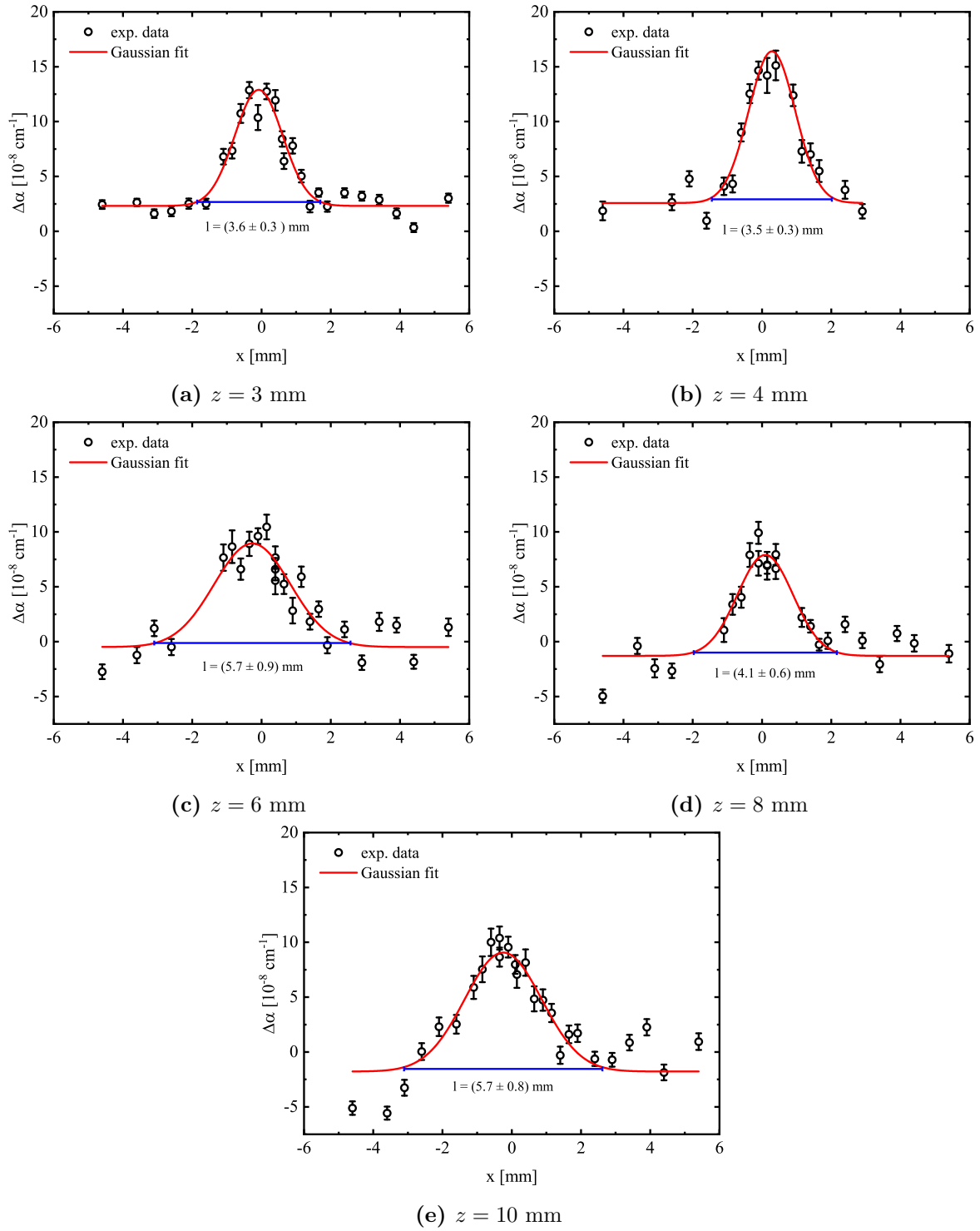
Figure 5.17: $\Delta\alpha$ as a function of x at various z-positions together with Gaussian fits.

Here, x_c is the centre position of the Gaussian fit, and $\Delta\alpha_{off}$ is an offset value, which is approximately 0 by taking the scattering of the measurement into account. For all
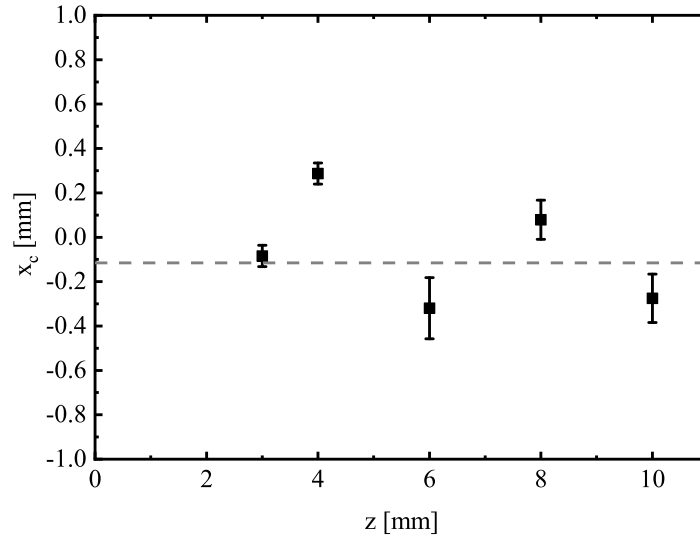
Figure 5.18: Centre position of the Gaussian fit of the radial scans as a function of the distance from the nozzle *z*.

z-positions, a Gaussian distribution for $\Delta\alpha$ was determined.

In figure 5.18, the centre positions x_c for the Gaussian fits of the radial scans are illustrated as a function of the distance from the nozzle *z*. $x_c = 0$ mm denotes the position of the symmetry axis of the kINPen-sci plasma jet in the centre of the nozzle. For the measured *z*-positions, the centre of the Gaussian fits were distributed between -0.4 mm and 0.4 mm to the centre of the nozzle. However, the weighted mean of the centre positions was at -0.12 mm, which indicates a slight asymmetry in the H_2O_2 distribution.
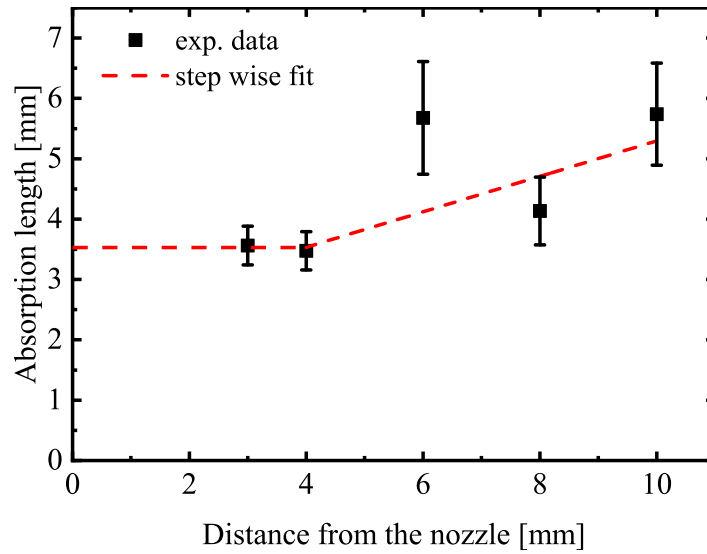
Figure 5.19: Stepwise fit of the absorption length as a function of the distance to the nozzle *z*.

In figure 5.19, the absorption length determined from the Gaussian fits according to equation 5.13 is depicted as a function of z together with a step wise linear approximation. For distances closer than $z = 3$ mm to the nozzle a constant absorption length was assumed, as it was found previously for HO_2 described in section 4.4.2. This assumption is in accordance with gas flow measurements, where an effective influx of the gas curtain into the effluent and thereby changing the gas mixture in the effluent starting from $z = 4$ mm has been reported. For the following analysis, the used effective absorption length obtained from the linear fits was:

$$l(z) = \begin{cases} 3.53 \text{ mm} & \text{for } z < 4 \text{ mm} \\ 0.29\,(z - 4 \text{ mm}) + 3.53 \text{ mm} & \text{for } z \geq 4 \text{ mm.} \end{cases} \tag{5.14}$$

5.3.3 Axial density distribution of H₂O₂ (line-of-sight average)

In figure 5.20, the line-of-sight averaged density distributions of H_2O_2 in the effluent of the kINPen-sci plasma jet obtained from an axial scan performed with the on/off-resonance method, and from fits of full spectra at various z-positions, are depicted as a function of the distance from the nozzle z. An absorption length according to equation 5.14 was used to determine the density of H_2O_2, which was assumed to be distributed homogeneously over this length. Within the error, the densities obtained from both methods are in agreement with each other. Between $z = 3$ mm and $z = 5$ mm, the density of H_2O_2 increased linearly from approximately $6 \cdot 10^{13}$ cm^{-3} to a plateau at approximately $9.5 \cdot 10^{13}$ cm^{-3} between $z = 5$ mm and $z = 6$ mm, and decreased also linearly back to approximately $6 \cdot 10^{13}$ cm^{-3} between $z = 6$ mm and $z = 10$ mm.
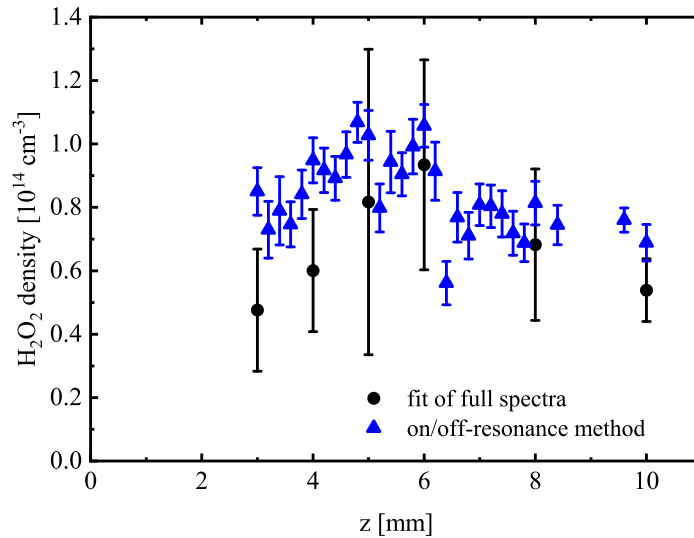

Figure 5.20: Line-of-sight averaged density of H_2O_2 at $x = 0$ mm as a function of z, obtained by the on/off-resonance method and from a fit of full spectra.

5.3.4 Radial density distribution of H_2O_2

In figure 5.21, the radial density distributions for H_2O_2 are illustrated for various z-positions. According to equation 4.49 and equation 4.50, these radial distributions were obtained from an Abel inversion of the radial scans at various z-positions as depicted in figure 5.17. For all radial scans, a distribution of H_2O_2 with a Gaussian shape was determined, which was due to the shape of the radial scans for $\Delta\alpha$. Except for the measurement at $z = 4$ mm, the maximum intensities increased close to the nozzle. However, for the measurement at $z = 4$ mm, a maximum density of twice the value for the maximum density at $z = 6$ mm and a factor of approximately 1.5 more than the value for the maximum density at $z = 3$ mm was obtained. This is in contrast to the observations for the line-of-light averaged densities. Furthermore, the maximum was shifted by approximately $x = 0.4$ mm compared to the symmetry axis through the plasma jet. Notably, the radial distribution for H_2O_2 depends strongly on the data quality for the radial scans. Since the cavity for H_2O_2 was by a factor of 10 more noisy than the cavity used to determine the densities of the HO_2 molecules, while the measured absorbances were only a factor of 3 larger than the valued obtained for HO_2, a larger error can be expected.
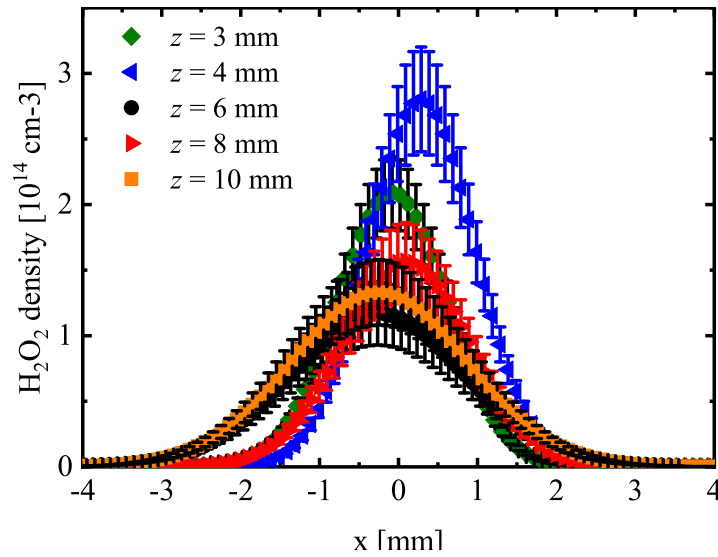

Figure 5.21: Density of H_2O_2 as a function of x for $y = 0$ mm at various z-positions, obtained by an Abel inversion of the radial scans depicted in figure 5.17.

5.3.5 Spatial density distribution of H_2O_2

Based on the measurements of $\Delta\alpha$ with the on/off-resonance method and of $\Delta\alpha$ obtained from the fit of full spectra, the axial distribution of the absorption coefficient was determined. In figure 5.22, $\Delta\alpha$ measured with the on/off-resonance method and calculated from a fit of full spectra, is depicted as a function of z together with a stepwise fit for $\Delta\alpha$ which was constant within the first 3 mm below the nozzle of the kINPen-sci plasma jet and approximated by a polynomial for larger z-distances. In order to determine the spatial distribution of H_2O_2 according to equation 4.62, the following definitions for $\Delta\alpha(x = 0, z)$ were obtained from the fit:

$$\Delta\alpha(x = 0, z) = \begin{cases} 7.43 \cdot 10^{-8} \text{ cm}^{-1} & z < 3 \text{ mm} \\ [-10.0 + 9.5z - 1.42z^2 + 0.069z^3] \cdot 10^{-8} \text{ cm}^{-1} & z \geq 3 \text{ mm}. \end{cases} \quad (5.15)$$

In figure 5.23, the localised density of H_2O_2 is illustrated in two different planes cut along the symmetry axis of the plasma jet at two y-positions. The density was interpolated to $z = 0$ mm assuming a constant absorption $\Delta\alpha(x = 0, z)$ as given by equation 5.15 and illustrated in figure 5.22. The black area in figure 5.23 denotes the region, where no measurements could be performed without disturbing the cavity mode. H_2O_2 was found to be mainly distributed within a cone with a diameter of approximately 3.5 mm at $z = 3$ mm and 5.3 mm at $z = 10$ mm. A maximum density of approximately $2 \cdot 10^{14}$ cm^{-3} was obtained in the centre of the effluent between 4 and 5 mm below the nozzle of the plasma jet. The density of H_2O_2 decreased as a function of z to $1.5 \cdot 10^{14}$ cm^{-3} at 10 mm in the centre of the effluent.
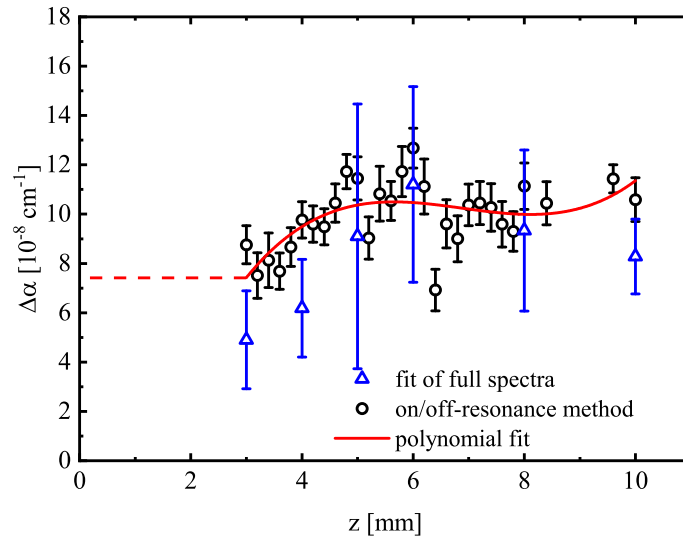

Figure 5.22: $\Delta\alpha$ as a function of z, obtained by the on/off-resonance method and from a fit of full spectra as depicted in figure 5.14, together with a stepwise fit for $\Delta\alpha$ which was constant within the fist 3 mm below the nozzle of the kINPen-sci plasma jet and approximated by a polynomial for larger z-distances.

(a) $y = 0$ mm

(b) $y = 1.5$ mm
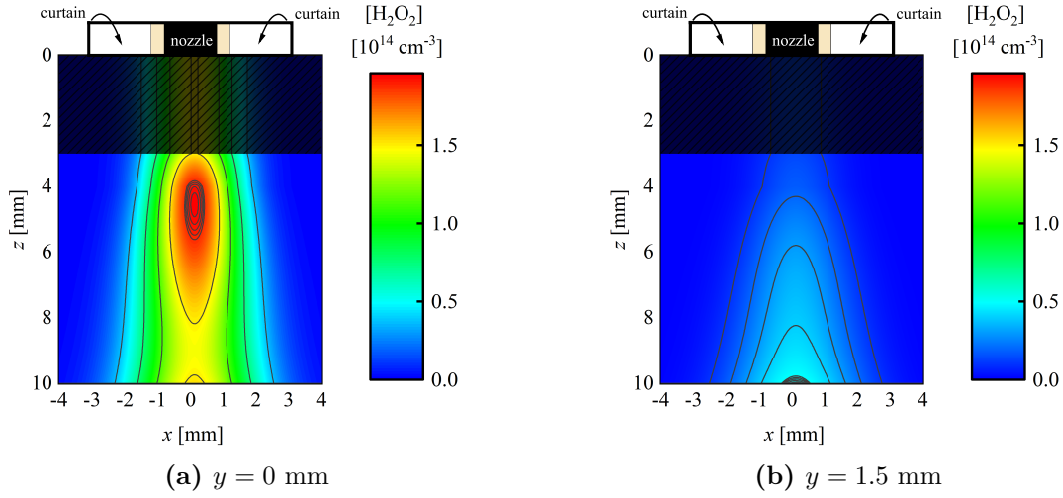
Figure 5.23: Localised density of H_2O_2 illustrated in two different planes cut along the symmetry axis of the plasma jet at two y-positions.

5.4 Summary

In this work, the spatial distribution of H_2O_2 in the effluent of a plasma jet has been determined for the first time by means of cw-cavity ring-down spectroscopy at a wavelength of approximately 8 µm. Full spectra were obtained between 1230.9 cm^{-1} and 1231.3 cm^{-1}. These spectra were fitted to the absorption spectrum for H_2O_2 according to the line positions reported in references [10–12]. A base line was used to account for underlying broad band absorptions of other species, such as HONO, N_2O_5 and HNO_3. The pressure broadening for H_2O_2 was assumed to be the same value for the individual transitions. Based on the fitting procedure, a pressure broadening coefficient of 0.06 cm^{-1}atm^{-1} was obtained.

By employing the on/off-resonance method, the effective absorption length $l(z)$ was obtained from radial scans of the absorption coefficient:

$$l(z) = \begin{cases} 3.53 \text{ mm} & \text{for } z < 4 \text{ mm} \\ 0.29\,(z - 4 \text{ mm}) + 3.53 \text{ mm} & \text{for } z \geq 4 \text{ mm}. \end{cases} \tag{5.16}$$

The on/off-resonance measurements agree within the error with results obtained from fits of full spectra at various z-positions. By applying an Abel inversion of the radial scans, and combining these data with an axial scan of the absorption coefficient, the spatial distribution for H_2O_2 was determined. A maximum localised density of approximately $2 \cdot 10^{14}$ cm^{-3} was found in the centre of the effluent between 4 and 5 mm below the nozzle of the plasma jet. With increasing z-distance, the density decreased to $1.5 \cdot 10^{14}$ cm^{-3} at 10 mm.

5.5 Bibliography

[1] J. Winter, H. Tresp, M. U. Hammer, S. Iséni, S. Kupsch, A. Schmidt-Bleker, K. Wende, M. Dünnbier, K. Masur, K.-D. Weltmann, and S. Reuter. Tracking plasma generated h$_2$o$_2$ from gas into liquid phase and revealing its dominant impact on human skin cells. *J. Phys. D: Appl. Phys.*, 47(285401), 2014.

[2] X. Lu, G. V. Naidis, M. Laroussi, S. Reuter, D. B. Graves, and K. Ostrikov. Reactive species in non-equilibrium atmospheric-pressure plasmas: Generation, transport, and biological effects. *Physics Reports*, 630(1-84), 2016.

[3] A. Privat-Maldonado, A. Schmidt, A. Lin, K.-D. Weltmann, K. Wende, A. Bogaerts, and S. Bekeschus. ROS from Physical Plasmas: Redox Chemistry for Biomedical Therapy. *Oxidative Medicine and Cellular Longevity*, 2019(9062098), 2019.

[4] A. Khlyustova, C. Labay, Z. Machala, M.-P. Ginebra, and C. Canal. Important parameters in plasma jets for the production of RONS in liquids for plasma medicine: A brief review. *Front. Chem. Sci. Eng.*, 13(2), 2019.

[5] J. Winter, K. Wende, K. Masur, S. Iséni, M. Dünnbier, M. U. Hammer, H. Tresp, K.-D. Weltmann, and S. Reuter. Feed gas humidity: a vital parameter affecting a cold atmospheric-pressure plasma jet and plasma-treated human skin cells. *J. Phys. D: Appl. Phys.*, 46(295401), 2013.

[6] M. Suresh, V. S. S. K. Kondeti, and P. J. Bruggeman. Production and diffusion of H$_2$O$_2$ during the interaction of a direct current pulsed atmospheric pressure plasma jet on a hydrogel. *J. Phys. D: Appl. Phys.*, 55(185201), 2022.

[7] H. J. Hathaway, B. L. Patenall, N. T. Thet, A. C. Sedgwick, G. T. Williams, A. T. A. Jenkins, S. L. Allinson, and R. D. Short. Delivery and quantification of hydrogen peroxide generated via cold atmospheric pressure plasma through biological material. *J. Phys. D: Appl. Phys.*, 52(505203), 2019.

[8] B. Ghimire1, E. J. Szili, B. L. Patenall, P. Lamichhane, N. Gaur, A. J. Robson, D. Trivedi1, N. T. Thet, A. T. A. Jenkins, E. H. Choi, and R. D. Short. Enhancement of hydrogen peroxide production from an atmospheric pressure argon plasma jet and implications to the antibacterial activity of plasma activated water. *Plasma Sources Sci. Technol.*, 30(035009), 2021.

[9] H. Jablonowski and T. von Woedtke. Research on plasma medicine-relevant plasma-liquid interaction: What happened in the past five years? *Clinical Plasma Medicine*, 3(42-52), 2015.

[10] S. Klee, M. Winnewisser, A. Perrin, and J.-M. Flaud. Absolute Line Intensities for the ν_6 Band of H$_2$O$_2$. *J. Mol. Spectrosc.*, 195(1), 1999.

[11] A. Perrin, J.-M. Flaud, C. Camy-Peyret, R. Schermaul, M. Winnewisser, J.-Y. Mandin, V. Dana, M. Badaoui, and J. Koput. Line Intensities in the Far-Infrared Spectrum of H$_2$O$_2$. *J. Mol. Spectrosc.*, 176(2), 1996.

[12] A. Perrin, A. Valentin, J.-M. Flaud, C. Camy-Peyret, L. Schriver, A. Schriver, and Ph. Arcas. The 9.7-μm Band of Hydrogen Peroxide: Line Positions and Intensities. *J. Mol. Spectrosc.*, 171(2), 1995.

[13] O. Bain and P. A. Giguère. Hydrogen Peroxide and its Analogues. *Can. J. Chem.*, 33(3), 1955.

[14] A. Schmidt-Bleker, J. Winter, A. Bösel, S. Reuter, and K.-D. Weltmann. On the plasma chemistry of a cold atmospheric argon plasma jet with shielding gas device. *Plasma Sources Sci. Technol.*, 25(015005), 2016.

[15] W. Plass, R. Maestle, K. Wittig, A. Voss, and A. Giesen. High-resolution knife-edge laser beam profiling. *Opt. Commun.*, 134(21-24), 1997.

[16] D. W. Allan. Statistics of Atomic Frequency Standards. *Proceeding of the IEEE*, 54(2), 1966.

[17] P. Werle, R. Mücke, and F. Slemr. The limits of signal averaging in atmospheric trace-gas monitoring by tunable diode-laser absorption spectroscopy (TDLAS). *Applied Physics B*, 57(131-139), 1993.

[18] D. A. Long, D. K. Havey, M. Okumura, H. M. Pickett, C. E. Miller, and J. T. Hodges. Laboratory measurements and theoretical calculations of o_2 a band electric quadrupole transitions. *Phys. Rev. A*, 80(042513), 2009.

[19] S. Kassi and A. Campargue. Cavity ring down spectroscopy. *J. Chem. Phys.*, 137(234201), 2012.

[20] M. Gianella, S. Reuter, S. A. Press, A. Schmidt-Bleker, J. H. van Helden, and G. A. D. Ritchie. HO_2 reaction kinetics in an atmospheric pressure plasma jet determined by cavity ring-down spectroscopy. *Plasma Sources Sci. Technol.*, 27(095013), 2018.

[21] G. Zhao, T. Hausmaninger, W. Ma, and O. Axner. Shot-noise-limited doppler-broadened noise-immune cavity-enhanced optical heterodyne molecular spectrometry. *Optics Letters*, 43(4), 2018.

[22] J. A. Barnes, A. R. Chi, L. S. Cutler, D. J. Healey, D. B. Leeson, T. E. McGunial, J. A. Jr. Mullen, W. L. Smith, R. L. Sydnor, R. D. C. Vessot, and G. M. R. Winkler. Characterization of Frequency Stability. *IEEE Transactions on Instrumentation and Measurement*, IM-20(2), 1971.

[23] I.E. Gordon, L.S. Rothman, and R.J. Hargreaves. The HITRAN2020 molecular spectroscopic database. *J. Quant. Spectrosc. Radiat. Transf.*, 277(107949), 2022.

[24] W. S. Barney, L. M. Wingen, M. J. Lakin, T. Brauers, J. Stutz, and B. J. Finlayson-Pitts. Infrared Absorption Cross-Section Measurements for Nitrous Acid (HONO) at Room Temperature. *J. Phys. Chem. A*, 104(1692-1699), 2000.

[25] W. S. Barney, L. M. Wingen, M. J. Lakin, T. Brauers, J. Stutz, and B. J. Finlayson-Pitts. Additions and Corrections to: Infrared Absorption Cross-Section Measurements for Nitrous Acid (HONO) at Room Temperature, 2000, Volume 104A. *J. Phys. Chem. A*, 105(16), 2001.

[26] D. Newnham, J. Ballard, and M. Page. Infrared absorbance cross-sections for nitrogen pentoxide vapour. *J. Quant. Spectrosc. Radiat. Transf.*, 50(6), 1993.

6 Consolidation of the spatial distributions for O, H, HO$_2$, and H$_2$O$_2$
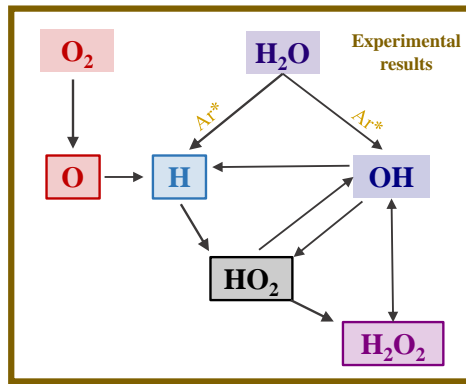
In this work, different absorption spectroscopy techniques at various wavelength regimes were employed, namely laser atomic absorption spectroscopy (LAAS) for the determination of Ar(^{3}P$_2$), picosecond two-photon absorption laser-induced fluorescence spectroscopy (ps-TALIF) for the determination of O atoms and H atoms, and continuous wave cavity ring-down spectroscopy (cw-CRDS) for the determination of HO$_2$ radicals and H$_2$O$_2$ molecules. The detection limits for the particular species in the effluent of the kINPen-sci plasma jet vary for the different diagnostic techniques mainly due to the sensitivity of the available detectors, which is larger in the visible region than in the ultraviolet or in the infrared region. For the cw-CRDS-measurements, the detection limit was determined by the noise of the cavity. In table 6.1, the detection limits for the measured species are summarised with the assumption that the species were distributed within 4 mm. This assumption has been used previously [1] and has been proven up to approximately 6 mm below the nozzle of the plasma jet.

In this chapter, the results for the determined spatial distributions for O atoms, H atoms, HO$_2$ radicals, and H$_2$O$_2$ molecules are compared to the boundaries of the flow for the Ar feed gas, which were obtained from Schlieren diagnostics [2] and from particle image flow velocimetry [3]. The impact of the plasma jet in the optical cavities was investigated by comparing the noise for both cavities used for the determination of HO$_2$ and H$_2$O$_2$. However, no information about the densities closer than 1 mm in case of the measurements for HO$_2$, and 3 mm in the case of the measurements for H$_2$O$_2$, could be achieved due to perturbation of the cavity modes by the nozzle of the plasma jet.

Table 6.1: Detection limits for the measurements of $Ar(^3P_2)$, H atoms, O atoms, HO_2 radicals, and H_2O_2 molecules.

species	diagnostic method	detection limit $[\text{cm}^{-3}]$
$Ar(^3P_2)$	LAAS	$\approx 1 \cdot 10^{13}$
H	ps-TALIF	$\approx 1 \cdot 10^{14}$
O	ps-TALIF	$\approx 1 \cdot 10^{14}$
HO_2	cw-CRDS	$\approx 4 \cdot 10^{13}$
H_2O_2	cw-CRDS	$\approx 2 \cdot 10^{13}$

With the distribution of the Ar feed gas flow, a combined absorption length for both HO_2 and H_2O_2 was deduced. Based on this estimated absorption length, the spatial distributions for HO_2 and H_2O_2 are re-evaluated. By a comparison of the determined asymmetries for the investigated atomic and molecular species with the optical emission obtained for $Ar(^3P_2)$, the impact of the plasma zone could be confirmed. The impact of the gas curtain close to the nozzle on the reactive species composition was further investigated by analysing the quenching of the effective lifetimes for O atoms. For all measured distributions, it was found that a certain amount of O_2 needs to be present within the plasma zone. Hence, investigations of the origin of this initial amount of O_2 by using an zirconia oxygen sensor are presented.

6.1 Shape and width of the radial distributions

Radial distributions of the densities were obtained for O, H, HO_2, and H_2O_2. All investigated molecular species were found to be distributed with a Gaussian shape. For HO_2 radicals as well as for H_2O_2 molecules the absorption length was obtained from radial scans through the effluent of the plasma jet at various distances from the nozzle z. The radial scans were approximated by a Gaussian fit, and the absorption lengths, which are equal to the lengths d_{HO_2} and $d_{H_2O_2}$, over which the species were distributed, were computed from the widths w_{HO_2} and $w_{H_2O_2}$ of these Gaussian fits according to:

$$d_{HO_2} = 2.576 \, w_{HO_2} \tag{6.1}$$

and

$$d_{H_2O_2} = 2.576 \, w_{H_2O_2}. \tag{6.2}$$

For the measurements of H atoms and of O atoms, the lengths d_H and d_O, over which the species were distributed, were obtained from the measured spatial distributions. The limits were chosen as the region where the densities were higher than twice the scattering of the data points at radial distances $\mid x \mid > 0.8$. In figure 6.1, the determined values for d_H, d_O, d_{HO_2}, and $d_{H_2O_2}$ for the species distributions of H, O, HO_2, and H_2O_2 are illustrated as a function of the distance to the nozzle z. The H and O atoms were
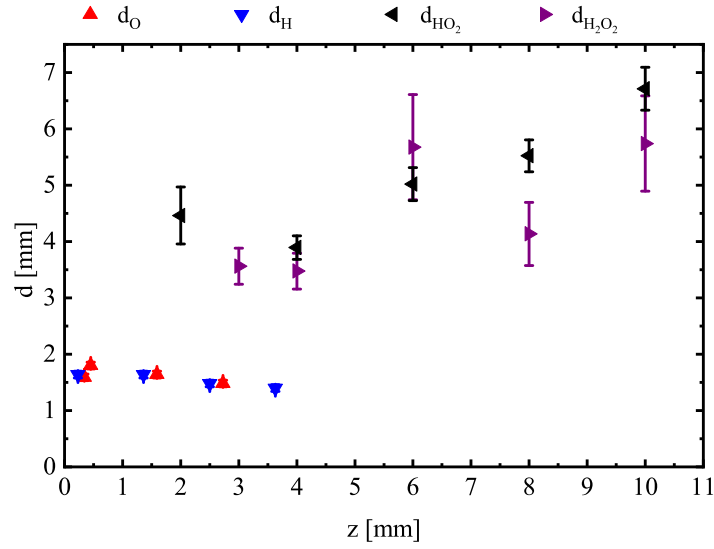
Figure 6.1: Lengths d, over which the species O, H, HO$_2$, and H$_2$O$_2$ were distributed as function of the distance to the nozzle z. The values for d_O, d_H, d_{HO_2}, and $d_{H_2O_2}$ were obtained from the width of the Gaussian fit of the radial scans through the effluent of the plasma jet for HO$_2$, and H$_2$O$_2$, and from the measures spatial distributions for H and O atoms.

distributed within the diameter of the nozzle, while the HO$_2$ and H$_2$O$_2$ molecules were distributed over a larger diameter. Notably, the measurements for the H and O atoms could be performed close to the nozzle up to $z = 0.25$ mm, while radial scans for HO$_2$ and H$_2$O$_2$ were obtained at distances larger than $z = 2$ mm.

In order to investigate if the species, in particular HO$_2$ and H$_2$O$_2$, were propagating with the feed gas flow, the obtained values for d were compared to the distribution of the Ar feed gas flow. The Ar atom distribution was obtained from Schlieren diagnostics reported by Schmidt-Bleker et al. [2], and by unpublished, preliminary investigations with particle image velocimetry [3]. In figure 6.2a, the measured Schlieren contrast of the plasma jet operated with 3 slm Ar is depicted as reported in reference [2]. Lateral profiles at various z-distances, obtained from a contourplot of the Schlieren contrast are illustrated in figure 6.2b. In this work, the length d_{Ar}^S, over which Ar was distributed, was obtained from these profiles. Therefore, the boundaries were determined, where the absolute value of the contrast was higher than $0.02 \times \mid c_{max} \mid$, with c_{max} the absolute value of the maximum contrast. This condition is in agreement with the area for a Gaussian function that contains 95% of the full area. For the left-sided boundary, the absolute minimum value of the contrast was chosen, and for the right-sided boundary the absolute maximum of the contrast value was used. The determination of boundaries that contain 99% of the area assuming a Gaussian distribution was not feasible due to the resolution of the experimental data. In order to reduce the noise of the data, the experimental values for d_{Ar}^S obtained from the Schlieren measurements were

(a) Contourplot of the contrast

(b) Lateral profiles at various z-positions

(c) Lengths d^S_{Ar}
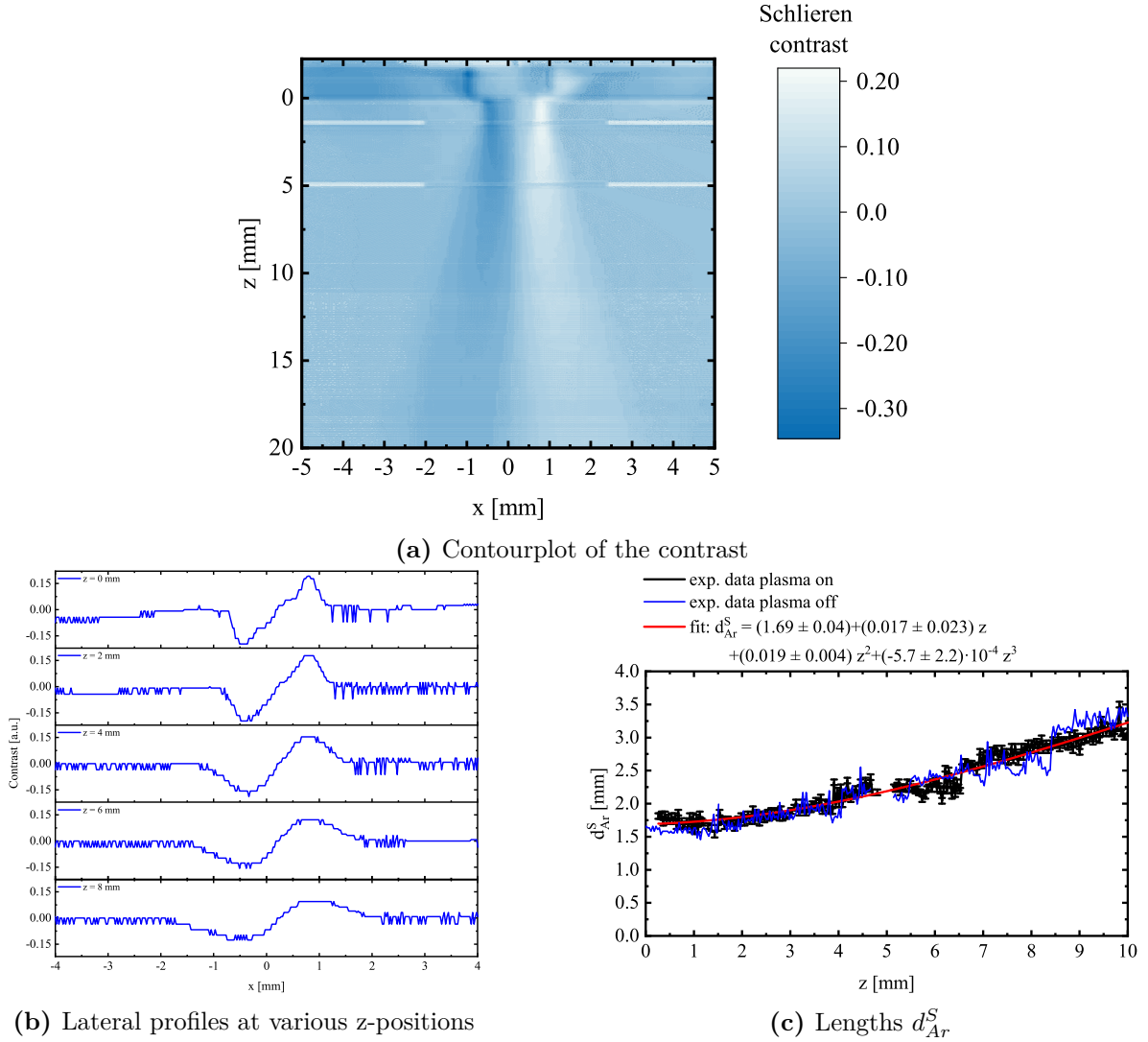
Figure 6.2: Distribution of Ar obtained from Schlieren diagnostics performed by Schmidt-Bleker et al. [2]. (a) Contourplot of the data taken from figure 3 in reference [2], (b) lateral profiles through the effluent of the plasma jet obtained from the contourplot of the contrast, and (c) lengths d^S_{Ar}, over which the Ar atoms were distributed, determined from the boundaries that contain 95% of the area of a Gaussian distribution as a function of the distance from the nozzle z.

approximated by a 3rd order polynomial with:

$$d^S_{Ar} = (1.69 \pm 0.04) + (1.7 \pm 2.3) \cdot 10^{-2} \cdot z + (1.9 \pm 0.4) \cdot 10^{-2} \cdot z^2 + (-5.7 \pm 2.2) \cdot 10^{-4} \cdot z^3, \quad (6.3)$$

which is depicted in figure 6.2c together with the experimental data for both, plasma on and plasma off. No significant difference was found concerning the distribution of the feed gas flow for the cases plasma on and plasma off. However, it should be noted that the Schlieren measurements were performed without a gas curtain, which might have an influence on the flow dynamics.

Another approach to obtain the radial distribution of the Ar feed gas flow is particle image flow velocimetry. In short, small particles of oil with a diameter of approximately 1 μm are mixed with the Ar feed gas. These particles are illuminated by a laser, and the scattered light is observed by a streak camera. From the movement of clouds of particles, the particle velocity can be determined, which is then equal to the gas velocity. The distribution of the feed gas flow is given by the boundaries between feed gas and surrounding air, where the gas velocity is decelerated to 0. In figure 6.3a, a contourplot

(a) Contourplot of the gas velocity

(b) Lateral profiles at various z-positions

(c) Lengths d_{Ar}^v
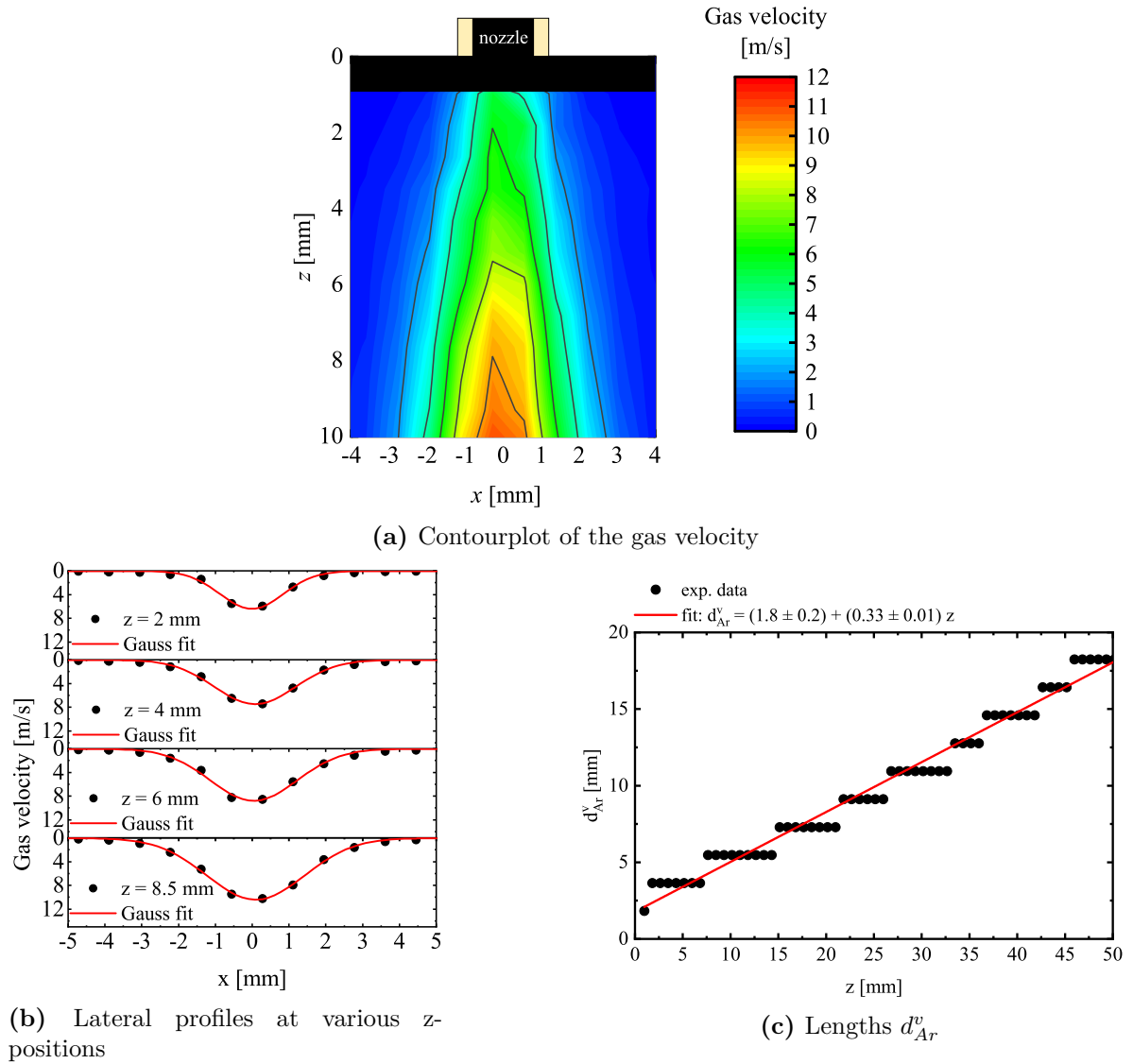
Figure 6.3: Gas velocity determined from particle image flow velocitmetry for the kINPen plasma jet with 4 slm Ar as the feed gas [3]. (a) Contourplot for the gas velocity, (b) lateral profiles through the effluent of the plasma jet obtained from the contourplot of the gas velocity, and (c) lengths d_{Ar}^S, over which the Ar atoms were distributed, determined from the boundaries that contain 99% of the area of a Gaussian distribution as a function of the distance from the nozzle z.

for the velocity distribution in the effluent of the kINPen operated with 4 slm feed gas is presented between $z = 0$ mm to $z = 10$ mm [3]. Due to the experimental setup, no information closer than $z = 1$ mm from the nozzle exit could be obtained. Notably, the absolute value of the velocity at distances closer than $z = 20$ mm remains underestimated, since the measurement was performed to obtain information for a larger scale up to $z = 100$ mm. However, the boundaries and the relative shape for the velocity distribution are unaffected by this. In figure 6.3b, lateral profiles of the velocity distributions at various z-positions are illustrated together with Gaussian fits. In this work, the distance d_{Ar}^v, over which the Ar atoms of the feed gas were distributed, was obtained from the full width at half maximum ($FWHM$) of the velocity distribution determined by particle image flow velocimetry according to $d_{Ar}^v = \frac{2.576}{\sqrt{2\ln(2)}} FWHM$. This condition is equal to the boundary condition that contain 99% of the area of a Gaussian distribution. The obtained values for d_{Ar}^v increased linearly as a function of the distance from the nozzle z with:

$$d_{Ar}^v = (1.8 \pm 0.2) + (0.33 \pm 0.01) \cdot z. \tag{6.4}$$

In figure 6.3c, the length d_{Ar}^v obtained from particle image velocimetry measurements is depicted as a function of z together with a linear fit.

The measured values for d_O, d_H, d_{HO_2}, and $d_{H_2O_2}$ for O atoms, H atoms, HO$_2$ radicals, and H$_2$O$_2$ molecules, respectively, were compared with the values for d obtained by Schlieren measurements in the case of plasma on (d_{Ar}^S) [2], and from preliminary particle
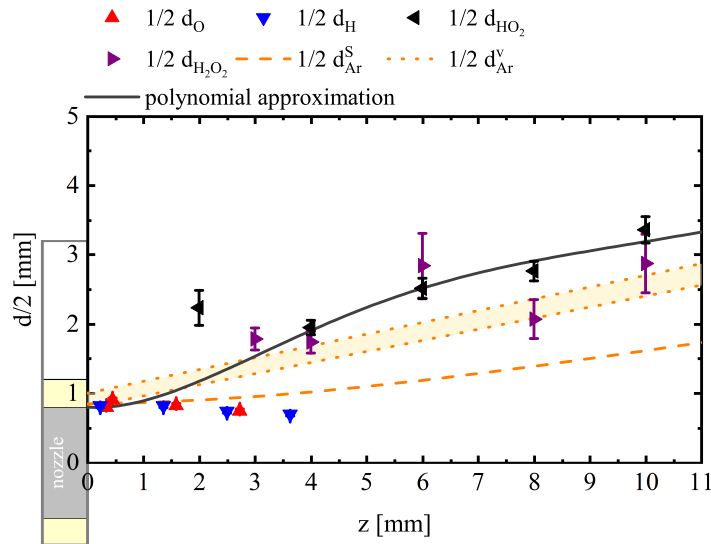
Figure 6.4: Determined values for d divided by a factor of 2 as a function of z. The lengths d_O, d_H, d_{HO_2}, and $d_{H_2O_2}$ were obtained from the measured spatial distributions of the densities, whereas d_{Ar}^S was determined from Schlieren diagnostics, and d_{Ar}^v was obtained from particle image flow velocimetry. A polynomial approximation for the distribution of HO$_2$ and H$_2$O$_2$, which is based on previous measurements and on the measured densities, is also presented.

image velocimetry measurements in the case of plasma off (d^v_{Ar}) [3]. Therefore, all determined values for d were divided by a factor of 2 in order to relate the lengths, over which the measured species were distributed, to the radius of the nozzle. In figure 6.4, the obtained values for d divided by a factor of 2 are depicted as a function of z. It was found that the HO$_2$ and H$_2$O$_2$ molecules were distributed over a length that was almost congruent with the length of the distribution of Ar obtained from Schlieren diagnostics and from particle image flow velocimetry. The O and H atoms distributions were congruent with the Ar flow within the first 1.5 mm from the nozzle, and contracted slightly within the next 2.5 mm. This could be due to a consumption of H and O atoms by O$_2$ due to the influx of the gas curtain, which was reported previously by [2, 4] to be starting efficiently at $z = 4$ mm. A distribution congruent with the Ar feed gas until $z = 1$ mm can be suspected for HO$_2$ and H$_2$O$_2$ as well, since the influx of the gas curtain is negligible close to the nozzle. This is on contrast to the value of the width of the radial scan for HO$_2$ at $z = 2$ mm reported in chapter 4. However, due to the noise of the data obtained close to the nozzle, the width of the Gaussian function on the radial scan for HO$_2$ at this specific position is most likely to be overestimated. In general, the uncertainty for the distribution of H$_2$O$_2$ is larger, since the measured signal was closer to the detection limit than the signal measured for HO$_2$. Based on the experimental data, the lengths d_{HO_2,H_2O_2}, over which HO$_2$ and H$_2$O$_2$ were distributed, was approximated by a 5$^{\text{th}}$ order polynomial:

$$d_{HO_2,H_2O_2} = 1.6 - 0.1 \cdot z + 0.33 \cdot z^2 - 0.057 \cdot z^3 + 0.0039 \cdot z^4 - 9.4 \cdot 10^{-5} \cdot z^5. \quad (6.5)$$

This polynomial divided by a factor of 2 is also depicted in figure 6.4. By using the polynomial approximation, information close to the nozzle can be extrapolated, which was not possible to obtain experimentally due to the inference of the plasma jet with the laser beam in the cavities.

6.1.1 Interference of the plasma jet with an optical cavity

According to the Allan deviation plot in reference [1], the detection limit for HO$_2$ was approximately $1.5 \cdot 10^{11}$ cm^{-3} if the molecules were localised in a volume with a diameter of 4 mm, and an order of magnitude worse when the kINPen-sci plasma jet was switched on. This is because the plasma jet interferes with the modes in the cavity by introducing random fluctuations of the refractive index due to the turbulent gas flow. However, it was not analysed if the gas flow by itself, or the plasma is mainly responsible for these changes. In this work, the Allan deviations of the cavity including the plasma jet, while it was either switched on or off, were investigated for the cavity used for the determination of the densities for H$_2$O$_2$. The sensitivity of the cavity used for H$_2$O$_2$, while the plasma jet was switched on, was the same as the sensitivity with the plasma switched off. This leads to the conclusion that the gas flow has a larger influence on the cavity modes than the plasma itself. By an Allan deviation plot, it was found that the upper limit for the Allan deviation was proportional to $\frac{1}{t}$, which indicates uncorrelated frequency modulations. The lower limit though was proportional
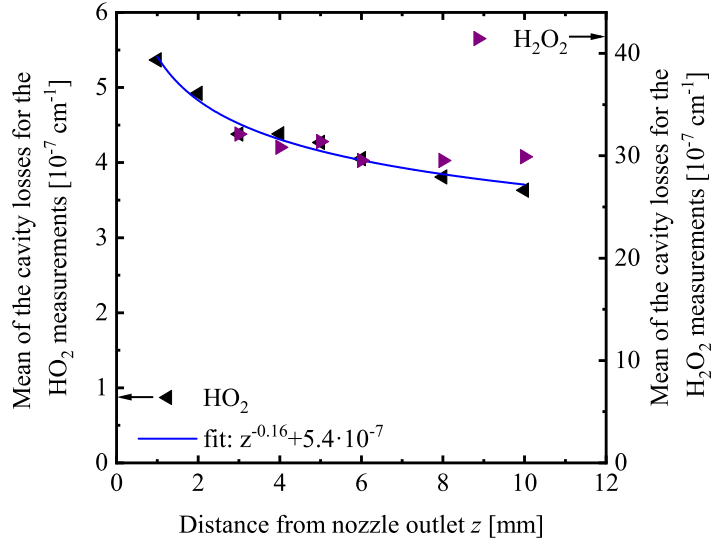
Figure 6.5: Mean of the cavity losses for the HO_2 measurements between 6638.33 cm^{-1} and 6638.49 cm^{-1} together with the mean of the cavity losses for the H_2O_2 between 1230.8 cm^{-1} and 1231.3 cm^{-1}, both as a function of the distance to the nozzle z.

to $\frac{1}{\sqrt{t}}$, which indicates uncorrelated phase noise. A more detailed analysis of the effects of the plasma jet on the cavity noise was not part of this work and remains for future investigations. It should be noted that generally the sensitivity of the Allan deviation is two orders of magnitude lower than the detection limit obtained from the scattering of data points of the baseline for both, full spectra and radial scans.

To investigate the non-absorption induced cavity losses, the mean of the cavity losses for the H_2O_2 at a spectral position without prominent absorption features, while the kINPen-sci plasma jet was switched off, was compared to the mean of the cavity losses for the HO_2 measurements at a spectral position with a small absorption of HO_2, while the kINPen-sci plasma jet was switched on. Unfortunately, no measurements for HO_2 have been performed, while the plasma jet was switched off. However, the contribution of absorption features of HO_2 to the non-absorption induced cavity losses at the spectral position chosen between 6638.33 cm^{-1} and 6638.49 cm^{-1} is small and can thus be neglected. In figure 6.5, the mean of the cavity losses for the HO_2 measurements between 6638.33 cm^{-1} and 6638.49 cm^{-1} with plasma on is depicted together with the mean of the cavity losses for the H_2O_2 between 1230.8 cm^{-1} and 1231.3 cm^{-1} with plasma off, both as a function of the distance to the nozzle z. For both measurements, a similar trend for the cavity losses was observed. The cavity losses decreased proportional to $z^{-0.16}$. This can be explained by the turbulence of the gas flow through the plasma jet: Close to the nozzle, the feed gas flow and the curtain gas flow is strongly decelerated by the static surrounding gas composition, which causes a lot of turbulences. With increasing distance from the nozzle, the velocity of the feed gas and the curtain gas flow decreases thereby reducing the turbulence. In conclusion, as the turbulence is reduced, the non-absorption induced cavity losses become smaller.

Table 6.2: Comparison of the cavity properties and sensitivity of the measurements for H_2O_2 at 1230.07 cm^{-1} and HO_2 at 6638.21 cm^{-1}.

	H_2O_2	HO_2
Mirror reflectivity	99.98%	99.998%
Cavity length	54.5 cm	80 cm
Free spectral range	275 MHz	188 MHz
Finesse	18,000	157,000
Mode width	0.015 MHz	0.001 MHz
τ_0	10.44 µs	133 µs
$FWHM$ of the beam [a]	2.5 mm	1.1 mm
beam diameter [b]	5.5 mm	2.5 mm

[a] in the focal points of the cavity
[b] in the focal points of the cavity, where 99% of
the energy of the laser beam is located

The absolute values for the cavity losses were larger by a factor of approximately 7.5 for the H_2O_2 measurements than for the HO_2 measurements. This was due to the different mirror reflectivities of the high reflective cavity mirrors. In table 6.2, the specifications including the mirror reflectivity, the cavity length, the free spectral range, the finesse, the mode width, the ring-down time for an evacuated cavity τ_0, the full width at half maximum of the laser beam in the focal point of the cavity, and the beam diameter of the laser beam in the focal points of the cavity, where 99% of the laser energy are located are summarised. In the mid-infrared region (MIR), where the experiments for H_2O_2 were performed, the reflectivity of the high reflective mirrors is typically one order of magnitude smaller than in the near-infrared region (NIR), where the HO_2 measurements were performed. This leads to a finesse of optical cavities in the MIR that is by a factor of approximately 10 smaller than the finesse of optical cavities in the NIR. Moreover, the diameter of the TEM$_{00}$ mode in the centre of the cavity in the MIR is larger by more than a factor of 2 compared to a cavity in the NIR due to the larger wavelength in the MIR compared to the NIR. This is the reason, why the smallest distance to the nozzle of the plasma jet for the H_2O_2 measurements was 3 mm, while for the HO_2 measurements the plasma jet could be approached to 1 mm below the nozzle, as otherwise the cavity modes are perturbed by the nozzle.

6.1.2 Re-evaluation of the densities for HO$_2$ and H$_2$O$_2$ for the corrected absorption length

Based on the polynomial approximation described by equation 6.5 for the distances $d_{\mathrm{HO_2,H_2O_2}}$ for HO$_2$ and H$_2$O$_2$, respectively, the density distribution along the symmetry axis of the kINPen-sci plasma jet as presented in chapter 4 and in chapter 5 was re-evaluated. In figure 6.6, the line-of-sight averaged densities of HO$_2$ and of H$_2$O$_2$ are depicted as a function of the distance to the nozzle z, where an absorption length $d_{\mathrm{HO_2,H_2O_2}}$ according to equation 6.5 was used. Close to the nozzle between $z = 0$ mm and $z = 3$ mm, the density of HO$_2$ remained constant at approximately $3.2 \cdot 10^{14}$ cm^{-3}. For further z distances, the density of HO$_2$ decreased linearly within the error bars by a factor of 3 to approximately $1.1 \cdot 10^{14}$ cm^{-3} at $z = 10$ mm. The density of H$_2$O$_2$ was constant between $z = 3$ mm and $z = 6$ mm at approximately $8 \cdot 10^{13}$ cm^{-3}, and decreased slightly between $z = 6$ mm and $z = 10$ mm by a factor of 0.75 to approximately $5 \cdot 10^{13}$ cm^{-3}.

In order to re-evaluate also the spatial distributions, the axial scans $\Delta\alpha_{HO_2}$ and $\Delta\alpha_{H_2O_2}$, obtained by on/off-resonance measurements, were approximated by two polynomial fits. Both, the polynomial fits and the experimental data for $\Delta\alpha_{HO_2}$, and $\Delta\alpha_{H_2O_2}$, respectively, are depicted in figure 6.7. Due to the lack of data points close to the nozzle for $\Delta\alpha$ for H$_2$O$_2$ within the first 3 mm below the nozzle, the polynomial fit in this region was chosen in such a way that the axial density distribution for H$_2$O$_2$, which was determined by the absorption length d_{HO_2,H_2O_2}, was constant within the first 3 mm. This assumption is based on the observation that the investigated reactive species are mainly produced within the plasma zone of the plasma jet and their density remains approximately constant over the first 3 mm, as it was determined for HO$_2$.
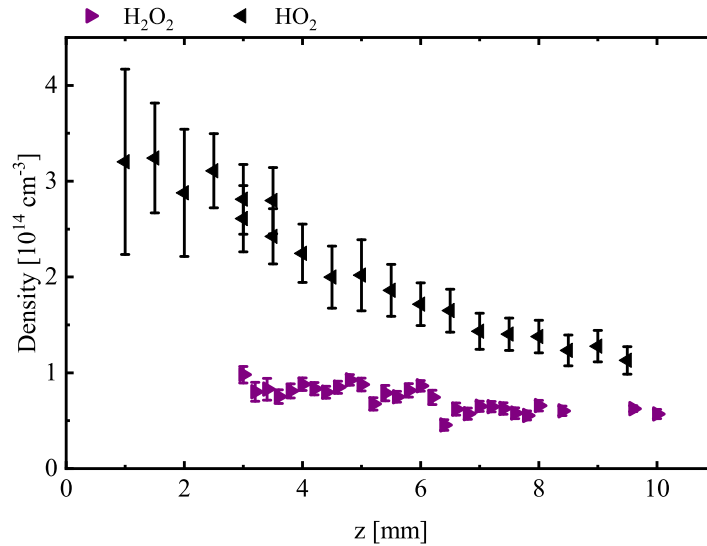

Figure 6.6: Line-of-sight averaged densities for HO$_2$ and H$_2$O$_2$; re-evaluation of the axial scans presented in the figure 4.13 and in figure 5.20 with the absorption length $d_{\mathrm{HO_2,H_2O_2}}$ according to equation 6.5.
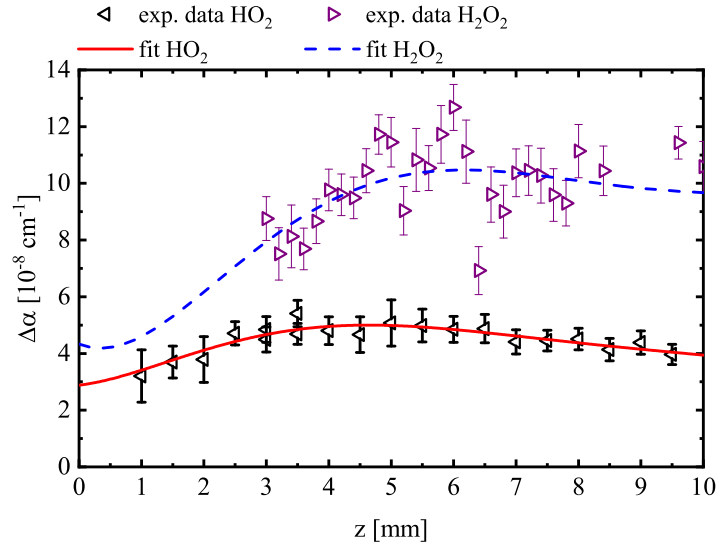
Figure 6.7: Re-evaluation of the polynomial fits for $\Delta\alpha_{HO_2}$, and $\Delta\alpha_{H_2O_2}$, as used to determine the spatial distribution of the densities, together with the experimental data depicted in figure 4.11 and figure 5.22.

According to equation 4.62, the spatial distributions for HO_2 and H_2O_2 were re-evaluated by using these polynomial approximations, which were given by:

$$\Delta\alpha_{HO_2} = 2.9 \cdot 10^{-8} + 2.6 \cdot 10^{-9} \cdot z + 3.9 \cdot 10^{-9} \cdot z^2 - 1.4 \cdot 10^{-9} \cdot z^3 \\ +1.8 \cdot 10^{-10} \cdot z^4 - 1.0 \cdot 10^{-11} \cdot z^5 + 2.3 \cdot 10^{-13} \cdot z^6, \tag{6.6}$$

and

$$\Delta\alpha_{H_2O_2} = 4.3 \cdot 10^{-8} - 8.9 \cdot 10^{-9} \cdot z + 1.5 \cdot 10^{-9} \cdot z^2 - 3.5 \cdot 10^{-9} \cdot z^3 \\ +3.5 \cdot 10^{-10} \cdot z^4 - 1.5 \cdot 10^{-11} \cdot z^5 + 2.3 \cdot 10^{-13} \cdot z^6. \tag{6.7}$$

In figure 6.8a, and in figure 6.8b, the re-evaluated localised densities of HO_2 and H_2O_2 are illustrated as contourplots in a plane cut along the symmetry axis through the centre of the nozzle. Lateral profiles of these contourplots at different z-positions are presented in figure 6.8c, and in figure 6.8d, respectively. The densities of HO_2 and H_2O_2 were mainly distributed within a cone with a diameter of approximately 1.6 mm at $z = 0$ mm and 5 mm at $z = 10$ mm. Maximum densities of approximately $10 \cdot 10^{14}$ cm^{-3} for HO_2 and of $2 \cdot 10^{14}$ cm^{-3} H_2O_2 were obtained in the centre of the effluent between $z = 0$ mm and $z = 1.5$ mm, and $z = 0$ mm and $z = 4$ mm, for HO_2, and H_2O_2, respectively. For larger z-distances, the density of H_2O_2 decreased to approximately $1 \cdot 10^{14}$ cm^{-3} at 6 mm and remained approximately constant thereafter. The density of HO_2 decreased from $z = 1.5$ mm to $2 \cdot 10^{14}$ cm^{-3} at $z = 10$ mm. A constant density for H_2O_2 at distances larger than the region of production is expected, since H_2O_2 is a species with a low number of consumption reactions. The decrease of the density of HO_2 can be explained by reactions with the surrounding gas composition due to the high reactivity of HO_2 radicals.

(a) Contourplot for HO$_2$

(b) Contouplot for H$_2$O$_2$

(c) Lateral profiles of the contourplot for HO$_2$

(d) Lateral profiles of the contourplot for H$_2$O$_2$
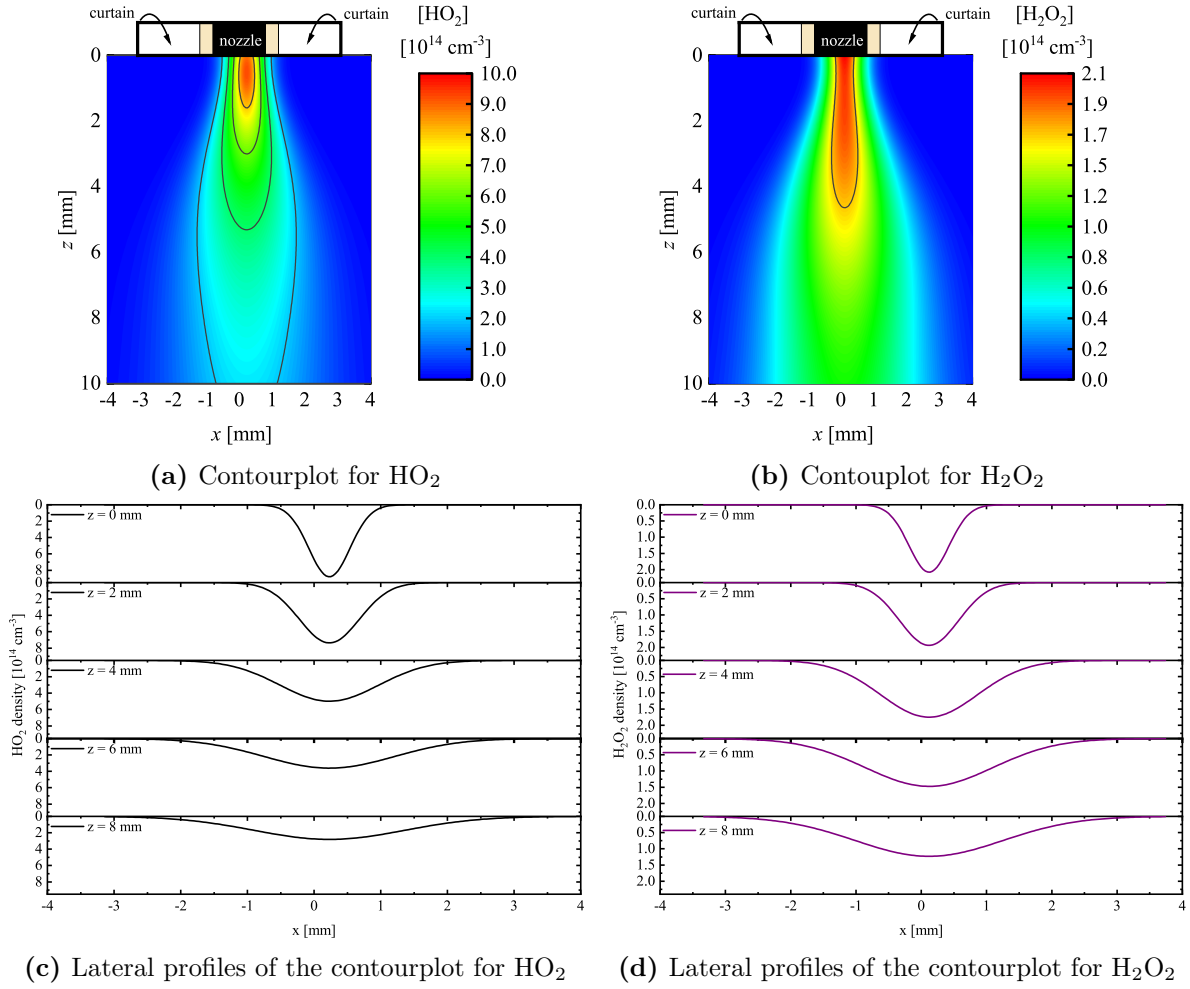
Figure 6.8: Re-evaluated localised densities of HO$_2$ and H$_2$O$_2$ illustrated as contourplots (a) and (b) in a plane cut along the symmetry axis through the centre of the nozzle and as lateral profiles (c) and (d) at different z-positions.

6.1.3 Asymmetry of the radial distributions

For all investigated spatial distributions of H, O, HO$_2$, and H$_2$O$_2$, an asymmetry was determined: The maxima of the densities close to the nozzle were shifted by approximately 0.25 mm to the centre of the nozzle. A similar asymmetry has also been found for the density of NO, reported by Iséni et al. [5]. In figure 6.9, the Ar emission between 845 nm and 855 nm obtained from an accumulation of 256 snapshots taken by an iCCD camera is depicted together with lateral profiles at various z-distances. This Ar emission pattern has the same shape and asymmetry as determined for the densities of H atoms. As the Ar emission is a result of metastable or electron impact reactions within the plasma zone or within the effluent close to the nozzle, an asymmetry of the discharge itself can be concluded. Due to inhomogeneties of the electrodes of the plasma jet, a specific direction for the filament inside could be preferred. Such a preferred direction leads to an localised increase of dissociation reactions of water, and finally to a localised
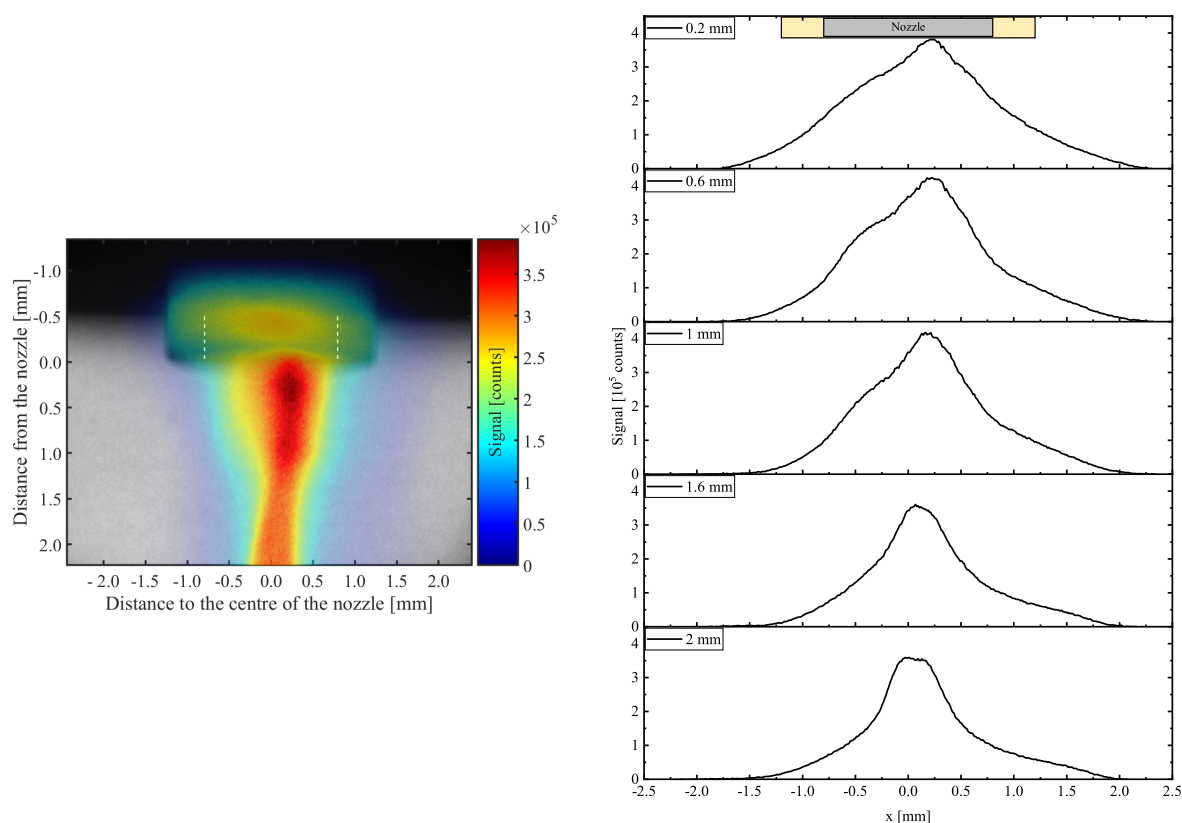
Figure 6.9: Ar emission between 845 nm and 855 nm, obtained from an accumulation of 256 snapshots taken by an iCCD camera. (a) overlay of the emission with a shadow image of the nozzle, (b) lateral profiles at various z-distances.

increase for the HO_2, and H_2O_2 production.

6.2 Impact of the gas curtain on the reactive species composition

In order to investigate the impact of the gas curtain close to the nozzle on the reactive species distributions, the gas curtain was varied from 100% O_2 to 100% N_2 while measuring the density of O atoms for dry Ar feed gas. If the gas curtain was the origin of the O atom density close to the nozzle, the density would be large for 100% O_2 and smaller for 100% N_2. However, it was found that the variation of the gas curtain was not influencing the absolute density of O atoms within the error bars (see also figure 3.12).

Another approach to investigate the influx of the gas curtain is the determination of the effective lifetime, which is is reduced due to quenching by species from the surrounding gas composition. With ps-TALIF, the effective lifetimes for O atoms in the excited state were determined experimentally. In figure 6.10, the effective lifetimes at $z = 0.25$ mm,

Figure 6.10: Effective lifetimes for O atoms in the excited state at $z = 0.25$ mm, $z = 1.37$ mm, $z = 2.37$ mm, and $z = 3.25$ mm as a function of the distance from the symmetry axis of the plasma jet x. A gas curtain of 5 slm O_2 was applied, the feed gas humidity in 3 slm Ar was 3000 ppm.
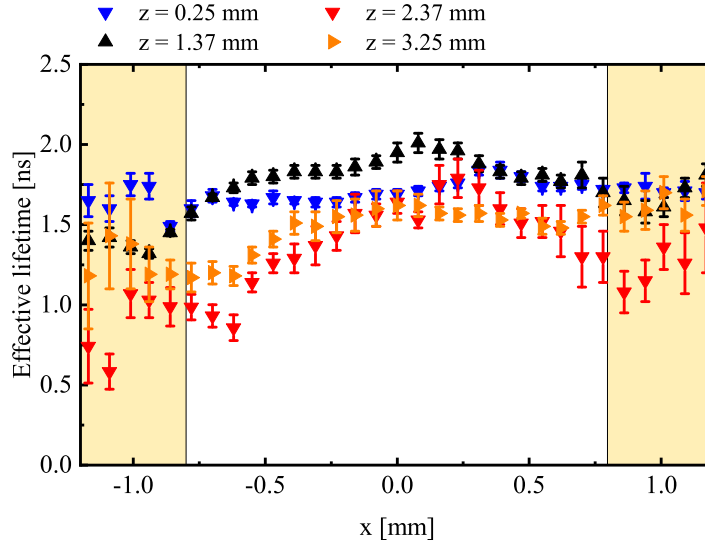
$z = 1.37$ mm, $z = 2.37$ mm, and $z = 3.25$ mm are depicted as a function of the distance from the symmetry axis of the plasma jet x, while a feed gas humidity of 3000 ppm at 3 slm Ar and a gas curtain of 5 slm O_2 were applied. At distances smaller than $z = 1.5$ mm, the effective lifetimes remained constant within the diameter of the nozzle. At larger distances z, a decrease of 30% of the effective lifetime at the position of the walls of the capillary was observed. The maximum of the effective lifetimes at distances larger than $z = 1.5$ mm was located between $x = 0$ mm and $x = 0.5$ mm, where also the maximum of the densities was determined. With increasing distance z from the nozzle, the maximum of the effective lifetime decreased from approximately 1.8 ns at $z = 0.25$ mm and $z = 1.37$ mm to 1.6 ns at $z = 3.25$ mm.

Based on the measured effective lifetimes $\tau_{\text{eff}}^{\text{meas}}$, and the quenching coefficients for O atoms by Ar, H_2O, and O_2, respectively, the density of O_2 can be determined by:

$$n_{O_2} = \frac{\frac{1}{\tau_{\text{eff}}^{\text{meas}}} - \frac{1}{\tau_{\text{nat}}} + n_{Ar} k_q^{Ar} + n_{H_2O} k_q^{H_2O}}{k_q^{O_2}} \qquad (6.8)$$

Here, $k_q^{Ar} = 1.4 \cdot 10^{-11}$ cm$^3/s$ [6], $k_q^{H_2O} = 11 \cdot 10^{-10}$ cm$^3/s$ [7], and $k_q^{O_2} = 9.4 \cdot 10^{-10}$ cm$^3/s$ [6] denote the quenching coefficients, $\tau_{\text{nat}} = 34.7$ ns is the natural lifetime for the O 3p ^3P_J state [6], and n_{Ar}, n_{H_2O}, and n_{O_2} are the densities of Ar, H_2O, and O_2, respectively. In figure 6.11, the densities of O_2 in the effluent, determined from the reduction of the effective lifetime of O atoms are depicted for various z-distances according to equation 6.8. Together with these densities, the density of O_2 obtained from molecular beam mass spectrometry investigations reported in reference [4] is presented. As the measurements by Dünnbier et al. were performed with a gas curtain composed of dry
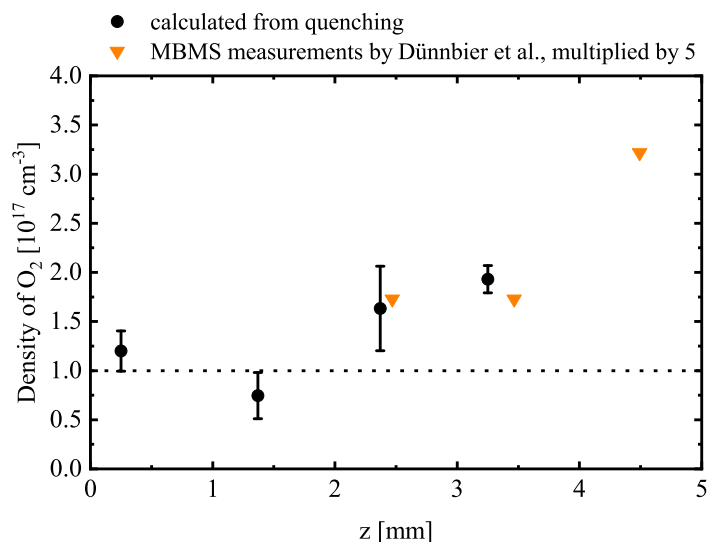
Figure 6.11: Densities of O_2 in the effluent for various z-distances, determined from the reduction of the effective lifetime of O atom together with the density of O_2 obtained from mass spectrometry investigations reported in reference [4]. As the measurements in reference [4] were performed with a gas curtain composed of dry air, the density of O_2 was multiplied by a factor of 5 in order to mimic the density of O_2 in the case of a gas curtain composed of pure O_2.

air, the density of O_2 was multiplied by a factor of 5 in order to mimic the density of O_2 in the case of a gas curtain composed of pure O_2.

Within the error, the densities of O_2 determined indirectly by ps-TALIF in this work are in agreement with the densities obtained by molecular beam mass spectrometry by Dünnbier et al. [4], while multiplying with a factor of 5. Between 0 and 1.5 mm from the nozzle, the O_2 density was constant at approximately $1 \cdot 10^{17}$ cm^{-3}. For further z-distances up to $z = 5$ mm, the density of O_2 increased linearly to approximately $3.5 \cdot 10^{17}$ cm^{-3}. The linear increase of O_2 molecules between $z = 1.5$ mm and $z = 5$ mm correlates with the linear decrease of the densities for O atoms, H atoms and HO_2 radicals in this region. At distances larger than 5 mm, the density of O_2 was approximately 3 orders of magnitude larger than the density of H and O atoms. This could explain the strong consumption of H atoms within the first 5 mm below the nozzle, as H atoms are consumed by the reaction with O_2 molecules to form HO_2 radicals. However, the production of HO_2 radicals within the effluent up to 5 mm below the nozzle due to the reaction of H atoms and O_2 molecules was smaller than other consumption reactions for HO_2, such as the reaction with H atoms, O atoms, and OH radicals. Based on the reaction rates and on the expected densities, the decrease of O atoms between $z = 1.5$ mm and $z = 5$ mm could also be due to the reaction of O atoms with O_2 molecules resulting in the formation of ozone.

In order to investigate the region between $z = 0$ mm and $z = 1.5$ mm in more detail, the effective lifetimes for O atoms in the excited state close to the nozzle at $z = 1$ mm were determined for dry Ar as a feed gas, while the gas curtain composition was varied. If
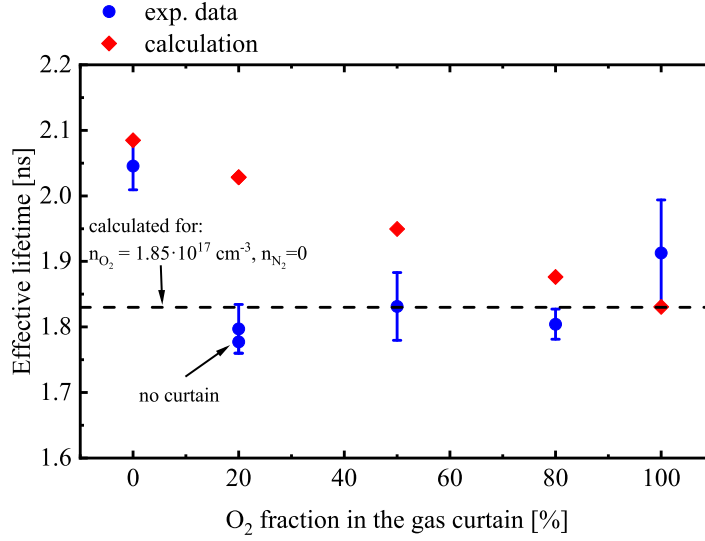
Figure 6.12: Effective lifetimes for O atoms in the excited state determined experimentally and by calculation (see equation 6.9) as a function of the oxygen fraction in the gas curtain at $z = 1$ mm at 3 slm dry Ar feed gas.

the density of O_2 molecules in the effluent originates from a diffusion of the gas curtain into the effluent, the effective lifetimes increase with a lower amount of O_2 and a higher amount of N_2 in the gas curtain due to a lower quenching efficiency of N_2 for O atoms. With the assumption that the diffusion of N_2 from the gas curtain into the feed gas is the similar to the diffusion of O_2, the effective lifetime τ_O^{eff} for O atoms in the excited state for various feed gas compositions with relative fractions χ_{O_2} of O_2 and $(1\text{-}\chi_{O_2})$ of N_2 can be described by:

$$\tau_O^{\text{eff}} = \left(\frac{1}{34.7 \text{ ns}} + n_{Ar} k_q^{Ar} + \underbrace{\chi_{O_2} N_{diff}}_{n_{O_2}} k_q^{O_2} + \underbrace{(1 - \chi_{O2}) N_{diff}}_{n_{N_2}} k_q^{N_2} \right)^{-1} . \qquad (6.9)$$

Here, N_{diff} is the density of O_2 and N_2 molecules that diffuse from the gas curtain into the effluent at $z = 1$ mm, $k_q^{Ar} = 1.4 \cdot 10^{-11}$ cm$^3/s$ [6], $k_q^{O_2} = 9.4 \cdot 10^{-10}$ cm$^3/s$ [6], and $k_q^{N_2} = 5.9 \cdot 10^{-10}$ cm$^3/s$ [8] are the quenching coefficients of O atoms by Ar, O_2, and N_2, respectively. The densities for Ar, O_2 and N_2 are denoted as n_{Ar}, n_{O_2}, and n_{N_2}. In figure 6.12, the experimentally determined lifetimes of O atoms in the excited state at $z = 1$ mm are depicted as a function of the oxygen fraction χ_{O_2} in the gas curtain together with the calculated lifetimes for a density of Ar of 2.45 cm^{-3}, and a total density N_{diff} of $1.85 \cdot 10^{17}$ cm^{-3}.

The measured effective lifetimes for O atoms in the excited state for an oxygen fraction equal to or larger than 20% in the gas curtain was, within the error, in agreement with an effective lifetime for O atoms in the excited state that was calculated for a constant density of O_2 of $1.85 \cdot 10^{17}$ cm^{-3} without considering a diffusion of the gas curtain into the effluent represented by the dashed line in figure 6.12. This is in contrast to

a decrease of the effective lifetime expected for an increasing amount of O$_2$ in the gas curtain that diffuses into the effluent. However, for a pure N$_2$ curtain, the measured effective lifetime was in agreement within the error with the calculated lifetime at a diffusion of $N_{diff} = 1.85 \cdot 10^{17}$ cm^{-3} from the gas curtain into the effluent. Based on the comparison of the measured and calculated effective lifetimes, it can be concluded that the diffusion of the gas curtain into the effluent up to $z = 1.5$ mm is negligible at least in the case for a gas curtain composition that contains more than 20% of O$_2$. This is in agreement with investigations by Schlieren diagnostics, and by particle image flow velocimetry: it was found that the gas composition of the effluent at distances smaller than $z = 1.5$ mm is determined by the feed gas composition coming from the plasma zone. The constant density of O$_2$ molecules between $z = 0$ mm and $z = 1.5$ mm determined for both, the variation of the effective lifetime of O atoms as a function of the distance from the nozzle at a gas curtain composition of 100% O$_2$ with 3000 ppm humidity in the feed gas, and as a function of the fraction of O$_2$ in the gas curtain at $z = 1$ mm at dry feed gas conditions, leads to the conclusion that a certain amount of O$_2$ needs to be present already within the plasma zone. Notably, the plasma processes are different for dry and humidified feed gas conditions. Hence, the residual value of $1.85 \cdot 10^{17}$ cm^{-3} for O$_2$ obtained for dry Ar feed gas is expected to differ from the value of approximately $1 \cdot 10^{17}$ cm^{-3} for O$_2$, which was determined to be present within the plasma zone with 3000 ppm humidity.

6.3 Origin of O$_2$ in the plasma zone

As HO$_2$ is produced by the reaction of H atoms and O$_2$ molecules, an initial amount of minimum $1 \cdot 10^{15}$ cm^{-3} of O$_2$ is necessary to obtain the measured densities of HO$_2$ close to the nozzle, which are depicted in figure 6.8a). With the assumption that O atoms were mainly produced by the dissociation of O$_2$, the lower limit for an initial concentration for O$_2$ in the plasma zone is $1.9 \cdot 10^{15}$ cm^{-3} to explain the measured O atom densities close to the nozzle, which are presented in figure 3.13b. By considering the effective lifetime of Ar(^{3}P$_2$), an initial amount of $(1.8 \pm 0.95) \cdot 10^{16}$ cm^{-3} for O$_2$ additionally to the feed gas humidity is necessary to explain the decay rates, where the reaction of Ar(^{3}P$_2$) + O$_2 \rightarrow$ Ar + O + O with a reaction rate of $k_{O_2} = 2.1 \cdot 10^{-10}$ cm^3/s [9] was assumed to be the dominant quenching reaction for Ar(^{3}P$_2$). According to the analysis of the effective lifetimes for O atoms, an initial amount of approximately $1 \cdot 10^{17}$cm^{-3} for O$_2$ was present during the experiments.

In order to investigate, if the density of O$_2$ within the plasma zone of the kINPen-sci plasma jet was caused by impurities within the feed gas due to leakage of the gas tubings, the content of O$_2$ in the feed gas was measured by a high-precision oxygen analyser (zirconia measurement cell, Zirox). Therefore, the nozzle was connected to the Zirox-sensor via a sealed cap mounted in the head of the plasma jet. No gas curtain was applied, and the plasma was switched off. For both cases, dry Ar feed gas and humidified Ar feed gas with 3000 ppm water, a concentration for O$_2$ of approximately

$5 \cdot 10^{14}$ cm^{-3} was obtained. This is approximately a factor of 8 lower than the density of O atoms that was determined by ps-TALIF. Thus, the determined density of O$_2$ in the plasma zone was not due to a leakage of the gas tubings.

To investigate, if the plasma causes turbulences within the nozzle that build vortex structures, thereupon sucking in O$_2$ from the surrounding gas composition, the plasma jet was operated within a sealed box. The head of the plasma jet was placed in an opening on top of the lid of the box, and no gas curtain was applied. The outlet of the box was connected to the Zirox-sensor. With dry Ar feed gas, the residual concentration of O$_2$ was approximately $1.5 \cdot 10^{14}$ cm-3 that was reduced to $1.3 \cdot 10^{14}$ cm^{-3} after switching the plasma jet on. After switching the plasma jet off again, a concentration of $1.5 \cdot 10^{14}$ cm^{-3} for O$_2$ was reached after 80 s, which is approximately the response time of the sensor connected to the box. In the case of a feed gas humidity of 3000 ppm, the residual concentration of $1.7 \cdot 10^{14}$ cm^{-3} for O$_2$ was reduced to less than $5 \cdot 10^{11}$ cm^{-3}, which is the detection limit of the Zirox-sensor. Within approximately 80 s, the residual concentration of $1.7 \cdot 10^{14}$ cm^{-3} for O$_2$ was reached after the plasma jet was switched off again. The stronger reduction of the residual concentration of O$_2$ in the case of feed gas humidity can be explained by a consumption of O$_2$ by H atoms for example. Based on the measurements with the Zirox-sensor, it can be concluded that the origin of the measured O$_2$ concentration in the plasma zone is not due to leakage of the gas tubings.

Since an initial amount of O$_2$ in the plasma zone of approximately $1.85 \cdot 10^{17}$ cm^{-3} in the case of dry Ar feed gas, and approximately $1 \cdot 10^{17}$ cm^{-3} in the case of Ar feed gas with 3000 ppm humidity, could not be determined to be due to leakages, plasma processes, such as the excitation dynamics, could be the reason. Schmidt-Bleker et al. reported a backwards directed excitation wave (towards the inside of the plasma zone) in the positive half wave of the applied voltage for a pure oxygen gas curtain and dry feed gas in a helium operated plasma jet [10]. The speed of this backwards directed wave was two orders of magnitude higher than the flow of the feed gas. Reuter et al. observed a similar feature for the same plasma jet operated with argon [11]. With such a backwards directed excitation wave, negative molecular oxygen ions could propagate from the effluent into the plasma zone and act as a source for O$_2$. Two ionisation waves within a voltage cycle were also observed in the presence of feed gas humidity during the investigations of Ar(^{3}P$_2$). A more detailed analysis of the origin of O$_2$ in the plasma zone remains for further investigations.

6.4 Summary

For the investigated molecular species, namely HO_2 and H_2O_2, Gaussian distributions with a centre position shifted by approximately $r_0 = 0.25$ mm from the symmetry axis of the kINPen-sci plasma jet were obtained. The atomic species O and H atoms were distributed within the diameter of the nozzle with a similar asymmetry, which was also determined for the emission pattern of excited Ar atoms. As the asymmetry was similar for all investigated species' distributions, the origin is most likely within the plasma zone: Due to inhomogeneities of the needle electrode, a specific position for the filamentary discharge is preferred, which results in a local increase of the density for $Ar(^3P_2)$ and thus of dissociation product, such as H atoms, OH radicals and O atoms. Consequently, the formation of HO_2 and H_2O_2 is also increased due to the higher density of precursors.

By comparing the width of the radial distributions with the diameter over which the feed gas is distributed that was obtained from Schlieren diagnostics [2] and particle image flow velocimetry [3], a combined absorption length for HO_2 and H_2O_2 was determined. Based on the corrected absorption length, the spatial density distributions for HO_2 and H_2O_2 were re-evaluated. The maxima were found close to the nozzle with $10 \cdot 10^{14}$ cm^{-3} for HO_2, and with $2.1 \cdot 10^{14}$cm^{-3} for H_2O_2. From $z = 1.5$ mm to $z = 10$ mm, both densities decreased to $5 \cdot 10^{14}$ cm^{-3}, and $1 \cdot 10^{14}$ cm^{-3}, respectively. It was found that both, HO_2, and H_2O_2 were mainly distributed within the boundaries for the Ar feed gas flow. This indicates, that most of the species densities were produced within the plasma zone. Furthermore, up to $z = 1.5$ mm, the impact of the gas curtain on the reactive species distribution is negligible, as the diffusion of the gas curtain into the effluent starts at approximately $z = 1.5$ mm and increases strongly starting from $z = 4$ mm. This was also confirmed by the analysis of the effective lifetime for O atoms, while varying the composition of the gas curtain.

By investigating the spatial distribution for the effective lifetime of O atoms in the excited state in TALIF, a density of approximately $1 \cdot 10^{17}$ cm^{-3} O_2 molecules was determined to be present within the plasma zone. This amount of O_2 was not a result of leakage, which was investigated by employing an oxygen sensor for the analysis of the feed gas and of the plasma jet operated in a closed box. An explanation for the O_2 density within the plasma zone could be the occurrence of counter-propagating ionisation waves, which were observed during the measurements for $Ar(^3P_2)$: With an additional ionisation wave within the second half of the excitation period, O_2 or air could have been sucked into the plasma zone. It is also likely, that O_2^--anions formed around a filament propagate into the plasma zone during the counter-propagating ionisation wave. A more detailed description remains for further investigations.

In conclusion, for the reactive species compositions, three different zones were determined. Close to the nozzle, between $z = 0$ mm and $z = 1.5$ mm, the reactive species composition is dominated by reactions within the plasma zone. Between $z = 1.5$ mm and $z = 5$ mm, atomic species were fully consumed by reactions with the gas curtain that diffused into the effluent. The densities of HO_2 and H_2O_2 decreased due to reactions

with the gas curtain. For further distances $z > 5$ mm, the production and consumption of HO_2 and H_2O_2 were lower resulting in a slight decrease of both densities.

6.5 Bibliography

[1] M. Gianella, S. Reuter, S. A. Press, A. Schmidt-Bleker, J. H. van Helden, and G. A. D. Ritchie. HO$_2$ reaction kinetics in an atmospheric pressure plasma jet determined by cavity ring-down spectroscopy. *Plasma Sources Sci. Technol.*, 27(095013), 2018.

[2] A. Schmidt-Bleker, S. Reuter, and K.-D. Weltmann. Quantitative schlieren diagnostics for the determination of ambient species density, gas temperature and calorimetric power of cold atmospheric plasma jets. *J. Phys. D: Appl. Phys.*, 48(175202), 2015.

[3] P. Mattern. Particle Image Flow Velocimetry for the kINPen plasma jet. Internal communications.

[4] M. Dünnbier, A. Schmidt-Bleker, J. Winter, M. Wolfram, R. Hippler, K.-D. Weltmann, and S. Reuter. Ambient air particle transport into the effluent of a cold atmospheric-pressure argon plasma jet investigated by molecular beam mass spectrometry. *J. Phys. D: Appl. Phys.*, 46(435203), 2013.

[5] S. Iseni, S. Zhang, A. F. H. van Gessel, S. Hofmann, B. T. J. van Ham, S. Reuter, K.-D. Weltmann, and P. J. Bruggeman. Nitric oxide density distributions in the effluent of an RF argon APPJ: effect of gas flow rate and substrate. *New J. Phys.*, 16(12301), 2014.

[6] K. Niemi, V. Schulz-von der Gathen, and H. F. Döbele. Absolute atomic oxygen density measurements by two-photon absorption laser-induced fluorescence spectroscopy in an RF-excited atmospheric pressure plasma jet. *Plasma Sources Sci. Technol.*, 14:375, 2005.

[7] S. Schröter, J. Bredin, A. R. Gibson, A. West, J. P. Dedrick, E. Wagenaars, K. Niemi, T. Gans, and D. O'Connell. The formation of atomic oxygen and hydrogen inatmospheric pressure plasmas containinghumidity: picosecond two-photon absorption laserinduced fluorescence and numerical simulations. *Plasma Sources Sci. Technol.*, 29(105001), 2020.

[8] K. Niemi, V. Schulz-von der Gathen, and H. F. Döbele. Absolute calibration of atomic density measurements by laser-induced fluorescence spectroscopy with two-photon excitation. *J. Phys. D: Appl. Phys.*, 34:2330, 2001.

[9] L. G. Piper, J. E. Velazco, and D. W. Setser. Quenching cross sections for electronic energy transfer reactions between metastable argon atoms and noble gases and small molecules. *J. Chem. Phys.*, 59(6):3323–40, 1973.

[10] A. Schmidt-Bleker, J. Winter, S. Iséni, M. Dünnbier, K.-D. Weltmann, and S. Reuter. Reactive species output of a plasma jet with a shielding gas device - combination of FTIR absorption spectroscopy and gas phase modelling. *J. Phys. D: Appl. Phys.*, 47(145201), 2014.

[11] S. Reuter, J. Winter, S. Iseni, S. Peters, A. Schmidt-Bleker, M. Dünnbier, J. Schäfer, R. Foest, and K.-D. Weltmann. Detection of ozone in a MHz argon plasma bullet jet. *Plasma Sources Sci. Technol.*, 21(034015), 2012.

7 Plasma chemical and reacting flow model to investigate the reaction kinetics in the effluent of the kINPen-sci plasma jet
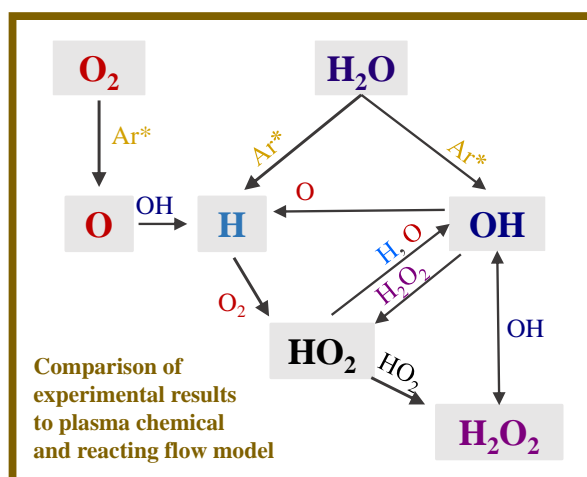
In order to determine the amount of initial O_2 that would have been necessary in the plasma zone to explain the obtained H and O atom densities, and to identify the most dominant reaction pathways, the experimental results were compared with predictions from a two-dimensional reacting flow model that was coupled with a local zero-dimensional plasma chemical model. Firstly, the plasma chemical and reacting flow model is described as adapted from reference [1]. Afterwards, the simulated density distributions are compared to the densities which were determined experimentally. Based on the comparison, the main production and consumption reactions are obtained by determining the rate constants.

7.1 Description of the plasma chemical and reacting flow model

The plasma chemical and reacting flow model is based on a two-dimensional axisymmetric model of the turbulent reacting flow coupled with a local zero-dimensional plasma chemical model for the kINPen plasma jet, reported by Semenov et al. [2]. The model describes the formation and transport of chemically reactive species in the plasma zone and the effluent of the jet, whereas the plasma zone is characterised by a local zero-dimensional model, and the gas flow and transport of reactive species are calculated by solving the boundary-layer form of the Navier-Stokes equations.

In the present study, the following species are taken into account: Electrons (e), ground state argon atoms (Ar), metastables of argon (Ar*) in the Ar(^{3}P$_{2,0}$) state, argon excimers (Ar$_2^*$) in the Ar$_2^3\Sigma_u^+$ state, argon cations (Ar$^+$), diargon cations (Ar$_2^+$), ground state nitrogen molecules (N$_2$), ground state oxygen molecules (O$_2$), water molecules (H$_2$O), electronically excited nitrogen molecules (N$_2^*$) in the N$_2$A$^3\Sigma_u^+$ state, electronically excited oxygen molecules (O$_2^*$) in the O$_2$ a$^1\Delta_g$ state, oxygen atoms (O), nitrogen atoms (N), hydrogen atoms (H), ground state hydroxyl radicals (OH), vibrationally excited hydroxyl radicals in the first two vibration levels (OH$_{v=1}^*$ and OH$_{v=2}^*$), hydrogen molecules (H$_2$), hydroperoxyl radicals (HO$_2$), hydrogen peroxide (H$_2$O$_2$), ozone (O$_3$), nitrogen monoxide (NO), nitrogen dioxide (NO$_2$), nitrate (NO$_3$), nitroxyl (HNO), nitrous acid (HNO$_2$), and nitric acid (HNO$_3$).

The governing equations of the model are solved in cylindrical coordinates (r, z), where the z-axis runs along the axis of the jet and r is the radial distance. The species mass fractions, ω_α, are determined by:

$$\rho\frac{d\omega_\alpha}{dt} = \frac{1}{r}\frac{\partial}{\partial r}\left(r\rho D_\alpha\frac{\partial \omega_\alpha}{\partial r}\right) + m_\alpha\left(G_\alpha + R_\alpha\right). \tag{7.1}$$

Here, α stands for the type of species, d/dt is the substantial derivative, ρ is the gas density, m_α is the mass, D_α is the diffusion coefficient, and G_α and R_α are chemical source terms, which represent the contribution of different chemical reactions. The substantial derivative is given by:

$$d/dt = \partial/\partial t + u\,\partial/\partial z + v\,\partial/\partial r. \tag{7.2}$$

Here, t is time, u and v are the axial and radial gas velocities, respectively. The velocity field and diffusion coefficient in equation (7.1) are obtained by solving the corresponding flow problem in the plasma zone and the effluent [2]. G_α are the rates for the plasma induced chemical reactions summarised in table 7.1 that describe the formation of primary reactive species (N, O, H, OH, N$_2^*$) due to dissociation and excitation of N$_2$, O$_2$, and H$_2$O.

The spatio-temporal dependence of the production and loss rates is given by a simplified

Table 7.1: List of reactions used in the plasma chemical model.

No.	Reaction[a]	Rate coefficient[b]	References
E1	$e + Ar \rightarrow e + e + Ar^+$	BOLSIG+	[3][c]
E2	$Ar^+ + Ar + M \rightarrow Ar_2^+ + M$	2.5×10^{-31}	[4]
E3	$e + Ar_2^+ \rightarrow Ar + Ar$	$5.38 \times 10^{-8} \, T_e^{-0.66}$	[5][d]
E4	$e + Ar \rightarrow e + Ar^*$	BOLSIG+	[3][c]
E5	$Ar^* + Ar + M \rightarrow Ar_2^* + M$	2.8×10^{-33}	[6]
E6	$Ar_2^* \rightarrow Ar + Ar$	3.5×10^5	[6]
E7	$Ar_2^* + Ar \rightarrow Ar + Ar + Ar$	1.0×10^{-14}	[7][e]
E8	$Ar^* + O_2 \rightarrow Ar + O + O$	2.1×10^{-10}	[8]
E9	$Ar^* + N_2 \rightarrow Ar + N + N$	1.8×10^{-11}	[8][f]
E10	$Ar^* + N_2 \rightarrow Ar + N_2^*$	1.8×10^{-11}	[8][f]
E11	$Ar^* + H_2O \quad\quad \rightarrow$ $Ar + H + OH$	7.8×10^{-10}	[9]
E12	$Ar_2^* + O_2 \quad\quad \rightarrow$ $Ar + Ar + O + O$	4.6×10^{-11}	[10]
E13	$Ar_2^* + N_2 \quad\quad \rightarrow$ $Ar + Ar + N + N$	6.0×10^{-12}	[7][f]
E14	$Ar_2^* + N_2 \rightarrow Ar + Ar + N_2^*$	6.0×10^{-12}	[7][f]
E15	$Ar_2^* + H_2O \quad\quad \rightarrow$ $Ar + Ar + OH + H$	7.8×10^{-10}	[9]

[a] M denotes a third body (the concentration of M is $2.44 \times 10^{19} \, cm^{-3}$).

[b] The units of rate coefficients are s^{-1}, $cm^3 \, s^{-1}$, $cm^6 \, s^{-1}$ for the first, second and third order reactions, respectively. The electron temperature is in units of eV.

[c] The reaction rates were computed as functions of T_e using the BOLSIG+ code [3]. The details of the computations are given in ref. [2].

[d] Reaction yields the excited Ar atom, which sequentially decays to the ground state.

[e] Reaction yields $Ar_2(^1\Sigma_u^+)$, which then dissociates into Ar atoms.

[f] Quenching rates of Ar^* ($3.6 \times 10^{-11} \, cm^3 \, s^{-1}$) and Ar_2^* ($1.2 \times 10^{-11} \, cm^3 \, s^{-1}$) by N_2 are branched for the formation of N and N_2^*

model:

$$G_\alpha(t, r, z) = G_\alpha(t, 0, z) \exp[-(r/r_0)^2]. \tag{7.3}$$

Here, r_0 is the characteristic radius of the power deposition profile in the jet, which describes the characteristic radius of the ionization wave propagating along the jet axis. The radius r_0 is estimated to be $0.1 - 0.5$ mm according to the data presented

in [11, 12], whereas the production terms $G_\alpha(t, 0, z)$ are defined by using a local zero-dimensional plasma chemical model described in detail in [2]. With this local zero-dimensional model, mass balance equations for the species concentrations and energy balance equations for the electron temperature are solved. The heating of electrons is modelled by prescribing the source of the power density, $Q(t, z)$, in the energy balance equation. The spatio-temporal dependence of $Q(t, z)$ is given by:

$$Q(t, z) = Q_t(t)Q_z(z). \tag{7.4}$$

Here, $Q_t(t)$ simulates the heating of electrons in the ionization wave and is described by a periodic rectangular pulse with an amplitude of Q_0 and width τ. The repetition rate is set to 1 MHz, which is equal to the frequency of the plasma jet. The axial profile of the power density, Q_z, is taken as constant inside the plasma zone and is given for the effluent by:

$$Q_z = \exp[-(z/z_0)^2]. \tag{7.5}$$

Here, z_0 is the characteristic length of the power density decay. The profile Q_z is chosen mainly by analogy with that used in [13], where a similar electrode configuration to that of the kINPen-sci plasma jet was considered.

R_α are the rates for the reactions listed in table 7.2, which are calculated from the product of the reagents, the rate coefficient given in the third column of table 7.2, and the corresponding stoichiometric coefficient. All the densities given by the plasma chemical and reacting flow model are periodic steady-state solutions. Further details about the model and its numerical implementation can be found in [2].

7.2 Comparison to numerical simulations

In figure 7.1, contour plots for the spatial distributions of H atoms, O atoms, HO_2 radicals, and H_2O_2 molecules obtained by the plasma chemical and reacting flow model are illustrated as a function of the radial distance from the centre of the nozzle x and the axial distance from the nozzle z. The model was evaluated for a feed gas composition of 3 slm Ar, 3000 ppm of water, and with 3.8% admixture of synthetic air that was composed of 80% N_2 and 20% O_2. The initial power density input was set to $Q_0 = 139$ kW cm^{-3}, while the filament duration was determined to $\tau = 70$ ns, the radius for the streamer head was $r_0 = 0.3$ mm, and characteristic length for the power density decay was $z_0 = 2.3$ mm.

The measured O and H atom densities are found to be distributed over the complete diameter of the nozzle as shown in figure 3.13, while the simulated densities depicted in figure 7.1a and in figure 7.1b, respectively, are limited by the assumption that the filament propagates only in a narrow radial range of $r = 0.3$ mm along the symmetry axis of the plasma jet. However, observations have shown that the excitation wave changes its direction due to inhomogeneities at the needle electrode and due to the
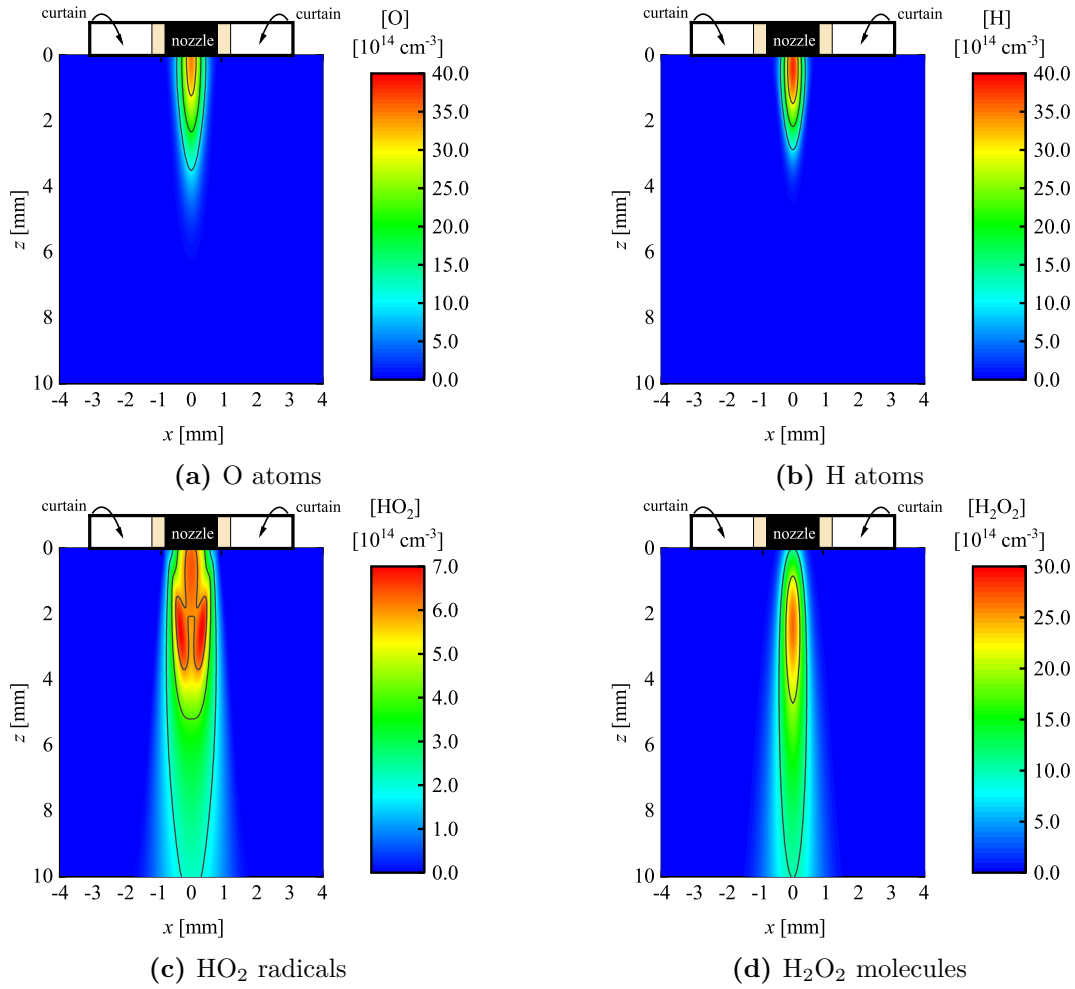
(a) O atoms

(b) H atoms

(c) HO₂ radicals

(d) H₂O₂ molecules

Figure 7.1: Spatial distributions for (a) H atoms, (b) O atoms, (c) HO_2 radicals, and (d) H_2O_2 molecules as a function of the radial distance to the symmetry axis of the plasma jet x and of the axial distance from the nozzle z, obtained from the plasma chemical and reacting flow model. The input parameter for the model were: 3 slm Ar for the feed gas with 3000 ppm humidity and 3.8% of synthetic air, $Q_0 = 139$ kW cm^{-3}, $\tau = 70$ ns, $r_0 = 0.3$ mm, and $z_0 = 2.3$ mm.

turbulent gas flow [28] that could explain the broader distributions obtained by the experiments. In the simulation, the atomic densities of O and H are decreasing to a value below the experimental detection limit in a shorter distance than observed in the experiments. If the error for the experimental values are taken into account, the experimental values are in agreement with the simulation. The maximum of the HO_2 density depicted in figure 7.1c was located at approximately 3 mm below the nozzle. Between $z = 2$ mm and $z = 4$ mm, the density of HO_2 increased by approximately $1 \cdot 10^{14}$ cm^{-3} to $7 \cdot 10^{14}$ cm^{-3} in the regions close to the position of the boundary for the capillary resulting in a toroidal density distribution. The increase of HO_2 at the position of the boundary for the capillary is due to the inwards diffusion of the gas curtain into the effluent thereby increasing the amount of O_2 and thus the production of HO_2
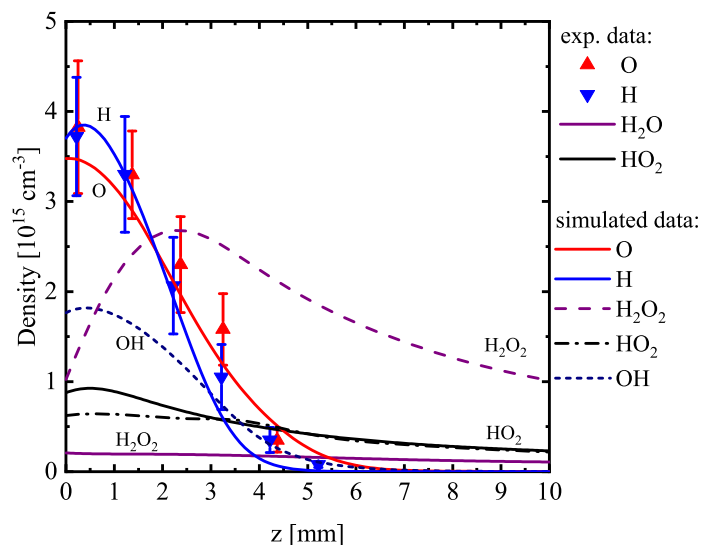
Figure 7.2: Number densities of O atoms, H atoms, HO_2 radicals, and H_2O_2 molecules along the symmetry axis of the plasma jet as determined experimentally and by the plasma chemical and reacting flow model.

radicals due to the reaction of O_2 with H atoms. Such a toroidal density distribution was not determined experimentally. This could be either due to the lower resolution in radial direction for the experimental method, or due to a wider distribution of H atoms in the experiment resulting in a density distribution for HO_2 with a Gaussian shape. A more detailed analysis remains for further investigations. For H_2O_2, the maximum density was located at approximately $z = 3$ mm as illustrated in figure 7.1d. However, the maximum value for H_2O_2 was by a factor of approximately 10 higher than the density determined experimentally that was located close to the nozzle. The differences between model and experimentally determined values could be due to an overestimation of species that were not measured. For instance, H_2O_2 depends strongly on the presence of OH, which has not been determined yet.

In figure 7.2, the densities of O atoms, H atoms, HO_2 radicals, and H_2O_2 molecules along the symmetry axis of the plasma jet are depicted as determined experimentally and by the plasma chemical and reacting flow model. Together with these results, the simulated density for OH is presented. The experimental data for O atoms, H atoms, and HO_2 radicals agree well with the values determined by the plasma chemical and reacting flow model when $1.86 \cdot 10^{17} \mathrm{cm}^{-3}$ of O_2, and $7.45 \cdot 10^{17} \mathrm{cm}^{-3}$ of N_2 were added to the humid argon feed gas in the simulation. However, the measured density for H_2O_2 is an order of magnitude lower than the density of H_2O_2 obtained by the plasma chemical and reacting flow model.

In order to identify the most dominant reaction pathways, the rate constants were investigated as a function of the distance from the nozzle z. The rate constants are a measure for the temporal evolution of the species densities due to a specific reaction and depend on the densities of the precursors involved, and on the corresponding rate coefficient. In figure 7.3, the rate constants for the main reactions pathways for H
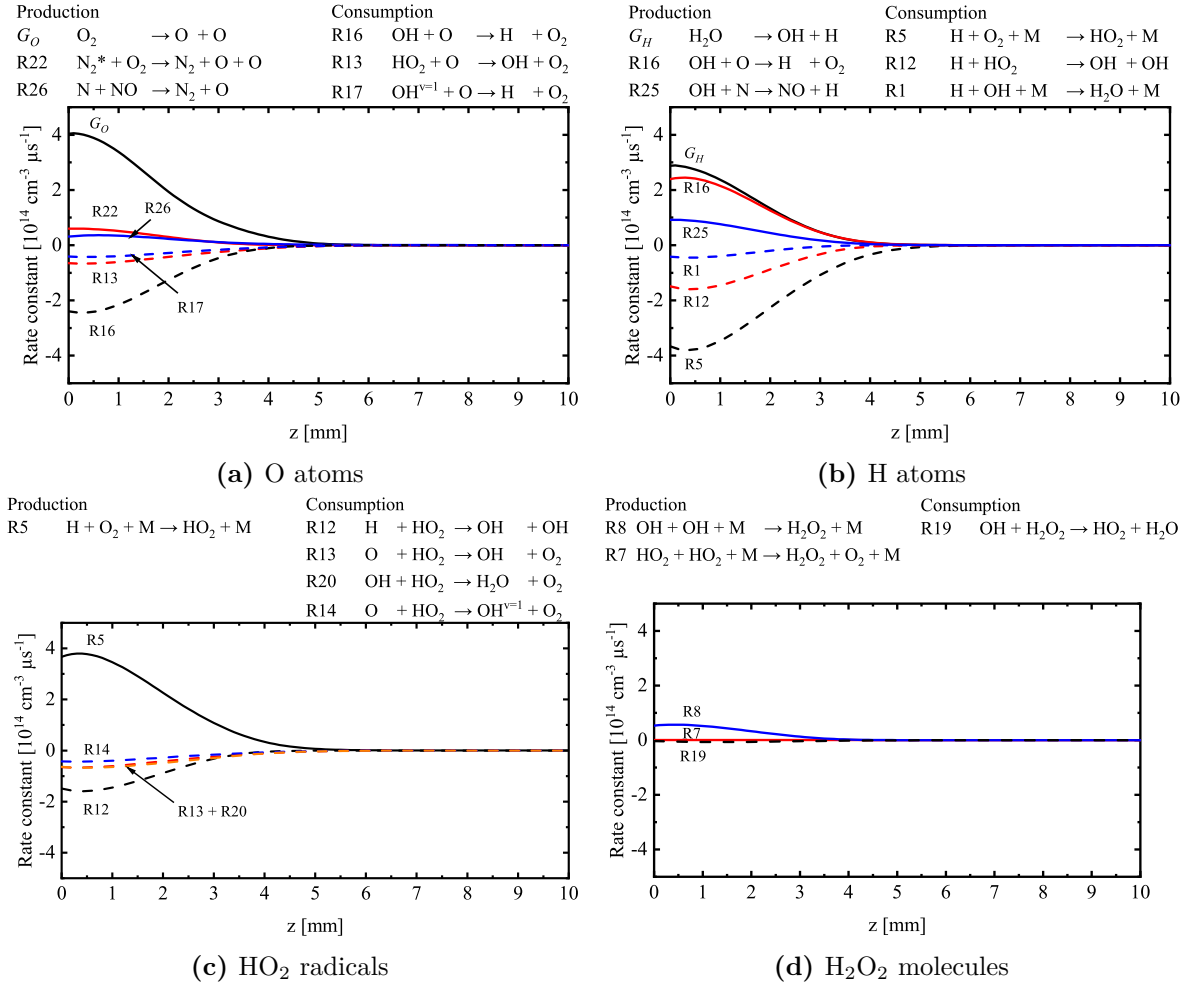
Production		Consumption	
G_O	$O_2 \rightarrow O + O$	R16	$OH + O \rightarrow H + O_2$
R22	$N_2^* + O_2 \rightarrow N_2 + O + O$	R13	$HO_2 + O \rightarrow OH + O_2$
R26	$N + NO \rightarrow N_2 + O$	R17	$OH^{v=1} + O \rightarrow H + O_2$

Production		Consumption	
G_H	$H_2O \rightarrow OH + H$	R5	$H + O_2 + M \rightarrow HO_2 + M$
R16	$OH + O \rightarrow H + O_2$	R12	$H + HO_2 \rightarrow OH + OH$
R25	$OH + N \rightarrow NO + H$	R1	$H + OH + M \rightarrow H_2O + M$

(a) O atoms

(b) H atoms

Production		Consumption	
R5	$H + O_2 + M \rightarrow HO_2 + M$	R12	$H + HO_2 \rightarrow OH + OH$
		R13	$O + HO_2 \rightarrow OH + O_2$
		R20	$OH + HO_2 \rightarrow H_2O + O_2$
		R14	$O + HO_2 \rightarrow OH^{v=1} + O_2$

Production		Consumption	
R8	$OH + OH + M \rightarrow H_2O_2 + M$	R19	$OH + H_2O_2 \rightarrow HO_2 + H_2O$
R7	$HO_2 + HO_2 + M \rightarrow H_2O_2 + O_2 + M$		

(c) HO$_2$ radicals

(d) H$_2$O$_2$ molecules

Figure 7.3: Production and consumption rate constants for (a) O atoms and (b) H atoms as a function of the axial distance z from the nozzle

atoms, O atoms, HO$_2$ radicals, and H$_2$O$_2$ molecules are shown as a function of the axial distance z. G_O and G_H denote the source terms for O and H atoms respectively, as resulting from the local plasma chemical model. The labels R_i correspond to the individual reactions presented in table 7.2, as obtained from the reacting flow model.

The production and consumption rates for all measured species were highest at the nozzle outlet. Within the first mm below the nozzle, the rate constants were almost constant. For further distances they decreased to 0 at approximately $z = 5$ mm. This is in agreement with the previous results: up to approximately 1 mm, the species densities were dominated by processes within the plasma zone. Notably, an amount of $1.86 \cdot 10^{17}$cm^{-3} for O$_2$ was added to the feed gas in the plasma zone to mimic the experimental results. This value is by approximately a factor of 2 higher than the amount of O$_2$ necessary to explain the measured effective lifetime of O atoms close to the nozzle. Since in the model also N$_2$ was added to the feed gas due to the assumption that air could have been drifted into the plasma zone by backwards directed ionisation waves, the power consumption by other species than O$_2$ has to be considered. For an admixture

of pure O_2, a lower density could have been sufficient to produce the measured O atom density. A more detailed analysis remains for further investigations. With the diffusion of the gas curtain into the effluent between approximately $z = 1.5$ mm to $z = 5$ mm, the species densities decreased strongly. For further distances z, radicals were mainly consumed and production reactions of HO_2 and H_2O_2 level off at a constant value.

According to the plasma chemcial and reacting flow model, O atoms were mainly produced by the dissociation of O_2 molecules by metastable Ar atoms and excimers described by the source term G_O. Although reactions with N_2 were considered in the model (R21 - R39), their impact was small compared to the impact of O_2. Notably, as a result of the simulation, H_2O was not a source for O atoms. As the main consumers for O atoms, OH (R16, R17) and HO_2 (R13) radicals were identified.

The H atom formation was not only governed by the dissociation of H_2O into OH and H due to the impact of metastable argon atoms and excimers, but also through reactions (R16) and (R17) of O with OH, which, as mentioned before, are dominant consumption pathway for the O atoms. The H atom consumption is mainly through the three-body reactions with O_2 (R5) and OH (R1), and to some extend through reaction (R12).

The dominant production and consumption reactions for HO_2 are in agreement with the reactions reported previously in reference [29]. In this work, the formation of HO_2 was due to the reaction of H atoms with O_2 molecules (R5), and the main consumers were H atoms (R12), O atoms (R13, R14), and OH radicals (R20).

H_2O_2 was mainly produced by the three body reaction of OH (R8) and to some extend of HO_2 (R7). The only consumption reaction that was considered was the reaction of OH radicals with H_2O_2, while producing HO_2 and H_2O (R19).

The formation of ozone as a stable end product is covered in the plasma chemical and reacting flow model through the three-body reaction (R4) of O with O_2. The corresponding rate, when compared with other O atom consumption pathways, is found to be a factor of 15 lower than the combined rate of the O with HO_2 reactions (R13 - R15), and a factor of about 30 lower than the combined rate of the O with OH reactions (R16 - R18). This is in agreement with the decrease of the ozone net production rate due to humidity admixtures greater than 1000 ppm to the feed gas, as previously reported by Winter et al. [30]; at such humidity admixtures, the consumption of O is dominated by OH and HO_2 rather than by O_2 to form ozone.

7.3 Summary

A plasma chemical and reacting flow model was used to identify the most dominant reaction pathways. The best agreement of the model with the experimental data was obtained for a feed gas composition of 3 slm Ar, 3000 ppm of water, and with 3.8% admixture of synthetic air that was composed of 80% N_2 and 20% O_2. The initial power density input was set to $Q_0 = 139$ kW cm^{-3}, while the filament duration was determined to $\tau = 70$ ns, the radius for the streamer head was $r_0 = 0.3$ mm, and characteristic length for the power density decay was $z_0 = 2.3$ mm.

All species were found to be within the diameter of the nozzle, which is in agreement with experimental results. However, the plasma chemical and reacting flow model is limited to ionisation waves along the symmetry axis of the plasma jet, though experimentally it was found that ionisation waves propagating into the effluent vary their direction. Except for H_2O_2, the maximum of the species' densities were determined close to the nozzle. Due to the diffusion of the gas curtain into the effluent, H and O atoms were fully consumed within the first 5 mm below the nozzle, while the densities of HO_2 and H_2O_2 increased between $z = 2$ mm and $z = 4$ mm. The axial density distributions for H atoms, O atoms, and HO_2 radicals were in agreement with the densities determined experimentally, while $1.86 \cdot 10^{17}$cm^{-3} of O_2 and $7.44 \cdot 10^{17}$cm^{-3} for N_2 were added to the feed gas. Notably, the simulated densities for H_2O_2 were a factor of 10 larger than the densities obtained experimentally. This could be due to an over- or underestimation of reactions that include OH radicals, which are strongly connected to the formation of H_2O_2. Furthermore, the experimentally observed counter-propagating ionisation waves were not included into the model, yet, which are an important mechanism for the generation of reactive species, and might be the reason for an additional amount of O_2 within the plasma zone.

The main production reactions for H atoms were determined to be the dissociation of H_2O, and reactions of O atoms and N atoms with OH radicals. H atoms were mainly consumed by O_2 molecules and by HO_2 and OH radicals. For O atoms, the main production was due to the dissociation of O_2 molecules, whereas O atoms were consumed by OH and HO_2 radicals. HO_2 was dominantly formed by the reaction of H atoms with O_2 molecules, and consumed by H atoms, O atoms, and OH radicals. The main production of H_2O_2 was due to the reactions of two OH radicals or two HO_2 radicals. OH radicals were the main consumers for H_2O_2.

By a comparison of the experimental results and the plasma chemical and reacting flow model, it was demonstrated that OH radicals play a key role in the reaction cycle for H_2O_2 as they are involved in several production and consumption reactions for H_2O_2 and its precursors. It was also shown that a certain amount of O_2 needs to be present in the plasma zone to obtain the experimentally determined densities.

Table 7.2: List of reactions used in the reacting flow model.

No.	Reaction[a]	Rate coefficient[b]	References
R1	$H + OH + M \rightarrow H_2O + M$	2.56×10^{-31}	[14]
R2	$H + O + M \rightarrow OH + M$	4.33×10^{-32}	[15]
R3	$H + H + M \rightarrow H_2 + M$	6.00×10^{-33}	[14]
R4	$O + O_2 + M \rightarrow O_3 + M$	5.90×10^{-34}	[16]
R5	$H + O_2 + M \rightarrow HO_2 + M$	2.12×10^{-32}	[17]
R6	$HO_2 + HO_2 \rightarrow H_2O_2 + O_2$	1.63×10^{-12}	[18]
R7	$HO_2 + HO_2 + M \rightarrow H_2O_2 + O_2 + M$	4.98×10^{-32}	[18]
R8	$OH + OH + M \rightarrow H_2O_2 + M$	6.86×10^{-31}	[16]
R9	$OH + OH \rightarrow O + H_2O$	1.87×10^{-12}	[16]
R10	$H + HO_2 \rightarrow H_2 + O_2$	6.66×10^{-12}	[14]
R11	$H + HO_2 \rightarrow H_2O + O$	2.79×10^{-12}	[14]
R12	$H + HO_2 \rightarrow OH + OH$	6.46×10^{-11}	[14]
R13	$O + HO_2 \rightarrow OH + O_2$	3.01×10^{-11}	[18, 19]
R14	$O + HO_2 \rightarrow OH^*_{v=1} + O_2$	1.97×10^{-11}	[18, 19]
R15	$O + HO_2 \rightarrow OH^*_{v=2} + O_2$	7.54×10^{-12}	[18, 19]
R16	$OH + O \rightarrow H + O_2$	3.90×10^{-11}	[19]
R17	$OH^*_{v=1} + O \rightarrow H + O_2$	1.00×10^{-10}	[19]
R18	$OH^*_{v=2} + O \rightarrow H + O_2$	2.50×10^{-10}	[19]
R19	$OH + H_2O_2 \rightarrow HO_2 + H_2O$	1.70×10^{-12}	[18]
R20	$OH + HO_2 \rightarrow H_2O + O_2$	5.80×10^{-11}	[20]
R21	$N_2^* + O \rightarrow NO + N$	7.00×10^{-12}	[21]
R22	$N_2^* + O_2 \rightarrow N_2 + O + O$	2.54×10^{-12}	[21]
R23	$N_2^* + O_2 \rightarrow N_2 + O_2^*$	1.30×10^{-12}	[21]
R24	$O_2^* + N_2^* \rightarrow N_2 + O + O$	2.00×10^{-11}	[22]
R25	$N + OH \rightarrow NO + H$	5.05×10^{-11}	[23]
R26	$N + NO \rightarrow N_2 + O$	2.92×10^{-11}	[24]
R27	$O + NO + M \rightarrow NO_2 + M$	9.90×10^{-32}	[16]
R28	$O + NO_2 + M \rightarrow NO_3 + M$	8.90×10^{-32}	[16]
R29	$O + NO_2 \rightarrow NO + O_2$	1.03×10^{-11}	[18]
R30	$O + NO_3 \rightarrow NO_2 + O_2$	1.70×10^{-11}	[18]
R31	$N + O + M \rightarrow NO + M$	9.16×10^{-33}	[25]
R32	$H + NO + M \rightarrow HNO + M$	3.86×10^{-32}	[26]
R33	$H + NO_2 \rightarrow OH + NO$	1.40×10^{-10}	[26]
R34	$H + NO_3 \rightarrow OH + NO_2$	1.10×10^{-10}	[27]
R35	$O + HNO \rightarrow OH + NO$	5.99×10^{-11}	[26]
R36	$OH + NO + M \rightarrow HNO_2 + M$	6.88×10^{-31}	[24]
R37	$OH + NO_2 + M \rightarrow HNO_3 + M$	2.60×10^{-30}	[16]
R38	$OH + NO_3 \rightarrow HO_2 + NO_2$	2.00×10^{-11}	[18]
R39	$OH + HNO_2 \rightarrow H_2O + NO_2$	5.01×10^{-12}	[26]

[a] M denotes a third body (the concentration of M is $2.45 \times 10^{19}\,\mathrm{cm}^{-3}$).

[b] The units of rate coefficients are $\mathrm{cm}^3\,\mathrm{s}^{-1}$, $\mathrm{cm}^6\,\mathrm{s}^{-1}$ for the second and third order reactions, respectively. The gas temperature is $300\,\mathrm{K}$.

7.4 Bibliography

[1] S.-J. Klose, J. Ellis, F. Riedel, S. Schröter, K. Niemi, I. L. Semenov, K.-D. Weltmann, T. Gans, D. O'Connell, and J. H. van Helden. The spatial distribution of hydrogen and oxygen atoms in a cold atmospheric pressure plasma jet. *Plasma Sources Sci. Technol.*, 29(125018), 2020.

[2] I. L. Semenov and K.-D. Weltmann. Modelling of turbulent reacting flow for a cold atmospheric pressure argon plasma jet. *Plasma Sources Sci. Technol.*, 29(5):055001, 2020.

[3] G. J. M. Hagelaar and L. C. Pitchford. Solving the boltzmann equation to obtain electron transport coefficients and rate coefficients for fluid models. *Plasma Sources Sci. Technol.*, 14(4):722–33, 2005.

[4] W. Van Gaens and A. Bogaerts. Kinetic modelling for an atmospheric pressure argon plasma jet in humid air. *J. Phys. D: Appl. Phys.*, 46(27):275201, 2013.

[5] Y. Fu, J. Krek, G. M. Parsey, and J. P. Verboncoeur. Characterizing the dominant ions in low-temperature argon plasmas in the range of 1–800 Torr. *Phys. Plasmas*, 25(3):033505, 2018.

[6] J. W. Keto, R. E. Gleason Jr, and G. K. Walters. Production mechanisms and radiative lifetimes of argon and xenon molecules emitting in the ultraviolet. *Phys. Rev. Lett.*, 33(23):1365, 1974.

[7] R. Mehnert, O. Brede, and R. Hermann. Quenching of the argon (4s) levels and of the excimer $Ar_2(^3\Sigma_u^+)$ by N_2, N_2O, SF_6 and CF_3H - a pulse radiolysis study. *Int. J. Radiat. Appl. Instrum.: Part C Radiat. Phys. Chem.*, 28(5-6):455–60, 1986.

[8] L. G. Piper, J. E. Velazco, and D. W. Setser. Quenching cross sections for electronic energy transfer reactions between metastable argon atoms and noble gases and small molecules. *J. Chem. Phys.*, 59(6):3323–40, 1973.

[9] S. Novicki and J. Krenos. Absolute quenching cross section for collisions between $Ar(^3P_{0,2})$ and H_2O. *J. Chem. Phys.*, 89(11):7031–3, 1988.

[10] J. W. Keto, C. F. Hart, and C.-Y. Kuo. Electron beam excited mixtures of O_2 in argon. III. Energy transfer to O_2 and O_3. *J. Chem. Phys.*, 74(8):4450–4, 1981.

[11] S. Reuter, J. Winter, S. Iséni, S. Peters, A. Schmidt-Bleker, M. Dünnbier, J. Schäfer, R. Foest, and K.-D. Weltmann. Detection of ozone in a MHz argon plasma bullet jet. *Plasma Sources Sci. Technol.*, 21(3):034015, 2012.

[12] S. Hübner, S. Hofmann, E. M. Van Veldhuizen, and P. J. Bruggeman. Electron densities and energies of a guided argon streamer in argon and air environments. *Plasma Sources Sci. Technol.*, 22(6):065011, 2013.

[13] W. Van Gaens, P. J. Bruggeman, and A. Bogaerts. Numerical analysis of the NO and O generation mechanism in a needle-type plasma jet. *New J. Phys.*, 16(6):063054, 2014.

[14] D. L. Baulch, C. J. Cobos, R. A. Cox, C. Esser, P. Frank, T. Just, J. A. Kerr, M. J. Pilling, J. Troe, R. W. Walker, et al. Evaluated kinetic data for combustion modelling. *J. Phys. Chem. Ref. Data*, 21(3):411–734, 1992.

[15] W. Tsang and R. F. Hampson. Chemical kinetic data base for combustion chemistry. part I. Methane and related compounds. *J. Phys. Chem. Ref. Data*, 15(3):1087–279, 1986.

[16] R. Atkinson, D. L. Baulch, R. A. Cox, R. F. Hampson Jr., J. A. Kerr, M. J. Rossi, and J. Troe. Evaluated kinetic, photochemical and heterogeneous data for atmospheric chemistry: Supplement V. IUPAC Subcommittee on Gas Kinetic Data Evaluation for Atmospheric Chemistry. *J. Phys. Chem. Ref. Data*, 26(3):521–1011, 1997.

[17] J. V. Michael, M.-C. Su, J. W. Sutherland, J. J. Carroll, and A. F. Wagner. Rate constants for $H+O_2+M-> HO_2+M$ in seven bath gases. *J. Phys. Chem. A*, 106(21):5297–313, 2002.

[18] R. Atkinson, D. L. Baulch, R. A. Cox, J. N. Crowley, R. F. Hampson, R. G. Hynes, M. E. Jenkin, M. J. Rossi, and J. Troe. Evaluated kinetic and photochemical data for atmospheric chemistry: Volume I - gas phase reactions of O_x, HO_x, NO_x and SO_x species. *Atmospheric Chem. Phys.*, 4(6):1461–738, 2004.

[19] U. Makhlouf, R. H. Picard, and J. R. Winick. Photochemical-dynamical modeling of the measured response of airglow to gravity waves: 1. Basic model for OH airglow. *J. Geophys. Res.*, 100(D6):11289–311, 1995.

[20] B. A. Thrush and J. P. T. Wilkinson. The rate of reaction of HO_2 radicals with HO and with NO. *Chem. Phys. Lett.*, 81(1):1–3, 1981.

[21] I. A. Kossyi, A. Y. Kostinsky, A. A. Matveyev, and V. P. Silakov. Kinetic scheme of the non-equilibrium discharge in nitrogen-oxygen mixtures. *Plasma Sources Sci. Technol.*, 1(3):207–20, 1992.

[22] J. T. Herron. Evaluated chemical kinetics data for reactions of $N(^2D)$, $N(^2P)$, and $N_2(A^3\Sigma_u^+)$ in the gas phase. *J. Phys. Chem. Ref. Data*, 28(5):1453–83, 1999.

[23] R. Atkinson, D. L. Baulch, R. A. Cox, R. F. Hampson Jr, J. A. Kerr, and J. Troe. Evaluated kinetic and photochemical data for atmospheric chemistry: supplement III. IUPAC subcommittee on gas kinetic data evaluation for atmospheric chemistry. *J. Phys. Chem. Ref. Data*, 18(2):881–1097, 1989.

[24] W. B. DeMore, S. P. Sander, D. M. Golden, R. F. Hampson, M. J. Kurylo, C. J. Howard, A. R. Ravishankara, C. E. Kolb, and M. J. Molina. *JPL Publication 97-4: Chemical Kinetics and Photochemical Data for Use in Stratospheric Modeling*. Pasadena, California: Jet Propulsion Laboratory, California Institute of Technology, 1997.

[25] I. M. Campbell and C. N. Gray. Rate constants for $O(^3P)$ recombination and association with $N(^4S)$. *Chem. Phys. Lett.*, 18(4):607–9, 1973.

[26] W. Tsang and J. T. Herron. Chemical kinetic data base for propellant combustion I. Reactions involving NO, NO$_2$, HNO, HNO$_2$, HCN and N$_2$O. *J. Phys. Chem. Ref. Data*, 20(4):609–63, 1991.

[27] R. B. Boodaghians, C. E. Canosa-Mas, P. J. Carpenter, and R. P. Wayne. The reactions of NO$_3$ with OH and H. *J. Chem. Soc. Faraday Trans.*, 84(7):931–48, 1988.

[28] S. Iséni, A. Schmidt-Bleker, J. Winter, K.-D. Weltmann, and S. Reuter. Atmospheric pressure streamer follows the turbulent argon air boundary in a MHz argon plasma jet investigated by OH-tracer PLIF spectroscopy. *J. Phys. D: Appl. Phys.*, 47(152001), 2014.

[29] M. Gianella, S. Reuter, S. A. Press, A. Schmidt-Bleker, J. H. van Helden, and G. A. D. Ritchie. HO$_2$ reaction kinetics in an atmospheric pressure plasma jet determined by cavity ring-down spectroscopy. *Plasma Sources Sci. Technol.*, 27(095013), 2018.

[30] J. Winter, K. Wende, K. Masur, S. Iséni, M. Dünnbier, M. U. Hammer, H. Tresp, K.-D. Weltmann, and S. Reuter. Feed gas humidity: a vital parameter affecting a cold atmospheric-pressure plasma jet and plasma-treated human skin cells. *J. Phys. D: Appl. Phys.*, 46(295401), 2013.

8 Conclusions

In this work, spatial distributions for reactive stable and transient species that are involved in the reaction cycle of H_2O_2 were determined directly in the effluent of a kINPen-sci plasma jet. Therefore, several diagnostic techniques have been employed and adapted for the use for cold atmospheric pressure plasma jets.

Firstly, the impact of humidity in the feed gas of the kINPen-sci plasma jet on the excitation dynamics and on the formation of $Ar(^3P_2)$ atoms was investigated by means of laser atomic absorption spectroscopy (LAAS) at 811.53 nm. By analysing the temporal evolution of the density of $Ar(^3P_2)$ atoms, features correlating to counter-propagating ionisation waves have been observed, in particular for a high amount of humidity in the feed gas at distances close to the nozzle. The quenching coefficient of $Ar(^3P_2)$ atoms was found to be similar to the rate coefficient of dissociation of water by $Ar(^3P_2)$ atoms, which indicates that water is the dominant quenching species for $Ar(^3P_2)$ atoms. Although the densities for $Ar(^3P_2)$ atoms are reducing for higher contents of humidity in the feed gas, the efficiency of the dissociation of water was higher for larger humidities.

H atoms and OH radicals are a direct product of the dissociation of water, while O atoms could be a result of a secondary dissociation reaction of OH. In this work, the spatial distributions for O atoms and for H atoms were obtained by picosecond TALIF (ps-TALIF). The employment of laser pulses with a duration of picoseconds enabled the determination of the effective lifetime for O atoms. However, quenching reactions for H atoms lead to effective lifetimes lower than the detection limit of the experimental setup. Hence, the effective lifetime for H atoms was calculated from quenching coefficients reported in literature. Similar distributions for the densities of O and H atoms have been determined, which lead to the conclusion that an additional amount of O_2 had to be present within the plasma zone of the plasma jet. It was found that the gas curtain at distances smaller than 1.5 mm to the nozzle had no impact on the densities of O and H atoms. The maximum densities for O and H atoms were found at the exit of the nozzle to be $(3.8 \pm 0.7) \cdot 10^{15}$ cm^{-3} and $(3.5 \pm 0.7) \cdot 10^{15}$ cm^{-3}, respectively. Within the first 5 mm below the nozzle, the densities for O and H atoms decreased linearly to a density below $1 \cdot 10^{14}$ cm^{-3}, which was the detection limit.

HO_2 radicals are an important precursor for the formation H_2O_2. In this work, it was demonstrated, how spatially resolved density distributions in a CAPJ can be obtained by cw-CRDS in a time efficient way, called on/off-resonance method. Instead of taking full spectra for the determination of the densities for HO_2, it was sufficient to measure at two wavelengths; on the peak of the absorption feature at 6638.2 cm^{-1} (on-resonance) and at a the side at 6637.6 cm^{-1} (off-resonance). The absorption coefficient obtained

from full spectra was found to be similar to the absorption coefficient determined by
the on/off-resonance method. By performing radial scans at various distances from the
nozzle, the effective absorption lengths, which are crucial for the determination of the
densities, were determined. An Abel inversion was applied to axial and radial scans in
order to determine a spatial map of the density of HO_2 in the effluent of the kINPen-sci.
It was found that HO_2 was distributed with a Gaussian shape in radial direction. The
maximum was determined to be $(4.8 \pm 0.6) \cdot 10^{14}$ cm^{-3} on the axis 4 mm below the
nozzle. As HO_2 is a result of the reaction of H atoms with O_2 molecules, the measured
densities close to the nozzle lead to the conclusion that a certain amount of O_2 has to
be present within the plasma zone of the plasma jet.

H_2O_2 molecules are typically investigated within a liquid or collected over a large vol-
ume in order to obtain a density that is large enough to be detected by absorption
spectroscopy methods. In this work, the spatial distributions for H_2O_2 were obtained
directly within the effluent of the kINPen-sci plasma jet. Therefore, cw-CRDS at a wave-
length of 8 µm was employed. By performing radial scans with the on/off-resonance
method, the effective absorption lengths were determined. Abel inversion was applied
to determine the spatial distribution. Again, it was found that H_2O_2 was distributed
with a Gaussian shape in radial direction. The maximum density close to the symmetry
axis of the plasma jet was found to be $2 \cdot 10^{14}$ cm^{-3} at a distance of 4 mm below the
nozzle. Due to the experimental setup, no information closer to the nozzle could be
gained.

The experimental results for the determined spatial distributions for O atoms, H atoms,
HO_2 radicals, and H_2O_2 molecules were compared to the boundaries of the flow for the
Ar feed gas, which were obtained previously from Schlieren diagnostics and from particle
image flow velocimetry. It was found that all investigated species were distributed
within the boundaries of the Ar feed gas flow, which confirms the large impact of the
plasma zone on the reactive species composition. Due to the impact of the plasma jet
on the cavity modes in the cw-CRDS experiment, no information closer than 1 mm
in the case of HO_2, and 3 mm in the case of H_2O_2 to the nozzle could be obtained.
However, from the determined absorption lengths for HO_2 and H_2O_2 together with
the distribution of the Ar feed gas flow, an absorption length for axial distances closer
than 1 mm from the nozzle could be deduced for both HO_2 and H_2O_2. Based on
this estimated absorption length, the spatial distributions for HO_2 and H_2O_2 were re-
evaluated. The maxima of the densities were found close to the nozzle with $10 \cdot 10^{14}$ cm^{-3}
for HO_2, and with $2.1 \cdot 10^{14}$ cm^{-3} for H_2O_2. From $z = 1.5$ mm to $z = 10$ mm, both
densities decreased to $5 \cdot 10^{14}$ cm^{-3} and $1 \cdot 10^{14}$ cm^{-3}, respectively.

The impact of the gas curtain close to the nozzle on the reactive species composition was
further investigated by analysing the quenching of the effective lifetimes for O atoms.
For all measured distributions, it was found that a certain amount of O_2 needs to be
present within the plasma zone, which was not a result from leakage of O_2 into the gas
tubings or into the head of the kINPen-sci plasma jet. In order to determine the amount
of initial O_2 that would have been necessary in the plasma zone to explain the obtained
H and O atom densities, and to identify the most dominant reaction pathways, the

experimental results were compared with predictions from a two-dimensional reacting flow model that was coupled with a local zero-dimensional plasma chemical model.

Based on the experimental results, and on the comparison of these results to the numerical simulations, three different zones in the plasma jet could be identified. A schematic of these zones and the chemistry occurring in each zone is depicted in figure 8.1.

Between $z = 0$ mm and $z = 1.5$ mm, the reactive species composition is determined by reactions within the plasma zone of the plasma jet. In contrast to previous expectations, all investigated reactive species, notably even the larger molecules HO_2 and H_2O_2, were mainly produced within the plasma zone. Therefore, an amount of approximately $1 \cdot 10^{17}$ cm^{-3} O_2 in the case of a feed gas humidity of 3000 ppm and for all gas curtain compositions, and of $1.85 \cdot 10^{17}$ cm^{-3} O_2 in the case of dry Ar feed gas and a gas curtain composition that contains more than 20% O_2, has to be present within the plasma zone. The amount of O_2 estimated to explain the observations of this work could be due to different excitation dynamics for the different humidity contents in the feed gas: counter-propagating ionisation waves towards the plasma zone during the second half wave of the excitation cycle lead to the propagation of negative ions, such as O_2^{-2}, that were formed by electron impact reactions with the surrounding atmosphere of a filament, into the plasma zone. With these counter-propagating ionisation waves, also air could have been sucked into the plasma zone. The water content in the feed gas influences the excitation dynamics and thus probability of the counter-propagating ionisation waves as this was shown for the temporal evolution of the densities for $Ar(^3P_2)$ atoms. A detailed analysis of these counter-propagating ionisation waves remains for
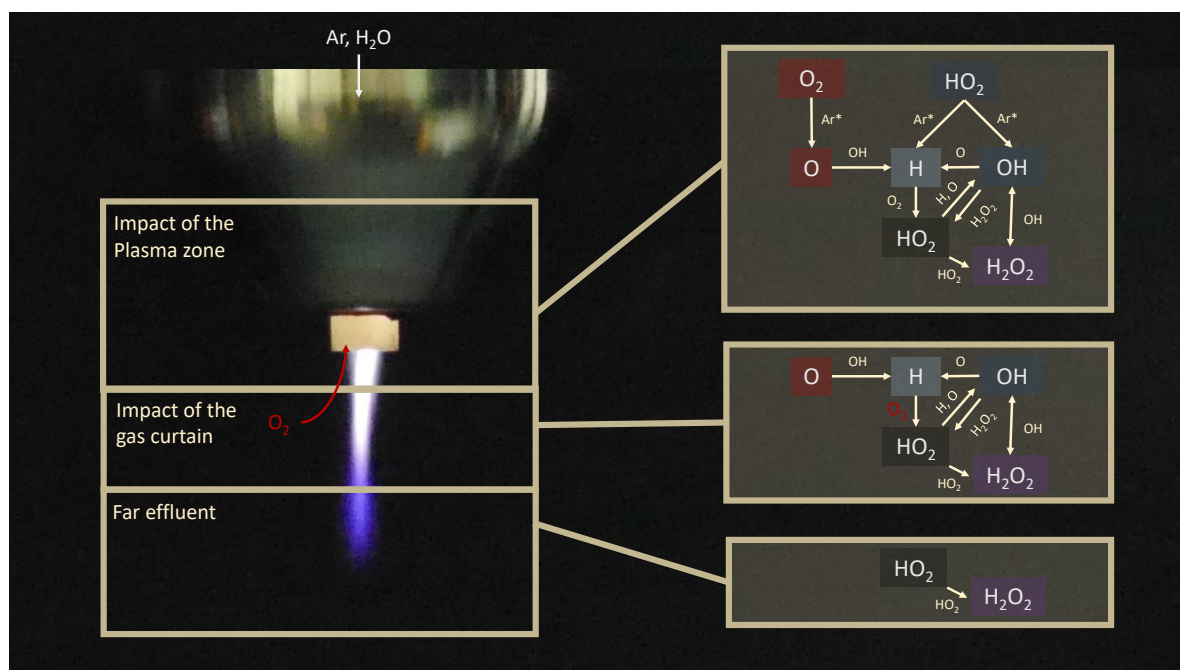

Figure 8.1: The three different zones in the effluent for the kINPen-sci plasma jet that impact the reaction cycle for H_2O_2.

further investigations.

Between $z = 1.5$ mm and $z = 5$ mm, reactions with the molecules in the gas curtain lead to a strong consumption of atoms and molecular radicals. However, the impact of the gas curtain on the formation of H_2O_2 is negligible. Since OH plays a key role on the formation of HO_2 and H_2O_2, the determination of its spatial density distribution is crucial to obtain further insights into the formation and consumption of HO_2 and H_2O_2. In particular for biomedical applications, the density of OH radicals is relevant for the investigation of plasma-related processes. However, its determination was not possible within the timeframe of the reported work.

At distances larger than $z = 5$ mm, no atomic radicals have been determined, and the number densities for molecular radicals decreased by approximately a factor of 2 compared to the densities close to the nozzle. Typically, a biological sample is positioned at distances larger than $z = 10$ mm below the nozzle. Based on the analysis of the densities in the effluent without the impact of a surface below the plasma jet, it can be concluded that basically HO_2 radicals and H_2O_2 molecules can interact with a biological sample at these distances. The impact of such a surface or a biological sample on the reactive species composition remains for further investigations. Nevertheless, since most of the reactive species composition is determined by reactions within the plasma zone, no significant changes are expected.

In order to tailor the reactive species composition, admixtures to the feed gas have been proven beneficial. In particular by admixtures of water or O_2, the densities of HO_2 and H_2O_2 can be increased. By applying a gas curtain, the densities of atomic species and molecular radicals can be reduced. For further insights, how the gas curtain influences the reactive species composition, additional investigations are needed.

Acknowledgements

Many great people at different laboratories have contributed to this work and without them this thesis would not have been at this stage. First and foremost I would like to express my gratitude to my esteemed supervisors Dr. Jean-Pierre van Helden and Prof. Dr. Jürgen Röpcke for their guiding advices and unwavering support during the last 4 years. I would also like to offer my special thanks to Prof. Dr. Klaus-Dieter Weltmann for the facilitation of this PhD-project at the Leibniz Institute for Plasma Science and Technology (INP).

The staff members of the Plasma Diagnostics group past and present have been an invaluable support at every stage of this work. Without the support of all technical staff members, this work could not have been produced. In particular, I would like to thank Prof. Dr. Ronny Brandenburg for his time and the numerous insightful discussions during the complete PhD project. I would like to extend my thanks to Dr. Robert Bansemer for his contribution to the experiments for the determination of $Ar(^3P_2)$, to Dr. Igor Semenov for the development of the plasma chemical and reacting flow model and the subsequent discussions about the reaction chemistry in the kINPen-sci plasma jet, and to Dr. James Ellis for his contribution to the publication of the measurements for O and H atoms with ps-TALIF and his relentless support with the English language. I would also like to thank Thijs Keur and Levin Krös for having the honor to supervise them and to bring the magic and hard work of performing continuous wave cavity ring-down spectroscopy to the next generation.

I would like to express my sincere gratitude to Prof. Grant Ritchie for his encouraging support during my research stays at the Department of Chemistry at the University of Oxford in the United Kingdom. Special thanks go to Dr. Katherine Manfred, Dr. Michele Gianella, for their continuous supervision and encouragement, and the master students Sioned Press and Helen Norman for their assistance during the measurements for HO_2. I am proud and honoured for being a part-time member of the outstanding Ritchie group.

I would also like to thank Prof. Dr. Timo Gans and Prof. Deborah O'Connell at the York Plasma Institute for the hospitality of my research stay and their support during the measurements for O and H atoms with ps-TALIF at the Department of Physics at the University of York in the United Kingdom. Special thanks go also to Dr. Frederik Riedel, Dr. Kari Niemi, Richard Armitage, and Dr. Sandra Schröter for their assistance, and the staff of the YPI for the warm welcome.

I am deeply grateful to my partner, my nuclear family and my Shoto Shorinji Kempo-family for their relentless encouragement and belief in me.